DISSERTATION

The Hydrothermal Route To Imide-linked Network- and Framework Materials

ausgeführt zum Zwecke der Erlangung des akademischen Grades eines
Doktors der Naturwissenschaften

unter der Leitung von
Prof. Dipl.-Chem. Dipl.-Ing. Dr.rer.nat. Miriam M. Unterlass, MSc
Fachbereich Chemie der Universität Konstanz

eingereicht an der
Technischen Universität Wien
Fakultät für Technische Chemie

von

Marianne Lahnsteiner, MSc.
[redacted]

[redacted]

Wien, am 28.02.2023

[redacted]

Für meine Eltern Ingrid und Max.

Kurzfassung

Hoch stabile und funktionelle organische Polymernetzwerke (OPNs) sind für grüne Anwendungen wie Gassorption und -trennung, Katalyse und Elektronik von großem Interesse. Besonders vielversprechend sind Polyimid (PI) Netzwerke aufgrund ihrer hervorragenden chemischen, thermischen und mechanischen Stabilität sowie ihrer Affinität für CO_2-Gasmoleküle. Leider erfordert die Herstellung von PIs typischerweise umweltgefährliche Lösungsmittel und Katalysatoren, was die Nachhaltigkeit der Materialien erheblich beeinträchtigt. In den letzten Jahren wurde die hydrothermale Polymerisation (HTP), die ausschließlich Wasser als Lösungsmittel verwendet, als grüne synthetische Alternative entwickelt und gründlich untersucht, um *lineare* PIs zu generieren. Bis 2021 war HTP von PIs jedoch auf lineare Strukturen beschränkt.

In dieser Dissertation wurde gezeigt, dass es möglich ist, HTP auf drei Dimensionen zu erweitern: Es wurden amorphe PI-Netzwerke erhalten, die eine thermische Stabilität bis zu 595 °C und eine trimodale Porosität aufweisen, die von ultramikroporös ($<0{,}8$ nm) bis hin zu meso- und makroporös reicht. Durch Variation der Reaktionsbedingungen wurde das Verhalten der Netzwerke in HT-Bedingungen aufgeklärt und eine Hypothese für die mikromorphologische Evolution aufgestellt. Schließlich wurde gezeigt, dass Upscaling und Verarbeitung des PI-Netzwerkpulvers durch Warmpressen möglich ist.

Außerdem wurde mittels eines Molekülmodelsystem gezeigt, dass Imidereversibilität unter hydrothermalen Bedigungen möglich ist, was die Voraussetzung für die Erzeugung von kristallinen OPNs (i.e., covalent organic frameworks aka COFs) ist. Jedoch erst die Zugabe von Anilin, das ähnlich wie Mineralisatoren in anorganischer HTP agiert, ermöglichte die Entstehung von höhermolekularen 2D PI-COFs. Leider führte Anilin auch zu einer Mischung von untrennbaren Nebenprodukten, die die dreidimensionale Anordnung der 2D PI-COFs verhinderte und somit keine permanente Porosität erreicht werden konnte.

Schließlich wurde gezeigt, dass HTP tatsächlich in der Lage ist, kristalline Netzwerke ohne die Notwendigkeit von Anilin als Zusatzstoff zu erzeugen. Aufgrund mehrerer Festkörperanalysetechniken wird vorgeschlagen, dass H-bonded organic frameworks (HOFs) erhalten wurden, die auf linearen PI-Rückgraten basieren, die über Seitengruppen über Wasserstoffbrückenbindungen vernetzt sind. Es wurde die Vermutung angestellt, dass die Bildung von PI-HOFs temperaturabhängig ist, wo erhöhte Reaktionstemperaturen zu einer Transformation zu linearen PIs bei gleichzeitiger Entfernung von Seitengruppen führt. Es wurde angenommen, dass HTP entscheidend für die Kristallinität beider Produkte ist, da eine Erhitzung im Festkörper zu weitgehend amorphen Produkten führte.

Insgesamt zeigte diese Arbeit, dass heißes Wasser in der Lage ist, nicht nur amorphe Netzwerk-PIs zu produzieren, sondern auch Bedingungen für die Entstehung einer Fernordnung in Netzwerk-PIs bereitzustellen.

Abstract

Highly stable and functional organic polymer networks (OPNs) are of interest for green applications such as gas sorption and separation, catalysis, and electronics. Especially, network polyimides (PIs) are promising due to their outstanding chemical, thermal and mechanical stabilities as well as their affinity for CO_2 gas molecules. Unfortunately, PIs' preparation typically requires hazardous solvents and catalysts, which gravely diminish the materials' sustainability. In recent years, hydrothermal polymerization (HTP) – which employs solely water as solvent – was developed and thoroughly investigated as a green synthetic alternative to generate *linear* PIs. Until 2021, HTP had been limited to *linear* PI materials.

Within in this thesis it was shown that it is possible to extend HTP of PIs to three dimensions: Amorphous PI networks were obtained, which exhibited thermal stabilities up to 595 °C and a trimodal porosity which ranged from ultra-microporous (<0.8 nm), to meso- as well as macroporous. By varying the reaction conditions, the networks' behavior in HT conditions was elucidated. I.e., the formation of an intermediate multitopic monomer salt could be identified as well as a hypothesis for the micromorphological evolution was devised. Finally, it was shown that up-scaling and processing via warm-pressing of the PI network powder is feasible.

Furthermore, it was proven that HTP provides imide reversibility, which is necessary to produce crystalline PI networks (aka covalent organic frameworks (COFs)), using a small molecule model system. However, it was shown that the addition of aniline was necessary to generate extended 2D PI-COF sheets, acting similarly to mineralizers in inorganic HTP. Unfortunately, aniline also led to a mix of inseparable side-products, which prevented the sheets' three dimensional (3D) arrangement and hence no permanent porosity could be achieved.

Finally, it was shown that HTP is indeed capable of generating crystalline framework materials without the necessity of aniline as additive. On the basis of several solid-state techniques it is proposed that H-bonded frameworks (HOFs) were obtained, which are based on linear PI-backbones that are laterally H-bonded via side-groups. The PI-HOFs' formation is believed to be T-dependent, where elevated reaction temperatures (T_Rs) lead to a transformation to linear PIs accompanied by side-group removal. HTP was assumed crucial for both products' crystallinity, as solid-state heat treatment led to largely amorphous products.

Overall, this thesis showed that hot water is able to not only produce amorphous *network* PIs but also provides reversibility conditions for inducing long range order in PI *framework* materials.

Danksagung

An dieser Stelle möchte ich mich bei Prof. Miriam Unterlass für ihr wissenschaftliches Guiding, für das entgegengebrachte Verständnis in allen Angelegenheiten sowie für ihre Unterstützung bedanken. Es waren sehr lehrreiche Jahre in denen ich mich sowohl als Wissenschaftlerin als auch persönlich stark weiterentwickelt habe.
Auch Prof. David Mecerreyes gebührt großer Dank für die Einladung zu einem Forschungsaufenthalt in Spanien, auch wenn dieser aufgrund der COVID Pandemie nie stattgefunden hat. Danke auch Nicolas Goujon für die anschließende sehr gute Zusammenarbeit über die Ferne.
Großer Dank geht außerdem an Prof. Herwig Peterlik für die vielen Stunden die er in SAXS Messungen und Datenauswertungen investiert hat. Unsere fachlichen Diskussionen haben mir große Freude bereitet und ich durfte dabei sehr viel lernen.
Bedanken möchte ich mich auch bei meinen Kolleg*innen aus der Arbeitsgruppe deren Unterstützung, Beistand und Know-How unerlässlich für die Fertigstellung dieser Dissertation waren. Besonders hervorzuheben sind Hipassia Moura, die viele Stunden mit mir am Elektronenmikroskop verbrachte und Eleonora Hochreiner aufgrund ihrer großartigen Arbeit während ihres Praktikums.
Weiters möchte ich allen meinen Dank aussprechen die mich mit fachlichem Wissen und Messungen unterstütz haben: Jérôme Roeser (Gassorption), Thomas Konegger (Mercury Intrusion Porosimetry, Warmpressen und mechanische Tests), Werner Artner (Röntgendiffraktometrie), Johannes Theiner (Elementaranalyse), Hanspeter Kählig (Festkörper NMR), Karin Föttinger und Gernot Pacholik (Inerte Thermische Behandlung und MS Analyse), Johannes Bernardi (Transmissions Elektronenmikroskopie) und Frances Allen (Helium Ionen Mikroskopie).
Besonderer Dank geht an das Frauennetzwerk FemChem, welches mich aufgefangen hat als meine Arbeitsgruppe die TU verließ. Das wohlgesinnte, unterstützende und hilfsbereite Klima und die großartigen Projekte haben mir besonders in der Schlussphase der Dissertation Kraft und Motivation gegeben.
Ich möchte mich auch herzlich bei meinen Eltern, Ingrid und Max, bei meinen Schwestern Lisa und Pauline, bei meinem Freund Fabian und meinen Freundinnen Helena, Marie-Claire und Katharina für die immense Geduld, die motivierenden Worte und den bedingungslosen Rückhalt bedanken.
Außerdem darf ich mich für die Zeit und Expertise meiner beiden Gutachter*innen, Prof. David Mecerreys und Karin Föttinger, bedanken.

Table of Contents

List of Abbreviations and Symbols

Abbreviations

^{13}C-CPMAS	^{13}C cross polarization magic angle spinning
^{1}H-NMR	^{1}H-nuclear magnetic resonance
2D	two dimensional
3D	three dimensional
4-MPA	4-methyl phthalic anhydride
aaHTP-AP	aniline assisted HTP in sealed ampoules
aaHTP-MW	aniline assisted HTP in microwave reactors
ATR-FT-IR	attenuated total reflectance Fourier transform infra red
Bz	Benzidine
COF	covalent organic framework
CP	critical point
CPP	conjugated porous polymer
CTF	covalent triazine framework
DAT	diaminotriazine
DCC	dynamic covalent chemistry
DCM	dichloromethane
DMF	dimethylformamide
DMSO	dimethylsulfoxide
DSC	differential scanning calorimetry
EA	organic elemental microanalysis
equiv.	equivalent
EU	European Union

FWHM	full width at half maximum
HCP	hypercrosslinked polymer
HIM	Helium ion microscopy
HOAc	acetic acid
HOF	H-bonded organic framework
HPLC	high-performance liquid chromatography
HPP	high-performance polymers
HT	hydrothermal
HTP	hydrothermal polymerization
HTP-AC	HTP in unstirred batch autoclaves
HTP-AP	HTP in sealed ampoules
HTP-MW	HTP in microwave reactors
htR	hydrothermal regime
HTS	hydrothermal synthesis
HTW	high-temperature water
ICDD	international center for diffraction data
ITT-MS	inert thermal treatment coupled to mass spectrometry
LC	liquid crystal
LCD	liquid crystal display
LiPo	Lithium polymer
MAD	median absolute deviation
MC	model compound
MeOH	methanol
ML	mass loss
MIP	mercury intrusion porosimetry
Mpc-network-PIM	metal containing porphyrin network PIM
MPI	microporous polyimide
MS	monomer salt
MS(MA-Bz)	monomer salt from MA and Bz

MS(MA-PDA)	monomer salt from MA and PDA
ncR	near critical regime
NMP	N-methyl pyrrolidone
OPN	organic polymer network
PA	phthalic anhydride
PAA	poly (amic acid)
PBPI	*p*-biphenylene pyromellitimide
PDA	*p*-phenylene diamine
PDF	powder diffraction files
PI	polyimide
PI-HOF	PI-based HOF
PI(TAPB-PMA)	PI network from TAPB and PMA
PI-COF	PI linked COF
PI-COF-2	PI-linked COF from TAPB and PMA
PI-COF-2_{AP}	PI-COF-2 via HTP in sealed ampoules
PIM	polymer with intrinsic microporosity
PMA	pyromellitic acid
PMA-An	product mixture obtained from PMA and aniline
PMDA	pyromellitic dianhydride
POP	porous organic polymer
PPBA	*p*-phenylene 1,4-pyromellite-bisamide
PPBI	*p*-phenylene pyromellite-bisimide
PPIA	*p*-phenylene pyromellit-(imide-amide)
PPPI	*p*-phenylene pyromellitimide
PSD	pore size distribution
p-XDC	*p*-xylylene dichloride
PXRD	powder X-ray diffraction
RT	room temperature
SA_{BET}	surface area obtained via Brunauer-Emmet-Teller method

SAXS	small angle X-ray scattering
$scCO_2$	supercritical CO_2
scR	supercritical regime
SDGs	sustainable development goals
SEM	scanning electron microscopy
SiO_2/PI(TAPB-PMA)	silica and PI(TAPB-PMA) hybrid material
^{s}MAD	median absolute deviation after correction
S_B	smectic lamellar LC motif
S_E	smectic herringbone LC motif
S_NAr	nucleophilic aromatic substitution
SSP	solid state polymerization
ssPI(TAPB-PMA)	PI(TAPB-PMA) from SSP
TAPB	1,3,5-tris(4-aminophenyl)benzene
TEM	transmission electron microscopy
TFA	trifluoro acetic acid
TGA	thermogravimetric analysis
THF	tetrahydrofurane
TPHCA	triphenylene-2,3,6,7,10,11-hexacarboxylic acid
WAXS	wide angle X-ray scattering

Symbols

(hkl)	Miller indices
$a,\ b,\ c$	lattice parameters
Cu-K$_\alpha$	X-ray energy used for PXRD and SAXS measurements
D	crystallite domain size
d_{hkl}	spacing between successive (hkl) planes
η	viscosity
ϵ	static dielectric constant
f	branch functionality
F_{q}	form factor
H	thickness of lamellae
I_{q}	intensity of Bragg reflections
$\mathrm{k_1}$	reaction constant
$\mathrm{k_{-1}}$	reaction constant of the back reaction
K_{w}	ionic product of water
m/z	mass-to-charge ratio
$\tilde{\nu}$	wavenumber
p	pressure
q	scattering vector
ρ	density
S_{q}	structural factor
T	temperature
T_{c}	critical temperature
T_{d}	decomposition temperature
T_{g}	glass transition temperature
T_{ML}	temperature of mass loss
t_{R}	reaction time
T_{R}	reaction temperature
$V\,\%$	volume percent
$wt.\,\%$	weight percent

List of Figures

List of Tables

1 Introduction

Modern society faces numerous challenges. The recent outbreak of COVID-19 quickly turned into a pandemic forcing physical-distancing measures on many areas around the world. As a consequence, the process of global digitalization was further accelerated leading to an increased demand for technology that enables fast and accessible online communication and data transfer all over the globe. At the same time, resources for state-of-the-art technical devices and non-renewable energy sources have been depleting over the past decades. On top, the world has been shaken by the ramifications of the climate crisis to an extent that civil actions as "Fridays for Future" are demanding a rapid change in our largely fossil fuel-based lifestyle. This has been partly reflected in the "2030 Agenda for Sustainable Development" adopted by all United Nations member states with the focal point on the 17 Sustainable Development Goals (SDGs). The established SDGs tackle issues like poverty, health, and education in regard to climate change.[1] Furthermore, in July 2021, the European Union (EU) presented the "European Green Deal", setting the goal of being the first climate neutral continent by 2050. Within this deal, the EU is striving towards a 55 % reduction of emissions from cars and increasing the share of renewable energy sources to 40 % by 2030.[2]

In order to tackle these pressing issues and reach the goals of the European Green Deal, new and sustainable alternatives to harmful and out-dated technologies are necessary. In the past decades, innovative inventions paved the way for pioneering technology, completely changing our way of communication, data processing, mobility, and even social co-existence. For example liquid crystal displays (LCDs) allowed the generation of the many opto-electronic devices which are nowadays indispensable in our daily lives such as computer monitors, instrument panels, and mobile phones.[3] Furthermore, the new generation of lithium-ion batteries (Nobel Prize in Chemistry

2019), Li polymer (LiPo) batteries, power all our portable electronic devices, enabling the continuous exchange of information in our mobile society.[4] Moreover, LiPo batteries' high energy density, lightweight design, and long life-span drove the development of all-electric vehicles to a point where they are able to compete in terms of operating range as well as economically with fuel-based vehicles.

In many of these innovations, highly functional materials have played a key role. Specifically, organic and polymer materials are crucial in technically demanding applications due to their great versatility and unique properties, which are hardly met by any other type of material. The large amount of available organic scaffolds with a great variety of functionalities provides sheer endless possibilities for generating fine-tuned, purpose-specific polymer materials.

Many high-tech applications require high materials' resilience towards strenuous operating conditions. High-Performance Polymers (HPPs) are a class of organic polymers exhibiting high thermal stability and are hence of special interest for such applications. Typically, HPPs are built-up by an aromatic, linear backbone with strong inter-chain interactions. As a result, temperature stabilities up to 300 °C in air and up to 500 °C under inert atmosphere are observed.[5,6] A representative example for HPPs are aromatic polyimides (PIs). Their extraordinary thermal stability makes them perfect candidates for replacing metals and glass in many fields of high-performance applications such as electronics, aerospace and automotive industries. A prominent example is Kapton®, a PI that was designed as an insulating thin film for electronic applications in the 1960's and quickly became the best selling HPP in the world.[6,7]

A recent advancement of conventional HPPs are three dimensional (3D) network polymers. Due to their 3D structure, some network polymers exhibit unique properties like porosity, swellability, malleability, and in some cases enhanced crystallinity, just to name a few. These properties make network polymers promising candidates for future high-tech applications like gas storage, catalysis, and electronic materials. Especially porous organic polymers (POPs) are of interest, as they exhibit permanent porosity with possible pore sizes of less than 2 nm.[8] This results in high surface areas comparable to zeolites and activated carbon. POPs are typically amorphous structures due to the irreversibility of the polymerization reaction. Inducing re-

versibility in the bond-formation reaction fosters the generation of long-range order in the 3D structure, resulting in crystalline network polymers, e.g., covalent organic frameworks (COFs). Due to their crystallinity, COFs exhibit uniform pores which are advantageous for applications where a precise topology is needed.[9]

The generation of POPs and COFs typically requires harsh synthetic conditions like high-boiling organic solvents and toxic catalysts. As green materials are a prerequisite for green applications, an alternative synthetic route is necessary. Unterlass and co-workers recently reported on the green method hydrothermal polymerization (HTP), solely employing the co-monomers and hot water to generate highly crystalline and temperature stable PIs.[10] Although further organic moieties have been synthesized via this method (polybenzimidazoles, polyperinones, and polyazomethines),[11,12] HTP has been limited to linear organic HPPs until 2021.

In this thesis, it is explored if the benign synthetic method HTP can be utilized to generate polymer materials that combine high-performance properties with a 3D network structure. First, the necessary theoretical background is set out in Chapter 2 followed by this thesis' aims and objectives in Chapter 3. Afterwards, the results are discussed in three subchapters: In 4.1, the general feasibility of synthesizing a 3D PI network via HTP will be discussed. Moreover, the resulting properties (thermal stability, morphology, porosity, and processability) will be presented. In Chapter 4.2, the general reversibility of the imide moiety in HTP will be elucidated by using a small molecule model system. Furthermore, it will be discussed if the reversibility can be transferred to extended structures via the use of additives alongside the potential formation of a side-product. Finally, in Chapter 4.3, it will be discussed if the reversibility under hydrothermal (HT) conditions can be sufficient to generate framework polymers without the necessity of additives.

2 Theoretical Background

2.1 Organic Polymer Networks

Organic polymer networks (OPNs) have become omnipresent in many aspects of our daily lives due to their great versatility. In contrast to their inorganic equivalents (e.g., zeolites and mesoporous metal oxides), OPNs are made up of exclusively light elements (C, H, N, S, and O) which makes them light-weight and versatile materials. OPNs are among the most commonly used polymeric materials as they are available to a broad field of applications ranging from adhesives[13] and rubbers[14] to gas storage[8], electronic materials,[15,16] and catalysis[17].

The broad field of OPNs can be viewed from various angles, such as polymer chemistry, high-performance materials and crystalline solids, just to name a few. For the purpose of this thesis, the focus lies on the perspective of solid-state behavior and topology of OPNs.

2.1.1 Definition and Properties

The basic concept of a network is nicely illustrated by two macroscopic examples from everyday live: in Figure 1A, a fishing net is displayed, where multiple flexible strands are tied together using knots. The flexibility leads to an overall disordered structure. On the other hand, Fig.1B shows a more ordered version, i.e., a construction framework where stiff segments are connected generating a grid with precise voids. Analogously, OPNs are constructed of segments (aka strands) that are connected via junctions (c.f. knots in a fishing net or connections in a construction framework). The junctions need to have three or more groups ("branch functional-

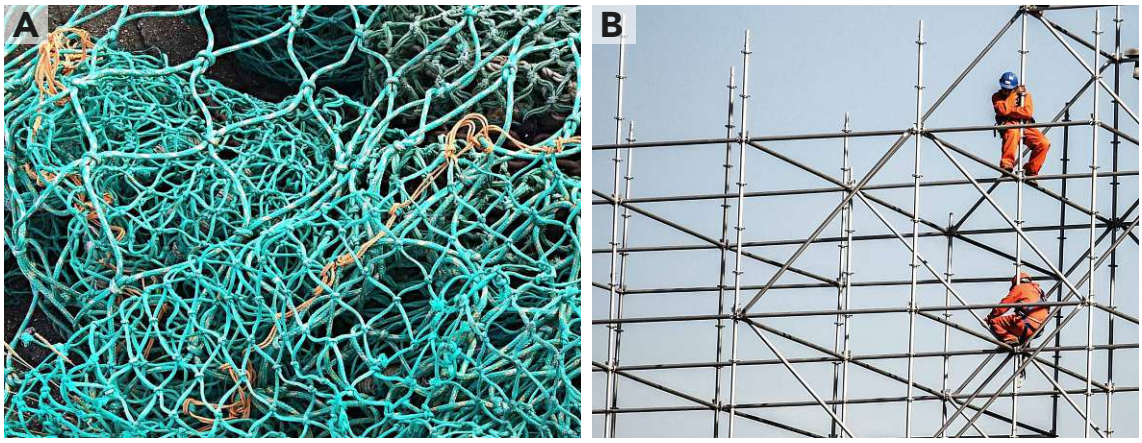

Figure 1: Everday live examples of networks. A: A fishing net with different mesh sizes. B: A construction framework resulting in a highly ordered structure with precise voids. Photos downloaded from pixabay.com and pexels.com, respectively.

ity", $f > 2$) which connect f strands building up a three dimensional (3D) structure with a sequence of bonds with infinite[a] continuation.[9,18,19] The majority of OPNs bear flexible strands such as linear polymer chains or flexible, short molecules, which would correspond to the strands of a fishing net. Their random connectivity and topology leads to different length scales of the segments (i.e., loops) and the voids in between them. As a result, OPNs can display a great variety of useful properties such as elasticity, permanent porosity, and malleability.[20] In a few cases, the strands can also be rigid cyclic and hetereocyclic moieties which compare to the example of a construction framework. Here, a more ordered structure with precise voids is obtained, where even long-range order, aka crystallinity, is possible. These exceptional OPNs are referred to as frameworks rather than networks in literature.

According to Johnson, the junctions employed in OPNs can fall in any part of the spectrum of bonding interactions.[9] They can be of physical nature, i.e., van der Waals interactions or H-bonding, or of chemical nature, i.e., covalent bonds. Conventionally, networks are hence referred to as "supramolecular" or "covalent" networks in literature.[9]

According to the type and the amount of bonds present, OPNs can be divided into four major classes: (i) *Gels* are based on either covalent or supramolecular bonds, which are swollen in e.g., water or organic solvents (e.g., gelatine, polyacrylamide hydrogel). Typically, gels are soft but can undergo quite large deformations.[9]

[a] Infinite as in continuation to the surface of the macroscopic sample in contrast to finite molecules.

(ii) *Elastomers* are most often composed of covalently bonded macromolecules and exhibit elasticity which allows for reversibly stretching to high extensions (e.g., vulcanized natural- and silicone rubbers).[9] (iii) *Thermoplastics* comprise macromolecules linked via usually very strong non-covalent interactions which lead to rigid solids below their glass transition temperatures (T_g). Above their T_g, the solids turn into processable, viscoelastic fluids. Examples are polyethylene, polypropylene, and polyvinylchlorides, which are the three most produced plastics globally (aka commodity and engineering plastics, i.e., packaging and construction industry).[9,21] (iv) The last group are *thermostes*, normally engendering covalent bonds as junctions and stiff moieties for strands. Consequently, thermosets are highly rigid materials which are typically insoluble in all solvents, not processable after synthesis, and exhibit a decomposition temperature (T_d) instead of a T_g. Examples are polyurethanes and epoxy resins. Some of the thermoset OPNs feature outstanding thermal, mechanical and chemical stabilities and are therefore considered HPP,[5,6] which makes them highly interesting for applications in electronics, aerospace and automotive industries. Due to their outstanding properties, thermoset OPNs are the main focus of this thesis and hence will be discussed in greater detail in the following chapters.

2.1.2 Network Formation and Structure

There are two main ways an OPN can be formed: (i) linear polymer chains are connected via crosslinks or (ii) the 3D structure is constructed using multifunctional monomers (A_2/B_f method; $f > 2$)[b]. Both chain-growth polymerizations and step-growth polymerizations can be used.

Chain-growth polymerization proceeds via adding one monomer at a time to a growing polymer strand. Incorporating multifunctional monomers allows for crosslinking polymer chains resulting in an OPN with a certain degree of crosslinking (e.g., divinylbenzene for radical polymerizations).[9] Modern radical polymerization tech-

[b] Please note, that the branch functionality f of both A and B monomer can exceed 2 in order to obtain a 3D network structure. As in most cases only one monomer's branch functionality is greater than 2 and in order to emphasise that *at least* one's f must exceed 2, the term A_2/B_f method will be used throughout this thesis.

niques are widely used for network synthesis such as nitroxide mediated polymerization[22], atom transfer radical polymerization[23,24], and reversible addition-fragmentation chain transfer polymerization.[25,26]

Moreover, step-growth polymerizations can be utilized, where both polyadditions (without by-products) as well as polycondensations (with a condensation by-product, e.g., H_2O) are possible.[27] For linear polymers, monomers with $f = 2$ are used (e.g., A_2 and B_2). First, the monomers react to dimers, then oligomers and finally to polymers. To obtain networks, both (i) crosslinking and (ii) A_2/B_f method can be used:

(i) A prepolymer is obtained via step-growth polymerization and is in a second step linked via a crosslinking agent. For example, phenolic resins are obtained via firstly condensation of phenol with formaldehyde to obtain the prepolymer (i.e., *Novolac*), which is soluble or even liquid. Second, hexamethylene tetraamine is added as crosslinking agent, which results in a stable, insoluble network used for construction purposes.[28]

(ii) For the A_2/B_f method, multifunctional monomers are used where at least one monomer exhibits $f > 2$ (e.g., A_2 and B_3). Upon reaction, highly branched polymers are formed.[29] Possible types of reactions are boroxine, amide, imine, and imide condensations, as well as metal-catalyzed reactions (e.g., Friedel-Crafts alkylations and Suzuki couplings).[8]

The network structure of an OPN is determined by both chemical composition and topological structure, which further govern its properties.[20] Chemical composition is determined via the type of chemical moieties used and is crucial for introducing functionality in the final network. Topology on the other hand solely describes how the junctions and strands are arranged and connected within the network regardless of their chemical composition.[20] To impart certain desired properties in an OPN, both the chemical composition and topology can be tuned.

First, chemical composition can be addressed via introducing specific functionalities in the used monomers or precursors. The availability of a great variety of organic scaffolds provides a broad foundation for fine-tuning OPNs' properties. For exam-

ple, the type of linking function determines acid- and base stability, i.e., boroxine linkers are susceptible to acid hydrolysis, whereas imide functions are highly resistant towards acids. Introducing heteroatoms, like nitrogen, can lead to enhanced CO_2 capture properties.[30] Cyclic- and heterocyclic functions contribute to OPNs' thermal and chemical resistance. Furthermore, incorporating redox-active sites can make them suitable candidates for battery electrode materials.[31,32] Also, monomers that induce π-conjugation across several repeating units not only increase stability but are also thought to be suitable for applications such as in light emitting- and harvesting materials.[33,34]

Second, properties like elasticity and porosity are a direct consequence of network topology. Therefore, it is not only of interest what functionalities an OPN features, but also how its topology can be comprehended and also tuned. The largest share of OPNs are amorphous or semicrystalline.[20] This is due to irreversible reactions used, which proceed until a percolated network is formed. This statistical process leads to amorphous materials which consequently comprise of topological features covering various length scales.[20] Specifically, in the range of 10-100 nm OPNs' topology shows inhomogeneities in junction/strand distribution, which is caused by concentration fluctuations during network formation.[35] Between 1 and 10 nm, the topology is governed by dangling/unreacted functionalities, entanglements, and loops. Lastly, at a molecular scale (< 1 nm), properties are mainly dictated by the atomic connectivity, i.e., chemical composition of the monomers. However, the most important topological feature at this length scale is the branch functionality, which dictates the maximum number of strands connected to a junction.[20]

In order to obtain defect-free and highly ordered OPNs, structural control over the network formation process is key. One possibility is to induce reversibility in the bond formation. There are examples of crystalline, thermoplastic OPNs (e.g., Nylon and Kevlar®) which exhibit enhanced crystallinity due to strategies like slow quenching. This leads to reversibility of their secondary intermolecular interactions (e.g., van der Waals or H-bonding), hence facilitating the generation of an ordered structure.[36] Recently, this concept was extended to the class of covalently bonded OPNs: In 2005, the first fully crystalline, covalently bonded OPNs (based on boroxines and boronate esters) have been reported and the term

"covalent organic frameworks" (COFs) was coined by Yaghi and co-workers.[37] Again, reversibility of the bond formation was key, leading to error-correction within the material resulting in outstanding crystallinity (this will be discussed in detail in chapter 2.2.2). Additionally, the use of rigid, multifunctional monomers with defined spatial orientation of branch-functionalities leads to uniform pores in both size and shape. While this feature enables applications such as molecule specific gas storage and separation, some of the typical network properties (i.e., elasticity and processability) are lost.

Combining rigid, functional monomers with the concept of (both amorphous and crystalline) OPNs, thermoset OPNs with permanent porosity are obtained. In the past decades, porous OPNs have gained significance in the realm of porous materials due to their outstanding surface areas, stabilities, and functionalities. Both amorphous and crystalline porous OPNs will be discussed in the following chapter.

2.2 Porous Organic Polymer Networks

Porous materials can be classified according to their pore widths: Macroporous materials have pores larger than 50 nm, mesoporous materials' pore widths range from 2-50 nm, and microporous materials are defined as materials with pores smaller than 2 nm. The term *nanopore* comprises all three categories but with a maximum diameter of $\sim$100 nm.[38] This classification stems from the behavior of the different pores during physisorption experiments typically employing N_2 as analyzing gas. Depending on the pore size, different "physisorption isotherms" are obtained (see Figure 2). Such isotherms describe the amount of gas adsorbed with increasing relative pressure p/p^0 (p^0 is the saturation pressure at operation temperature, i.e., 77 K for N_2).[38]

In the case of microporous materials, a Type I isotherm is observed: As micropores are in the size range of molecular dimensions ($\sim$1 nm), only a monolayer of gas molecules can be adsorbed. Therefore, the amount adsorbed increases quickly at low p/p^0 but then approaches a limiting value.[38]

Non- or macroporous materials exhibit a Type II isotherm, where an unrestricted mono- and multilayer formation up to high p/p^0 can be observed. In case of monolayer formation, a sharp knee at the point of completion of monolayer coverage can be discerned. Subsequently, the uptake is increasing without limit when $p/p^0 = 1$. If there is no identifiable monolayer formation, a Type III isotherm results.[38]

Mesoporous adsorbents display a Type IV isotherm: After mono- and multilayer formation, pore condensation takes place, i.e., the gas condenses to a liquid-like phase in the confined space. Finally, a typical saturation plateau is reached.[38]

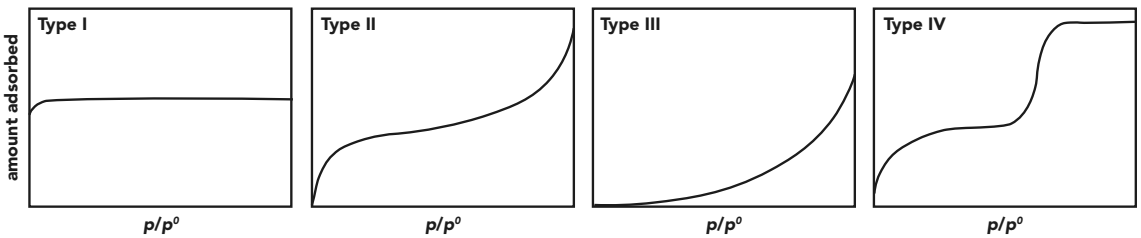

Figure 2: Physisorption isotherms. Type I isotherms are indicative for microporous adsorbents, Type II and Type III for non- and macroporous adsorbents, and Type IV for mesoporous adsorbents.

As a consequence of their size ranges, the three types of pores also result in different materials properties. The smallest pores, i.e., micropores, are mostly responsible for high and accessible surface areas ($>1000\,m^2\,g^{-1}$).[8] This can beneficial for e.g., catalysis as it implies a greater abundance of catalytic sites within the material. Furthermore, guest molecules sorbed inside micropores interact with the pore walls most efficiently if their dispersion force fields overlap, i.e, pore dimensions match molecular diameters.[39] As micropores are in the size range of small molecules ($\sim 1\,nm$), they are available to selective processes like selective adsorption, and heterogeneous catalysis.[40,41] Matching the dimensions of host materials and guest molecules has hence been a focal point with the prominent examples of microporous zeolites, which are widely used for catalysis, oil refining, ion-exchange, and gas sorption on industrial scales.[40,42] However, some processes (e.g., catalytic conversion) rely on molecular transport rates, and therefore their performances sometimes suffer from limited diffusion within micropores.[41] In contrast, meso- and macropores allow greater molecular mobility throughout the material, enhancing the rate of molecular exchange between the transport media and the material. Combining micro-, meso- and macropores, i.e., introducing hierarchical pore structures, has been shown to provide materials with both selective properties and enhanced molecular transport.[40,43,44]

Conventional nanoporous materials (i.e., zeolites and activated carbon) are well established in industry, however they often suffer from either low functional versatility or are ill-defined in both topology and surface chemistry, which leads to low chemo- and/or size-selectivtiy.[45] In contrast, porous OPNs offer functionality per design as well as in some cases topological control. This makes way for novel technologies (such as H-storage and batteries) necessary for tackling challenging energy and environmental issues.[8,17] The large family of porous OPNs includes both amorphous and crystalline examples. Types of amorphous OPNs are hypercrosslinked polymers (HCPs), polymers of intrinsic microporosity (PIMs), conjugated porous polymers (CPPs) and are sometimes summarized within the umbrella term "porous orgnic polymers" (POPs)[c]. Therefore, the term POPs will be used for amorphous, porous

[c] In literature, the denotation of these polymer classes is somewhat arbitrary and no clear hierarchy could be discerned.

OPNs throughout this thesis. Examples of crystalline porous OPNs are, e.g., COFs and hydrogen-bonded organic frameworks (HOFs).[46]

In the following section 2.2.1, the advancement of POPs, three different types (HCP, PIM, and CPP) and their synthetic strategies will be discussed. In Chapter 2.2.2, two of their crystalline counterparts (COFs and HOFs) will be elaborated and how topological control can be achieved.

2.2.1 Amorphous Porous Polymer Networks

POPs can be generated from a broad range of building blocks via various types of non-reversible reactions that form covalent bonds. Consequently, many different classes of POPs with various properties result. The key feature that combines them is permanent porosity, i.e., the pores do not collapse upon solvent removal. POPs often exhibit very high surface areas but no long range order. As a consequence, their pores are not monodisperse and their topology is typically ill-defined.[8,47]

Hypercrosslinked Polymers

The first reported POPs were HCPs. In the 1970s, Davankov and co-workers were the first to perform post-synthetic crosslinking of conventional polystyrene. These hypercrosslinked polysterenes ($>40\%$) are also known as "Davankov-resins".[48] Therefore, a lightly cross-linked precursor was immersed in e.g., dichloromethane (DCM). Consequently, swelling caused large free volume between polymer chains. To "lock" the polymer in its swollen state, crosslinks (e.g., *p*-xylylene dichloride (*p*-XDC)) were introduced via Friedl-Crafts alkylation, cf. Figure 3A. This yielded nanoporous structures with surface areas of 600-2000 $m^2\,g^{-1}$. Hypercrosslinked polystyrenes are now commercially available materials which offer a broad range of microporosity and surface functionality.[49] For example, they can easily be modified via sulfonation or hydroxylation, which makes them ideal candidates for high pressure liquid chromatography (HPLC) column materials.[50]

Later on, alternative synthetic approaches towards HCPs were investigated. For example, the direct Friedl-Crafts alkylation via self-condensation or copolymeriza-

tion using the monomers *o*-, *m*-, and *p*-XDC, 4,4'-Bis(chloromethyl)-1,1'-biphenyl, and bis(chloromethyl)anthracene was performed by Wood et al. in 2007.[51] Furthermore, the crosslinking of polyanilines with diiodoalkanes or formaldehyde via nucleophilic substitutions[52] or with aromatic moietites via Ullmann and Buchwald coupling[53] was introduced by Germain and co-workers.

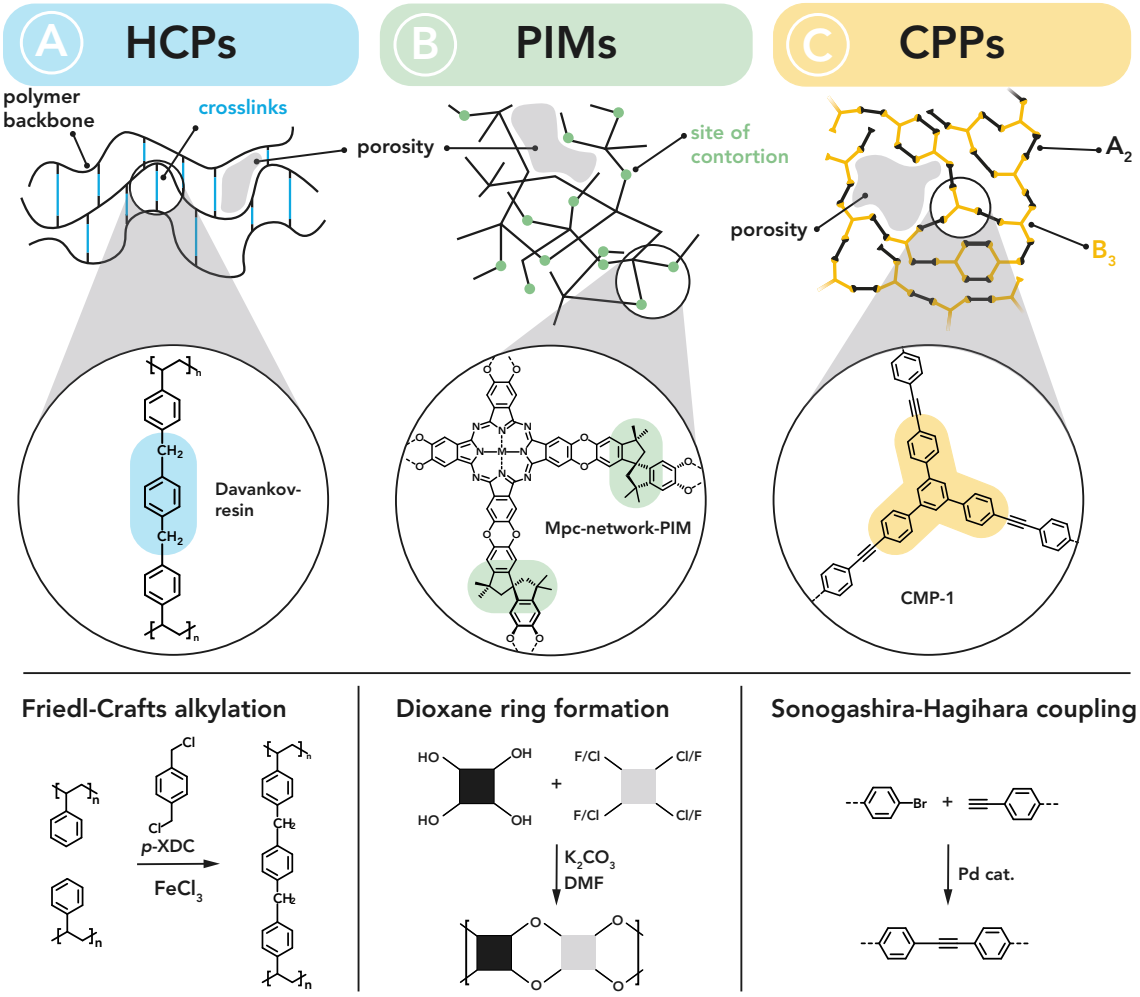

Figure 3: Overview over three amorphous porous OPN types. A: Schematic of a HCP. The first HCP was polystyrene which was cross-linked (blue) via Friedl-Crafts alkylation using e.g., *p*-xylylene dichloride (*p*-XDC) as crosslinker. B: Schematic of a PIM. The first reported PIM was phthalocyanine-based and coordinated via a metal ion ("Mpc-network-PIM"). The connecting moieties are fused dioxane rings which result in rigidity of the network. C: Schematic of a CPP from multifunctional monomers (i.e., A_2 and B_3). The first reported CPPs (e.g., CMP-1) were generated via Sonogashira-Hagihara coupling of conjugated monomers leading to extended conjugation throughout the network.

Polymers of Intrinsic Microporosity

In contrast to HCPs, PIMs are constructed using the A_2/B_f method. The key to their permanent porosity is the use of not only rigid monomers, but also the

presence of a "site of contortion". This site of contortion introduces a kink in the polymer backbone leading to inefficient packing in the solid state. This generates free volume aka porosity (see Figure 3B top). Therefore, PIMs are defined as "continuous networks of interconnected intermolecular voids that form as a direct consequence of shape and rigidity of the component macromolecules"[49]. Notably, PIMs are not necessarily cross-linked networks, but also stiff, contorted polymer chains (with $f = 2$) were found to exhibit high free volumes. These polymers are however not thermoset, but amenable to solution based processing.[45]

The first PIMs were synthesized by Budd and McKeown in the early 2000s.[17] Specifically, they reported on phthalocyanine and porphyrin networks containing metal ions (e.g., Zn^{2+} and Cu^{2+}) using monomers with a spiro-center (i.e., a tetrahedral carbon atom that is shared by two rings) as cite of contortion. In Figure 3B, an example for a metal containing porphyrin network PIM (Mpc-network-PIM) is depicted as an example. The comonomer combination of catechol units and halogenated benzene moieties enables the aromatic nucleophilic substitution (S_NAr) resulting in a fused dioxane ring. The spiro-center dictates the non-linear shape and together with the rigidity induced by the fused rings imparts microporosity. As a result, these networks exhibited surface areas of roughly 900 $m^2\,g^{-1}$.[17] Subsequently, employing different monomers (e.g., triptycene and fluorene) and linking functions (e.g., amides and imides) led to the tunability of PIMs gas permeability and separation properties.[54,55]

In addition to their microporosity, PIMs are typically highly stable in respect to temperature and chemical strain. Storage under ambient conditions for several years is possible, as well as contact with acids, bases and oxidizing agents.[49] This is caused by their structural features (i.e., strong covalent bonds, rigid and/or cyclic backbones, and aromatic moieties) which compare to those of HPP. These properties paved the way for many industrially relevant applications, such as gas separation membranes, adsorption of organic pollutants, heterogeneous catalysis, and hydrogen storage.[17,47,56]

Microporous Polyimides

A noteworthy subclass of POPs are microporous PIs (MPIs). In general, fully aro-

matic PIs are at the very peak of thermal stability among HPPs (above 500 °C) due to their extremely rigid heteroaromatic skeleton and highly stable imide moieties. Therefore, MPIs have gained increasing attention within the POPs field but also due to their other outstanding properties: large surface areas, high mechanical strengths, and chemical stabilities. Furthermore, the imide moieties cause high abundance of nitrogen and oxygen atoms which favourably interact with CO_2 or NH_3 gas molecules. Consequently, MPIs are promising candidates for applications in gas capture/separation[57,58] but also for energy storage.[59,60]

MPIs are classified according to their topological structure either as PIM-PIs or HCP-PIs. PIM-PIs are linear PIs employing one monomer containing a spiro-center or a triptycene moiety.[54,61,62] Their rigid and contorted backbones prevent the dense packing of the polymer chains and therefore lead to surface areas of up to $1000\,m^2\,g^{-1}$. HCP-PIs on the other hand are 3D networks obtained via the A_2/B_f method. Typically, dianhydrides are condensed with polyamines via solution condensation or solvothermal reactions.[58,63–66] The high degree of crosslinking combined with the rigid backbone leads too abundant micro- and mesopores as well as surface areas up to $2403\,m^2\,g^{-1}$. Therefore, HCP-MPIs are especially interesting for applications with demanding operation conditions.

Conjugated Porous Polymers

Another subfamily of POPs are CPPs (see Figure 3C). This class stands out due to combining high surface areas/permanent porosity and an extended π-conjugation throughout the network.[67] Some of the extended π-systems are highly efficient luminescent materials with high charge carrier mobility, which makes them promising for light harvesting in e.g., optoelectronic applications.[68] Furthermore, CPPs are interesting for energy storage, e.g., via chemically storing H_2 molecules employing reversible hydrogenation/dehydrogenation of alkyne/alkene bonds within the network.[69,70] Additionally, exciton migration throughout the network can be used for chemical sensing via fluorescence-on and -off detection.[71,72]

The underlying strategy is based on connecting π-conjugated building blocks in a way that extends the conjugation, hence creating a fully conjugated network. A

broad range of available conjugated moieties such as simple phenyl units, extended arenes, fused aromatic rings, phenylethynylene derivatives, and heterocyclic units have been employed in the synthesis of CPPs.[34] Again, using the A_2/B_f method, these units are stitched together via strong covalent bonds which at the same time maintain their π-conjugation. To do so, a variety of reactive groups is available, such as bromoarenes, iodoarenes, aromatic boronic acids, cyano-substituted arenes, aromatic aldehydes, ethynyl-substituted arenes and amino-substituted arenes.[34] The obtained conjugated π-systems are inherently rigid leading to permanent porosity with average pore sizes below 2 nm.

The first CPPs were synthesized by Cooper et al. in 2007.[73] They reported on the Sonogashira-Hagihara coupling of aromatic alkynes with aromatic halides leading to poly(aryleneethynylene) networks. Ever since, the field of CPPs gained increasing significance and many different polymerization reaction types have been investigated. First, other metal catalyzed methods have been explored, such as Suzuki-Miyuara-,[74] Glaser-,[75] and Yamamoto coupling[72]. Later on, also synthetic strategies without metal catalysts were studied, using polymerization reactions like cyclotrimerization[76], Schiff-base formation[77], Knoevenagel condensation[78], and Friedl-Crafts type reactions[79]. Some reaction types are also tolerant towards building blocks bearing functional groups (e.g., alcohol, amine, fluoride, nitro, pyridyl and methyl groups). This allows for tuning the network's hydrophobicity for e.g., dye adsorbtion.[80]

Taken together, the availability of different reaction types and the diversity of building blocks make CPPs a broad platform for advanced functional material design. It is even possible to gain partly control over pore volumes. Specifically, it was shown that strut length, linker geometry (ortho, meta, para), the use of copolymerizations (three reactive components, statistical), and tuning reaction conditions like temperature and solvents can lead to higher surface areas.[34] Despite surface areas of up to $\sim$2000 $m^2 g^{-1}$, CPPs typically exhibit a broad range of pore sizes which are often a mixture of micro- and mesopores. This is caused by the irreversibility of the underlying polymerization reactions which are therefore governed by kinetic control. Consequently, the preparation of discrete pores still

remains a challenge in the field of CPPs.[34,81–83]

Summing up, the broad field of POPs offers the design of highly versatile materials for various applications. They exhibit stability, functionality, permanent porosity and high surface areas regardless of their amorphicity. However, topological control and hence precise structural definition is not achieved within this polymer class.

2.2.2 Crystalline Frameworks

Today, the vast majority of OPNs are amorphous, but the realm of crystalline organic frameworks is continuously growing. In contrast to amorphous POPs, organic frameworks exhibit long range order and precise topology. This leads to uniform pores in both shape and size per design. Both covalent bonds (i.e., in COFs) as well as secondary interactions (e.g., in HOFs) are amenable to the formation of a crystalline OPN. Notably, monomeric precursors for crystalline OPNs are termed "tectons" and their branch functionality is often referred to as "di-, tri-,.., multitopic" in literature, describing their ability to influence the final materials' topology. In the next section, it will be elaborated how to use such tectons and their multitopic properties to gain control over these materials' topology. Specifically, two examples, i.e., COFs and HOFs will be discussed.

2.2.2.1 Covalent Organic Frameworks

It was not until the 21st century that it was possible to generate extended crystalline OPNs based on covalent bonds, aka COFs.[37] COFs are composed of organic building blocks which result in defined voids. The materials' properties are low mass-density (as low as $0.17\,g\,cm^{-3}$),[84] permanent porosity (up to $\sim 4000\,m^2\,g^{-1}$),[84] and high thermal stability. Therefore, they are highly interesting for applications in gas storage and separation, as well as catalysis. Conventionally, inorganic framework materials, aka zeolites, are widely used for such applications in industry; e.g., petrochemical cracking.[42] However, the design of zeolites suffers from low versatility of the available precursors and their porosity is often limited to the microporous region (< 2nm). In contrast, COFs offer great versatility due to the plethora of available organic scaffolds and reported pore sizes up to 5.3 nm.[85] Therefore, COFs combine the framework properties of zeolites with the great versatility of POPs. To do so, it is necessary to induce crystallinity via gaining topological control over the OPN formation process. Therefore, specific synthetic strategies need to be employed. Like for some POPs, the A_2/B_f method is applied to generate COFs. However, to achieve atom precision and induce crystallinity, two design principles are crucial: (i) reticular chemistry and (ii) dynamic covalent chemistry (DCC). The

two principles will be elaborated in the following.

Design Principles and Strategies

Per definition, "reticular chemistry is the study of linking discrete chemical entities through strong covalent bonds into extended frameworks and large discrete molecular structures."[86] This means, that the chemical structure and topology of a COF can be rationally designed via carefully selecting the chemical entities, aka monomers. Therefore, the monomers need to feature specific functionalities that allow the formation of linkages in a chemically and geometrically defined fashion. Specifically, there are four aspects to consider while selecting the monomers: (i) the type of interactions they will engender when linked, (ii) their directionality, (iii) their geometry, and (iv) their dimensions (i.e., length and size). All aspects will guide the synthesis to a specific structure, i.e., direct the assembly of an ordered framework. Hence, these monomers are often referred to as building blocks in literature. Depending on the spatial geometry of the building blocks, various structures with specific pore shapes are obtained and depending on the size/length, the pore size will be determined. Typically, rigid and symmetric building blocks are used because they lead to the most symmetric possible framework, according to the principle of reticular synthesis.[84]

When designing a potential framework, the first step is to identify a target topology and deconstruct it into its basic geometric units. For example, when targeting a hexagonal topology, the basic units are e.g., trigonal (C_{3h}) and linear (C_{2h}); cf. Figure 4. These units are then analyzed in regard to their points of extension, aka connectivity. In the case of the hexagonal example, the trigonal unit has three points of connectivity and the linear one only two. Consequently, the corresponding molecular building blocks need to be tri- and difunctional (also referred to as di- and tritopic) in order to generate a hexagonal framework. Using planar building blocks, various 2D structures can be obtained, such as tetragonal, rhombic, trigonal, and dual-pore kagome (see Figure 4). The stacking of these 2D layers can lead to continuous nano-channels with diameters determined via the dimensions of the used building blocks. When using at least one building block with a T_d geometry, 3D structures can be achieved, e.g., diamondoid. 3D topologies often

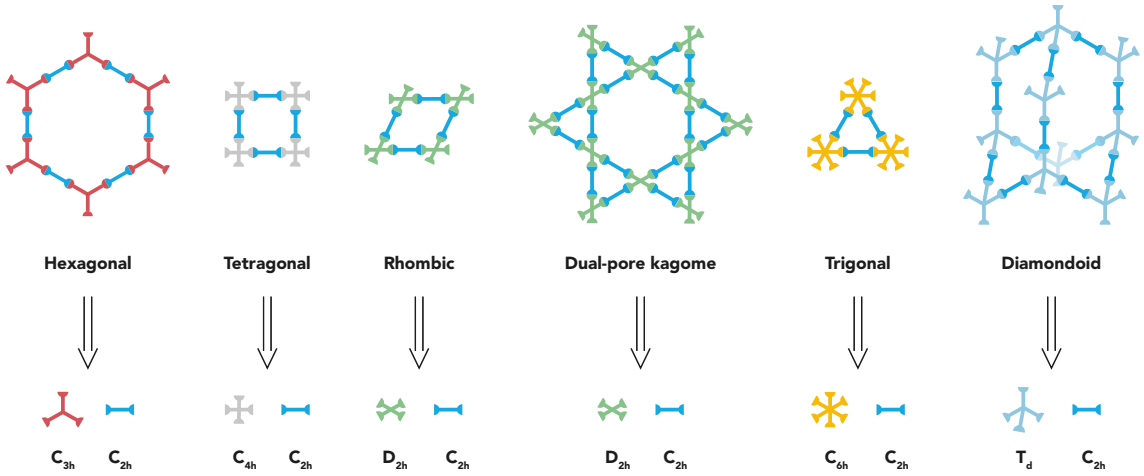

Figure 4: Overview over topologies achieved via reticular synthesis and their underlying geometrical building blocks. From left to right: Hexagonal made up from C_{3h} and C_{2h} elements, tetragonal made up from C_{4h} and C_{2h} elements, rhombic made up from D_{2h} and C_{2h} elements, dual-pore kagome made up from D_{2h} and C_{2h} elements, trigonal made up from C_{6h} and C_{2h} elements, and diamondoid made up from T_d and C_{2h} elements. The first five topologies result in a 2D COF, while the last one yields a 3D COF.

tend to interpenetrate yielding different pore sizes and shapes. The majority of COFs are 2D because planar building blocks are readily available compared to non-planar ones.[86] In Figure 4, some of the possible framework topologies and their corresponding building blocks are depicted.

However, a reticular approach alone does not lead to crystallinity. Some POPs' precursors would also match a reticular strategy, yet no crystallinity is obtained. One of the reasons for the lack of crystallinity is that kinetically controlled reaction processes are employed, which lead to irreversible covalent bonds. In contrast, thermodynamic control allows for microscopic reversibility which further leads to crystalline extended structures.[86] Therefore, the covalent bond needs to have the ability to be formed, broken and again reformed under equilibrium control leading to the thermodynamically most stable product (see Figure 5, product C). This concept, i.e., dynamic covalent chemistry (DCC) is based on the understandings of supramolecular chemistry. Supramolecular chemistry is a discipline where superstructures (e.g., proteins) are afforded via reversible, weak, non-covalent bonds (e.g., H-bonds) dominated by thermodynamic control.[87,88] Both, supramolecular chemistry and DCC, involve bonding processes that are reversible and the formation of products that are in continuous equilibrium. This commonality does not only lead to thermodynamic control, but also enables

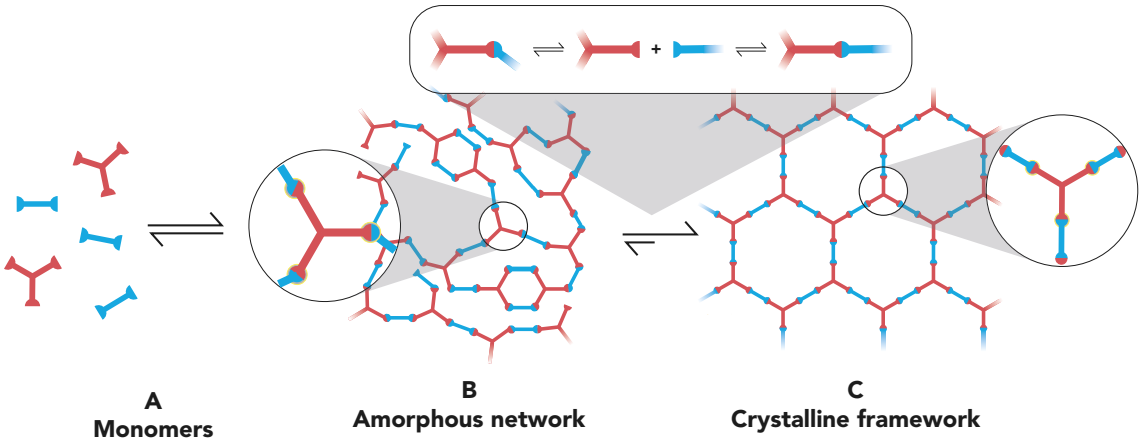

Figure 5: Dynamic covalent chemistry concept. The covalent bonds formed between A: the monomers form B: an amorphous network, i.e., the kinetic product are broken and then C: are reformed as the thermodynamic product, a crystalline framework.

"error-checking" or "proof-reading", which eradicates thermodynamically unstable products. This is especially important when generating thermoset materials, as post-synthetic purification is challenging to impossible. On the one hand, the formation of covalent bonds is in general less reversible than non-covalent interactions because of their inertness. This means that the equilibration process is much slower compared to supramolecular chemistry, which often makes catalysts necessary. On the other hand, covalent bonds are much stronger and therefore the obtained extended structures, i.e., COFs, are much more robust compared to non-covalent aggregates.[89] To realize DCC in COF synthesis, the desired covalent bonds (i.e., linker types) and the corresponding reaction media/catalysts need to be chosen in a way that allows reversibility.

Linkage Types and Synthetic Methods

In general, all synthetic methodologies for covalent bond formation are of potential interest for COF synthesis as long as the reaction conditions are found where reversibility is possible. Over the past two decades, various reaction types and synthetic methods have been found amenable to DCC and successfully yielded COFs.

To achieve a thermodynamic equilibrium, the reaction media (solvent mixtures and ratios) and the conditions (T, p, and the presence absence of additives/catalysts) need to be carefully tuned. Synthetic methods include ionothermal and mechanochemical synthesis, however typically, COF polymerizations are performed under solvothermal conditions in either flame sealed pyrex tubes or mi-

crowave assisted synthesis. Used solvents are organic, aprotic and polar at temperatures between 85 and 250 °C. Especially the ratios of solvent mixtures need to be balanced with care, as the solubility of the building blocks is crucial for achieving thermodynamic control. Often, catalysts are necessary like acetic acid, or isoquinoline. Finally, a closed reaction system is necessary in order to ensure precise stoichiometry and inert atmosphere.[90] New reaction conditions needed to be found for every new linkage, often even for every new monomer system employed. A few examples, their synthetic conditions, and their relative stabilities are discussed below.

The first COFs reported by Yaghi and co-workers in 2005, were focusing on 2D, boron based COFs.[37] Reacting boronic acids in a mixture of mesitylene:dioxane in a 1:1 ratio at 120°C yielded a boroxine-linked COF with high crystallinity. Combining boronic acids with catechols in the same solvent ratio at 100 °C resulted in a COF made up of boronate ester linkages (cf. Figure 6A). The water molecules released during the condensation reaction are crucial for the reversibility of the reaction. At the same time, this is the reason why boron-based types of COFs suffer from hydrolytic and oxidative strain.[91] Therefore, also other linkage types were explored in recent years. Nitrogen containing functionalities like imine and hydrazone (i.e., based on Schiff-base chemistry, cf. Figure 6B) were used.[92,93] Reacting aldehydes with amines in a mixture of 10:2 dioxane:aqueous acetic acid resulted in imine-based COFs. Replacing the amines with hydrazine units and adding mesitylene to the solvent mixture enabled the synthesis of hydrazone-linked COFs. Both COFs showed higher stability towards hydrolysis relative to their boron-linked counterparts. However, the created Schiff-base-linked COFs are acid labile, as acetic acid is necessary for catalyzing the linkage formation. Attempts to stabilize the bonds are tedious and limited to 2D frameworks.[94,95] Another linkage type with promising stability was explored: triazines (Figure 6C). Triazine-linked COFs, also referred to as covalent triazine frameworks (CTFs), are generated from a cyclotrimerization reaction of nitriles. However, CTFs require harsh reaction conditions (400 °C, molten $ZnCl_2$ acting as medium as well as catalyst) to ensure reversibility.[76] As not many building blocks withstand such conditions, CTFs suffer from low versatility. Some of the highest chemical, thermal and mechanical

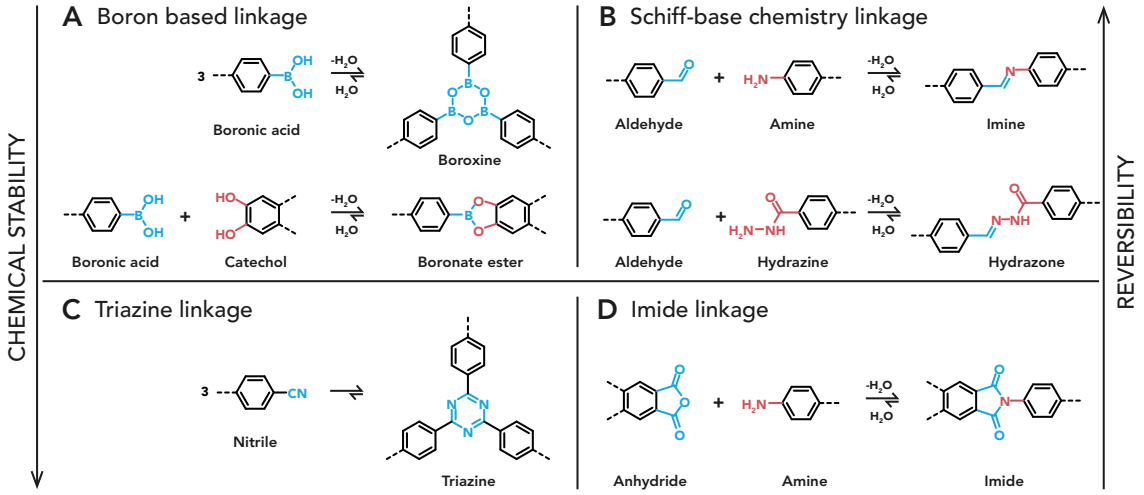

Figure 6: Linkage chemistry used for COF synthesis. A: Boron based linkages; top: boroxine from selfcondensation of boronic acids, bottom: boronate ester from condensation of boronic acid moieties and catechol units. B: Schiff-base chemistry linkages; top: imine from the reaction of an aldehyde with an amine moiety, bottom: hydrazone from the reaction of an aldehyde with hydrazine moiety. C: Triazine linkages from cyclotrimerization of nitriles. D: Imide linkage from cyclocondensation of anhydride with amine moieties.

stabilities were observed for exclusively aromatic and heterocyclic linkages, e.g., imide-linked COFs (PI-COFs; cf. Figure 6D).[85,96] PI-COFs are obtained from polycyclocondensations using anhydride and amine functionalities. The enhanced stabilities makes them especially interesting for applications where the working conditions pose high chemical, mechanical, and thermal strain. In contrast to imine-linked COFs, reversibility is achieved via basic conditions (e.g., isoquinoline as catalyst) and at much higher temperatures (90-120 vs. 200-250 °C).[85,96] Therefore, high boiling solvents like N-methyl pyrrolidone (NMP) are often mixed with mesytilene or dioxane. Unfortunately, these robust linkages introduce a different problem: higher chemical stability counteracts the principle of DCC leading to a trade-off between stability and crystallinity.[97] As a result, compared to many other COF classes, PI-COFs are challenging to crystallize and high reaction temperatures are necessary. Therefore, PI-COFs are among the least represented class in COF literature.[85,96,98–107]

Properties and Applications

Chemical and thermal stabilities are not the only properties governed by different linkage types. By selecting a specific linkage type, various properties can be achieved and exploited for specific properties. At first, COFs were identified as ideal materials for gas storage applications due to their strong covalent bonds and high surface

areas. On top of high surface areas, the lewis basic nature of nitrogen containing linkages leads to enhanced affinity towards binding CO_2 within in the framework which can be exploited for gas storage/separation applications.[108–110] Furthermore, linkages that generate extended π-conjugation lead to in-plane conductivity which, e.g., enables enhanced charge carrier mobility.[111]

In addition to different linkage types, a plethora of available building blocks makes way for the design of materials with outstanding properties. The concept of employing highly functional building blocks to design OPNs on a molecular level was already discussed for amorphous POPs. However, amorphicity limits certain applications due to ill-defined structures. In contrast, COFs offer precise molecular design and well-defined topology. Together, this opens up a great potential in terms of materials design for different properties and applications.

As mentioned above, typical building blocks are aromatic and therefore rigid, such as benzene, di-, tri-, tetra-phenylene, and naphthalene, as required for reticular synthesis. On top, various functionalities like heterocycles or carbonyl groups can be incorporated and hence tuning of properties is possible. For example, COFs can be designed to possess redox-active skeletons using e.g., anthraquinone units. Defined channels for, i.e., ion transport within the COF structure makes them highly interesting as organic electrode materials for Li-ion batteries.[106] Generally, solvent stability, easily accessible catalytic sites and facile mass transport throughout the COF makes them ideal candidates for catalysis. For example, Pd(II) ions were coordinated to imine bonds within an imine based COF which generated a highly efficient catalyst for Suzuki-Miyaura reactions.[112] Furthermore, Lotsch and co-workers showed that a hydrazone-based COF doped with platinum could be utilized for photocatalytic hydrogen production.[113] Wan and co-workers reported on the synthesis of a photoconductive, boron-based COF using pyrene building blocks. They showed that harvesting visible light was achieved, which makes the material highly interesting for applications in optoelectronics or photovoltaics.[114]

Moreover, it is possible to introduce functional groups in the building blocks that are tolerated during the reticulation process such as alkyl chains in different lengths or hydroxy groups.[115,116] Such "channel wall functionalizations" can either be used to tune the pore sizes or allow post-synthetic modifications. This was reported to

lead to enhanced CO_2 uptake and gas sorption selectivity.[115,116] Many more COFs with outstanding properties and potential applications (e.g., chemical sensing,[104] medical applications,[117,118] and waste water treatment[100,119]) have been reported in literature.

Summing up, COFs combine the advantages of crystalline zeolite materials with the great structural diversity of amorphous OPNs. Their designability in both structural as well as electronic aspects leads to highly functional and tunable properties which is hardly met by any other class of materials. On the downside, the COFs with the highest crystallinity, like boron- and imine based COFs, are not the most stable and cannot be devised for applications with harsh operation conditions. On the other hand, COFs with high stability (i.e., triazine- and imide based COFs) are tedious to crystallize. Solving the predicament of stability versus crystallinity therefore remains subject of current research.[97,120]

2.2.2.2 H-bonded Organic Frameworks

It is not always necessary to use covalent bonds to form a durable and functional material. Secondary bonds can also construct highly stable structures depending on the type of interactions, their strength and their number. Specifically, H-bonds are omnipresent and dominate the assembly of many supramolecular systems. The use of H-bonds for the self-assembly of discrete organic molecules to produce potentially porous materials was already proposed in the 1990s. Yet, it was not until 2010 that a HOF with permanent porosity was reported and the term HOF was coined by Chen and co-workers.[121] Like COFs, HOFs are highly crystalline, porous materials that are formed via reversible bond formation using carefully selected, rigid organic building blocks. In contrast to COFs, HOFs are self-assembled through much weaker H-bonds compared to covalent bonds. These H-bonds are flexible and highly reversible and therefore engender certain advantages in the obtained materials. Moreover, HOFs are obtained from mild synthetic conditions, are solution processable, and they exhibit easy regeneration and healing. On the downside, HOFs are not as stable as COFs and collapsing of pores often prevents permanent porosity. Nevertheless, their unique features make HOFs a potentially tunable platform for the construction of functional materials.[122]

Concept and Design Strategies

As the H-bonds in HOFs are weaker than covalent bonds, their reversibility is higher. Consequently, highly crystalline structures are possible. However, challenges lie in the construction of stable, rigid and permanently porous HOFs. The concept and design strategies to overcome these challenges are summarized below.

First, the conceptual basis of utilizing H-bonds for the assembly of superstructures needs to be set out. The basic H-bond is found as a type of interaction between two water molecules, where the hydrogen atom is in between two oxygen atoms with negative partial charge. This can be extended to other systems, including highly electronegative atoms such as nitrogen and fluorine. Typical H-bond energies are found in the range of 10-40 $kJ\,mol^{-1}$, with a few exceptions reaching up to 170 $kJ\,mol^{-1}$. These bond energies are much lower than the energies found for covalent bonds (300-600 $kJ\,mol^{-1}$).[123] Consequently, H-bonds are less rigid and

exhibit less directionality compared to covalent bonds. This leads to increased difficulty when rationally designing extended frameworks. Generally, H-bonds can be distinguished in weak, moderate and strong bonds. Weak H-bonds impart long bonding distances and poor directionality which can cause the framework to collapse upon desolvation. In contrast, stronger H-bonds feature shorter bonding distances and better directionality through defined bond angles. Consequently, the self-assembly of extended organic structures is supported which makes strong H-bonds attractive for many supramolecular systems.[122]

This concept of using rigid building blocks and directional bonds is similar to the principle of reticular chemistry used in COF design, however even the strongest H-bonds' spatial orientation is much less pronounced compared to covalent bonds. Therefore a few guidelines to enhance directionality need to be considered:

For one, using building blocks with equal numbers of H-bonding donors and acceptors leads to the formation of dimers, trimers or even chains. Moreover, multiple number of H-bonds are more rigid and impose a greater directionality than a single H-bond. The majority of HOFs reported are single-component systems, but there are also reported examples using more than one component, albeit this poses a greater challenge in crystallization.[122] Building blocks and their engendered types of H-bonding will be summarized below.

Building Blocks and H-Bonding Motifs

So far, various H-bonding motifs have been exploited for HOF design. Single component systems such as diaminotriazine (DAT), carboxylic acid, different heterocycles, and urea (Figure 7A), as well as multi-component systems including acidic-basic components (Figure 7B).

In 1997, Wuest and co-workers were the first to report on crystalline H-bonded structures using the DAT motif, one of which was later found to exhibit permanent porosity.[121,124] This discovery was a milestone and paved the way for the emerging field of HOFs. Since then, various scaffolds engendering DAT as H-bonding motif have been successfully used for HOF formation.[125–127] DAT motifs form dimers and

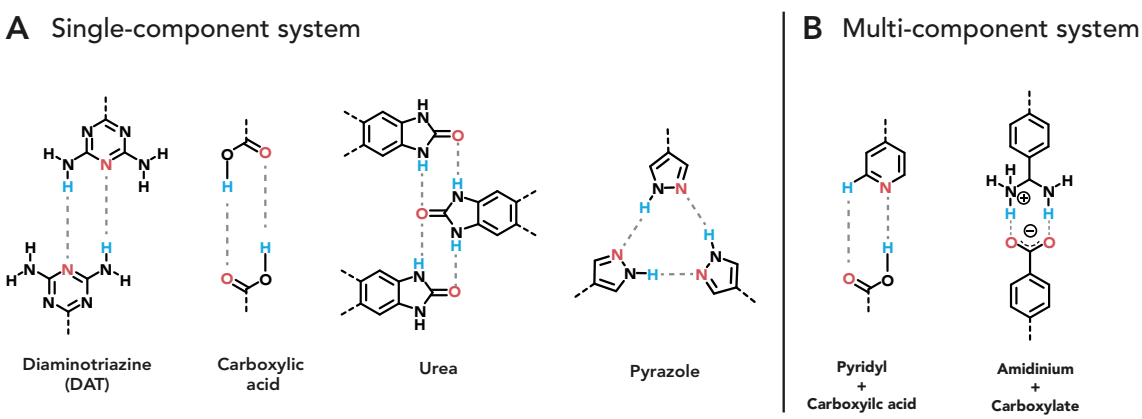

Figure 7: H-bonding motifs employed for HOF synthesis. Marked in blue are H-bonding donors and in red H-bonding acceptors. A: Single-component H-bonding motifs. From left to right: DAT, carboxylic acid, urea, pyrazole. B: Multi-component H-bonding motifs. Left: pyridyl combined with carboxylic acid moieties; Right: charge assisted H-bonding motifs amidinium combined with carboxylate.

additionally have two other free amino groups which enable the formation of 2D and 3D frameworks with various topologies and interpenetration.[128]

Another motif available is the simple carboxylic acid. It is easily accessible via synthesis and provides high directionality. In 2015, the first HOF based on carboxylic acid motifs was reported by Zentner and co-workers with a surface area of 1095 $m^2 g^{-1}$.[129] Subsequently, many HOFs using carboxylic acid motifs were reported. Especially, tritopic carboxy linkers have been used, which form interconnected dimers resulting in hexagonal layers which further interpenetrate giving complex 2D structures.[130]

The oldest H-bonding motif is urea and was also successfully used in HOF synthesis (cf. Figure 7A). Combined with a triptycene scaffold, the HOF with the highest surface area so far was reported (3425 $m^2 g^{-1}$).[131]

Furthermore, also heterocyclic motifs can be utilized for HOF synthesis. For example, when combining a rigid skeleton with pyrazole, pyridine, and imidazole rings, HOFs with permanent porosity can be obtained. Miljanic and co-workers reported on using tripyrazole building blocks to synthesize a series of hexagonal HOFs with surface areas up to 1820 $m^2 g^{-1}$.[132] Other examples of used heterocycles are pyridine and imidazole.[133,134]

Besides single-component systems, also the combination of multiple tectons can serve as systems for HOF formation (cf. Figure 7B). The great advantage of such multi-component systems is the increase in structural versatility. Combining pyri-

dine and carboxylic acids forms a H-bonding motif that is amenable to framework formation (see Figure 7B left). For example, Schröder and co-workers used X-shaped, tetrafunctional tectons to generate HOFs with permanent porosity.[135,136] However, the implementation in HOF design and synthesis is quite difficult compared to their single-component counterparts. A possible solution is the use of strongly acidic and basic tectons because they form robust, charge assisted H-bonds. For example, the combination of amidinium with carboxylate has been used for the construction microporous HOFs (see Figure 7B right).[137,138]

From a synthetic perspective, HOFs are typically obtained from precipitation from polar solvents such as ethanol, propanol, dimethylformamide (DMF), and even water. Precipitation can occur via stirring/sonication at room temperatute (RT), slow evaporation of volatile solvents, or heating to temperatures between 60 and 90 °C. After collection of the single crystals or powders, often-times the samples need to be activated, i.e., solvent removed from the pores. Activation is achieved via solvent exchange, e.g., DMF is exchanged with the more volatile acetone and subsequent drying under vacuum ("vacuum activation"). However, this step bears difficulties due to the potential collapse of the framework structure during the process. A gentler activation method, that is considered most effective, is washing with supercritical CO_2 ($scCO_2$; "CO_2 activation").[125,127,129,130,137–139] CO_2 activation is also well established in COF synthesis, e.g., for vacuum-sensitive imine-linked COFs.[120,140] However, activation is generally more challenging for HOFs than for COFs due to the weaker H-bonds. Moreover, many HOFs are soluble in common exchange solvents. Hence, to expand the scope of HOFs, more suitable activation strategies are required.[122]

Permanent porosity

Solvent guest molecules stemming from synthesis exhibit a template effect, which theoretically could induce extremely high surface areas. However, due to the lability of H-bonds, the framework often cannot be retained after guest removal. To obtain HOFs with high stability and robust frameworks, several strategies are necessary:

(*i*) The introduction of stronger intermolecular interactions, i.e., multiple H-

bonds or charge-assisted H-bonds.

(*ii*) Employing rigid building blocks. Stiff backbones can increase the framework stability to an extent, where even weak H-bonds are sufficient to produce permanently porous HOFs.[141]

(*iii*) Inducing interpenetration leads to more rigid and thermodynamically stabilized frameworks.[130] However, as this may decrease or even block the pores, controlling the degree of interpenetration is critical for achieving HOFs with large surface areas.[142]

(*iv*) The introduction of additional intermolecular interactions. Adding aromatic moieties that enable π-π stacking or van der Waals forces can have a stabilizing effect.[122,142]

Implementing the above described strategies does not only lead to permanent porosity after activation, but also to stabilities towards thermal and chemical strain. Despite the weak interactions employed in HOFs, their thermal resistance is reported to range between 220 and 420 °C.[143] These stabilities are comparable to those of COFs, if not as high. Moreover, HOFs are stable towards common solvents including water. This is especially beneficial for applications with exposure towards water vapor, i.e., flue gas. Some carboxylic acid based HOFs are even stable in acids. However, strongly polar solvents such as dimethyl sulfoxide (DMSO) can interfere with H-bonds and therefore cause leaching of building blocks from the framework.[122] Despite the above described strategies, to date only a few dozen HOFs are reported to exhibit permanent porosity. Challenging activation caused an inhibited development of HOFs compared to their more stable counterparts COFs.

Applications

Despite the activation challenges, HOFs are promising materials once permanent porosity is achieved. Their good thermal and chemical stabilities and their microporosity makes them suitable for several environmentally important applications. Similar to COF materials, their high surface areas, low densities and distinct pores, make HOFs ideal candidates for gas storage and separation applications. For example, HOF materials have shown high uptake of H_2, CH_4, and CO_2.[144] Furthermore,

HOFs exhibit adsorptive separation of CO_2 from N_2 and CH_4, which is highly desired for carbon capture and sequestration from the atmosphere.[145]

In contrast to COFs, HOFs are easily recyclable and solution processable. These properties lead to advantages in certain applications. For example, in proton exchange membrane fuel cells, processabilitiy is highly sought after. COFs have already been shown to perform well as proton exchange membrane materials,[146,147] however exhibit poor processability due to their thermoset nature. In contrast, HOF materials are promising alternatives due to their simple synthesis and solution processability. Furthermore, HOFs based on strongly acidic and basic H-bonding motifs showed high proton conductivity and even outperform COFs at ambient conditions[148]

HOF materials are a quite young field of research and pose a promising new platform for the design of functional materials. HOFs are readily affordable via mild and simple synthesis and their main properties are both flexibility and robustness. Specifically, they are solution processable, recyclable, and thermally/chemically stable. This unique feature makes HOFs highly interesting for industrial applications in the future. However, so far only a few dozen examples were reported to exhibit permanent porosity caused by the relatively weak H-bond interactions used. For the same reason, also applications are restricted: the lack of strong interactions between guest and host HOF restricts gas sorption applications and missing structural integrity only allows for limited operation conditions. Consequently, alternative synthetic procedures and milder activation strategies are subject of current research in the field.

Summing up, OPNs (both amorphous and crystalline) show great potential for the advancement of modern day materials science and future applications. Such highly functional and performing materials are key to tackle the environmental- and energy issues of our generation. Unfortunately, most of these OPNs require toxic and expensive solvents and catalysts and are highly energy demanding in their synthesis. To ensure environmentally benign processes from start to finish, an alternative synthetic method is required. Recently, the green method HTP has been developed for

generating highly performing polymers.[149] HTP enables organic synthesis in nothing but water, hence poses great potential as an alternative to classical, harmful procedures. HTP's origin, basic principles and its development will be discussed in detail in the following chapter.

2.3 Hydrothermal Synthesis

2.3.1 Historical Outline and Definition

The term *"hydrothermal"* (HT) has its origin in geology, as it was used to describe the conditions present in water veins underneath the earth's crust. These conditions are temperatures above boiling point and elevated pressures leading to mineral formation and ore deposits. Geologists tried to gain an understanding of these processes in order to understand mineral genesis, which led to the development of the geomimetic hydrothermal technique.[150] In 1845, von Schafhäutel was the first to synthesize quartz microcrystals hydrothermally.[151] Subsequently, hydrothermal synthesis (HTS) became an attractive method to mimic the natural conditions existing under the earth's crust for synthesis in the laboratory. Many other minerals followed (e.g., feldspars, wollastonite, and analcite), which led to roughly 150 obtained mineral species even before 1900.[152]

The first commercial applications were focused on mineral extractions and ore beneficiations such as the process for obtaining refined bauxite invented by J. Bayer in 1892.[150] This simple process employs sodium hydroxide at elevated temperatures and pressures in a confined vessel which allows for leaching of $Al(OH)_4$ from iron oxides. It was due to the findings of Nacken (large single crystals of quartz)[153] and Barrer (zeolites)[154] that the focus was shifted towards industrially utilizing the hydrothermal technique to synthesize inorganic materials. However, it was only in the 1940s as during World War II an acute shortage of piezoelectric oscillators lead to industrial scale applications of HTS in order to generate large size quartz crystals.[155] Later on, during the 20$^{\text{th}}$ century, even more inorganic network minerals were obtained synthetically via HTS, e.g., zeolites[156] (both with and without natural analoga), sapphire[157], diamond,[158] and even crystals of noble metals like gold.[159] Today, Japan is the largest producer of commercial quartz in the world ($>50\,\%$ of world's annual production) and owns the largest hydrothermal set-up globally.[160]

In the past decades, the hydrothermal technique has made great progress and stretched out to various fields of science. Therefore, many similar definitions of the term hydrothermal exist. For the purpose of HTS, the definition of Yoshimura

appeared as the best fit: "The term hydrothermal refers to any homogeneous or heterogeneous reaction in the presence of aqueous solvents above room temperature and at pressure greater than 1 bar in a closed system."[161] Similarly, in synthetic chemistry, when other (organic) solvents than water serve as media, the term solvothermal is used. Due to the harsh conditions present during a HT reaction, highly stable autoclaves are needed. Typically, these autoclaves are made from steel or thick-walled pyrex- or quartz glass tubes. For the synthesis of artificial quartz and sapphire crystals, often seed crystals are used to enhance crystallinity, reduce defects and increase the crystallite sizes.[157,162] Using such set-ups allows the large scale production of e.g., industrially relevant quartz or zeolite products with outstanding crystallinity.

In the beginning of hydrothermal synthesis as a research topic, the focus centered rather on the preparation of new minerals than on the collection of reproducible data of the used reaction conditions. This changed when during industrial revolution the technical advancements enabled the development of improved set-ups and the in depth investigations of physical chemists lead to an understanding of the reaction kinetics and phase relations present in HTS.[150,160] The physico-chemical findings are discussed in the next section.

2.3.2 Physico-Chemical Aspects

One of the key elements of HTS is the reaction of otherwise difficult to dissolve reagents. This means that the physical properties of water present under high T and p conditions differ greatly from the ones at RT. Specifically, liquid H_2O at $T > 100\,°C$ is termed high-temperature water (HTW) and can be divided into three regimes: (i) hydrothermal regime (htR; $100 < T \leq 250\,°C$), (ii) near critical regime (ncR; $250 < T \leq 350\,°C$), and (iii) supercritical regime (scR; $T > T_c = 374\,°C$). Typically, HTW is generated via heating water in e.g., an autoclave, to the desired T at isochoric conditions. For HTS, the chosen volume of water inside the autoclave is usually between 50-80 V % at RT. Upon heating to $T > 100\,°C$, a dynamic system is generated where both liquid and gaseous phases of water co-exist under autogenously

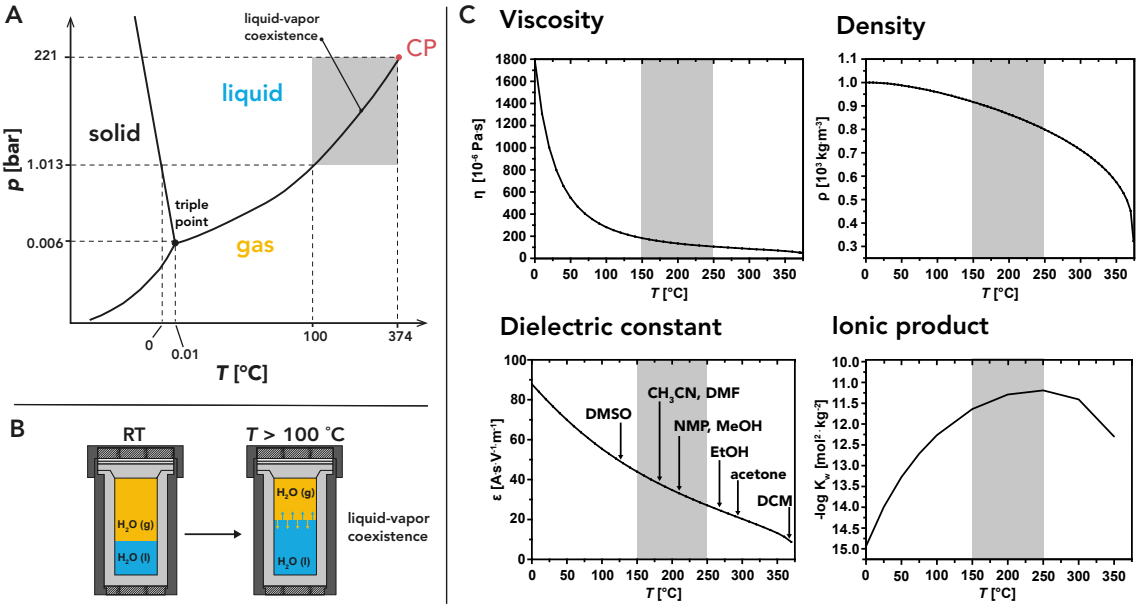

Figure 8: Physico-chemistry of HTW. A: Phase diagram of water, adapted from Baumgartner et al.[10] B: Schematic of the generation of HTW in a steel autoclave when filled to 30 $V\%$ at RT and $T > 100\,°C$ resulting in liquid-vapor coexistance. Illustration made by D. A. Cerrón-Infantes. C: Behavior of physico-chemical properties (density ρ, static dielectric constant ϵ, viscosity η and the ionic product K_w) of HTW with increasing T.[10,165–167] Diagrams by M. M. Unterlass.

built pressure p ($p > 1$ bar; according to the phase diagram of H_2O). In such a system, $H_2O_{(l)}$ constantly evaporates and $H_2O_{(g)}$ constantly condenses. Physico-chemical investigations showed that parameters like density ρ, static dielectric constant ϵ, viscosity η and the ionic product K_w change drastically.[163] This behavior can be explained by breaking of the H-bond network present in water at RT to loose H_2O clusters at roughly 300 °C.[164]

As a result, both ρ and η decrease quickly with rising T which leads to an increase in diffusion.[165] This is especially important in non-stirred, diffusion-controlled reactions, as are typical in HTS performed in autoclaves. Furthermore, also ϵ (which is a measure for the polarity of a solvent) decreases with increasing T.[166] Specifically, ϵ values decrease to a point where they are similar to common organic, aprotic, polar solvents such as DMF, NMP, methanol (MeOH) or DCM. Consequently, water suddenly gains the property of dissolving a great variety of (even apolar) substances, which are water-insoluble in ambient conditions. In contrast, K_w rises with T, leading to a maximum three-fold acceleration of the autoprotolysis at 250°C compared RT.[167] As a result, HTW does not only act as a solvent but also as an acido-basic bicatalyst, which is essential for the formation of various minerals (i.e., metal oxides, aluminosilicates and silicates).[149,155–157,168] All

of these properties make HTW a highly relevant reaction medium.

However, HTW alone is sometimes not sufficient to dissolve some synthetically important reagents and/or uneconomically high T would be necessary. Therefore, it is common to employ so-called "mineralizers" to help bring the reactants in solution in order to gain especially large crystals. For example, for the synthesis of zeolites it is typical to use alkaline additives (usually hydroxides like NaOH and KOH), which enhance the solubilization via ionization of the silanol groups and breaking of siloxane bonds.[42] Furthermore, solubilization of the intermediate amorphous solid is increased and hence a soluble active species is generated which slowly crystallizes and forms the desired zeolite.[156] In addition to the acceleration of the dissolution and condensation rates, it is assumed that also the conversion rate between the different species is increased. Similar to the behavior of a catalyst, mineralizers are typically not consumed during the reaction.[42] Also, carbonates and halides (i.e., NaCl, KF, KCl, KBr and LiF) were found to have mineralizing effects on the synthesis of e.g., perovskites and rare earth vandanates.[169,170]

2.3.3 Transfer to Organic Synthesis

HTS was developed as a method to synthesize and crystallize inorganic materials. In recent years it was shown that HTS can also be applied to organic synthesis. As contradictory as this may seem at first sight, its feasibility is based on two pillars: First, the above described physical properties of HTW are able to dissolve even apolar organic substances as well as catalyze their reactions. Second, the molecular entities created in both inorganic as well as organic products via HTS are cyclic moieties. In striking analogy, the formation of these cyclic moieties is based on cyclocondensation reaction, i.e., through the formation of a cyclic moiety connecting the units accompanied by the release of a low-molecular weight by-product such as H_2O. Analogously, the first organic molecules synthesized via HTS were cyclic imides. Specifically, in 1991, Hodgkin et al. were the first to report on the formation of diaminobisimides via reacting aromatic dianhydrides with aromatic diamines in HTW by the elimination of H_2O.[171,172] The feasibility of imide moieties via HTS

soon led to the synthesis of polyimides which created a subclass of HTS: Hydrothermal polymerization (HTP).[173–175]

Despite the fact that HTS typically creates highly crystalline inorganic materials, HTP solely yielded amorphous products at first. In 2014, Unterlass and co-workers were the first to generate a highly crystalline PI via HTP.[10] Specifically, poly(*p*-phenylene pyromellitimide) (PPPI) was found to exhibit a higher degree of crystallinity than its classically prepared analogue.[10] Since then, Unterlass and co-workers reported on the HTP of three linear and crystalline PIs with both 5- and 6-membered cyclic imide functions.[10,176,177] Recently, the scope of HTP has been extended to also other organic polymer classes: Polyazomethines,[12] polybenzimidazoles,[11] and polyamides.[178] In general, the majority of polymers obtained via HTP are of a linear fashion and only a few examples of 3D structures exist. In fact the polyamide mentioned above was the first 3D organic network via HTP reported, however it was not fully synthesized via HTP but rather "devitrified" in HTW after classical polymerization.[178] The first reports on the HTP of COFs included keto- enamine-linked, azine-linked, and imine-linked COFs.[179–181] The first hydrothermally generated PI network was amorphous and synthesized and published within the scope of this thesis.[182] Just recently, after this thesis was started, the first HTP of PI-COFs, was published by Kim and co-workers.[103] Moreover, HTS can also been applied to the synthesis of small organic molecules. Specifically, rylene bisimides,[183] benzimidazoles,[184] quinoxalines,[185] the fused bisbenzoylimidazole perinone[186] and fused pyrazoles[187] were afforded.

The basic principles of HTS used for inorganic and organic syntheses are the same, yet the precise conditions differ. First, the reaction temperatures (T_R) need to be lower for organic synthesis, because the precursors' thermal stabilities are quite poor compared to their inorganic analogues. The used T_R for the HTS of inorganic network materials sometimes surpasses T_c of water and hence the synthesis proceeds in the scR. This is however not an option for organic HTS/HTP. In a typical organic HTS/HTP experiment, one operates within $150 < °C\ T \leq 250\ °C$, i.e., in the htR (gray boxes in Figure 8A and C). Furthermore, organic materials are not obtained

as single crystals like inorganic materials, but rather as powders made up from microparticles.

Second, the used mineralizers also differ for organic syntheses. Inorganic HTS often employs inorganic salts or bases to enable crystallization. In contrast, for organic HTS/HTP typically no mineralizers are used at all. In some cases non-nucleophilic organic bases or acids were added to help crystallize the products, however these additives are typically not called mineralizers in literature.[188]

Third, to the author's knowledge, until now organic synthesis in HTW has not yet been established in industrial scale production. Nevertheless, HTS/HTP impresses with straightforward synthetic procedures and easy to handle work-ups compared to classical protocols. No harmful and expensive solvents or catalysts are necessary and the only waste generated are benign water residues.

In summary, the scope of HTS/HTP for organic synthesis has advanced rapidly. Due to the growing number of accessible functionalities, the straightforward synthetic requirements, and the environmentally benign conditions make HTS/HTP a powerful and green synthetic alternative for the design and synthesis of highly functional materials.

2.3.4 Classical vs. Hydrothermal Synthesis of Polyimides

Polyimides are known to be amongst the mechanically toughest synthetic polymeric materials. They exhibit high resistances towards heat, chemicals, and mechanical strain and are therefore classified as HPPs.[6] The definition of HPP is strongly linked to the performance under high temperature conditions. Specifically, long-term durability at 177 °C and thermal decompositions at $T > 450$ °C.[6] Consequently, PIs find use in applications with harsh operating conditions such as aerospace and electronic industries.[6,189] The most prominent example is the largest selling PI to date: Du Pont's Kapton®, which retains its properties up to 400 °C and is mostly used for insulating wire coating.[6]

Various factors contribute to the high-performance properties of PIs, e.g., primary bond strengths, resonance stabilization, second order bonds, and rigid intrachain structure.[6] PIs belong to the few exceptions of thermoset polymers that are non-

crosslinked. Therefore, their thermal stabilities rely on other molecular features: Aromatic moieties linked via cyclic imide functions. When introducing additional crosslinking into aromatic PIs, MPIs can be obtained exhibiting excellent stabilities (up to 530 °C) and gas sorption properties.[57,58,63,64] With increasing crystallinity, the bulk modulus of a polymer approaches its crystallite modulus, hence PI-COFs are expected to exhibit increased mechanical stabilities compared to amorphous MPIs.[190]

Classical Synthesis of PIs

Classically, both linear and network PIs are usually obtained via condensing amine- and anhydride monomers accompanied by the release of H_2O as by-product. Due to the low solubility of the majority of monomers, harsh and high-boiling aprotic polar solvents are used, e.g., NMP and *m*-cresol. Furthermore, high T_Rs and condensation promoters (i.e., isoquinoline) are necessary.[85,189]

Linear PIs are generated via a two-step polycondensation (cf. Figure 9A). First, the difunctional comonomers are reacted to a poly(amic acid) (PAA) intermediate in NMP/isoquinoline at RT. The PAA is formed through a nucleophilic attack of one nitrogen of the diamines at one of the electrophilic carbonyl carbon atoms of the anhydrides (leading to amide linking functions), accompanied by the opening of the anhydride ring and formation of the acid functions. PAAs are still soluble and therefore processable, which allows for generating desired shapes. Afterwards, the reaction is heated to $T > 200$ °C which converts PAA to the desired PI[189] via a second nucleophilic attack of the amide nitrogens at the pendant CO_2H functions and subsequent condensation reaction (release of H_2O).

The synthesis of cross-linked PIs employs similar reaction conditions, however typically a one-step condensation reaction is used without the isolation of a processable intermediate. Applying the A_2/B_f method, multifunctional amine- and anhydride monomers are condensed to MPIs and COFs. Typical reaction conditions involve *m*-cresol and/or NMP and the addition of isoquinoline as catalyst. Both COFs and MPI's are treated with Soxhlet extraction to remove residual high-boiling solvents. Most MPI protocols include a stepwise heating regime (with a maximum T_R of 220 °C and a total reaction time of up to 72 h) to avoid gelation and increase

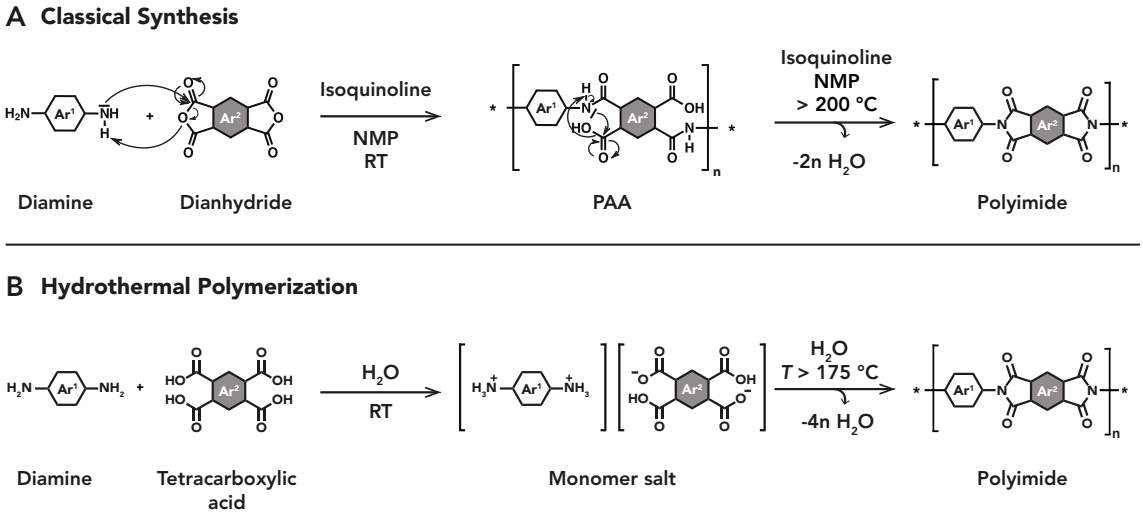

Figure 9: Classical synthesis vs. HTP of linear PIs. A: Classical synthesis of linear PIs via the PAA intermediate. B: HTP of linear PIs via MS as intermediate.

the degree of cross-linking.[57,58,61,63,64,191] PI-COF synthetic procedures demand even higher T_Rs of up to 250 °C.

Both linear and network PIs require harsh reaction conditions employing harmful and expensive solvents and catalysts via multiple steps. HTP, as green alternative, has already yielded linear PIs with outstanding crystallinity and will be discussed in detail in the following.

Hydrothermal Polymerization of Polyimides

In contrast to classical methods, HTP of PI is a one-pot/one-step synthesis with water as a benign solvent and without the need of a catalyst. The highly insoluble and apolar precursors are brought into solution and hence in reaction upon heating above $T = 175$ °C, which is lower to classical reaction temperatures. Instead of the dianhydrides, sometimes tetracarboxylic acids are used, due the fact that anhydrides immediately hydrolyze under HT conditions. After the polymerization and upon cooling, HTW turns back into ambient water and with this gains back its polar properties which leads to the precipitation of the products. Subsequently, the products can simply be collected via filtration while neither toxic waste is generated nor further purification steps are needed.

Despite the fact that HTP has been used for the synthesis of PIs since the early 2000s, little was known about the mechanism and any possible intermediates. Already in 1999, Morton et al. proposed that the imidization under hydrothermal conditions

proceeds via a salt-type intermediate with a 1:1 stoichiometry.[192] However, it took 12 more years to prove the existence of such intermediates. In 2011, Unterlass and co-workers conducted a mechanistic study of the HTS of aromatic polyimides.[193] Within this study, it was demonstrated that the first step of the polymerization is indeed a so-called "*monomer salt*" (MS) formed by the comonomers in a 1:1 ratio via an acid-base reaction, as a consequence of the pK_aH difference between amine and carboxylic acid functions and mediated by the protic solvent water (see Figure 9B). In fact, all publications on HTP of linear polyimides that followed, exclusively reported on the intermediary formation of a MS in the form of diammonium dicarboxylic acid-dicarboxylates.[10,11,176,177,186,188,194–196] The existence of MS with a 1:1 ratio plays an important role in HTP: MSs provide ideal stoichiometries, which is highly beneficial for step-growth polymerizations as they follow Carothers' law, stating that "perfect" stoichiometries are required to obtain high conversion and high degrees of polymerization.

Compared to classical syntheses of PIs, HTP not only provides easy handling and ideal stoichiometries, but it most importantly leads to enhanced crystallinity. Therefore, HTP seems a promising method not only for linear PIs but also for 3D network PIs and eventually crystalline PI-COFs.

3 Aims and Objectives

Currently, the world is confronted with pressing issues such as climate crisis. In order to preserve our environment yet keep advancing as a society, novel and environmentally benign technologies are required. From a materials chemist's perspective two possible key aspects are the development of highly functional materials for such technologies as well as their environmentally friendly synthesis.
PIs are HPP with great significance as materials in demanding applications due to their ability to withstand strenuous working conditions. Previously, HTP was introduced as a green, straight forward and cheap method for the synthesis of PIs with improved thermal-, mechanical- and chemical stabilities compared to their classical analogues. However, so far HTP was limited to linear PIs. In contrast, porous, network PIs would open up a whole new palette of green applications such as exhaust gas separation/storage, catalysis, and even battery applications. Therefore, expanding the scope of HTP towards both amorphous and crystalline network PIs was targeted:

(*i*) First, it was set out to establish the general feasibility of an amorphous PI network via HTP and to investigate its mechanism of formation and the resulting materials properties. Therefore, testing various synthetic parameters and in depth characterization of intermediates and products were the main strategies. Especially, the materials' network architecture and porosity should be investigated thoroughly as well as potential up-scaling and processing.

(*ii*) Second, it was aimed not only for the basic formation of network PIs but to show that the green method HTP is capable of generating crystalline PI frameworks. Therefore, one objective was the proof of concept that HTW indeed provides reversibility conditions for the imide moiety in a small molecule model system, which allows error-correction and hence crystallinity. Next, applying this

fundamental understanding to extended PI networks was targeted. Therefore, three different monomer systems should be tested using various HTP set-ups, HT reaction conditions and the addition of aniline as modulator. Monitoring the products' crystallinity, possible side-products and T-dependent behavior should broaden the knowledge of the formation of crystalline PI frameworks in HT conditions.

4 Results and Discussion

4.1 Polyimide Network

The majority of the results presented in this chapter have already been published in the article "Hydrothermal polymerization of porous aromatic polyimide networks and machine learning-assisted computational morphology evolution interpretation."[182] *The article's content is paraphrased troughout this chapter, direct quotations are marked using quotation marks and citation.*

In this chapter, the general feasibility of generating a highly condensed, aromatic, 3D PI network via HTP is presented. First, the HTP process is discussed, including a multifunctional MS as an intermediate. Subsequently, two commonly used HTP methods are presented: microwave-assisted HTP (HTP-MW) and HTP in unstirred batch autoclaves (HTP-AC). The resulting polymer networks' properties are summarized as elucidated via several solid-state techniques. After discussing the general feasibility of HTP, the detailed investigation of the HTP-AC method is summarized. Accordingly, a reaction screening gives insights on how the resulting PI networks are influenced by different reaction parameters. A plethora of morphologies were observed within the screening's products and are discussed in detail. As a result, a hypothesis on the morphological evolution in reference to spectroscopy data is proposed. In addition, the possibility of scaling up HTP-MW of the PI network from milligram to grams is presented. Finally, solvent-free warm-pressing is introduced as a green processing method for the PI network obtained from HTP-MW.

4.1.1 Synthesis and Characterization of a Polyimide Network

For the HTP of a 3D PI network 1,3,5-tris(4-aminophenyl)benzene (TAPB) and pyromellitic acid (PMA) were chosen as comonomers (see Figure 10A). Both are aromatic and rigid building blocks which were expected to result in a network ac-

cording to the A_2B_f method exhibiting permanent porosity and high thermal and chemical stabilities. The network will be referred to as PI(TAPB-PMA) throughout this chapter. Indeed, at the time this thesis was started, several publications existed on the conventional synthesis of PI(TAPB-PMA). All of these reports found a 3D network with porosities in the size range 0.5-3.7 nm (which are classified as microporous)[38] and Brunauer-Emmett-Teller surface areas (SA_{BET}) between 570 and 1295 $m^2 g^{-1}$.[57,64,85,197] As described in Chapter 2.3, these synthetic protocols employed organic solvents (*m*-cresol, NMP) and catalysts (isoquinoline).[57,64,85,197] Furthermore, in contrast to the linear monomer (PMA) chosen for HTP, its anhydride pyromelltic dianhydride (PMDA) was used in these conventional syntheses. PMDA is known to hydrolyze to PMA under atmospheric humidity conditions, which does not pose a problem under inert and H_2O free conditions during conventional syntheses. However, under HT conditions, PMDA is quickly hydrolyzed. Therefore, using the free acid PMA in HTP is equally possible.[173]

Until 2021, the successful HTP of a PI network has not yet been reported. There was solely one publication reporting on the HTP of amorphous polymer networks, specifically three different poly(amide imide) networks, employing mellitic acid combined with different linear, aromatic diamines. However, the reported products were not fully condensed networks or frameworks, but rather consisted of oligomers that could only be converted to network-type higher molecular weight species by thermal annealing through solid-state postcondensation at 340 °C.[198] Since then, two publications of the HTP of 3D PI networks (i.e., covalent organic frameworks) have been published, which will be discussed in Chapter 4.2.

In general, the formation of different PIs in HTP was shown to typically proceed via MS intermediates (as discussed in Chapter 2.3).[173,174,192,199] In fact, so far all publications on HTP of linear polyimides exclusively reported on a polycyclocondensation via the intermediary formation of a MS during the heating phase of HTP (< 80 °C).[10,11,176,177,186,188,194–196] Therefore, the formation of a MS as an intermediate was also expected for the multitopic monomer system chosen in this work. Consequently, the preparation of a MS from TAPB and PMA was attempted before the actual HTP experiment was conducted.

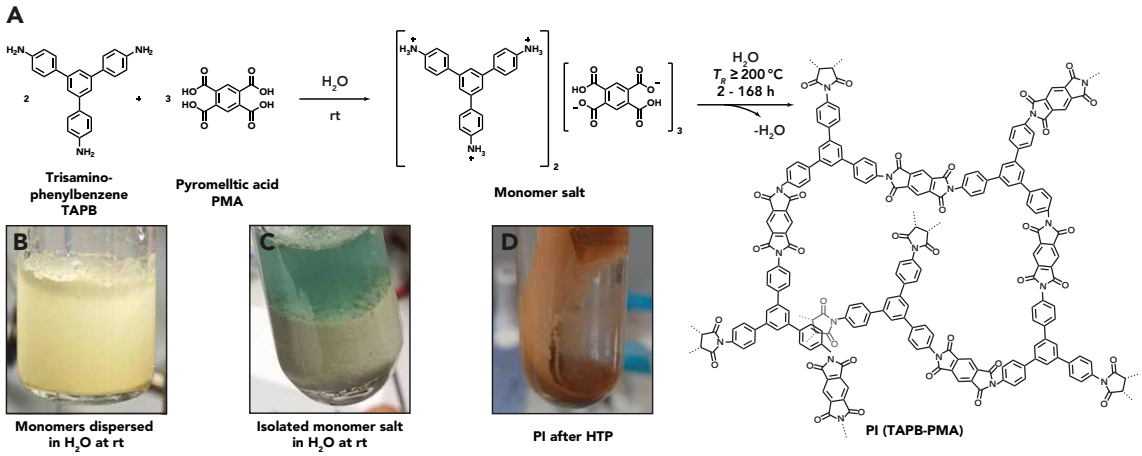

Figure 10: Hydrothermal synthesis route of the network PI(TAPB-PMA). A: Reaction equation of the hydrothermal polymerization of PI(TAPB-PMA) from the comonomers TAPB and PMA via the monomer salt $[H_3TAPB^{3+}]_2[PMA^{2-}]_3$. B: Aspects of comonomer mixture. C: Monomer salt. D: PI product after HTP. Figure adapted from Lahnsteiner et al..[182]

Hydrothermal Polymerization via a Monomer Salt Intermediate

For the synthesis of the MS, PMA was dissolved in deionized water in a microwave reactor at 230 °C. Subsequently, TAPB was added and the mixture was stirred overnight at RT (see Figure 10A and Chapter B.2.2 for synthetic details).[193] A green powder (Figure 10C) was isolated and analyzed.

The obtained green powder was identified as a salt via attenuated total reflectance Fourier transformation infra red (ATR-FT-IR) spectroscopy (Figure 11A). Specifically, ATR-FT-IR spectra showed aryl-NH_3^+ modes ($\mathbf{m_b}$: $\tilde{\nu} \approx 2850\,cm^{-1}$ and $\mathbf{m_c}$: $\tilde{\nu} = 2580\,cm^{-1}$), stemming from the TAPB monomer's protonated amine moieties. Furthermore, a carboxylic acid (C=O) mode ($\mathbf{c_a}$: $\tilde{\nu} \approx 1690\,cm^{-1}$) and both asymmetric and symmetric aryl-CO_2^- modes ($\mathbf{c_b}$: $\tilde{\nu} \approx 1635\,cm^{-1}$ and $\mathbf{c_c}$: $\tilde{\nu} \approx 1570\,cm^{-1}$) (see Figure 11A) pointed at the MS's anion (partly deprotonated PMA) containing both carboxylic acid as well as carboxylate moieties. The mode with the highest wavenumber ($\mathbf{m_a}$: $\tilde{\nu} \approx 3650\text{-}3300\,cm^{-1}$) was attributed to intermolecular H-bonding. Two possibilities were identified: (i) H-bonding between aryl-CO_2^- and aryl-CO_2H of two neighbouring deprotonated PMA anions; and (ii) H-bonding between aryl-CO_2^- of one deprotonated PMA anion and crystal water intercalated in the MS solid.[10,188]

Additional analyses further proved that a MS was formed between the two comonomers TAPB and PMA in water at low T_R (i.e., RT). Powder X-ray diffraction (PXRD) analysis evinced that the MS was highly crystalline as of the many and sharp reflections between 2 and 30 °(2θ, Cu-K_α) as visible in Figure 11B).

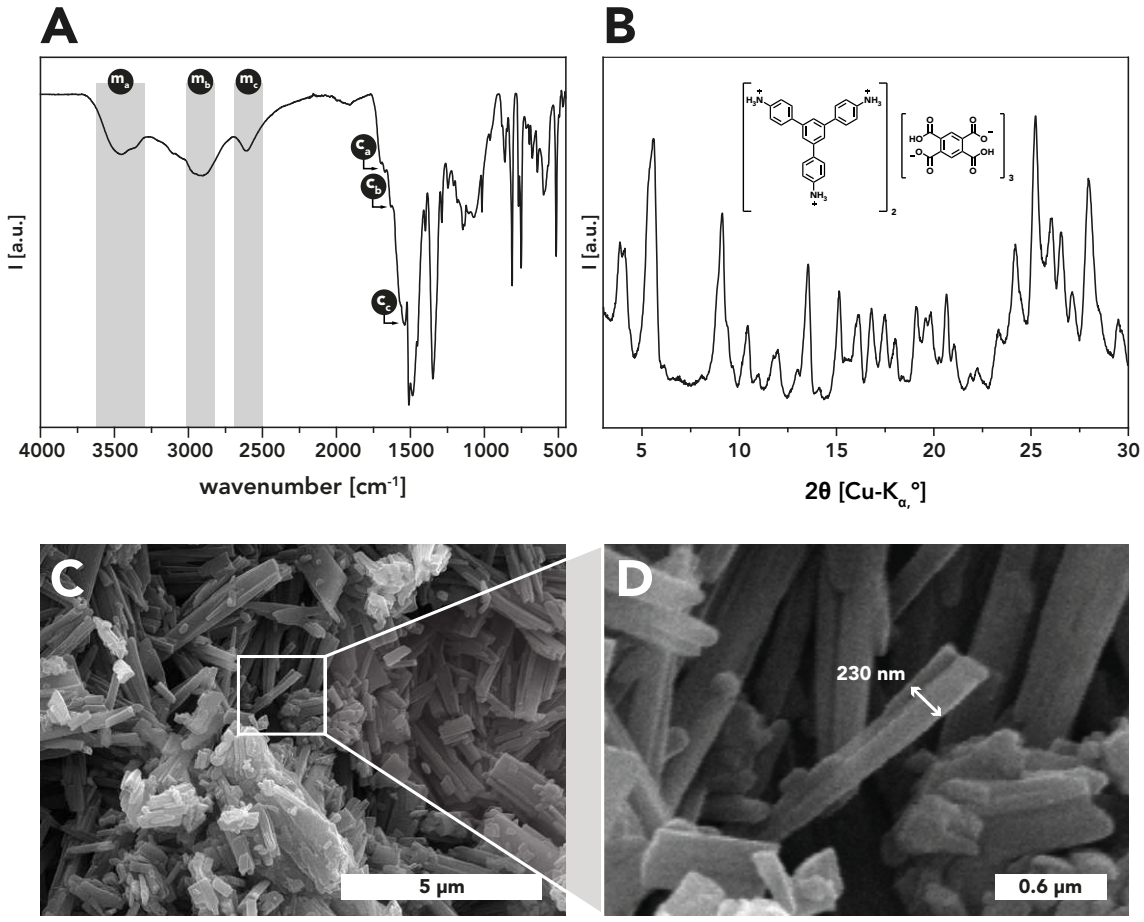

Figure 11: Characterization of the intermediary MS $[H_3TAPB^{3+}]_2[PMA^{2-}]_3$. A: ATR-FT-IR spectrum where relevant modes were indicated using letters ($\mathbf{m_a}$: H-bonding between crystal water, carboxylate and/or carboxylic acids in the solid crystal; $\mathbf{m_b}$ & $\mathbf{m_c}$: aryl-ammonium modes; $\mathbf{c_a}$: carboxylic acid mode; $\mathbf{c_b}$ & $\mathbf{c_c}$: asymmetric and symmetric carboxylate modes. B: PXRD pattern showed manifold and sharp reflections indicative of high crystallinity. C and D: SEM images revealing angular particles with an average width of 0.5-1 μm.

Moreover, ^{1}H-nuclear magnetic resonance (NMR) spectroscopy revealed a 2:3 ratio of anion to cation, which confirmed the chemical composition of the MS to be $[H_3TAPB^{3+}]_2[PMA^{2-}]_3$ (see appendix, Figure A9). Scanning electron microscopy (SEM) images showed angular particles with a width of $\sim$200-250 nm (see Figure 11C). These morphologies were found to be analogous to those described by Unterlass and co-workers in their studies of MS intermediates of aromatic PIs.[193,194] Consequently, MS ($[H_3TAPB^{3+}]_2[PMA^{2-}]_3$) formation was assumed to play a role during HTP of PI(TAPB-PMA).

After elucidating the behavior of the employed monomers at low T_R, the full condensation towards the polymer PI(TAPB-PMA) was approached. Two different HTP set-ups were tested, which will be discussed in the next section. The first set-up discussed will be the HTP-MW set-up, followed by the unstirred batch

autoclave set-up. Both set-ups fulfill the requirements of a confined, in the used pressure range explosion proof, reactor and are commonly used for HTP of linear PIs and therefore seemed a suitable choice.

Microwave-Assisted Hydrothermal Polymerization

First, HTP-MW was investigated. As the MS inevitably formed during the heating process, the comonomers TAPB and PMA were directly employed in HTP. For HTP-MW, the comonomers were suspended in H_2O at RT in a glass vial (see Figure 10B and Chapter B.2.2 for synthetic details) and the resulting yellow suspension was subsequently heated as fast as possible to 200 °C in a microwave reactor. The reaction mixture was stirred vigorously for the chosen reaction time $t_R = 4$ h. As the microwave reactor was equipped with a window, a rapid color change from the yellow suspension to first a dark blue solution, subsequently a green solution, and finally a brown suspension could be observed. The dark blue solution appeared when the hydrothermal regime in terms of T was almost reached ($\sim$180 °C). The blue color was assumed to be caused by the fully conjugated TAPB monomer (as neutral and/or ionic species) solubilized in water. Next, the green color immediately reminded of the isolated MS solid. The matching colors corroborated the hypothesis that the MS formed as an intermediate before polycondensation. The last color change to a brown suspension pointed at the polymerization process starting ($\sim$200 °C), as the collected product's color was also brown. After the desired t_R, the vial was cooled down to 70 °C using compressed air. The obtained homogeneous, brown powder was filtered, washed with distilled water, ethanol, and acetone, and dried *in vacuo* at 80 °C.

These visual observations (i.e., color changes) led to the conclusion that with increasing T_R HTP proceeds as follows: (i) monomers solubilize as ionic species (blue) once HT conditions are reached, (ii) ionic species shortly form a MS (green) and (iii) at $T_R = 200$ °C, the MS polymerizes via oligomers to the fully condensed PI(TAPB-PMA) with progressing t_R.

If full condensation was in fact achieved was investigated next. However, PI networks are thermoset (by definition of a polymer network; c.f. Chapter 2.1) which makes them virtually insoluble. Hence, only solid-state analysis techniques were

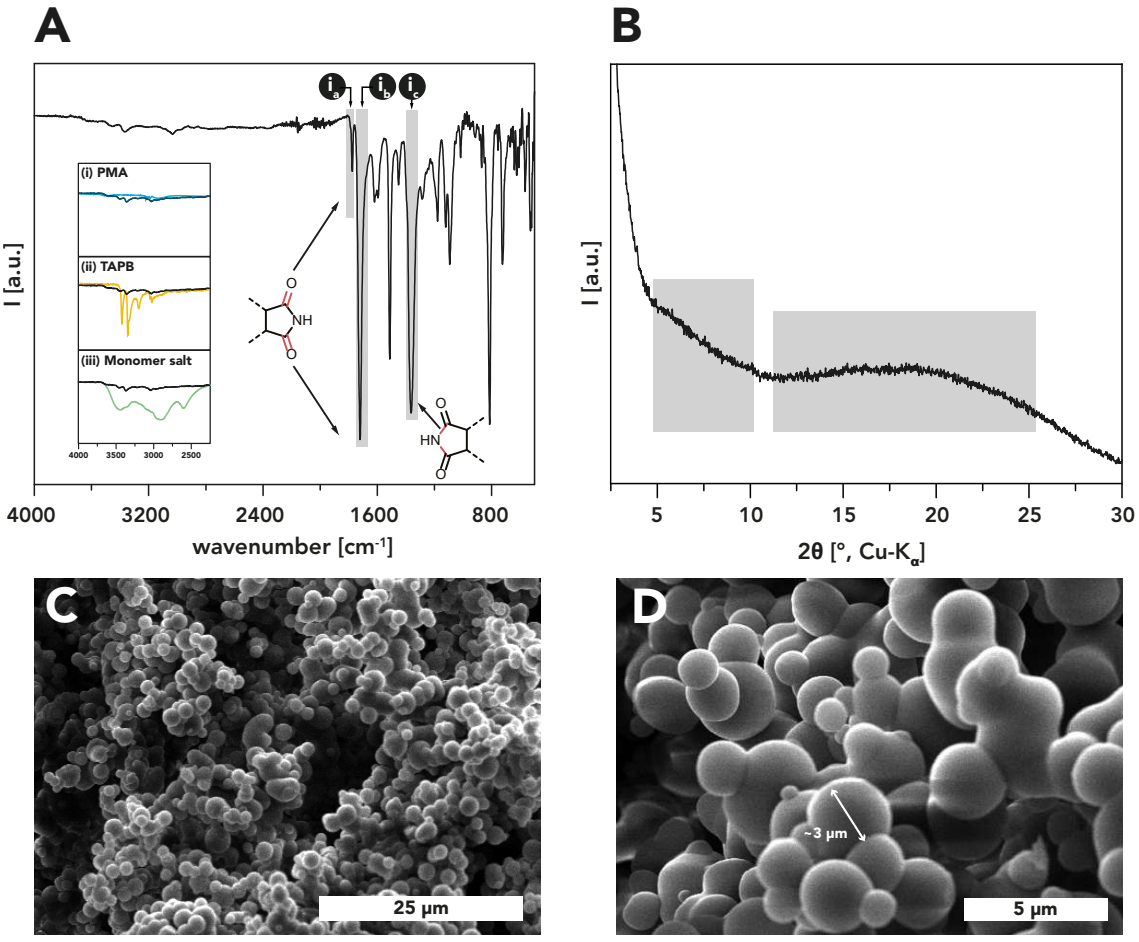

Figure 12: Characterization of PI(TAPB-PMA) via HTP-MW. A: ATR-FT-IR spectrum where the three typical imide modes ($\mathbf{i_a}$: $\tilde{\nu}_{as}$(C=O) ≈ 1775 cm^{-1}, $\mathbf{i_b}$: $\tilde{\nu}_{s}$(C=O) ≈ 1720 cm^{-1}, and $\mathbf{i_c}$: $\tilde{\nu}$(C-N) ≈ 1365 cm^{-1}) are marked with gray boxes. Insets show the H-bonding region 4000-2250 cm^{-1} of spectra of PMA (blue curve), (ii) TAPB (yellow curve), and the MS (green curve). B: PXRD pattern where amorphous halos are marked with gray boxes. C and D: SEM images featuring near-monodisperse microspheres with an average diameter of ∼1.5-3 μm.

available. Consequently, it was not possible to determine the product's molecular weight, yet ATR-FT-IR spectroscopy pointed at full condensation towards PI(TAPB-PMA). The spectrum featured the typical imide modes (see Figure 12A): the asymmetric and symmetric C=O stretch modes $\mathbf{i_a}$: $\tilde{\nu}_{as}$(C=O) ≈ 1775 cm^{-1} and $\mathbf{i_b}$: $\tilde{\nu}_{s}$(C=O) ≈ 1720 cm^{-1}, as well as the C-N stretch $\mathbf{i_c}$: $\tilde{\nu}$(C-N) ≈ 1365 cm^{-1}. Furthermore, modes stemming from the comonomers were missing, i.e., the amine vibrations (∼3400-3300 cm^{-1}) of TAPB and the carboxylic acid vibrations (i.e., ∼1850-1790 cm^{-1}) of PMA (see inset in Figure 12A). This strongly indicated the absence of unreacted monomers in the PI(TAPB-PMA) product. Moreover, ATR-FT-IR spectroscopy confirmed that the MS intermediate was fully consumed during the condensation reaction as the corresponding modes were also absent. Together, this

suggested a substantial degree of condensation to a point where end groups of potential oligomers were not detectable.

Afterwards, PI(TAPB-PMA) was further analyzed for crystallinity. PXRD showed no long range order but two amorphous halos in the region of ∼5-8° and ∼15-25° (2θ, Cu-K_α) marked with gray boxes (see Figure 12B). The area of ∼5-8°2θ (Cu-K_α) matches the region of Bragg reflections reported for the hexagonal lattice of the classically synthesized PI-COF based on the same comonomers (i.e., PI-COF-2 by Fang et al.)[85]. This suggests that somewhat of an order could be starting to form within the amorphous PI(TAPB-PMA). The halo at larger 2θ angles corresponds to typical macromolecular packing distances, e.g., π-π-stacking between polymer chains. This kind of stacking behavior is conceivable to be the case for PI(TAPB-PMA) for its aromatic moieties. Additionally, the sample was examined via microscopy. SEM analysis revealed most stunningly monodisperse microspheres as the dominant morphology along with small amounts of what looked like annealed microspheres forming a bulk solid (Figure 12C and D, and supporting information of the publication by Lahnsteiner et al.).[182]

In conclusion, HTP-MW turned out to be a suitable method to synthesize a fully condensed, amorphous PI network, i.e., PI(TAPB-PMA), hydrothermally. Another typical method used for HTP is the synthesis in unstirred batch autoclaves, which will be discussed in the following section.

Hydrothermal Synthesis in Unstirred Batch Autoclaves

As for the HTP-MW experiments, the comonomers TAPB and PMA were directly employed in HTP in an unstirred batch autoclave. Therefore, the comonomers were suspended in H_2O at RT and subsequently sealed tightly in a steel autoclave. The autoclave was immediately heated to 200 °C for $t_R = 24$ h, which are typical conditions used for HTP experiments in batch autoclaves (see Chapter 2.3). Afterwards, the autoclave was allowed to cool down slowly to RT. In contrast to the powder-like aspect of the HTP-MW sample, the product from HTP-AC could be collected as an intact, sponge-like, monolithic solid (see Figure 13A and Chapter B.2.2 for synthetic details). The monolith was filtered, washed with distilled water, ethanol, and acetone, and dried *in vacuo* at 80 °C.

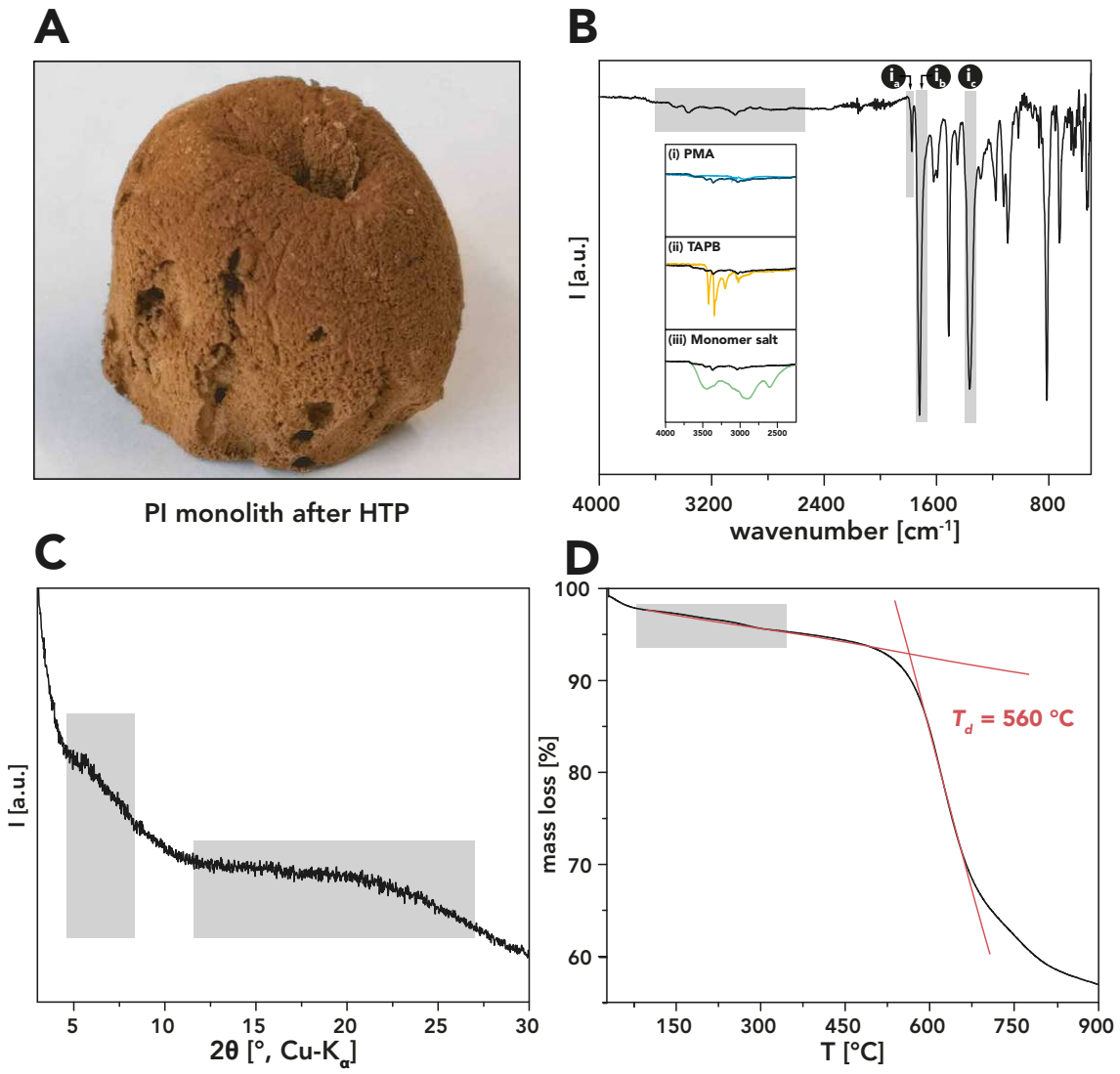

Figure 13: Characterization of PI(TAPB-PMA) synthesized HTP-AC at 200 °C for 24 h. A: Photograph of the PI monolith. B: ATR-FT-IR spectrum of PI(TAPB-PMA) with characteristic imide modes indicated with gray boxes ($\mathbf{i_a}$: $\tilde{\nu}_{as}$(C=O) ≈ 1775 cm^{-1}, $\mathbf{i_b}$: $\tilde{\nu}_{s}$(C=O) ≈ 1720 cm^{-1}, and $\mathbf{i_c}$: $\tilde{\nu}$(C-N) ≈ 1365 cm^{-1}); insets showed the H-bonding region 4000-2250 cm^{-1} of spectra of PMA (blue curve), (ii) TAPB (yellow curve), and the MS (green curve). C: PXRD pattern of PI(TAPB-PMA) with the two amorphous halos highlighted. D: TGA of PI(TAPB-PMA) under N_2 flow. Gray box highlighting initial weight loss due to water evaporating and red tangents indicating T_d. Figure adapted from Lahnsteiner et al..[182]

The characterization of the monolith is depicted in Figure 13B-D. ATR-FT-IR spectroscopy again pointed at a high degree of condensation (Figure 13B): Modes belonging to the comonomers or the MS were absent (see inset in Figure 13B) and the three typical imide modes ($\mathbf{i_a}$, $\mathbf{i_b}$, and $\mathbf{i_c}$) were present. Moreover, the monolith's thermal stability was investigated via thermogravimetric analysis (TGA, see Figure 13C). The T_d was determined corresponding to EN ISO 11358, aka "tangents' method": Therefore, the point of intersection (mass loss starting point) of the starting-mass baseline and the tangent to the TG curve at the point of maximum gradient was

used. This method yielded the quite high T_d of $\sim$550 °C. Only a small initial weight loss of $\sim$4 *wt.*% was observed in the range of 30-200 °C. This was associated with remaining H_2O molecules entrapped in the material, stemming from the synthesis in water. Evaporating water molecules upon heating during the TGA analysis could cause the observed weight loss. Except this initial weight loss and the overall decomposition of the whole PI, TGA did not show any other major degradation or condensation steps. Consequently, TGA showed that neither monomers, MS, nor short oligomers were present in PI(TAPB-PMA).

Additionally, PXRD of the monolith evinced that the obtained network was amorphous as it lacked any sharp reflections. As for HTP-MW, two amorphous halos in roughly the same 2θ regions ($\sim$5 - 8° and $\sim$15-25 ° (2θ, Cu-K_α)) were identified as depicted in Figure 13C.

Together, these results demonstrated the successful HTP of PI(TAPB-PMA) in a second set-up, i.e., an unstirred batch autoclave. The main difference between HTP-MW and HTP-AC turned out to be their products' macroscopic appearances. In contrast to the homogeneous powder obtained by HTP-MW, HTP-AC generated an intriguing monolith (see Figure 13A). The monolith's network architecture and the thereby imparted porosity features will be discussed in the following part of this chapter.

Network Architecture and Porosity

To elucidate the PI(TAPB-PMA) monolith's architecture, three different analyses were carried out. First, gas sorption experiments were performed to investigate potential microporosity. Second, mercury-intrusion porosimetry (MIP) was employed to identify meso- and macropores within the monolith. Finally, microscopy was used to confirm the findings from MIP.

First, low pressure gas sorption was used to study the monolith's microporosity. N_2 was chosen as analyzing gas, because it is most commonly used for organic networks and frameworks. The sample was degassed at 140 °C for 24 h before the sorption experiment was performed at 77 K. The obtained adsorption points were used to calculate the SA_{BET}. The value found was surprisingly low ($SA_{BET} = 23.92\,m^2\,g^{-1}$, see Figure A5 in the appendix for isotherm) and pointed at the absence of micro-

porosity altogether. However, the reason for the low SA_{BET} was not necessarily the lack of porosity in the material, but a matter of suitable adsorbates for the size range of pores investigated. Ritter and co-workers found in a study on linear PIs that nitrogen molecules are too slow to diffuse easily into very small pores. In contrast, carbon dioxide has a smaller kinetic diameter and a higher kinetic energy, which enables the molecule to even enter pores with a diameter below 0.8 nm (aka ultra-micropores).[200] Furthermore, they argued that the interactions of the highly polar imide moiety with carbon dioxide contribute to increasing the solubility and entrance of CO_2 into PIs. They concluded that nitrogen is suitable to characterize pores which are bigger than 1 nm, while carbon dioxide sorption is more suitable for ultramicropores.[200]

Therefore, the low pressure gas sorption experiments were repeated using CO_2 as analyzing gas. Accordingly, permanent porosity was elucidated via low-pressure carbon dioxide sorption studies employing both 195 K and 273 K. The sample was pretreated under vacuum at 120 °C for 24 h. The isotherm collected turned out to be a typical type-I isotherm which indicated that the sample in fact contained microporosity (Figure 14A).[38] Indeed, the surface area obtained from CO_2 adsorption at 195 K was found to be much higher ($SA_{BET} = 207\,m^2\,g^{-1}$) compared to N_2 adsorption. The adsorption points collected at 273 K were used to derive the pore size distribution (PSD) by fitting a Monte Carlo model for carbon adsorbents. PSD analysis showed that the majority of the pores were smaller than 0.8 nm, which confirmed that the monolith is in fact ultra-microporous (Figure 14B).[200]

After investigating the monolith's microporous environment, its porosity regarding larger pores (i.e., meso- and macropores) was studied via MIP. MIP revealed that the majority of porosity where macropores in the size range of 1-100 μm (see Figure 14C). Furthermore, pores in the size range 0.1-2 μm where observed. Finally, small relative amounts of mesoporosity (< 50 nm) could be identified. At a total Hg uptake of $306.82\,mm^3/0.0423\,g$, a very high specific pore volume of $7250\,mm^3\,g^{-1}$ was determined. However, MIP has its limitations and therefore data interpretation should be done with care. For example, MIP assumes all pores to be interconnected and none of the so-called "ink-bottle" type pores are present. Ink-bottle type pores

are pores with throats much narrower than the pore space itself ("neck-entrance"). During MIP these pores do not get filled with mercury until the applied mercury pressure reaches the level for filling its neck entrances.

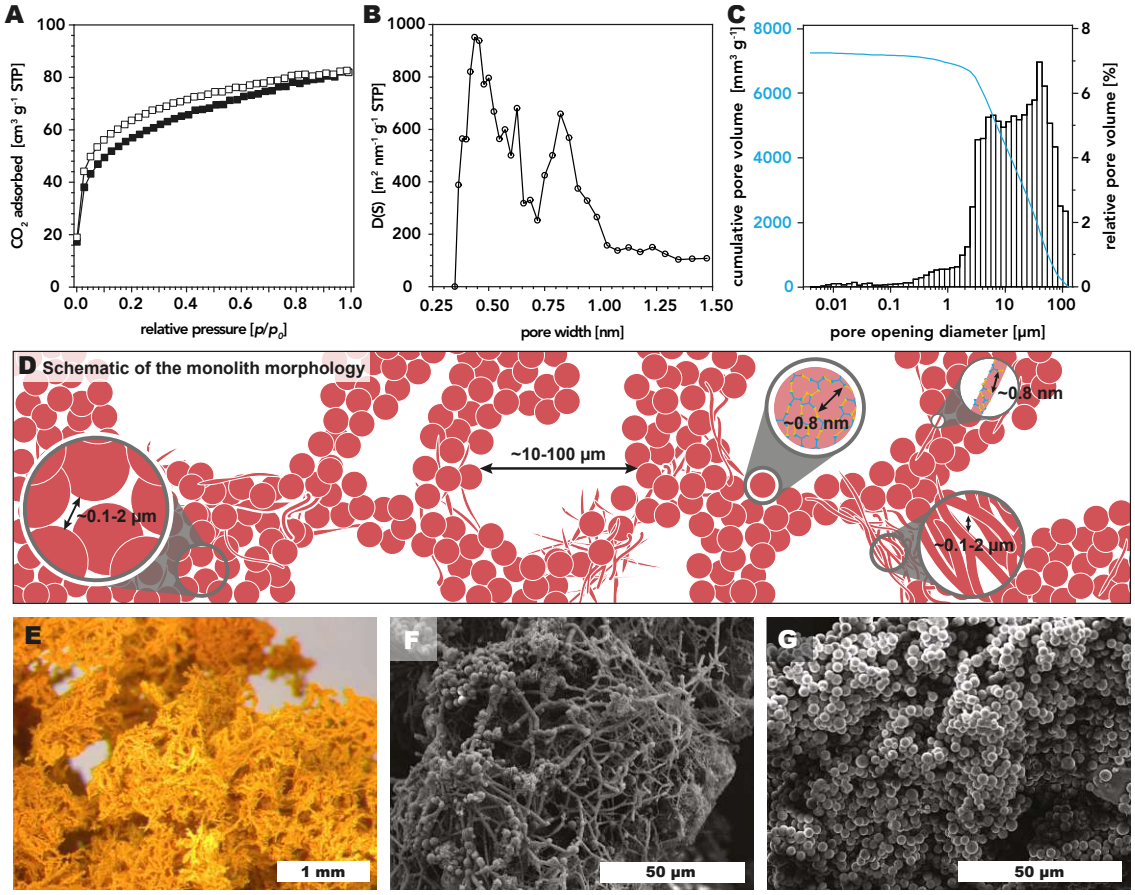

Figure 14: PI(TAPB-PMA) monolith structure and porosity. A: Low pressure CO_2 physisorption isotherm measured at 195 K (adsorption: black squares; desorption: white squares). B: PSD analysis showed a majority of ultramicropores (< 1 nm). C: Pore opening diameter distribution obtained by Hg intrusion porosimetry (max. intrusion pressure 400 MPa). D: Schematic of the monolith micromorphology. E: Microscopy image of the monolith. F: SEM image of the monolith featuring coexisting microspheres and microfibers. G: SEM image of the monolith featuring exclusively near-monodisperse micro-spheres. Figure adapted from *Lahnsteiner* et al..[182]

Therefore, such pores are systematically underestimated in size.[201] If this is the case can be assessed via the extrusion curve obtained by MIP. Hg is supposed to almost completely leave the material during extrusion. If the measured volume does not decrease during extrusion, Hg is most likely entrapped in bottle-neck pores. The extrusion curve for the PI(TAPB-PMA) monolith showed a similar behavior (see appendix Figure A4 for intrusion/extrusion curve). However, ink-bottle type pores could be excluded because of two reasons: First, only residues of the sample were found after the measurement, indicating the monolith walls breaking at the end of the measurement and therefore generating larger voids for Hg to remain in.

Furthermore, the pore volume and pores sizes assessed via MIP nicely corresponded to the findings of microscopy.

Both light microscopy and SEM analysis were performed. Light microscopy images showed a network structure composed of large voids ($\sim 100\,\mu$m) which matched the majority of pore sizes found via MIP (see Figure 14E). SEM analysis provided a more in depth picture. SEM images exhibited near-monodisperse microspheres ($\sim$3-5 μm in diameter) alongside roundish, elongated fiber particles with a length of $\sim 20\,\mu$m and a diameter of $\sim 1\,\mu$m (Figure 14F and G). These spheres and fibers agglomerated to densely packed structures generating the cell walls. The interstitial voids between those microparticles were in a size range of $< 2\,\mu$m which is also in good agreement with the findings of MIP.

When comparing the porosity of PI(TAPB-PMA) from HTP-AC to PI(TAPB-PMA) synthesized by conventional methods (as described in Chapter 2.3) two major differences stand out: (i) The cumulative pore volume of the PI(TAPB-PMA) monolith was one order of magnitude larger than for PI(TAPB-PMA) synthesized by Fang et al.[64,85] This quite large difference is probably caused by the macroscopic architecture of the monolith, which leads to an increased amount of meso- and macropores. In contrast, the conventional analogues are typically obtained as powders which exclusively feature micropores. (ii) SA_{BET} of PI(TAPB-PMA) by HTP was significantly smaller than from conventional synthesis.[57,64,85,202] HTP yielded 207 $m^2\,g^{-1}$, whereas conventional syntheses were able to generate SA_{BET}s up to 1297 $m^2\,g^{-1}$.[85] A possible explanation for the lower SA_{BET} from HTP is the big difference in polarity of solvent used. The lower polarity of the solvents used in conventional syntheses could cause increased swelling of the branches of the network. Therefore, a higher amount of pores in the microporous range are generated. In contrast, the more polar water molecules are less able to create swelling in the network. Hence, it was hypothesized that the segments of the network were more closely packed during HTP. This is supported by the fact that only ultra-micropores where observed in PSD analysis. Furthermore, most conventional synthetic protocols employ CO_2 activation (i.e., drying with $scCO_2$) as the last step to avoid collapsing of the structure during solvent molecules leaving the material. CO_2 activation was not performed

within the HTP protocol. Therefore, a post-synthetic collapse of micropores within the PI(TAPB-PMA) monolith could not be excluded. It was concluded that the different synthetic methods (HTP-AC vs. conventional synthesis) lead to opposing porosities (macro- and ultramicroporous vs. microporous).

In summary, CO_2 sorption, MIP and microscopy analyses revealed that the PI(TAPB-PMA) monolith structure was a highly porous, hierarchically organized material (Figure 14D). Three types of porosity were identified and fit in the very large size range of $> 0.8\,\text{nm}$ - $100\,\mu\text{m}$ (Figure 14D). Despite a relative low SA_{BET} determined via gas sorption, MIP confirmed a very high specific pore volume. Given these intriguing findings on the architecture of the material synthesized at typical HTP conditions ($T_R = 200\,°C$ and $t_R = 24\,\text{h}$, in an unstirred batch autoclave), a detailed study on varying the reaction conditions will be discussed in Chapter 4.1.2.

4.1.2 Screening of Reaction Parameters in Unstirred Batch Autoclaves

As the PI(TAPB-PMA) monolith obtained by HTP-AC was quite intriguing in architecture and porosity, this set-up was chosen for a broad screening of reaction conditions. In particular, various reaction conditions were tested to determine if the properties could be tuned through the reaction parameters. Specifically, T_R, t_R, and the use of the additive acetic acid (HOAc) were chosen. T_R was varied as previous organic HTP have shown that in some cases a minimum T_R was necessary,[183] and that increasing T_R was able to accelerate HT cycloconden-sations.[186] Furthermore, t_R was varied since it was observed to affect condensation and crystallinity.[188] Lastly, the effects of the addition of HOAc was investigated, as its use as morphology modulator in HTP has been reported[188] and was thought to potentially also be able to alter the degrees of condensation and crystallinity. Two reaction temperatures (T_Rs = 200 and 250 °C), 12 reaction times (t_Rs = 2, 4, 6, 8, 12, 16, 20, 24, 48, 60, 72, and 168 h) and with or without acetic acid (HOAc) were chosen as reaction conditions which led to 48 experiments. The 48 products were synthesized as described in Chapter 4.1.1 in an unstirred batch autoclave (see Chapter B.2.2 for synthetic details) and analyzed via ATR-FT-IR spectroscopy, PXRD measurements, TGA and SEM.

Attenuated Total Reflectance-Fourier-Transform-IR Spectroscopy

The vast majority of products exhibited almost identical ATR-FT-IR spectra, indicating a high degree of condensation and full conversion. As was the case for the initial experiment (t_R = 24 h, T_R = 200 °C), no modes corresponding to -NH_2 or -CO_2H/-CO_2^- were found and therefore the presence of monomers, MS or end-groups was excluded. The previously established imide modes $\mathbf{i_a}$, $\mathbf{i_b}$, and $\mathbf{i_c}$ (1775, 1720, and 1365 cm^{-1}) were also present in almost all products (see supporting information to the paper by Lahnsteiner et al.[182]). In fact, only six samples showed differences in ATR-FT-IR spectra (see Figure 15). All of them were synthesized at 250 °C and t_Rs longer than 60 h regardless of the addition of acetic acid. Compared to samples with lower t_R ($\leq$ 48 h), their imide modes were observed to decrease in intensity

with increasing t_R until they almost disappeared at $t_R = 168$ h (Figure 15A and B). This could be a sign for decomposition of the PI. Contradictorily, the spectra still featured sharp peaks and the majority of the modes, including the fingerprint region, remained mainly unaffected. Moreover, new peaks appeared, which could not be assigned to monomers, MS nor the imide moiety. Specifically, several modes in the H-bonding region ($\tilde{\nu} \approx 3625$, 3450, 3325, 3200, 3020, 2820, 2690, and 2550 cm^{-1}) seemed to gain intensity with increasing t_R.

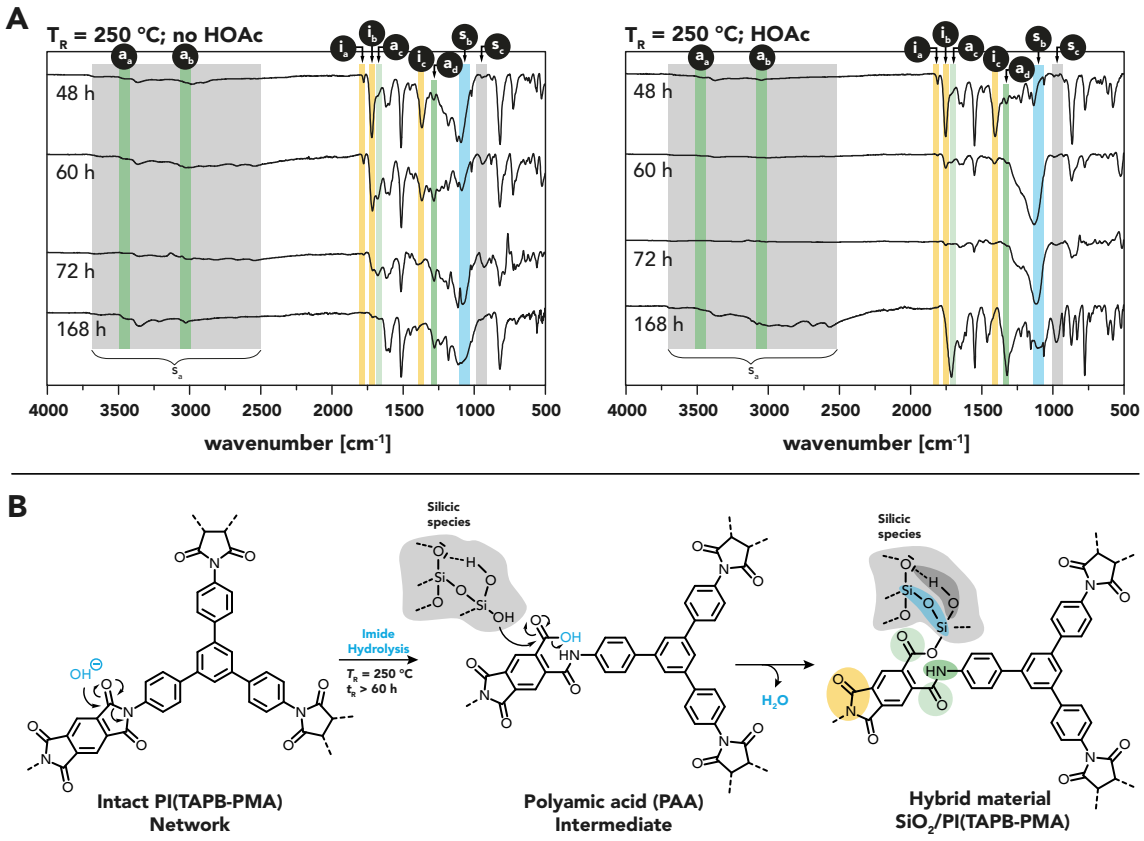

Figure 15: ATR-FT-IR spectra of PI(TAPB-PMA) synthesized at $T_R = 250$ °C, $t_R = 48$, 60, 72, and 168 h. A: Without HOAc present. B: With HOAc present. Modes assigned to the imide moieties were marked in yellow ($\mathbf{i_a}$, $\mathbf{i_b}$, and $\mathbf{i_c}$); modes assigned to amide moieties were marked in green ($\mathbf{a_a}$, $\mathbf{a_b}$, and $\mathbf{a_c}$); the mode assigned to Si-O-Si vibrations was marked in blue ($\mathbf{s_b}$) and modes assigned to Si-OH and H-bonding were marked in gray ($\mathbf{s_a}$ and $\mathbf{s_c}$). C: Hypothesis on the formation of a SiO_2/PI(TAPB-PMA) hybrid material. Moieties attributed to modes in ATR-FT-IR spectrum were marked in matching colors.

This trend was more pronounced in the presence of HOAc during synthesis (see Figure 15B; gray area named $\mathbf{s_a}$). Moreover, the two weak but sharp modes $\mathbf{a_c}$: $\tilde{\nu} \approx 1680$ cm^{-1} and $\mathbf{a_d}$: $\tilde{\nu} \approx 1280$ cm^{-1} appeared, most pronounced at $t_R = 168$ h and in the presence of HOAc. In the fingerprint region two more modes were observed: (i) a strong broad mode at $\mathbf{s_b}$: $\tilde{\nu} \approx 1100$ cm^{-1} which increased from $t_R = 60$ to $t_R = 168$ h, and (ii) a weak and broad mode $\mathbf{s_c}$: $\tilde{\nu} \approx 900$ cm^{-1} which was only found at $t_R = 60$ h

and 72 h, but absent at 168 h. Mode $\mathbf{s_b}$ was found to match the asymmetric siloxane (Si-O-Si) vibration in shape and wavenumber ($\tilde{\nu} \approx 1180\,\mathrm{cm^{-1}}$) reported in the literature.[203] Moreover, both the weak mode at $900\,\mathrm{cm^{-1}}$ and the modes in the H-bonding region fit to silanol (Si-OH) groups, which occur at $\tilde{\nu} \approx 3500\text{-}3000\,\mathrm{cm^{-1}}$ according to literature.[203] These modes indicated that a Si-species is present in the corresponding samples.

At first glance, this finding was quite surprising as only organic substances were used in the synthesis. When considering the whole HTP set-up, a possible source of Si-species in the reaction products was identified to be the borosilicate glass liners used as reaction vessels during HTP. Specifically, long t_R (> 60 h) and high T_R, such as 250 °C, were hypothesized to lead to the dissolution of SiO_2 from the glass walls into the aqueous reaction mixture. However, this did not explain the absence of imide modes in the respective ATR-FT-IR spectra. There were no signs of decomposition, hence it was assumed that the cyclic imides must have opened via hydrolysis. The hydrolysis proceeds via breaking the C-N bond, and consequently was expected to lead to RCO_2^-/RCO_2H and RNH_2/RNH_3^+ moieties. However, the corresponding modes were not found via ATR-FT-IR spectroscopy. Therefore, it was hypothesized that the imide moieties did not just open, but reacted further with Si-OH functions generating a covalently linked hybrid material. In particular, it was suggested that the condensation of amic acid intermediates with Si-OH resulted in silyl ester linking functions between SiO_2 and PI(TAPB-PMA) segments, leading to a hybrid material SiO_2/PI(TAPB-PMA) (see Figure 15B). Indeed, mode $\mathbf{a_c} \approx 1680\,\mathrm{cm^{-1}}$ matched with silyl ester C=O[204] or amide I modes.[205] Moreover, $\mathbf{a_d} \approx 1280\,\mathrm{cm^{-1}}$ matched the amide III C=O mode.[205] Furthermore, two modes which are typically found for amides were observed in the H-bonding region: Amide A/B vibration $\mathbf{a_a}$ and amide N-H stretching mode $\mathbf{a_b}$ at 3450 and $3025\,\mathrm{cm^{-1}}$ (green boxes within the H-bonding region in Figure 15A and B), respectively.[205,206]

From ATR-FT-IR analysis it was concluded that the vast majority of PI(TAPB-PMA) samples were chemically identical. Only when exposed to long t_R and high T_R, it was hypothesized that parts of the glass liners dissolved as silicic species which precipitated as SiO_2. Strikingly, ATR-FT-IR data also pointed at PI(TAPB-PMA) reacting with the silicic species, generating a covalently-linked

hybrid material SiO_2/PI(TAPB-PMA).

Powder X-Ray Diffraction Analysis

PXRD was performed on all PI(TAPB-PMA) samples to investigate possible differences in crystallinity within the reaction screening. The majority of PXRD patterns exhibited two amorphous features as found for the PI(TAPB-PMA) monolith described above (Chapter 4.1.1, Figure 13). Again, a few samples were observed to differ from the bulk. In accordance with the results from ATR-FT-IR analysis, the affected samples were obtained from HTP-AC for long reaction times at $T_R = 250\,°C$. In addition to the amorphous halos, those samples showed 3-5 weak, but relatively sharp reflections. Specifically, 3 reflections (β, δ, and ϵ in Figure 16A) appeared at $t_R \geq 48\,h$ and both with and without HOAc. The same three plus two more (α and γ in Figure 16B) appeared for the sample obtained at $T_R = 250\,°C$ and $t_R = 168\,h$ ($= 7\,d$) when HOAc was present: (α) 16.1 ° (2θ, Cu-K_α), corresponding to $d_{hkl} = 5.5\,Å$ ($n = 1$); (β) 17.5 ° (2θ, Cu-K_α), corresponding to $d_{hkl} = 5\,Å$ ($n = 1$); (γ) 18.6 ° (2θ, Cu-K_α), corresponding to $d_{hkl} = 4.8\,Å$ ($n = 1$); (δ) 25.2 ° (2θ, Cu-K_α), corresponding to $d_{hkl} = 3.5\,Å$ ($n = 1$); (ϵ) 27.9 ° (2θ, Cu-K_α), corresponding to $d_{hkl} = 3.2\,Å$ ($n = 1$).An obvious explanation for these new reflections would be that dissolved silica species from the glass liner reprecipitated and crystallized during HTP, yielding e.g., quartz crystals. However, when comparing the diffractograms of the affected samples with the diffractogram of α-quartz, no matching reflections were found.

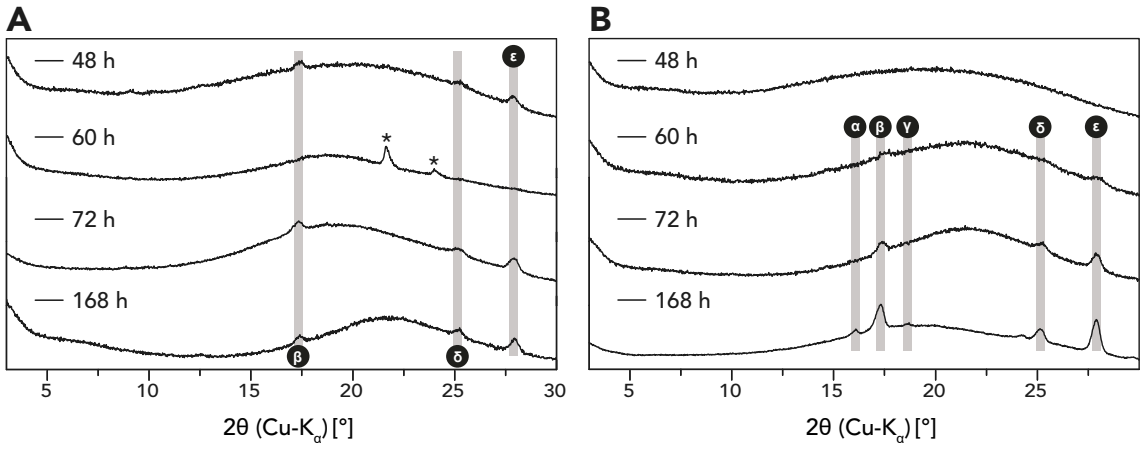

Figure 16: PXRD patterns of PI(TAPB-PMA) synthesized at $T_R = 250\,°C$, $t_R = 48$, 60, 72, and 168 h. A: Without HOAc present. B: With HOAc present. Reflections stemming from Vaseline used for mounting the sample were marked with asterisks.

Moreover, the diffractograms were also compared to the powder diffraction files (PDF) of eleven more SiO_2 polymorphs found via the International Center for Diffraction Data (ICDD) database (β-quartz: PDF 01-089-8951; α-tridymite: PDF 01-073-6613; β-tridymite: PDF 04-005-4647; α-cristobalite: PDF 04-018-0236; β-crystobalite: PDF 01-089-3435; keatite: PDF 01-077-3514; moganite: PDF 00-052-1425; coesite: PDF 01-077-1725; seifertite: PDF 04-023-2204; melanophlogite: PDF 04-015-4104; stishovite: PDF 00-045-1374; see supporting information to the publication by Lahnsteiner et al.[182] for overlay of the patterns). As no matches were found and because ATR-FT-IR spectra suggested that covalent linking via e.g., SiO(C=O)-R occurred, it was assumed that the new reflections corresponded to a hybrid material with a somewhat long range order. Notably, similar reflections were also found by one of my co-workers in 2017, where the HTS of SiO_2-PI hybrids via the linker compound 3-(aminopropyl)triethoxysilane was reported.[188]

Summing up, PXRD measurements showed that the majority of PI(TAPB-PMA) reaction products were fairly identical in crystallinity (i.e., amorphous) regardless of t_R and the addition of HOAc when synthesized at $T_R = 200\,°C$. Even at $T_R = 250\,°C$ and $t_R \leq 24\,h$, products showed an amorphous character. However, PXRD patterns suddenly showed emerging crystallinity at $T_R = 250\,°C$ and t_R longer than 24 h. This finding corroborated the hypothesis from ATR-FT-IR analysis that dissolved silicic species reacted with PI(TAPB-PMA) during HTP yielding a SiO_2/PI(TAPB-PMA) hybrid material.

Thermogravimetric Analysis

To gain more insights in the materials' molecular set-up (i.e., organic vs. inorganic components) thermal stabilities and char yields were analyzed by TGA (see supporting information to the paper by Lahnsteiner[182] et al. for all graphs). T_ds were determined via the tangents' method (according to EN ISO 11358) and turned out to be within a range of $T_d \approx 525$-$595\,°C$ for all samples synthesized at $T_R = 200\,°C$ and until $t_R = 60$ h when synthesized at $T_R = 250\,°C$. To determine a possible trend of the observed variation ($\pm 35\,°C$) in terms of reaction conditions, T_d was plotted against t_R (see Figure 17A). No clear correlation between T_d and t_R was observed for samples synthesized at 200 °C, regardless if HOAc was used or not (Figure 17A,

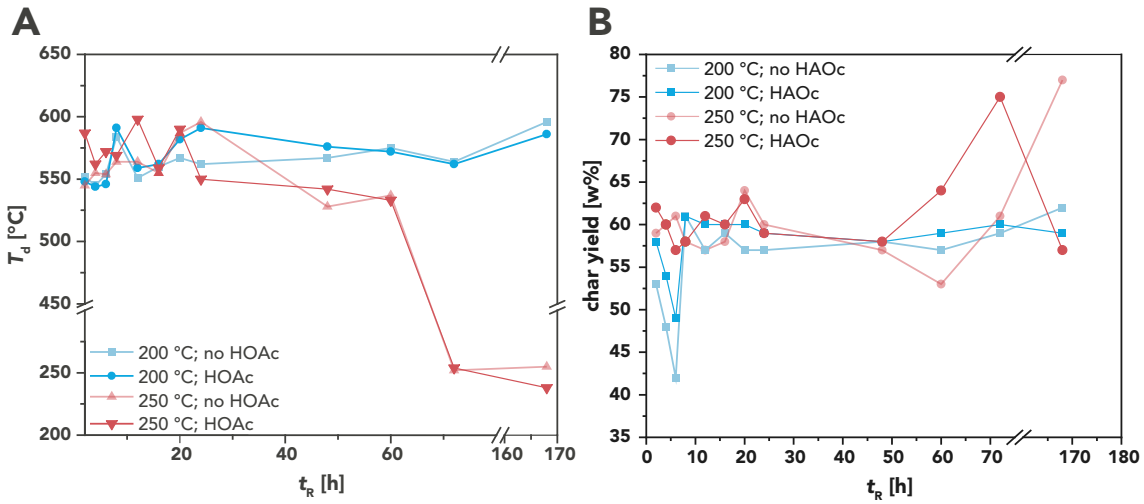

Figure 17: Correlation of reaction conditions of the PI(TAPB-PMA) samples with decomposition temperatures T_d and char yields, respectively. A: Decomposition temperatures T_d of all PI(TAPB-PMA) samples versus t_R. B: Char yields of all PI(TAPB-PMA) samples versus t_R.

curves in blue shades). The same was true for samples synthesized at 250 °C until $t_R = 60$ h, both with and without HOAc (Figure 17A, curves in red shades). These fluctuating T_d values could be explained by marginally varying degrees of condensation between samples. Based on this assumption, networks of slightly different "sizes" were generated, which affected T_d values, however could not be detected via ATR-FT-IR spectroscopy. Nevertheless, the majority of samples are highly T stable and therefore classified as HPP. Notably, T_d values decreased severely once $t_R = 60$ h was surpassed at $T_R = 250$ °C. The values dropped to more than half (~ 250 °C) compared to the median $\widetilde{T_d} \approx 562$ °C. This clearly showed that samples from HTP-AC at long reaction times (> 60 h) at 250 °C are no longer extended networks, but are composed of smaller molecular entities, i.e., oligomers.

In addition to T_d, char yields were analyzed. The char yield was determined from the residual mass (in *wt.%*) of the thermogravimetrically analyzed sample at $T_{max.} = 900$ °C. In Figure 17B, char yields were plotted against t_R. For the majority of samples, char yields between 42 and 59 *wt.%* were determined. However, especially two samples showed a quite large deviation: (i) 7 d, without HOAc = 77 *wt.%* and (ii) 72 h, with HOAc = 75 *wt.%*. The substantial gain in char yields was attributed to a mineral species present in the material, which did not decompose at the temperatures used for TGA. The reaction conditions where this increase was observed ($T_R = 250$ °C and $t_R > 60$ h), coincided with the conditions where ATR-FT-IR spectroscopy and PXRD results pointed at the formation

of a SiO_2/PI(TAPB-PMA) hybrid material. Thus the hypothesis was further corroborated that the species suspected in the material were indeed SiO_2 species.

"Finally, the samples' macroscopic aspects were inspected in detail. Macromorphologically, the samples within the screening differed relatively strongly. The observed macromorphologies ranged from elastic, sponge-like monoliths to brittle monoliths and powders, and correlated with the HTP conditions. At short t_R (< 48 h) elastic, spongy monoliths were obtained. Beyond $t_R = 48$ h, at first brittle monoliths were obtained, and subsequently mixtures of macroscopic pieces of different sizes with fine powders. Notably, at $t_R = 72$ h and 168 h, such mixtures were obtained exclusively. The most intact monoliths were also the most elastic ones, and were obtained after 12-24 h at 200 °C. The monoliths were found to be generally more intact and elastic in the absence of HOAc."[182] Due to the great variety of macromorphologies observed throughout the screening and the different micromorphologies found for the initial PI(TAPB-PMA) monolith (discussed in Chapter 4.1.1), a detailed SEM analysis of all 48 samples was performed, yielding 437 images (all SEM images were published as a stand alone data set[207]). The micromorphologies observed turned out to be fairly complex and therefore will be discussed in detail in the following.

4.1.3 Micromorphological Evolution

The following chapter was taken fully from the publication by Lahnsteiner *et al.*.[182]

"Several distinct micromorphological features were observed to co-exist to different degrees throughout the samples. Specifically, eight distinct morphologies were distinguished. The distinct morphologies, plus that of the MS, were summarized in Figure 18: (i) cuboid monomer salt crystals, $\sim$1-5 μm in length times $\sim$100-200 nm in width (Figure 18A); (ii) thin roundish needle-like fibers, $\sim$100-200 nm in width and several μm in length (Figure 18B); (iii) thicker coalesced roundish fibers that feature branching, $\sim$1 μm in thickness and several μm in length (Figure 18C); (iv) pearl-chain fibers; several μm in length and featuring globular slubs of $\sim$2 μm in diameter (Figure 18D); (v) near-monodisperse spherical particles, $\sim$2-5 μm in diameter (Figure 18E), (vi) roundish nanoparticles, $\leq$100 nm in diameter, henceforth referred to as "seeds" (Figure 18F); (vii) wrinkle-textured microspheres, $\sim$2-5 μm in diameter (Figure 18G), hollow spheres, $\sim$2-5 μm in diameter (Figure 18H), and (viii) spherulitic structures, up to $\sim$50 μm in length and up to $\sim$180 ° in circle segment angle, composed of twisted fibers of $\sim$5-10 μm in diameter and $\sim$50 μm in length (Figure 18I). From expert analysis of the SEM micrographs of all investigated samples (439 micrographs in total) produced in the screening, the morphological evolution of the PI(TAPB-PMA) networks as a function of T_R, t_R, and the presence of HOAc, was devised, summarized in Figure 19. In Figure 19, every panel was created to represent a pair of T_R and with/without HOAc: Figure 19A (200 °C| without HOAc), Figure 19B (200 °C| with HOAc), Figure 19C (250 °C| without HOAc), Figure 19D (250 °C| with HOAc). t_R was plotted on the x-axis, and white circles on the x-axis indicated at which specific t_R HTP experiments were carried out. Schematics for each of the previously described eight distinct micromorphologies were used to illustrate in which sample a morphology was found. Black bold arrows indicated the timespan over which the morphology was found, with the size of the arrow tips illustrating the relative abundance of the morphology. Through this display, the following steps of the morphology evolution during the HTP of PI(TAPB-PMA) became clear:

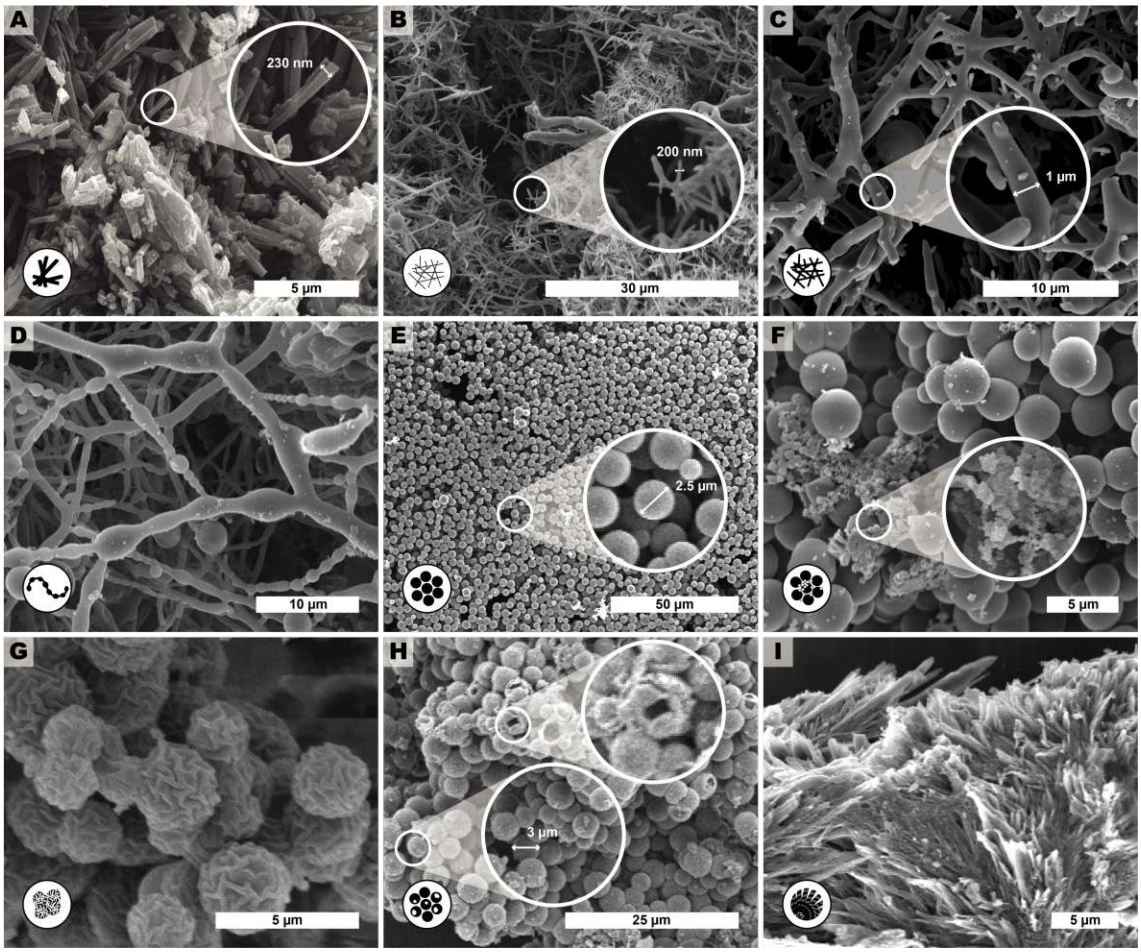

Figure 18: Representative SEM images of products of extended reaction condition screening of PI(TAPB–PMA). The described morphologies are: A: monomer salt crystallites ($t_R = 24$ h, $T_R =$ RT), B: fibers ($t_R = 2$ h, $T_R = 200$ °C.), C: thicker fibers ($t_R = 6$ h, $T_R = 200$ °C), D: pearl-chain fibers ($t_R = 12$ h, $T_R = 200$ °C), E: near-monodisperse particles ($t_R = 48$ h, $T_R = 250$ °C), F: seed particles on top of microspheres ($t_R = 72$ h, $T_R = 200$ °C), G: wrinkle-textured microspheres ($t_R = 60$ h, $T_R = 250$ °C), H: hollow spheres ($t_R = 72$ h, $T_R = 250$ °C, with HOAc) and I: angular particles ($t_R = 72$ h, $T_R = 250$ °C). Figure taken from Lahnsteiner et al..[182]

(i) Figure 19A ($T_R = 200$ °C | no HOAc):

(1) Thin fibers were found only briefly, at short t_R of 2-4 h. For their matching dimensions, it was assumed that the thin fibers resulted from MS crystals (SEM in Figure 18A) which had been serving as solid templates on which first formed PI(TAPB-PMA) were deposited (see schematic of the micromorphological evolution, Figure 20). (2) The thicker coalesced fibers were also found over a medium t_R (4-60 h), compared to corresponding HTP (same T_R) with HOAc (there they were found at 8-168 h). The relative amounts of both thick and thin fibers decreased with increasing t_R. (3) Spherical microparticles started to appear at $t_R = 8$ h and persisted until the longest t_R of 168 h. Their relative amount increased with t_R. It was hypothesized that the degree of polymerization increased from the morphologies

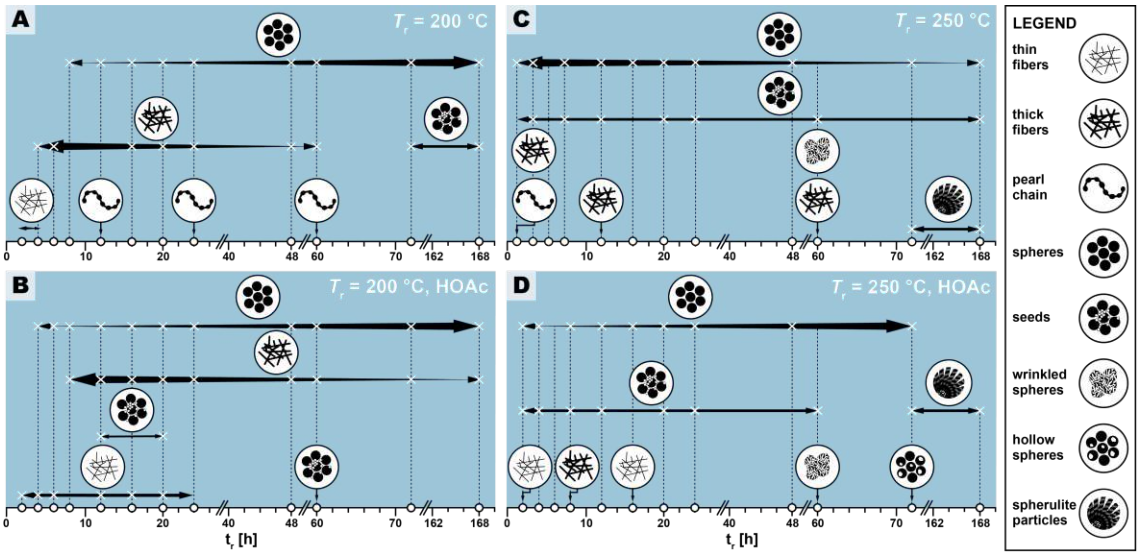

Figure 19: Appearance and relative abundance of limit micromorphologies in SEM images of PI(TAPB–PMA) reaction condition screening. Legend of limit morphologies is shown on the right. A–C: Appearance (x) and relative abundance (thickness of arrows) deduced from manual inspection of SEM images. White circles on the x-axis indicate at which specific time HTP experiments were performed. Each panel represents a pair of T_R and HOAc presence/absence, specifically A: (200 °C; no HOAc), B: (200 °C; with HOAc), C: (250 °C; no HOAc), and D: (250 °C; with HOAc). Figure taken from Lahnsteiner et al..[182]

thin fibers to thick fibers to spheres (cf. Figure 20). (4) Pearl-chain morphologies were only found in three samples ($t_R = 12$, 24, 72 h) and neither in large amounts nor repeatedly (i.e., in several consecutive samples). A possible explanation could be that they were somewhat of a snapshot of the thicker fibers softening and separating into the spherical particles. Therefore, they would be short-lived, and hence were not found in many samples. (5) Additionally "seed" nanoparticles were observed at long $t_R = 72$ and 168 h.

(ii) Figure 19B ($T_R = 200$ °C | with HOAc):

The morphologies found and the overall trends with respect to their appearance and abundance were similar to the samples prepared at the same T_R but in the absence of HOAc. Yet, several morphologies were present over slightly different timescales. (1) The thin fiber morphologies appeared earlier and persisted for longer times, i.e., $2\,h \leq t_R \leq 20\,h$ (compared to $2\,h \leq t_R \leq 4\,h$ in the absence of HOAc). (2) the spherical particles also appeared earlier and persisted for longer times, i.e., $4\,h \leq t_R \leq 168\,h$ (compared to $8\,h \leq t_R \leq 4\,h$ in the absence of HOAc). As for HTP in the presence of HOAc, their abundance increased with increasing t_R. The observation that thin fiber morphologies appeared earlier than in the

absence of HOAc pointed at HOAc was initially accelerating the monomer salt dissolution and initial reaction to oligomers. However, that these morphologies persisted for longer t_R pointed at HOAc actually slowed down the subsequent polymerization. (3) In contrast, the thick fibers appeared later and persisted for longer, i.e., $8\,h \leq t_R \leq 20\,h$ (compared to $2\,h \leq t_R \leq 4\,h$ in the absence of HOAc). Again, this suggested that HOAc slightly slowed down the polymerization at 200 °C. The thick fibers' abundance also increased with increasing t_R, as for ($T_R = 200$ °C | no HOAc). (4) Pearl-chain morphologies were not found at all. As argued earlier, they were believed to be short-lived, and hence not finding them in SEM images was most likely nothing more than coincidental.

(5) Seed particles were found significantly earlier, i.e., at $t_R = 12$, 20, and 60 h. It was assumed that these small particles (≤ 100 nm in diameter) correspond to SiO_2. Indications of SiO_2 were not found in ATR-FT-IR or XRD for these reaction times and in SEM only very small relative amounts were observed. Hence, the absence of indication for SiO_2 at the corresponding t_R in ATR-FT-IR and PXRD was likely explained through both techniques' sensitivity (in PXRD for amorphous structures). That these SiO_2 nanoparticle morphologies appeared earlier in the presence of HOAc is consistent with the literature: Geochemical studies have shown that e.g., quartz can dissolve in H_2O in small quantities,[208] and that such dissolution is up to one order of magnitude faster in the presence of (organic) acids.[209–211]

(iii) Figure 19B ($T_R = 250$ °C | no HOAc):

(1) No thin fibers were found at any t_R, pointing at HTP being much more rapid at 250 °C, which was expected. (2) Thick fibers were found in three instances and in low amounts, i.e., at $t_R = 2$, 12, and 60 h. (3) Spherical particles were present through the entire t_R span studied, and their abundance decreased with increasing t_R. Again, this pointed at HTP being much faster at the higher T_R of 250 °C. (4) Seed particles were also present through the entire time span studied, at low but constant abundance. This was found to be consistent with the literature on SiO_2 dissolution in H_2O and its re-precipitation being faster with increased T_R.[208] (5) Pearl-chain morphologies were only found in one sample, at the lowest tested t_R of 2 h. (6) Additionally, a "wrinkle-covered sphere" morphology was found at

$t_R = 60$ h. It was hypothesized that these intriguing morphologies also corresponded to SiO_2/SiO_2-PI hybrids. In fact, such morphologies have been described by Oehler in a geochemical study on the hydrothermal crystallization of silica gels.[212] Oehler described them as "honeycomb-textured microspheres", likely for the particles' surface textures resembling honeycomb-weathering in sandstone, and explained these morphologies as the result of a complex crystallization process of subsequent steps with different growth rates.

(7) Finally, spherulitic objects were observed at $t_R = 72$ and 168 h. These were composed of twisted fibers $\sim$5-10 μm in diameter and $\sim$50 μm in length. These fibers could be composed of the ordered SiO_2/PI(TAPB-PMA) hybrid which was hypothesized to form during HTP at 250 °C in Chapter 4.1.1 from ATR-FT-IR and XRD data. Spherulitic structures have been identified to be the most common crystal habit across all crystalline substances, and numerous naturally solution-grown minerals form spherulites.[213] In fact, chalcedony, i.e., fibrous quartz, is the most well-known spherulite-forming mineral.[213] Fibrous quartz is often consisting of twisted fibers, and, fibrous quartz is typically generated hydrothermally.[214] Hence, finding spherulites of twisted fibers at long t_R at the higher T_R of 250 °C was in agreement with the hypothesis of silica-rich SiO_2/PI(TAPB-PMA) hybrids.

(iv) Figure 19B ($T_R = 250$ textdegree C | with HOAc):

The observed micromorphologies were similar to those found at 250 °C without HOAc, but were found over different time spans. Morphologies related to PI(TAPB-PMA) were found later than without HOAc at 250 °C, suggesting that the presence of HOAC slowed down the HTP at this T_R. In contrast, morphologies related to SiO_2 or SiO_2/PI(TAPB-PMA) seemed to be favorably formed in the presence of HOAc. (1) Thin fibers were found at $t_R = 2$ h and 16 h. Since these were related to the early stages of HTP, i.e., an initial polymer deposition on external MS nuclei, their existence pointed at HOAc slowing down the HTP (compared to 250 °C no HOAC). (2) Thick fibers were only found in one sample, at $t_R = 8$ h. (3) Spherical particles were found at $2\,\text{h} \leq t_R \leq 72\,\text{h}$, and interestingly, their amount increased with increasing t_R. Again, this further substantiated the hypothesis that HOAc at 250 °C slows down HTP. For comparison, without HOAc at 250 °C, spherical

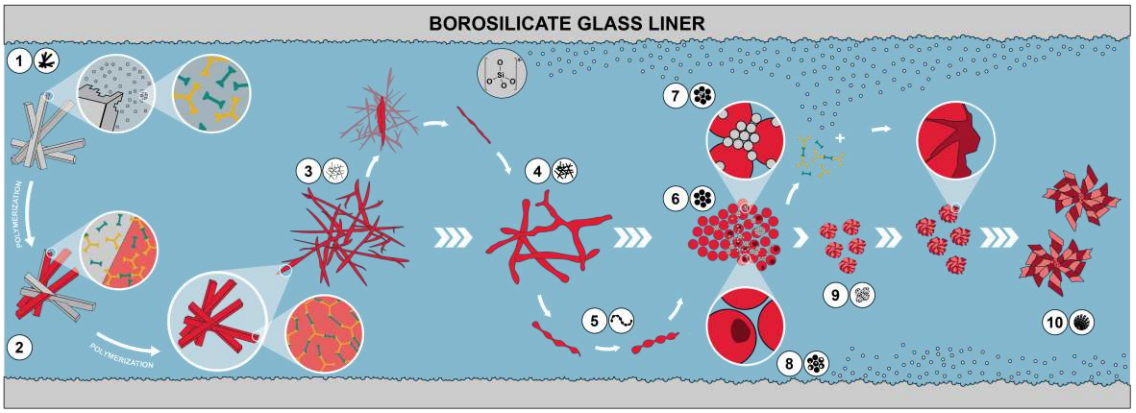

Figure 20: Proposed hypothesis of the morphological evolution leading to monodisperse PI particles. (1) Dissolution of a small fraction of MS crystallites. (2) polymerization of dissolved MS and deposition on yet undissolved MS crystallites leading to (3) thin fibers. (4) softening of thin fibers and merging into thicker fibers. (5) further softening and separation via pearl chain-like structures into (6) spheres, (which assemble into particle networks building up the monoliths (not shown). At 250 °C, (7) dissolution of SiO_2 from glass liners and reprecipitation as nanometric SiO_2 particles; dissolved SiO_2 species react with PI networks forming hybrid materials on the surface of existing PI spheres; (8) monomers leaching out from PI particles creates hollow spheres. SiO_2/PI hybrids' growth generates (9) wrinkled sphere and subsequently (10) spherulite morphologies. Figure taken from Lahnsteiner et al.[182]

particles were present from the beginning and their abundance decreased with t_R. (4) Pearl-chain morphologies were not observed. (5) Seed particles were present at $2\,h \leq t_R \leq 60\,h$, and their abundance stayed constant throughout that time span. (6) Wrinkle-covered spheres were found at $t_R = 6\,h$, and (7) fibrous spherulites were found at the highest t_R of 72 h and 168 h.

Finally, (8) hollow sphere morphologies were observed. Hollow morphologies are often generally pointing at the dissolution of an object's interior, because the outer surface is already covered with another material that does not dissolve. Such morphologies are known for various solution-synthesized materials, including e.g., $CaCO_3$.[215]

The overall morphological transformation was summarized in Figure 20. It was hypothesized that first, at low t_R, the MS $[H_3TAPB_3^+]_2[PMA_2^-]_3$ formed as angular crystallites. Second, some MS dissolved in HTW and started polymerizing to PI(TAPB-PMA). At short t_R, it was assumed that PI(TAPB-PMA) was not fully condensed, but rather consisted of oligomeric network fragments. Third, these initial PI(TAPB-PMA) fragments deposited onto not yet dissolved MS crystals and hence, thin needles were found that roughly matched the dimensions of MS crys-

tals. Fourth, more MS dissolved, polymerized, and deposited onto the thin fibers as external nuclei, leading to thick fibers. Fifth, these fibers softened and, driven by minimizing their interface with H_2O, started splitting into more roundish morphologies. The pearl-chain morphologies were believed to be a snapshot of this splitting. Sixth, the morphologies which resulted from the splitting of thick fibers were near-monodisperse spherical PI(TAPB-PMA) particles. Seventh, at prolonged reaction times at 200 °C ($t_R > 60$ h) and at 250 °C right from the beginning, silica (likely in the form of silicic acids) dissolved from the glass liners and started precipitating as nanoparticles, which were referred to as "seeds". Eighth, SiO_2-rich hybrids formed through reaction of SiO_2 seeds and further silicic acid species with the present PI(TAPB-PMA). The morphologies related to hybrid formation included wrinkle-covered spheres to fibrous spherulites and hollow spheres (which were speculated to arise from PI leaching out/depolymerizing before subsequently forming hybrids)." [182]

To assess if solid-state polymerization (SSP) contributed to the morphology evolution, SSP was investigated next.

Solid State Polymerization using a Monomer Salt Precursor

The feasibility of SSP of a PI via a MS precursor has been proven by Unterlass and co-workers.[194] Furthermore, it has been reported that MSs can undergo SSP under HT conditions when they are not soluble resulting in SSP of MS particles in dispersion in HTW. Therefore, it was of interest to investigate (i) if SPP was also possible for $[H_3TAPB^{3+}]_2[PMA^{2-}]_3$, (ii) how the isolated MS behaved under SSP conditions and (iii) if SSP played a role during HTP of the PI(TAPB-PMA) network.

For the SSP experiment, $[H_3TAPB^{3+}]_2[PMA^{2-}]_3$ was placed in a round bottom flask, containing a stirring bar, and was subsequently evacuated. Afterwards, while continuously applying vacuum, the flask was placed in an oil bath which was set at 200 °C for 8 h while stirring vigorously. A color change from pale green to yellow and finally to beige was observed after several hours of heating. When cooled down to RT, the beige, solid powder was collected and thouroughly analyzed via ATR-FT-IR spectroscopy, PXRD measurements, TGA, and SEM.

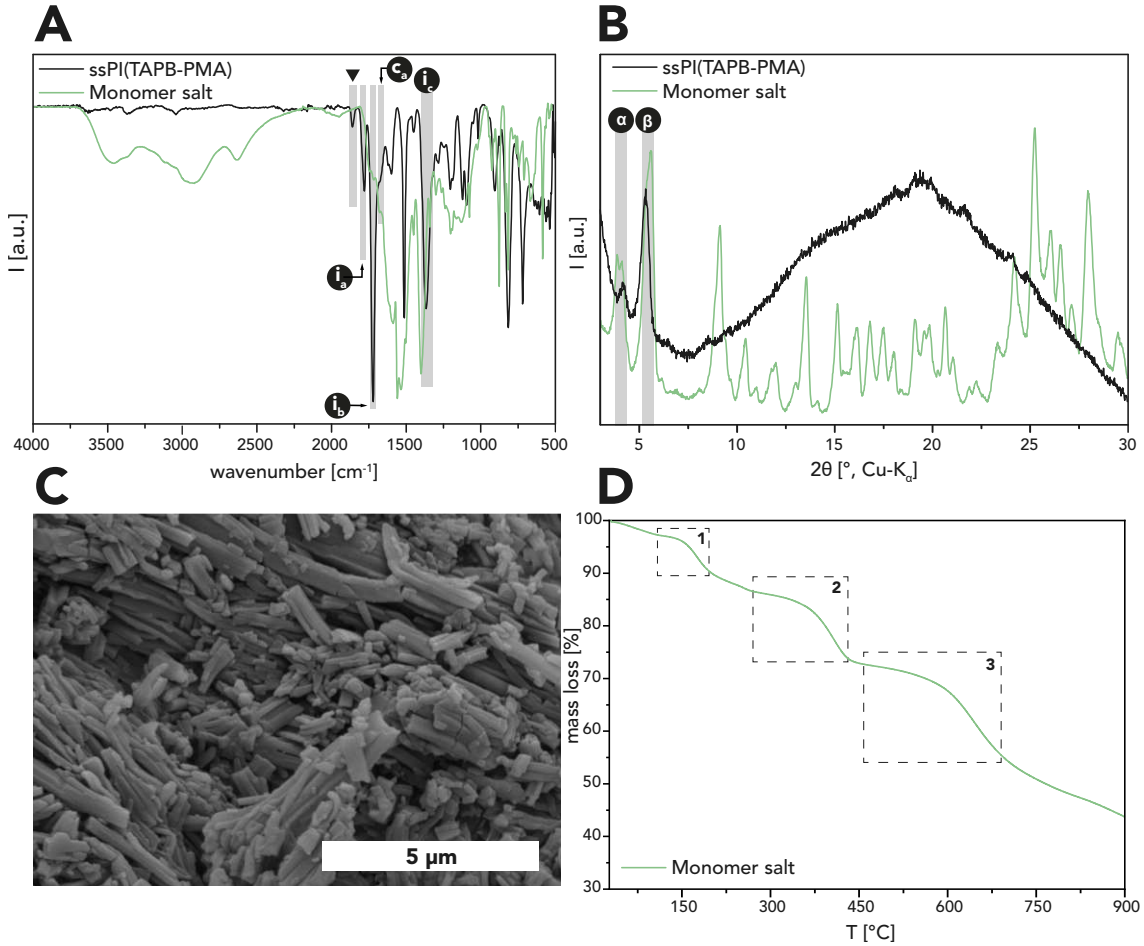

Figure 21: Characterization of ssPI(TAPB-PMA). A: ATR-FT-IR of ssPI(TAPB-PMA) (black) compared to the spectrum of the MS (green) B: Diffractogram of ssPI(TAPB-PMA) (black) compared to the monomer salt (green). C: SEM image of ssPI(TAPB-PMA) showing similar shapes and sizes (i.e., angular particles with a diameter of $\sim 0.5\,\mu$m) as the MS. D: TGA curve of the MS with three mass losses indicated by dashed boxes.

ATR-FT-IR analysis of the SSP product (ssPI(TAPB-PMA)) revealed that the condensation towards imide indeed occurred. The spectra showed the typical imide modes which have already been identified in the last chapter (see Figure 21A, modes $\mathbf{i_a}$, $\mathbf{i_b}$ and $\mathbf{i_c}$). At $\tilde{\nu} \approx 1860\,\mathrm{cm}^{-1}$ (marked with a black triangle in Figure 21), a weak but sharp mode was observed, which could neither be assigned to PI(TAPB-PMA), nor one of the monomers or the MS. Additionally, a weak shoulder at $\tilde{\nu} \approx 1680\,\mathrm{cm}^{-1}$ (Figure 21A, mode $\mathbf{c_a}$) was observed and attributed to the C=O stretch of carboxylic acid moieties of PMA. This pointed at residual MS molecules present in ssPI(TAPB-PMA).

PXRD evinced that during SSP amorphization took place as a prominent, broad, amorphous halo ($\sim$ 7-27 °(2θ, Cu-K$_\alpha$)) was observed for ssPI(TAPB-PMA) (see Figure 21B). Moreover, the diffractogram showed two distinct reflections: $\alpha =$

4.2 °(2θ, Cu-K_α) and $\beta = 5.6$ °(2θ, Cu-K_α). These reflections precisely matched the first two reflections present in the MS diffractogram (Figure 21A green curve). Together with ATR-FT-IR spectroscopy results, this pointed at full condensation was not reached within the reaction conditions of the conducted SSP experiment. TGA of the MS (see Figure 21D) revealed three mass losses. Before the first mass loss occurred, a decreasing trend in the curve indicated physisorbed water evaporating (until $\sim$90 °C). The first step (at $\sim$150 °C) could be the release of crystal water incorporated in the MS solid. In the second step, at $\sim$360 °C, the polycondensation point was assumed to be reached, kicking-off the polymerization reaction. The last step at $\sim$590 °C marked the degradation of ssPI(TAPB-PMA). Finally, SEM analysis clearly evinced that PI(TAPB-PMA) from SSP appeared as shape copies of the MS crystals (see Figure 21C), i.e., cuboid particles with a width of $< 1\mu$m. This was in accordance with previous reports on the morphology of PIs from SSP of MSs.[194,216] The morphologies found for both HTP-MW and HTP-AC were not shape copies of MS but quite different shapes (roundish particles and fibres). Therefore, it was concluded that SSP did not play a key-role in the formation of the PI(TAPB-PMA) network and the morphology evolution.

Computational Image Analysis

Within the reaction screening of HTP-AC, nine distinct morphologies were identified. A hypothesis for the morphological evolution of PI(TAPB-PMA) was devised through manual expert interpretation of 437 SEM images. The respective images were highly complex, often featuring several of the identified distinct morphologies in one and the same picture. Since manual interpretation proved quite tedious, a more efficient analysis in an automated fashion was sought after. Automated image analysis yielded a computational image analysis pipeline, which was capable of differentiating between different morphologies in one image. Furthermore, it was able to identify clusters of morphologies and automatically correlate their presence or absence with reaction parameters. This allowed for formulating a hypothesis of morphology evolution in HTP that was found to be in good agreement with the manual morphology analysis described above. The details of the automated image analysis are not discussed further at this point, as the computational aspect of

this study is not the focal point of this thesis. A comprehensive discussion of the development and application of the image analysis pipeline can be found in the publication by Lahnsteiner et al..[182]

4.1.4 Up-scale and Processing

HTP of PI(TAPB-PMA) turned out to be a robust synthetic method, which yielded a material with intriguing properties, therefore potential processing was investigated. Both products from HTP-MW and HTP-AC were fully condensed PI(TAPB-PMA) networks and could therefore serve as precursors for potential processing. However, HTP-AC yielded a monolithic material which was not suitable for further processing in a desired shape via e.g., sintering.

In contrast, HTP-MW did not yield a monolithic structure due to vigorous stirring. Instead, powders of exclusively near-monodisperse spherical microparticles were obtained. Opposed to the monolithic product, these powders were nicely suitable for processing via sintering. Furthermore, the spherical morphology of the microparticles led to the assumption that PI(TAPB-PMA) featured some degree of flexibility on a molecular level. This might allow for creep at increased temperatures in the dry state. It was assumed that if PI(TAPB-PMA) provided sufficient creep, then sintering into bigger objects should be possible.

Upscaling via Microwave-Assisted Hydrothermal Polymerization

The $\sim$70 mg PI(TAPB-PMA) powder obtained by HTP-MW (when using 30 mL vials, as described in Chapter 4.1.1) was however too little to successfully sinter the material. Therefore, HTP-MW was scaled-up employing a bigger microwave reactor featuring space for four 100 mL vials at the same time, which increased the synthetic volume by a factor of 16 for one experiment (reaction details can be found in Chapter B.2.2). Furthermore, the temperature was increased compared to the smaller microwave set-up because the heat transfer in the bigger vessels was observed to be less efficient. In particular, $T_R = 250\,°C$ and $t_R = 4\,h$, were chosen. In total four runs of 4 x 4 vessels were performed, and cumulatively, 7.364 g of PI(TAPB–PMA) were generated as fine brown powder (see Figure 22A).

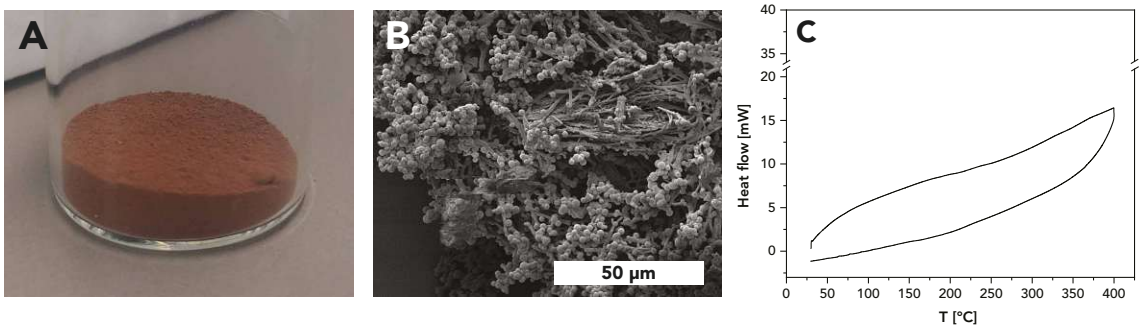

Figure 22: Up-scaling of PI(TAPB-PMA) via HTP-MW. A: Photograph of PI(TAPB-PMA) powder synthesized in a 100 mL microwave reactor at 250 °C, $t_R = 4$ h. B: SEM image of the upscaled PI(TAPB-PMA)(100 mL microwave reactor, four synthesis parallel), 250 °C, $t_R = 4$ h. C: DSC curve of the upscaled PI(TAPB-PMA) powder. Figure adapted from Lahnsteiner et al..[182]

ATR-FT-IR spectroscopy of all 16 batches were identical and proved the full condensation of the PI(TAPB-PMA) products and PXRD data showed that all products were amorphous (for all spectra and diffractograms see the supporting information to the publication by Lahnsteiner et al.[182]).

SEM analysis revealed that in contrast to the near-monodisperse spheres obtained from HTP-MW in small reactors (see Figure 12C), PI(TAPB-PMA) from the big vessels featured a mixture of both spheres and thick micro-fibers (see Figure 22B).

A property crucial for sintering would be any phase transition, i.e., melting point or T_g. Therefore, differential scanning calorimetry (DSC) of the upscaled PI(TAPB-PMA) was measured from 30 to 400 °C. No thermal phenomena were observed upon heating or cooling, i.e., neither first order (peaks) nor higher order (deflection points) phase transitions (see Figure 23C). The absence of a T_g until 400 °C as judged from the DSC trace was discouraging. However, sintering was still believed to be possible, as the morphology evolution observed and discussed in Chapter 4.1.3 implied that PI(TAPB-PMA) possesses the ability to soften. Therefore sintering by warmpressing was attempted, a technique widely used for the compaction of powder-based polymers and polymer-derived materials.[217]

Processing: Warmpressing of PI(TAPB-PMA) Powder

"For the warmpressing experiment, the combined powders from the 16 microwave batches were introduced into a steel cavity with an inner diameter of 40 mm and were uniaxially compacted at 80 MPa. As release agent between the steel punches and the powder, Kapton® foil was used. The temperature of the die was increased to 350 °C (heating rate 6 K min^{-1}), and the maximum temperature was held for

2 h. The pressure was adjusted accordingly when required. After cooling to RT, the pressure was reduced and the compacted part was removed from the mold. As a result, a whole, cylindrical pellet was obtained with the dimensions of diameter $d = 39.96$ mm and height $h = 5.06$ mm, which corresponded to a bulk density of 1.09 g cm^{-3} (see Figure 23A). Macroscopically, the pellet exhibited a smooth surface. In Figure 23B and C, SEM images of the pellet's outer surface as well as the fracture surface (after mechanical testing) revealed that the spherical particles were nicely consolidated during warmpressing, however stayed mostly intact and were still discernible."[182]

Porosity of the Pellet

In order to compare the porosity of the warmpressed pellet with the porosity of the monolith obtained via HTP-AC, MIP was performed once more (see Figure 23D). Owing to an apparent compression of the sample at intrusion pressures above 100 MPa, a compressibility correction was applied to the intrusion curve. Compared to the PI(TAPB-PMA) monolith, the warmpressed pellet showed a much smaller pore size distribution with the majority of the pores found between 0.2-0.5 μm. When consulting SEM analysis, these pores could be assigned to voids generated at the triple-points where the microspheres met during compressing. Only a very small amount of mesoporosity was detected. The lack of pores $> 1\,\mu$m (which represented the majority of macropores within the PI(TAPB-PMA) monolith) was to be expected as both the powder, as well as the pressed pellet missed the macroscopic architecture. The total porosity obtained from MIP after compressibility correction was 15 %; however, due to method-inherent limitations, this value did not include pores smaller than 4 nm.

Moreover, the pellet's microporosity was examined via low-pressure carbon dioxide (CO_2) sorption measurements at 195 K (Figure 23E). As for the monolith, again a typical type-I isotherm was observed and $SA_{BET} = 203\,m^2\,g^{-1}$ was calculated, which was within the error margin of $SA_{BET} = 207\,m^2\,g^{-1}$ for the non compacted particulate sample (monoliths were ground prior to gas sorption measurements). CO_2 sorption at 273 K gave a PSD with a maximum at 0.5 nm. Hence, it was concluded that PI(TAPB–PMA)s intrinsic ultramicroporosity was not affected by

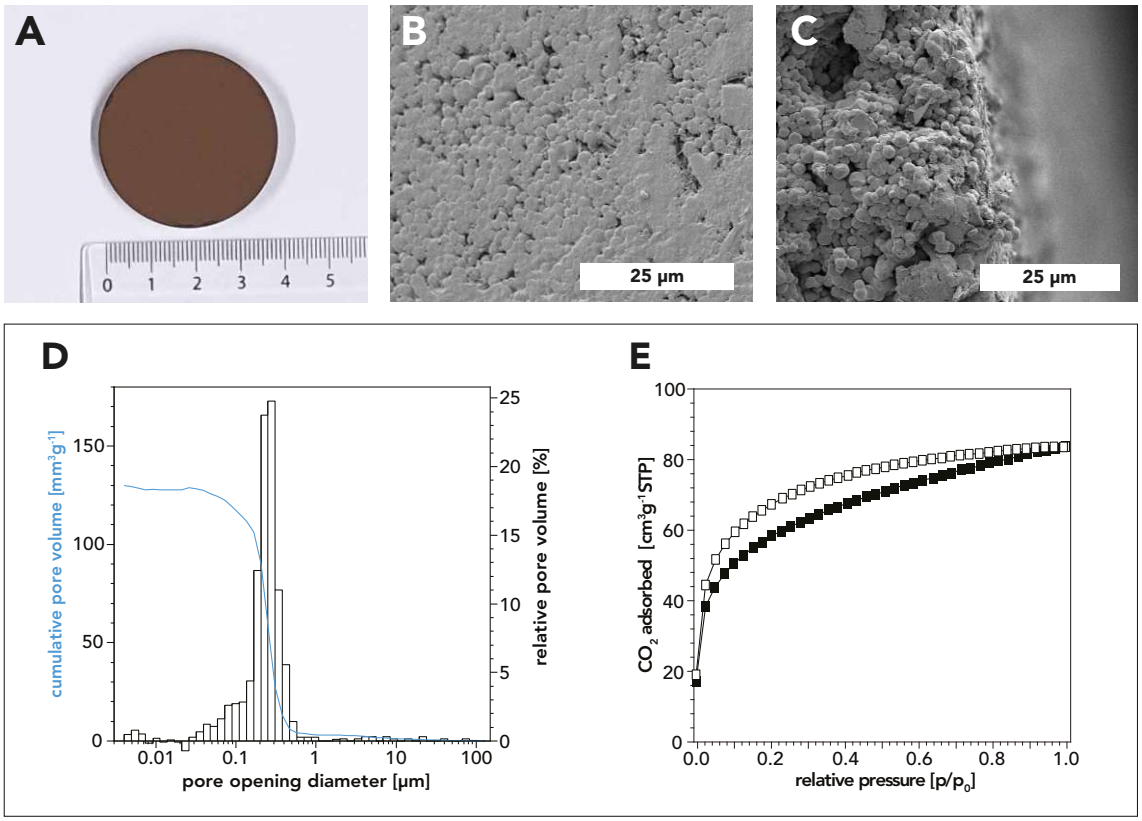

Figure 23: Characterization of warm-pressed PI(TAPB-PMA) pellet. A: Photograph of the PI(TAPB-PMA) pellet obtained via warm-pressing. B: SEM image of the outer surface of the pellet. C: SEM image of the fracture surface of the pellet after mechanical testing. D: Pore opening diameter distribution and cumulative pore volume (blue curve) from Hg porosimetry. E: low pressure CO_2 physisorption isotherm measured at 195 K. Figure adapted from Lahnsteiner et al..[182]

the processing via sintering."[182]

Mechanical Performance

"Finally, the pellet's mechanical performance was tested by flexural strength measurements using a three-point flexural test set-up, following EN ISO 178 (see appendix). The flexural strength of warm-pressed PI(TAPB–PMA) material was 36.0 ± 1.8 MPa. The flexural modulus was 2084 ± 34 MPa. The variability between individual specimens was low, suggesting an overall high homogeneity within the sample microstructure after warmpressing. Flexural yields strengths of $\sim$25-500 MPa and flexural moduli of $\sim$1.3–40 GPa were found for commercial PIs, which placed the PI(TAPB–PMA) specimen within the typical range, but at the lower end of performance. The slightly decreased mechanical properties compared to literature could be traced to the residual porosity present within the samples, as shown by MIP data."[182]

4.1.5 Summary

In this chapter, the feasibility of employing HTP for the synthesis of a 3D PI network has been proven. Specifically, two different HTP methods have been established for the multitopic monomer system TAPB and PMA: (i) HTP-MW and (ii) HTP-AC both proved to be suitable for the generation of fully condensed, highly T stable ($T_d > 550\,°C$), amorphous PI(TAPB-PMA) networks. A multitopic, all-organic monomer salt was identified as intermediate at low T_R, as has been previously reported in literature for linear PI analogues. An attempt in SSP also showed the potential of synthesizing PI(TAPB-PMA) without the necessity of a solvent altogether, although full conversion was not yet achieved.

All three methods yielded quite different product aspects: HTP-MW lead to powders consisting of near-monodisperse microspheres. HTP-AC yielded monolithic products comprising different micromorphologies and SSP resulted in a powder made up of angular micro-particles, which were observed to be shape copies of the intermediate MS.

The quite stunning monolith obtained via HTP-AC was further investigated towards porosity. Low-pressure gas sorption and MIP confirmed a hierarchical porous structure. A trimodal porosity ranging from ultra-micropores ($< 0.8\,nm$) to a small quantity of mesopores ($< 50\,nm$) and finally the majority of pores within 1-100 μm resulted in a very high specific pore volume of $7250\,mm^3\,g^{-1}$. Due to this interesting network architecture, a reaction screening was performed (t_R, T_R, presence/absence of HOAc) to determine if the inherent properties (i.e., amorphicity, thermal stability and morphology) could be tuned.

Within this screening, up to $t_R = 48\,h$ all products were found to be fully condensed, highly T stable networks. Furthermore, a complex micromorphological evolution was found to correlate with the studied reaction parameters. The observed morphologies comprised fiber-like structures and near monodisperse spherical particles as well as intermediate structures such as pearl-chain morphologies. At long t_R ($> 48\,h$ at $250\,°C$), silica dissolved from the glass liners in which the reactions were performed. It was hypothesized, that at even longer t_R dissolved silicic species reacted with the present PI networks towards hybrid materials.

Finally, scaling up the synthesis of PI(TAPB-PMA) using HTP-MW was demon-

strated. Further, it was shown that the powder was amenable to processing, i.e., green, solvent-free warmpressing. A dense cylindrical pellet was afforded, which retained its ultra-microporosity and a small amount of macropores, however no macropores $> 1\,\mu$m were observed due to the missing macroscopic architecture inherent to the monolith. Concerning mechanical properties, the pellet was found to exhibit mechanical performances comparable to commercial PIs.

Overall it was demonstrated that it is possible to follow the full route from synthesis of the PI(TAPB-PMA) network to a final material without the necessity of harmful solvents. Nevertheless, all PI(TAPB-PMA) products were exclusively amorphous networks, regardless of the different conditions used in the reaction screening.

After proving the general feasibility of generating an amorphous polyimide network via HTP, the next chapter will deal with inducing crystallinity. It will be discussed if creating a COF from the highly reactive monomers TAPB and PMA is possible. It will be elaborated how switching the acidic modulator HOAc to a basic modulator influences the reactivity of the monomer system within HT conditions and how this can be utilized for generating crystallinity.

4.2 From Network to Covalent Organic Framework

In this chapter, it will be shown that HTP is capable of generating a highly crystalline PI from the highly reactive monomers TAPB and PMA (aka PI-COF-2). First, it will be demonstrated that the corresponding imide linking moiety is generally reversible in HT conditions. Therefore, a proof of concept of imide metathesis in HT conditions will be provided using two different model compounds. Subsequently, the use of aniline as additive will be presented as key to the successful HTP of the desired PI-COF. A mechanism will be proposed engendering a dormant-species similar to that of controlled radical polymerizations. The usage of unstirred, flame-sealed ampoules for HTP (HTP-AP) will be presented as synthetic method. The results of testing different amounts of additive and reaction conditions will be summarized. Especially, the various products' crystallinity will be compared as investigated via small angle X-ray scattering (SAXS). Furthermore, the images of several microscopy techniques (SEM, transmission electron microscopy (TEM), and Helium ion microscopy (HIM)) will be analyzed. The bottleneck of the method will be identified as an inseparable product mixture with a small-molecule side-product. It will be discussed how the side-product is formed during HTP. Furthermore, it will be elaborated how the side-product formation correlates with the used quantity of aniline, as well as its influence on the quality of the crystal lattice of the COF. After proving the general feasibility of generating PI-COF-2 by additive-assisted HTP-AP (aaHTP-AP), additive-assisted HTP-MW (aaHTP-MW) will be introduced as an alternative, easy to use, and rapid synthetic method. Finally, it will be reflected on the proposed reaction mechanism and an outlook will be given on how the bottleneck of mixed products could be resolved.

4.2.1 Proof of Concept: Imide Reversibility under Hydrothermal Conditions

Reversibility and hence "error-checking" of the employed connecting moiety is the prerequisite for the generation of any COF. Therefore, the backward reaction needs to be possible under the chosen conditions to ensure thermodynamic control. Only

then DCC can take place and enables the formation of highly crystalline COFs, as discussed in detail in Chapter 2.2.2.1.

The most commonly used linkers in COF synthesis are imine moieties. Their reversibility was summarized by Belovich and Stoddard who identified three different types of equilibrium controlled reactions that imines can undergo: (i) Hydrolysis, where the imine reverts back to its precursors. (ii) Exchange reaction happens when a second amine triggers transimination and (iii) metathesis takes place when two different imines react with each other and switch their R groups.[218] In 2017, Vitaku and Dichtel applied the second pathway of formal transimination to COF synthesis, where they employed a finite di-imine instead of the typical amine precursor. As a result, even superior surface areas were obtained from both solvothermal and microwave-assisted synthesis compared to conventional syntheses.[219]

Imine and imide moieties are both formed via condensation reactions with H_2O as by-product. Therefore, it is assumed that imides undergo similar equilibrium controlled reactions as imines. That the imide formed between TAPB and PMA is indeed reversible in solvothermal conditions (i.e., partly opening the 5-membered ring and closing, cf. Fig.24) has been proven by the report on crystalline PI-COF-2 of Fang and co-workers in 2014.[85] However, so far reversibility studies have only been performed for imines and in solvothermal conditions. In general, reversibility and hence COF formation is believed to be highly dependent on the solubility and reactivity of the used monomers.

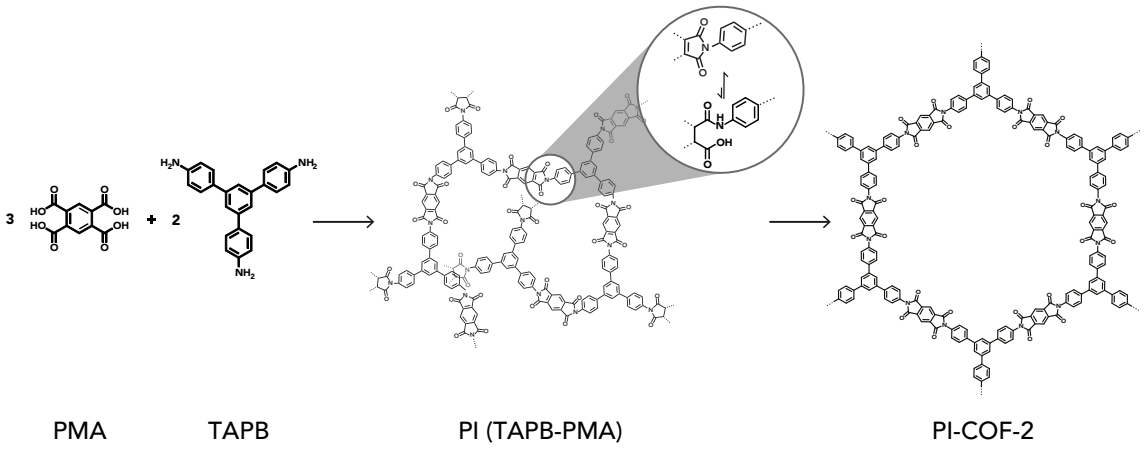

Figure 24: Reaction scheme of PMA and TAPB towards PI-COF-2. At first, the kinetic product, the amorphous network PI(TAPB-PMA), is formed. Upon (partly) reopening and subsequent reforming of the imide bond, eventually the thermodynamic product, crystalline PI-COF-2, is generated if the right conditions are present.

As HTP is much more limited in tuning reaction conditions (i.e., the full spectrum of solvent polarities is not available), it is assumed that achieving reversibility is even more challenging. To the date this thesis was started, the only COF synthesized using HTW was an amide framework by Stewart and co-workers.[178] In fact, it was only in 2021 that Kim et al. were able to generate PI-COFs via HTP for the first time.[103] They used triphenylene-2,3,6,7,10,11-hexacarboxylic acid (TPHCA) and three linear aromatic amines (*p*-phenylene diamine, benzidine, and diaminoterphenyl) as monomer systems. These systems are largely different compared to TAPB and PMA, as their tri- and bifunctional tectones feature opposite functionalities (tri/hexafunctional carboxylic acids and difunctional amines). Roughly one year later, in 2022, Lotsch and co-workers reported on the HTP of PI-COF-2 using 20 % *n*-hexanol and ~2.6 % pyridine as catalyst (200 °C and 6 days).[202] They achieved high crystallinity and a $SA_{BET} = 939\,m^2\,g^{-1}$, which is lower than Fang's SA_{BET} but still quite large. They argued, that the reason for amorphous results from HTP without the addition of alcohol might be the lack of solubility of TAPB or the lack of polarity differences in the reaction mixture.

In the previous Chapter 4.1, the monomer combination TAPB and PMA proved to be highly reactive in HTP, thus leading to amorphous networks (cf. Fig.24 PI(TAPB-PMA), the kinetic product), under any of the various to date tested reaction conditions.[182] To find out if HTP is able to generate a PI-COF from the monomer combination TAPB and PMA (see Figure 24), the reversibility under HT conditions needed to be investigated. To prove that the corresponding imides undergo exchange reactions in HTW, the metathesis reaction was chosen for a model compound study.

Modelcompound Synthesis

To test the imide metathesis reaction, two small molecule model compounds were synthesized using microwave-assisted synthesis (see Fig.25A). TAPB and two monofunctional anhydride precursors (phthalic anhydride (PA) and 4-methylphthalic anhydride (4-MPA)) were chosen because they resemble the monomer set-up used for PI(TAPB-PMA), but produce finite imides. Therefore, TAPB and the respective anhydride were weighed into a microwave reactor and suspended in 10 mL degassed

H_2O. Subsequently, the suspension was heated as fast as possible to 230 °C in the microwave. The reaction mixture was stirred vigorously for the chosen reaction time $t_R = 2\,h$. After the desired t_R, the vial was cooled down to 70 °C using compressed air. The obtained homogeneous, brown powders were filtered, washed with distilled water, ethanol, and acetone, and dried in vacuo at 80 °C. Model compound 1 (MC1, with aromatic moieties only) and model compound 2 (MC2, substituted with a CH_3 moiety in position 3, marked with a yellow circle) were afforded (see Figure 25A).

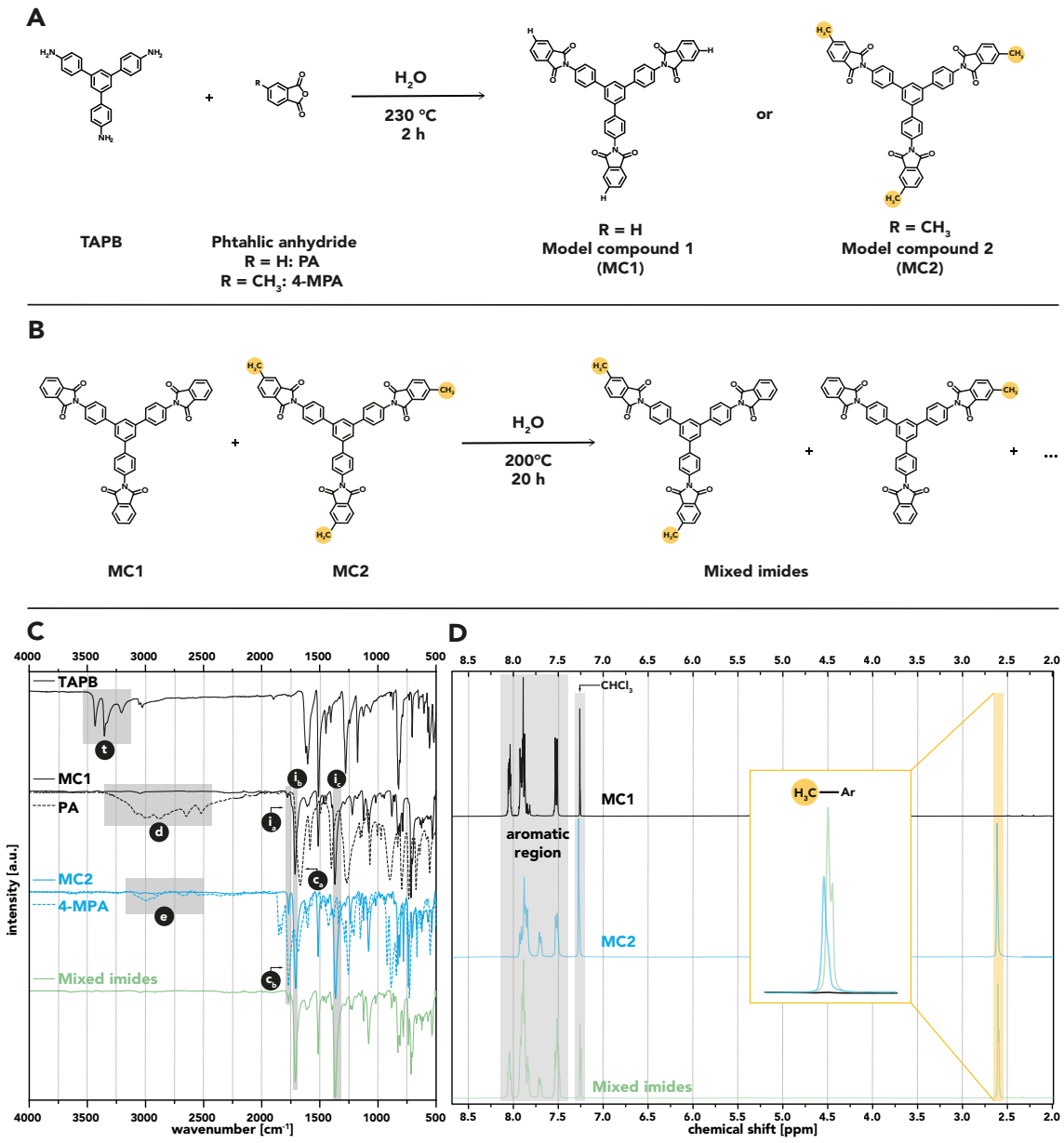

Figure 25: Modelcompound synthesis scheme. A: Reaction scheme of HTS of MC1 and MC2. B: Metathesis reaction between the two model compounds during HT conditions. C: ATR-FT-IR of MC1, MC2 and metathesis product after HT reaction. D: ^{1}H-NMR spectra of MC1, MC2, and the metathesis product after the HT reaction.

The compounds were characterized via ATR-FT-IR spectroscopy and ^{1}H-solution nuclear magnetic resonance (^{1}H-NMR) spectroscopy (see Figure 25C and D).

The ATR-FT-IR spectrum featured the typical imide modes (see Figure 25C): the asymmetric and symmetric C=O stretch modes[10] $\mathbf{i_a}$: $\tilde{\nu}_{as}(C{=}O) \approx 1775\,cm^{-1}$ and $\mathbf{i_b}$: $\tilde{\nu}_{s}(C{=}O) \approx 1720\,cm^{-1}$, as well as the C-N stretch $\mathbf{i_c}$: $\tilde{\nu}(C\text{-}N) \approx 1365\,cm^{-1}$. Furthermore, modes stemming from the co-monomers were missing, i.e., the amine vibrations ($\mathbf{t}$: $\tilde{\nu} \approx 3400\text{-}3300\,cm^{-1}$) of TAPB[182] and the carbonyl vibrations ($\mathbf{c_a}$: $\tilde{\nu} \approx 1670\,cm^{-1}$ and $\mathbf{c_a}$: $\tilde{\nu} \approx 1770\,cm^{-1}$) of the phthalic anhydrides. Also, both PA and 4-MPA exhibited O-H vibrations ($\mathbf{d}$ and $\mathbf{e} \approx 3300\text{-}2450\,cm^{-1}$), stemming from partial hydrolysis of the anhydride, which were absent in MC1 and MC2. ^{1}H-NMR spectroscopy confirmed the findings of ATR-FT-IR spectroscopy and proved that MC1 and MC2 were obtained successfully (see Figure 25D).

Imide Metathesis Reaction

To perform the imide metathesis under HT conditions, the compounds MC1 and MC2 were suspended in water and sealed in an unstirred batch autoclave for 20 h at 200 °C in a 1:1 ratio (see Figure 25B). The obtained product (brown powder) was analyzed via ATR-FT-IR spectroscopy, proving that the material did not decompose as it still showed all obligatory imide modes ($\mathbf{i_a}$, $\mathbf{i_b}$, and $\mathbf{i_c}$, see Figure 25C). Furthermore, solution ^{1}H-NMR spectroscopy was performed (Figure 25D), revealing the presence of a second methyl signal, with a slightly different chemical shift (2.59 vs. 2.61 ppm). This suggested that the imide moiety indeed reopened and formed a new bond, hence leading to mixed imides as a product. Please note that the structures for the mixed imides depicted in Figure 25B are just an approximation and are not the confirmed structures, as so far no further 2D-NMR analyses were performed.

After proving that the imide moiety in question is indeed reversible in HTW, a HTP set-up was established which allowed the desired imide reversibility. How this set-up was achieved will be discussed in the following section.

4.2.2 Introducing Crystallinity via a Dormant Species Approach

To the end of obtaining PI-COF-2, both additive-free HTP and HTP with addition of acetic acid as potential mineralizer where to date unsuccessful, as described in Chapter 4.1.[182] To provide a remedy to the highly reactive monomer system yielding amorphous products, the competitive base aniline was chosen as inspired by a recent study by Yaghi and co-workers.[220] They described that the presence of an increased amount of amine (i.e., aniline) enhanced the reversibility of the imine-bond formation, based on the imine-exchange strategy,[218,219] as discussed in section 4.2.1. This led to superior crystallinity compared to imine-COFs via other synthetic routes. Yaghi and co-workers postulated that the mechanism proceeds in analogy to inorganic mineralizers: Aniline inhibits nucleation and prevents imminent precipitation which leads to enhanced error correction and therefore higher degrees of crystallinity (see Figure 26A). This concept was proven highly successful for the generation of imine COF single crystals up to several μm in diameter.[220] Therefore, Yaghi's concept could be a promising approach for the formation of crystalline imide-frameworks in HTP. Especially the highly reactive monomer system TAPB and PMA used in this study could be rendered reversible using such an approach. However, the imine linkers studied by Yaghi and co-workers are more susceptible to hydrolysis and are therefore more reversible compared to the imide linkers under solvothermal conditions. This is supported by the fact that the imide metathesis reaction of MC1 and MC2 was only observed after 20 h under hydrothermal conditions at 200 °C without a modulator present. Imide metathesis or exchange in the case of an extended structure was therefore expected to be even slower. It was anticipated that the addition of a competing base to HTP at least slightly increases the reversibility. Consequently, it was assumed that the generation of PI-COF-2 from TAPB and PMA could be feasible without the necessity of increasing t_R or T_R to an extent were the organic structure is destroyed.

The base of choice needed to be as similar as possible in reactivity to the used aromatic triamine monomer TAPB. Only then similar rates of condensation and thus actual competition would be achieved. Aniline seemed the best fitting choice: (i) the

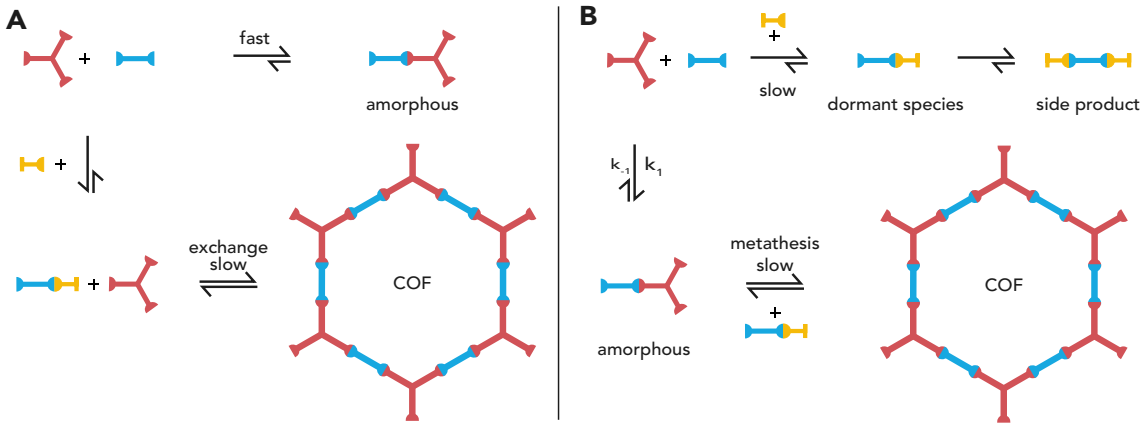

Figure 26: Proposed mechanisms of COF crystallization. A: Figure adapted from Yaghi et al[220]. Exchange strategy by Yaghi and co-workers similar to inorganic mineralizers: Without modulator (yellow), the equilibrium is shifted toward the product yielding amorphous or polycrystalline COFs. With modulator, the initial imine bond formation is still fast, but slow imine exchange enables the growth of single-crystalline COFs.[220] B: Dormant species similar to radical polymerization techniques: Without the modulator (yellow), the condensation is fast, leading to amorphous products. With modulator in equimolar amounts, a dormant-species is created. The equilibrium shifts towards the precursor side and the back reaction is accelerated (k_{-1} increases). The dormant-species participates in the slow metathesis reaction enabling error-correction. A possible side-reaction could remove one monomer from the equilibrium altogether.

reacting groups in TAPB are essentially *p*-phenylene-anilines, with the amine's reactivity as a nucleophile barely influenced by the *p*-phenylene moiety and, (ii) the reactivity of a primary amine as nucleophile is essentially governed by its pK_AH, which for aromatic primary amines falls in the range of 2-5, and both TAPB ($pK_AH = 4.9$) and aniline ($pK_AH = 4.6$)[a] fall into this range. Despite the success of Yaghi and co-workers' concept, it still bears certain drawbacks: Toxic organic solvents and overly excess amounts (≥ 50 equiv.) of organic base is used. In contrast, HTP uses the much greener solvent water. Furthermore, instead of employing high excesses of aniline, stoichiometric amounts will be used for HTP. The reason for the lower amount of aniline is that a slightly different mode of action is proposed:

Yaghi and co-workers assumed aniline behaves like a classical mineralizer (see Figure 26A): "In the absence of the modulator (yellow), the equilibrium is shifted toward the product, amorphous or polycrystalline COFs, whose formation is governed by fast nucleation and limited crystal growth. In the presence of the modulator, the initial imine bond formation is comparably fast; however, slow imine exchange enables the growth of single-crystalline COFs."[220] In contrast, in this work

[a]Value for TAPB was taken from SciFinder prediction and the value for aniline stems from experimental data taken from Engineering ToolBox, (2017). Amines, diamines and cyclic organic nitrogen compounds - pK_AH values. https://www.engineeringtoolbox.com/amine-diamine-pyridine-cyclic-quinoline-aminobenzene-structure-pka-carboxylic-dissociation-constant-d_1949.html

when adding equimolar amounts, aniline was expected to react with part of the carboxylic acid monomer PMA forming the less reactive product "PMA-An" (see Figure 26B and 27). Consequently, PMA's availability is temporarily reduced and hence does not engage in the condensation reaction with TAPB. This removes the linear monomers from the equilibrium and therefore shifts it towards the precursor side. Hence, the back reaction is accelerated, i.e., k_{-1} increases. Furthermore, the dormant-species is believed to participate in the slow metathesis reaction, which should lead to the formation of a crystalline COF. It was assumed that PMA-An corresponded to a dormant-species, in analogy to controlled radical polymerization techniques, such as nitroxide mediated or reverse addition-fragmentation chain transfer polymerizations slowing down the reaction rate of the condensation (see Figure 26B). However, it could not be excluded that a second equivalent of aniline reacts with the dormant-species to a highly unreactive side-product (see Figure 26B). This would lead to the removal of part of PMA from the equilibrium altogether and additionally lead to an impurity in the product. To elucidate the unwanted side-reaction, the behavior of PMA with two equiv. of aniline in HTW was investigated in detail.

Small Molecule Side-Reaction

To study the possible side-reaction, PMA was intentionally reacted with 2 equiv. of aniline in HTP-MW. In theory, the reaction would possibly lead to a quite complex mixture of compounds (see Fig.27). First, the reaction of 2 equiv. of aniline with PMA at complete condensation would lead to *p*-phenylene pyromellite-bisimide (Fig.27 PPBI, 2). At partial condensation, e.g., one imide moiety and one amide plus unreacted CO_2H or two amide moieties plus two unreacted CO_2H would result (Fig.27 intermediate products). The unreacted carboxylic acid moiety could further decarboxylate under the hydrothermal conditions resulting in either *p*-phenylene pyromellit-(imide-amide) (Fig.27 PPIA, 3) and/or *p*-phenylene 1,4-pyromellite-bisamide (Fig.27 1,4-PPBA (1c)) and its isomers (Fig.27 1,2- and 1,3-PPBA (1a and 1b); where 1a is considered less likely due to steric hinderance). Mixed products, albeit only composed of two compounds, namely PPBI and PPIA (2 and 3 in Fig.27), were recently described by Kuehl et al. in the context of a model

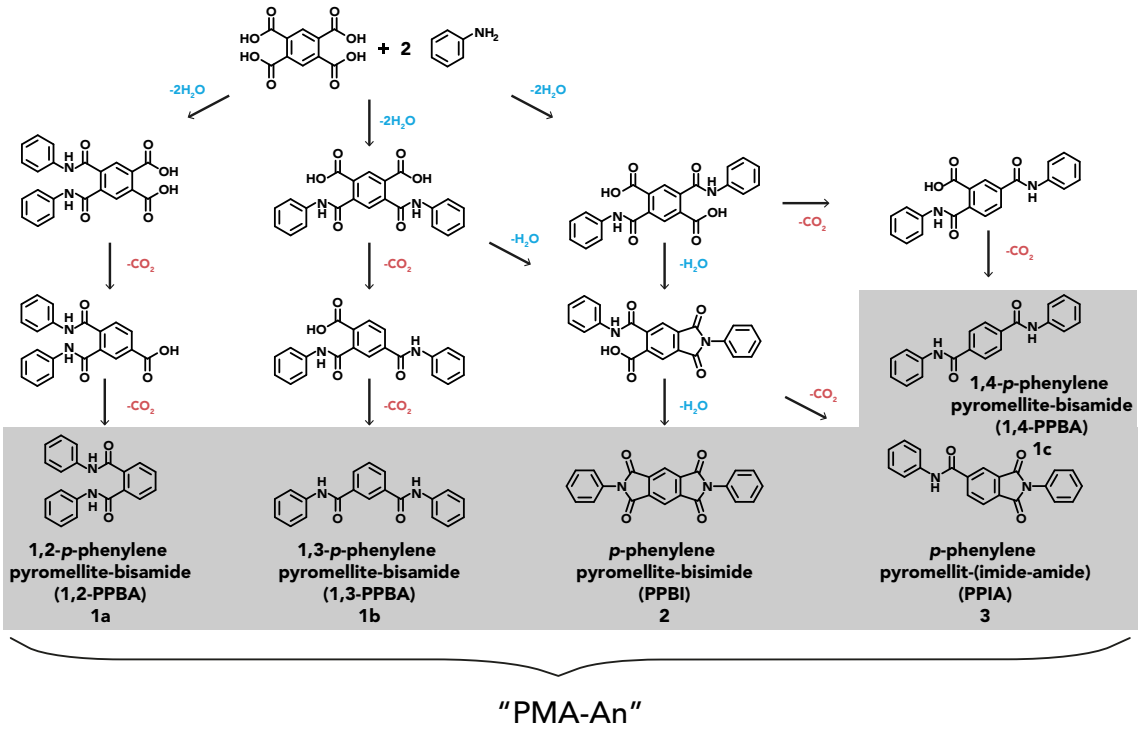

Figure 27: Possible HT reaction products of PMA with 2 equiv. of aniline, generating a mixture of *p*-phenylene pyromellite-bisamide (PPBA, 1) and its isomers (1,2 (1a); 1,3 (1b); and 1,4- PPBA (1c)), *p*-phenylene pyromellite-bisimide (PPBI, 2), and *p*-phenylene pyromellit(imide-amide) (PPIA, 3), as well as all intermediates.

compound study performed to elucidate the imide formation in PI-COFs.[221] They found that solvothermal synthesis solely gave PPBI whereas and microwave-assisted synthesis lead to decarboxylation and hence to the additional formation of PPIA. In this work, the mixture was expected to be more complex due to the use of HTW as a solvent. For clarity, the mixture of small molecules resulting from reaction of PMA with aniline is hereafter referred to as "PMA-An" (see Figure 27).

For the HTS of PMA-An as reference (PMA-An ref.), PMA was weighed into a glass microwave reactor and suspended in 10 mL degassed H_2O. Aniline was added and the mixture was sonicated for 5 min. The vessel was heated as fast as possible to 230 °C for 1 h. The reactor was cooled down to 70 °C using compressed air and the off-white solid was collected via filtration. The product was washed with water, acetone, and ethanol and subsequently dried overnight *in vacuo* at 80 °C. PMA-An ref. was then thoroughly characterized via ATR-FT-IR spectroscopy, ^{1}H-NMR spectroscopy, PXRD and SAXS analyses.

In Figure 28A, ATR-FT-IR spectra displayed the typical imide-modes[10] ($\mathbf{i_a}$: $\tilde{\nu}_{as} = 1785\,cm^{-1}$, $\mathbf{i_b}$: $\tilde{\nu}_{s} = 1720\,cm^{-1}$, and $\mathbf{i_c}$: $\tilde{\nu}(C\text{-}N) = 1365\,cm^{-1}$). The characteris-

tic modes stemming from the reactants PMA ($\tilde{\nu}$(O-H) = 3250-2755 cm^{-1}, $\tilde{\nu}$(C=O, acid/ester) = 1695 cm^{-1}) and aniline ($\tilde{\nu}$(N-H) = 3500-3300 cm^{-1}) were absent. This pointed at no residual monomers.

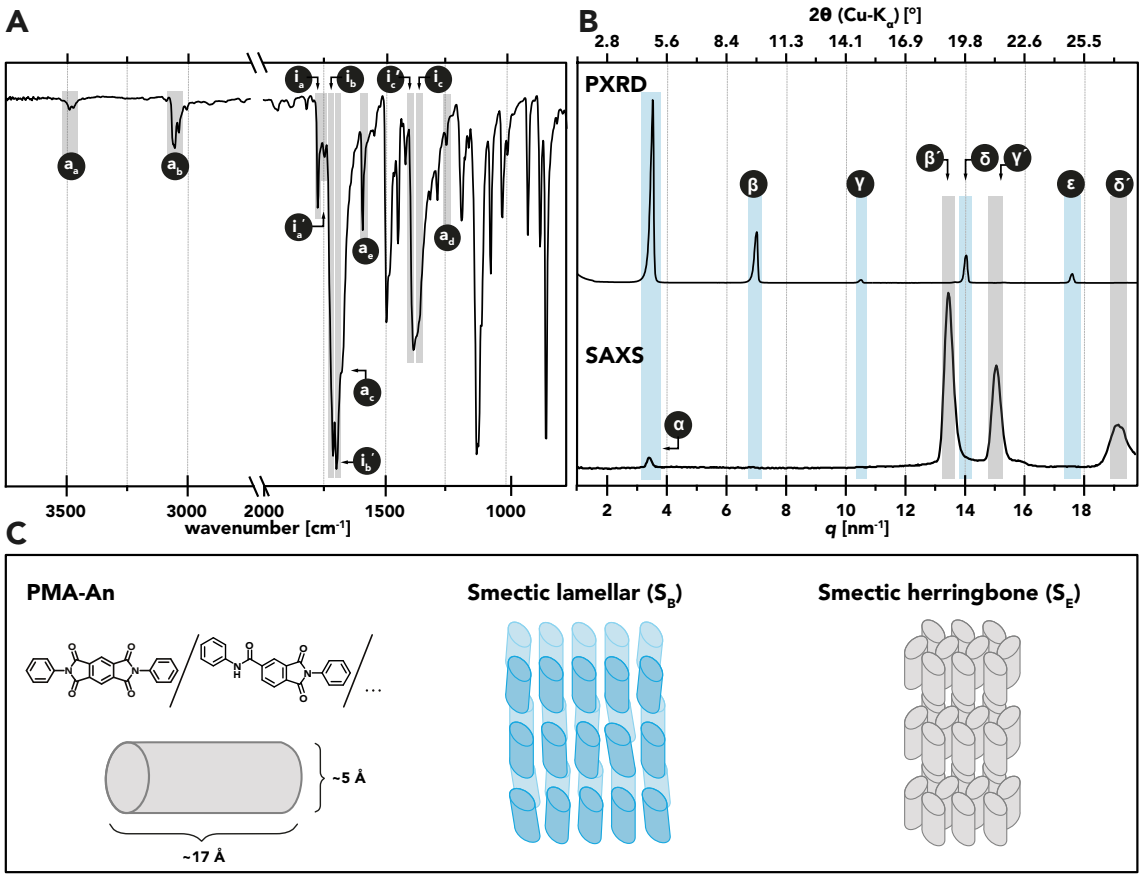

Figure 28: PMA-An reference characterization. A: ATR-FT-IR spectrum of PMA-An reference. B: PXRD and SAXS of PMA-An reference. C: Schematic of possible mesophases in which the small molecule mixture PMA-An could be arranging as hypothesized based on SAXS and PXRD data.

Moreover, a second set of symmetric, asymmetric C=O and C-N stretch imide modes $\tilde{\nu}$ = 1755, 1710 and 1395 cm^{-1} (Figure 28A, modes $\mathbf{i_a}$', $\mathbf{i_b}$' and $\mathbf{i_c}$') were observed. Additionally, the spectra showed amide modes: Amide A/B (mode $\mathbf{a_a}$: $\tilde{\nu}$ = 3490 cm^{-1}), amide N-H (mode $\mathbf{a_b}$: $\tilde{\nu}$ = 3065 cm^{-1}), amide I (mode $\mathbf{a_c}$: $\tilde{\nu}$ = 1685 cm^{-1}), amide II (mode $\mathbf{a_e}$: $\tilde{\nu}$ = 1600 cm^{-1}) and amide III (mode $\mathbf{a_d}$: $\tilde{\nu}$ = 1250 cm^{-1}). Consequently, it was assumed that PMA-An ref. was indeed a mixture of compounds.

However, ^{1}H-NMR spectroscopy only revealed signals for the bisimide PPBI (see Figure A10), which is in contradiction to ATR-FT-IR results. This can be explained by the poor solubility of PMA-An ref.: The NMR sample could only be partially dissolved in $CDCl_3$/deuterated trifluoro acetic acid (TFA-d_1) (5:1) and subsequently

filtered. Therefore, the obtained spectrum cannot be assumed fully representative of the complete content of PMA-An.

PXRD evinced the following reflections (see Figure 28B, top curve): $\alpha = 4.8°\,(2\theta,$ Cu-K$_\alpha$) ($q = 3.4\,\mathrm{nm^{-1}}$), $\beta = 9.9°\,(2\theta,$ Cu-K$_\alpha$) ($q = 7.0\,\mathrm{nm^{-1}}$), $\gamma = 14.9°\,(2\theta,$ Cu-K$_\alpha$) ($q = 10.6\,\mathrm{nm^{-1}}$), $\delta = 19.8°\,(2\theta,$ Cu-K$_\alpha$) ($q = 14.0\,\mathrm{nm^{-1}}$) and $\epsilon = 24.9°\,(2\theta,$ Cu-K$_\alpha$) ($q = 17.6\,\mathrm{nm^{-1}}$). The incidents occurred highly regular with the exact same q values (i.e., $3.45\,\mathrm{nm^{-1}}$) in between, which corresponds to a lamellar structural arrangement. As the small molecule mixture PMA-An (Figure 28C, left) contained exclusively calamitic mesogens of closely matching dimensions (~ 17 Å in length and ~ 5 Å in diameter, obtained via energy optimization; cf. Figure A14), they were expected to exhibit liquid crystal (LC)- type ordering in the solid state. According to the lamellar pattern found via PXRD, the corresponding LC-mesophase would be a smectic B-type (S$_\mathrm{B}$) arrangement (Figure 28C, middle).[222]

Moreover, SAXS was performed with the help of a collaboration partner and SAXS specialist. SAXS was chosen for reasons of comparability with the results of the PI-COF-2 samples, as COFs' expected unit cells are quite big, hence having smaller diffraction angles which are often not accessible via PXRD. Strikingly, when SAXS was performed a different pattern was observed on exactly the same batch of PMA-An ref. (Figure 28B, bottom curve). Specifically, reflections β': $q = 13.4$-$13.7\,\mathrm{nm^{-1}}$, γ': $q = 15.1$-$15.3\,\mathrm{nm^{-1}}$, and δ': $q = 19.1$-$19.4\,\mathrm{nm^{-1}}$) were found instead of β, γ, δ, and ϵ. This pattern however could also be indicative of a another smectic LC-type, e.g., smectic E-type (S$_\mathrm{E}$) arrangement (herringbone) (Figure 28C, right).[222] See Figure 28C for schematic representation of both LC-mesophases.

As both PXRD and SAXS measurements rely on the same principles, this was a quite unusual observation. One big difference between the two measurement types is the beam perspective relative to the sample position. SAXS is measured in transmission and PXRD in reflection. Therefore, the SAXS measurement of PMA-An ref. was repeated, but with the sample holder tilted in a 60 ° angle to mimic the PXRD beam perspective (see Figure 29A, bottom curve). Indeed, reflections from PXRD experiments β, γ and δ (marked in blue) became visible. Moreover, the measurement showed roughly inverse intensities for the reflections α and both β' and γ'. The fact that such a large tilting angle was necessary to make the reflections visible, pointed at

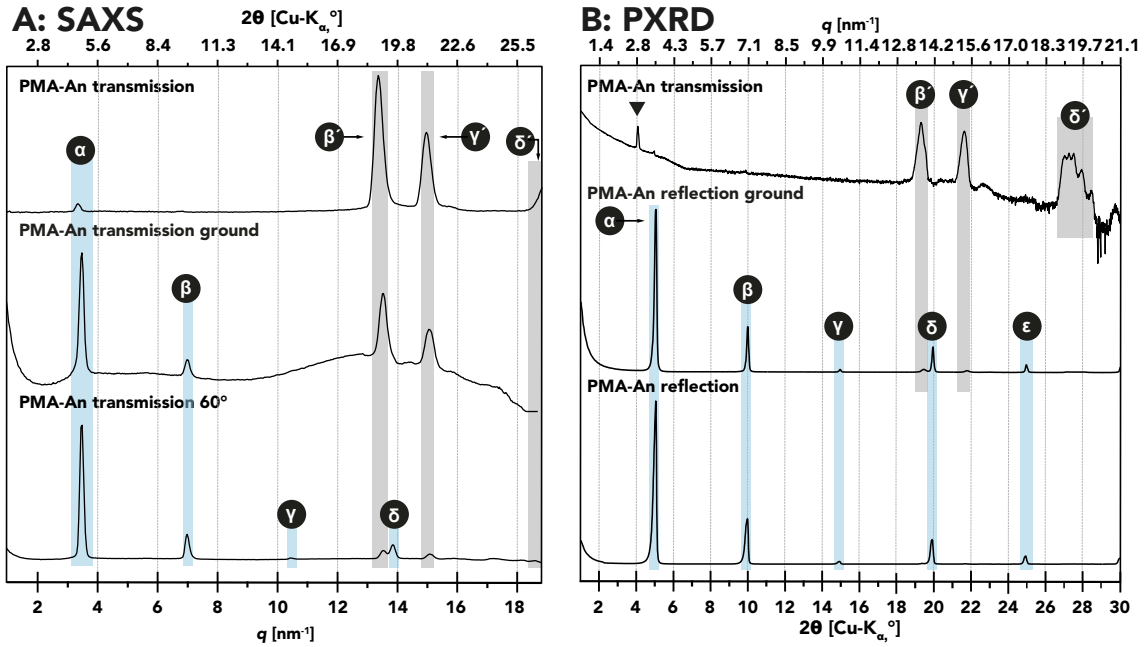

Figure 29: PMA-An ref. SAXS curves vs. PXRD patterns A: SAXS curves top to bottom: measured in transmission, then manually ground in transmission and with 60 ° rotation. B: PXRD measured in top to bottom: transmission, in reflection/ground manually, and pristine in reflection. Please note that a logarithmic scale was used for the transmission graph. Reflections marked in blue were assigned to S_B LC-arrangement, reflections marked in gray were assigned to possibly a different LC-arrangement. Finally, the reflection at $q = 2.8\,\mathrm{nm}^{-1}$ is marked with a triangle could not be assigned to either pattern.

the material being highly crystalline with a strong preferential orientation albeit not single crystalline. To cross-check, the typical PXRD sample mounting was changed to a transmission set-up where PMA-An ref. was placed in between Kapton® foil and the beam was arranged perpendicularly. Indeed, the same pattern appeared as observed via SAXS in transmission (see the top curve in Figure 29B, β', γ', and δ').

To provide further prove for the hypothesis of preferential orientation, PMA-An ref. was ground manually and PXRD as well as SAXS was repeated (see Figure 29A and B middle). In fact, in the case of PXRD, the reflections β' and γ' appeared (marked in gray), however were low in intensity. Similarly, SAXS of the ground PMA-An ref. sample still showed small incidents at β' and γ' (gray), but α (blue) was much more pronounced and additionally β (blue) became visible. The reason for the small effect of grinding could be that the PMA-An ref. solid was built up of layers which strongly interacted via secondary interactions. This intense stacking behavior of PMA-An ref. was also supported by the fact that no melting point was observed (measured at a rate of $10\,\mathrm{K\,min}^{-1}$ up to 300 °C in an OptiMelt automated melting point system from Stanford Research Systems) and its insolubility in common solvents (acetone,

dimethyl sulfoxide, tetrahydrofurane (THF), $CHCl_3$ and toluene; only a mixture of $CDCl_3$/TFA-d_1 5:1 was able to dissolve a small sample for ^{1}H-NMR analysis, see appendix).

In order to identify the LC-mesophase (S_B or S_E) present in PMA-An ref., an X-ray method was needed which would detect all reflections necessary for indexing. To do so, the collaboration partner performed X-ray scattering measurements of thoroughly ground PMA-An ref. using an image plate system. Adding an image plate detector in close proximity to the sample in front of the SAXS detector allows for detecting a wide q-range (0-30 nm^{-1}, cf. Fig.30B and appendix for measurement details). Furthermore, a small hole in the center of the image plate allows the SAXS beam to pass through, enabling simultaneous SAXS and wide angle X-ray scattering (WAXS) measurements. Consequently, these measurements are comparable to powder diffractograms obtained via PXRD measurements, although diminishing the resolution. Therefore, all necessary reflections were obtained and could be used for indexing (see indicated incidents in Fig.30A) as well as evaluating the lattice parameters: $a = 4.71$ Å, $b = 4.36$ Å, $c = 18.01$ ÅṠubsequently, the collaboration partner performed mathematical fitting (see Chapter A.1.1 for mathematical details) which revealed that PMA-An ref. provides reflections matching the lattice planes of an orthorhombic lattice. The following Miller indices (hkl) could hence be assigned to the already discussed reflections: $\alpha = (001)$, $\beta = (002)$, $\gamma = (003)$, $\delta = (004)$, $\epsilon = (005)$, $\beta' = (100)$, $\gamma' = (010)$, and $\delta' = (104)$.

It was concluded that PMA-An consists of a S_B-type LC-mesophase which is highly macroscopically oriented resulting in structural anisotropy. This explains why SAXS and PXRD yielded different patterns: if the X-rays hit PMA-An in transmission (i.e., typical for SAXS measurements), the in-plane (hk0) reflections (β', γ', δ') are observed. Rotating the X-rays 90 ° reveals the out-of-plane reflections (α, β, γ, δ) of the repeating plane, with $c = 18.01$ Å equalling the length of one PMA-An molecule (see Fig.30B). Solely upon thorough grinding a nearly isotropic powder could be obtained.

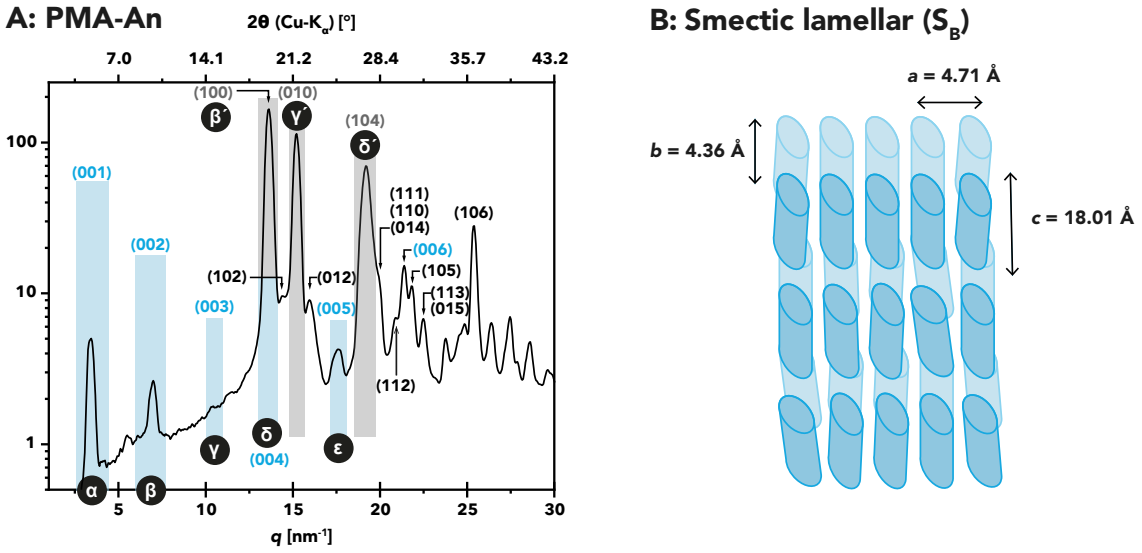

Figure 30: PMA-An ref. image plate measurements and indexing. A: Image plate measurements with a logarithmic scale provides necessary reflections for a thorough indexing. Mathematical fitting of the indicated reflections to an orthorhombic lattice provided (*hkl*) notations. Highlighted in blue are the out-of-plane reflections $\alpha = (001)$, $\beta = (002)$, $\gamma = (003)$, $\delta = (004)$, $\epsilon = (005)$, and (006). Highlighted in gray are the in-plane (hk0) reflections $\beta' = (100)$, $\gamma' = (010)$, and $\delta' = (104)$. (B) Schematic of the proposed S_B structure and the obtained lattice parameters $a = 4.71$ Å, $b = 4.36$ Å, $c = 18.01$ Å.

After elaborating on the possible side-reaction, the dormant-species approach was experimentally tested, which will be dealt with in the following section of this chapter.

4.2.3 Aniline-Assisted HTP in Flame Sealed Ampoules

In a first set of experiments, aaHTP was performed at a reaction temperature of $T_R = 200\,°C$ and a reaction time of $t_R = 72\,h$, employing seven different amounts of aniline (0, 1, 3, 5, 7, 10, and 15 equiv.; PI-COF-$2_{AP\text{-}0\text{-}15}$). This selection of equivalents of aniline included the stoichiometric equivalents (3 equiv.) as a dormant species is anticipated (see Figure 31A).

However, to test this hypothesis, less than stoichiometric amounts (0 and 1 equiv.) were used, as well as excess amounts, as used by Yaghi and co-workers, if not as high (5, 7, 10, and 15 equiv.). To ensure that the desired stoichiometries were kept, the HTP reactions were performed in unstirred, flame sealed ampoules (AP) (see Figure 31B and C for photos of the ampoules before and after flame-sealing, respectively). Moreover, the benchmark PI-COF-2 was also prepared for reference in a flame-sealed ampoule, according to the protocol provided by Fang and co-workers.[85] The ampoules after HTP with 0, 3, and 15 equiv. of aniline used

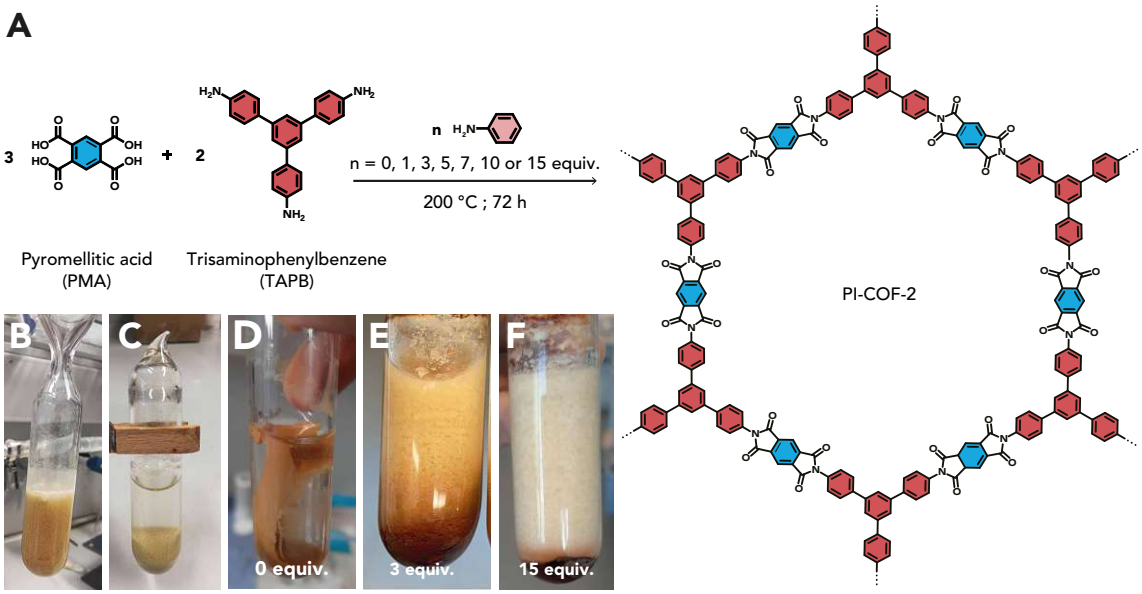

Figure 31: General reaction overview. A: HTP of PI-COF-2 from PMA and TAPB using different amounts of the additive aniline. B: Ampoule charged with reactants before sealing and C: after sealing. D-F: Aspects of reactions products after HTP with 0 (D), 3 (E), and 15 equiv. (F) of aniline performed in non-stirred, flame sealed ampoules.

are displayed in Figure 31D-F. From their aspects it became clear that the more aniline was added to the reaction mixture, the more inhomogeneous and lighter colored the product became. The product synthesized without aniline was obtained as one homogeneous brown phase (Figure 31D). In contrast in the presence of aniline, reproducibly two phases were found: a brown, compact bottom phase and an off-white top phase, which was a quite concentrated dispersion of whiteish particles in water. At medium amounts of aniline (e.g., 3 equiv., Figure 31E) the two phases mixed gradually. Just considering the products' aspects, it was hypothesized that the bottom phase was composed of PI. Indeed, the amorphous PI(TAPB-PMA) featured precisely this orange-brown color as discussed in the last chapter.[182] The top phase on the other hand looked nothing like the expected PI. With increasing amount of aniline, the whitish top phase increased relatively to the brown bottom phase. It was hypothesized that the top phase was mainly composed of the side-product PMA-An. At 10 and 15 equiv., a clear border between both was observed (Fig.31F) and hence the top and bottom phases were separated via decanting and analyzed separately.

Attenuated Total Reflectance Fourier Transform IR Spectroscopy

First, ATR-FT-IR spectroscopy was performed of PI-COF-2_{AP} samples which

showed gradually mixing phases. Specifically, the ampoule reactions' products containing 0, 1, 3, 5, and 7 equiv. of aniline are depicted in Figure 32A. Additionally, the benchmark PI-COF-2 (green curve) and the intentionally synthesized small molecule mixture PMA-An ref. are depicted as references. The characteristic modes stemming from the co-monomers and consequently also end-groups (PMA: $\tilde{\nu}$(O-H) = 3250-2755 cm^{-1}, $\tilde{\nu}$(C=O, acid/ester) = 1695 cm^{-1} and TAPB: $\tilde{\nu}$(N-H) = 3435 cm^{-1} and 3355 cm^{-1}) were absent in all spectra and therefore their representation was omitted in Figure 32A for reasons of space. Hence, from ATR-FT-IR analysis it was concluded that no residual starting compounds were present in the PI-COF-2$_{AP}$ materials. The typical imide-modes ($\mathbf{i_a}$: $\tilde{\nu}_{as}$ = 1785 cm^{-1}, $\mathbf{i_b}$: $\tilde{\nu}_{s}$ = 1720 cm^{-1}, and $\mathbf{i_c}$: $\tilde{\nu}$(C-N) = 1365 cm^{-1}) were found both in PI-COF-2$_{AP\text{-}0}$ and the benchmark PI-COF-2, in fact both spectra were identical to the spectrum of PI(TAPB-PMA) discussed in the last chapter. Moreover, the imide modes were present in all aniline containing PI-COF-2$_{AP}$ samples. Thus, according to ATR-FT-IR spectroscopy, the PI-COF-2$_{AP}$ materials could indeed be classified as PIs.

Interestingly, products prepared with >1 equiv. of aniline showed a second set of symmetric, asymmetric and C-N stretch imide modes $\tilde{\nu}$ = 1755, 1710 and 1395 cm^{-1} (Figure 32A, modes $\mathbf{i_a}$', $\mathbf{i_b}$' and $\mathbf{i_c}$') in addition to the imide modes found in PI-COF-2$_{AP\text{-}0}$ and the benchmark PI-COF-2 ($\mathbf{i_a}$, $\mathbf{i_b}$, $\mathbf{i_c}$). Furthermore, samples with ≥ 5 equiv. additionally feature amide modes[205]: Amide A/B (mode $\mathbf{a_a}$: $\tilde{\nu}$ = 3490 cm^{-1}), amide N-H (mode $\mathbf{a_b}$: $\tilde{\nu}$ = 3065 cm^{-1}), amide I (mode $\mathbf{a_c}$: $\tilde{\nu}$ = 1685 cm^{-1}), amide II (mode $\mathbf{a_e}$: $\tilde{\nu}$ = 1600 cm^{-1}) and amide III (mode $\mathbf{a_d}$: $\tilde{\nu}$ = 1250 cm^{-1}). Both, the second set of imide modes and the amide modes indicated the presence of additional species bearing imide and/amide functions, which was consistent with the hypothesis of the mixture of small molecules, which was labelled PMA-An in Figure 27. Indeed, ATR-FT-IR spectra of PMA-An ref. featured both sets of imide modes ($\mathbf{i_a}$, $\mathbf{i_b}$, $\mathbf{i_c}$, and $\mathbf{i_a}$', $\mathbf{i_b}$', $\mathbf{i_c}$') and the amide modes ($\mathbf{a_a}$, $\mathbf{a_b}$, $\mathbf{a_c}$, $\mathbf{a_d}$, and $\mathbf{a_e}$). Furthermore, the intensity of the second set of imide modes ($\mathbf{i_a}$', $\mathbf{i_b}$', and $\mathbf{i_c}$') and amide modes ($\mathbf{a_a}$, $\mathbf{a_b}$, $\mathbf{a_c}$, $\mathbf{a_d}$, and $\mathbf{a_e}$) increased in the PI-COF-2$_{AP}$ samples with increasing amount of aniline employed. PI-COF-2$_{AP\text{-}7}$, which contained the highest amount of aniline in this sample pool depicted in 32A, showed an almost identical spectrum compared to the PMA-An reference. Therefore, it was

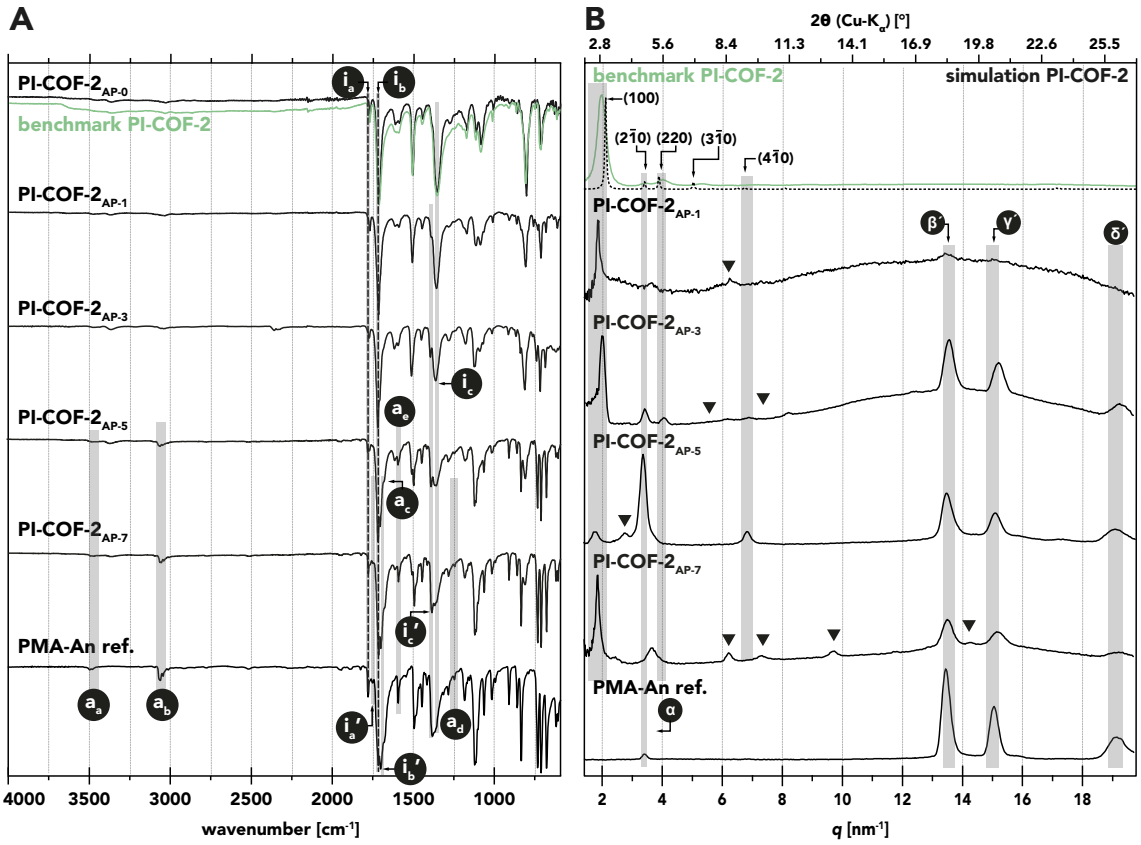

Figure 32: ATR-FT-IR spectroscopy and SAXS analyses of PI-COF-2_{AP} samples synthesized in sealed ampoules. A: from top to bottom, benchmark PI-COF-2 (green), products of HTP-AP with 0, 1, 3, 5, 7, equiv. (PI-COF-$2_{AP\text{-}1}$ - PI-COF-$2_{AP\text{-}7}$), and the side-product (PMA-An ref.). B: from top to bottom, benchmark PI-COF-2 (green) and its simulated pattern, the products of HTP-AP with 0, 1, 4, 5, 7 equiv. (PI-COF-$2_{AP\text{-}1}$ - PI-COF-$2_{AP\text{-}7}$), and the side-product (PMA-An ref.).

concluded that the products are indeed mixtures of a PI component (with at this point yet to be discussed crystallinity) and the mixture of small molecules PMA-An.

Small Angle X-Ray Scattering Analysis

For the large unit cell of PI-COF-2 and the correspondingly small $q/2\theta$ values, SAXS measurements were performed. SAXS curves of the same set of samples as used for ATR-FT-IR characterizations are displayed in Figure 32B. All products were crystalline, featuring sharp Bragg reflections, which was in stark contrast to PI-COF-$2_{AP\text{-}0}$ (not shown in Figure 32B, but in Figure A1) and the consistently amorphous PIs obtained previously without additives/ in presence of HOAc.[182] The SAXS curve of benchmark PI-COF-2 featured the five characteristic reflections (100) at $q = 2.1\,\mathrm{nm^{-1}}$, (2$\bar{1}$0) at $q = 3.5\,\mathrm{nm^{-1}}$, (220) at $q = 4.0\,\mathrm{nm^{-1}}$, (3$\bar{1}$0) at $q = 5.3\,\mathrm{nm^{-1}}$, and (4$\bar{1}$0) at $q = 7.0\,\mathrm{nm^{-1}}$. These reflections were found by Fang et al.,[85] with PI-COF-2's diffractogram reported to equally well match the orthorhombic space

group Cmcm (no.63) and the hexagonal space group P6/mmm (no. 191) as also evinced by simulations performed within their report.[85] In contrast to Fang et al., the reflections' (*hkl*) indices are here given for the hexagonal unit cell. The reflection (100) was also present in the samples PI-COF-2_{AP-1} - PI-COF-2_{AP-7}. This indicated that these materials, synthesized by aaHTP, contained indeed PI-COF-2. As reflections in the typical area of π-π stacking ($\sim$ 17-19 nm^{-1}) in between aromatic COF sheets overlap with δ' from PMA-An ref., it could not be concluded if a 3D structure was obtained.

Interestingly, the full width at half-maximum (FWHM) of (100) was significantly lower for most of the PI-COF-2_{AP} samples than for the classically synthesized benchmark PI-COF-2. Specifically, FWHM [(100), PI-COF-2_{AP-1}] = 0.162 nm, FWHM [(100), PI-COF-2_{AP-3}] = 0.199 nm, FWHM [(100), PI-COF-2_{AP-5}] = 0.209 nm, FWHM [(100), PI-COF-2_{AP-7}] = 0.152 nm, FWHM [(100), while FWHM [(100), PI-COF-2 benchmark] = 0.283 nm. As the FWHM can be used as an indicator for the quality of the crystal lattice, it was assumed that the here synthesized PI-COFs show higher crystallinity than the benchmark PI-COF-2. However, the SAXS curves of the PI-COF-2_{AP} samples differed in two other aspects: (i) Some samples such as PI-COF-2_{AP-1} and PI-COF-2_{AP-3} showed a broad and curved baseline, which in its shape is characteristic of amorphous SiO_2 ("glassy background"). (ii) In all cases, additional reflections at larger q values were present and abruptly increased with increasing amount of aniline from 1 to 3 equiv. (specifically, β': q = 13.44-13.66 nm^{-1}, γ': q = 15.05 15.30 nm^{-1}, and δ': q = 19.10 19.38 nm^{-1}). These reflections precisely matched the in-plane reflections found for PMA-An ref. as described in the previous section (Figure 28C in section 4.2.2). This clearly showed that the anticipated side-reaction indeed took place during HTP, resulting in the formation of the side-product PMA-An as a second phase.

Notably, two reflections ($(2\bar{1}0)$: q = 3.4 nm^{-1} and $(4\bar{1}0)$: q = 7.0 nm^{-1}) can be assigned to both PI-COF-2 as well to the S_B pattern of PMA-An ref. (α: q = 3.4 nm^{-1} and β: q = 7.0 nm^{-1}). Moreover, several small peaks were found (q = 2.9, 6.3, 7.4, 8.3, 9.7, and 14.3 nm^{-1}) in some curves, marked with a triangle (Figure 32B), which could neither be assigned to PI-COF-2 nor the side-product PMA-An. Additionally, PXRD measurements were performed for all PI-COF-2_{AP} samples

and the benchmark PI-COF-2 (see Figure A1).

Separated Phase Analysis

The top and bottom phase of the easily separable samples PI-COF-$2_{AP\text{-}10}$ and PI-COF-$2_{AP\text{-}15}$ were investigated via ATR-FT-IR spectroscopy (see Figure 33A). The top phases were marked in blue and the bottom phases in red. The spectrum of PI-COF-$2_{AP\text{-}10}$ top showed almost identical modes as PMA-An ref., which confirmed the hypothesis or PMA-An being the dominant species in the top phase. The bottom phase of PI-COF-$2_{AP\text{-}10}$ did not show any modes assigned to PMA-An, however the desired imide modes ($\mathbf{i_a} = 1785\,\mathrm{cm^{-1}}$, $\mathbf{i_b} = 1720\,\mathrm{cm^{-1}}$, $\mathbf{i_c} = 1365\,\mathrm{cm^{-1}}$) were also barley present. Instead, the modes stemming from the amine precursor TAPB (mode **t**: $\tilde{\nu}(\mathrm{NH_2}) \approx 3435\text{-}3355\,\mathrm{cm^{-1}}$) were clearly visible.

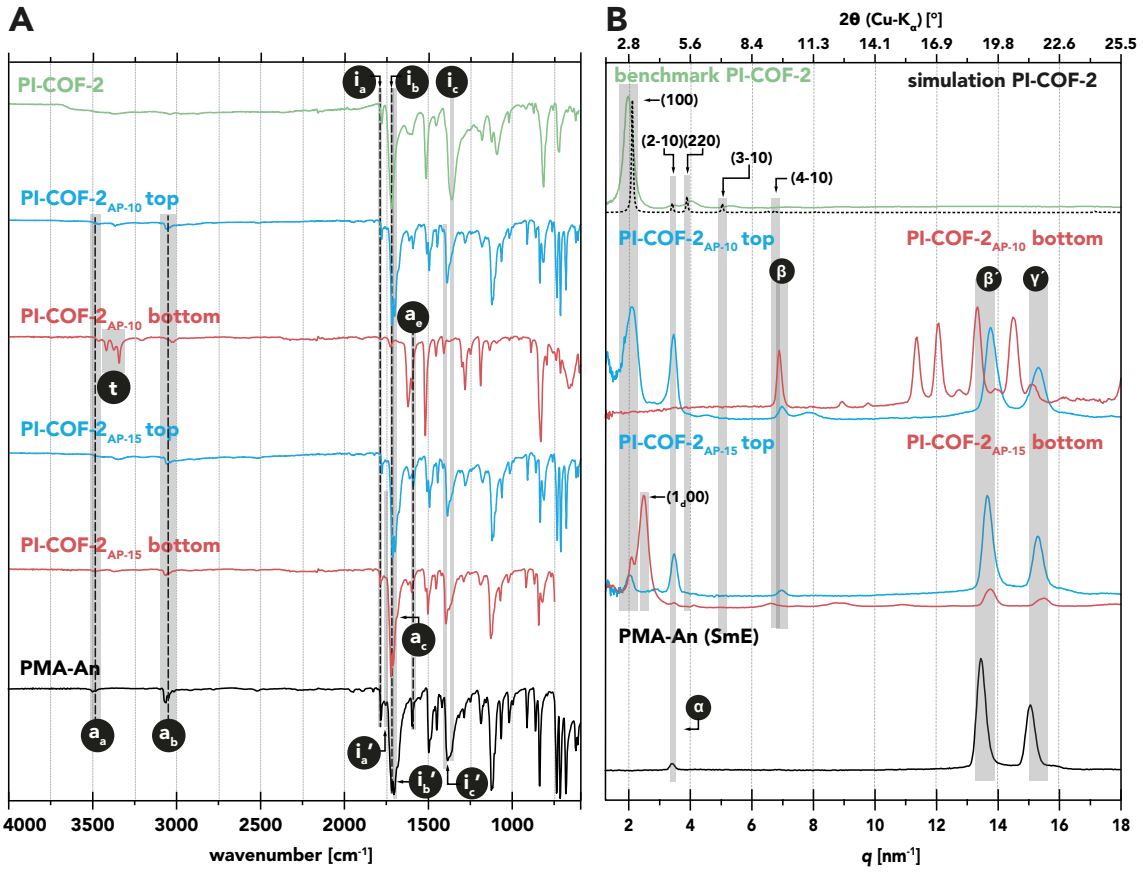

Figure 33: ATR-FT-IR and SAXS analyses of the separated top and bottom phases of PI-COF-$2_{AP\text{-}10}$ and PI-COF-$2_{AP\text{-}15}$ samples. A: from top to bottom, benchmark PI-COF-2, the separated top (blue) and bottom (red) phases of PI-COF-$2_{AP\text{-}10}$, and PI-COF-$2_{AP\text{-}15}$ and the reference PMA-An. B: from top to bottom, benchmark PI-COF-2 (green) and its simulated pattern, the separated top (blue) and bottom (red) phases of PI-COF-$2_{AP\text{-}10}$, and PI-COF-$2_{AP\text{-}15}$ and the reference PMA-An.

This pointed at the reaction equilibrium being shifted to the precursor side and therefore PI-COF-2 either degraded or never formed. In contrast, both PI-COF-$2_{AP\text{-}15}$ phases seemed to have the exact same spectrum, which was almost identical to the spectrum of PMA-An ref.. Consequently, PMA-An was present in both phases. Surprisingly, no signs of precursors/degradation were visible albeit even a higher amount of aniline was used compared to PI-COF-$2_{AP\text{-}10}$.

Again, SAXS analysis was carried out for the top and bottom phases of the easily separable samples PI-COF-$2_{AP\text{-}10}$ and PI-COF-$2_{AP\text{-}15}$. In Figure 33B, the top and bottom phases are again depicted as blue and red curves, respectively. PI-COF-$2_{AP\text{-}10}$ top and bottom showed completely different patterns: The top pattern revealed both PI-COF-2 and PMA-An ref. reflections, pointing at a product mixture as was already indicated by ATR-FT-IR spectroscopy. However, the bottom phase did not display any known reflections. Instead, many reflections in the region of high q values appeared, which did not match PMA-An ref. reflections nor the PI-COF reflections. This is in line with ATR-FT-IR spectroscopy results pointing at degradation rather than condensation during HTP in the presence of 10 equiv. aniline. PI-COF-$2_{AP\text{-}15}$ top and bottom phase featured a small reflection (100), indicating that they both contained PI-COF-2. Interestingly, PI-COF-$2_{AP\text{-}15}$ bottom showed a new reflection, close to (100) but slightly shifted at $q = 2.47\,\mathrm{nm^{-1}}$. This could be caused by the high PMA-An content, due to interference of the side-product distorting the hexagonal pores of PI-COF-2 in one dimension. This may result in a second phase with reflection (1_d00) instead of reflection (100). Furthermore, the PI-COF-2 reflections ($2\bar{1}0$) and (220) were present in the bottom phase but not in the top phase. This indicated that a higher amount of PI-COF-2 with a more intact crystal lattice was present in the bottom phase than in the top phase. Additionally, the relative intensity of the PMA-An reflections in comparison to (100) was larger for PI-COF-$2_{AP\text{-}15}$ top than for PI-COF-$2_{AP\text{-}15}$ bottom. Consequently, PMA-An was rendered dominant in the top phase, whereas the bottom phase mainly consisted of PI-COF-2 and its distorted analogue.

Taken together, PI-COF-$2_{AP\text{-}10}$ and PI-COF-$2_{AP\text{-}15}$'s heterogeneous results pointed at complex reaction kinetics during HTP when high amounts of aniline were added leading to degradation or distortion of the crystal lattice.

Nevertheless, in the case of PI-COF-$2_{AP\text{-}15}$, the biphasic aspect correlated with the two crystal phases identified by SAXS analysis. I.e., the top whiteish phase would mainly correspond to PMA-An, while the bottom brown phase would correspond to PI-COF-2. To verify this hypothesis is also true for samples which show a less sharp border between the phases, the synthesis of a PI-COF-2_{AP} sample with less equivalents of aniline was repeated. The addition of 3 equiv. of aniline led to the highest crystallinity of PI-COF-2 according to SAXS analysis and was therefore deemed the best candidate. After HTP-AP, the off-white top phase was manually separated from the brown bottom phase with a Pasteur pipette. The ATR-FT-IR and SAXS characterizations of top and bottom phase are displayed in Figure 34.

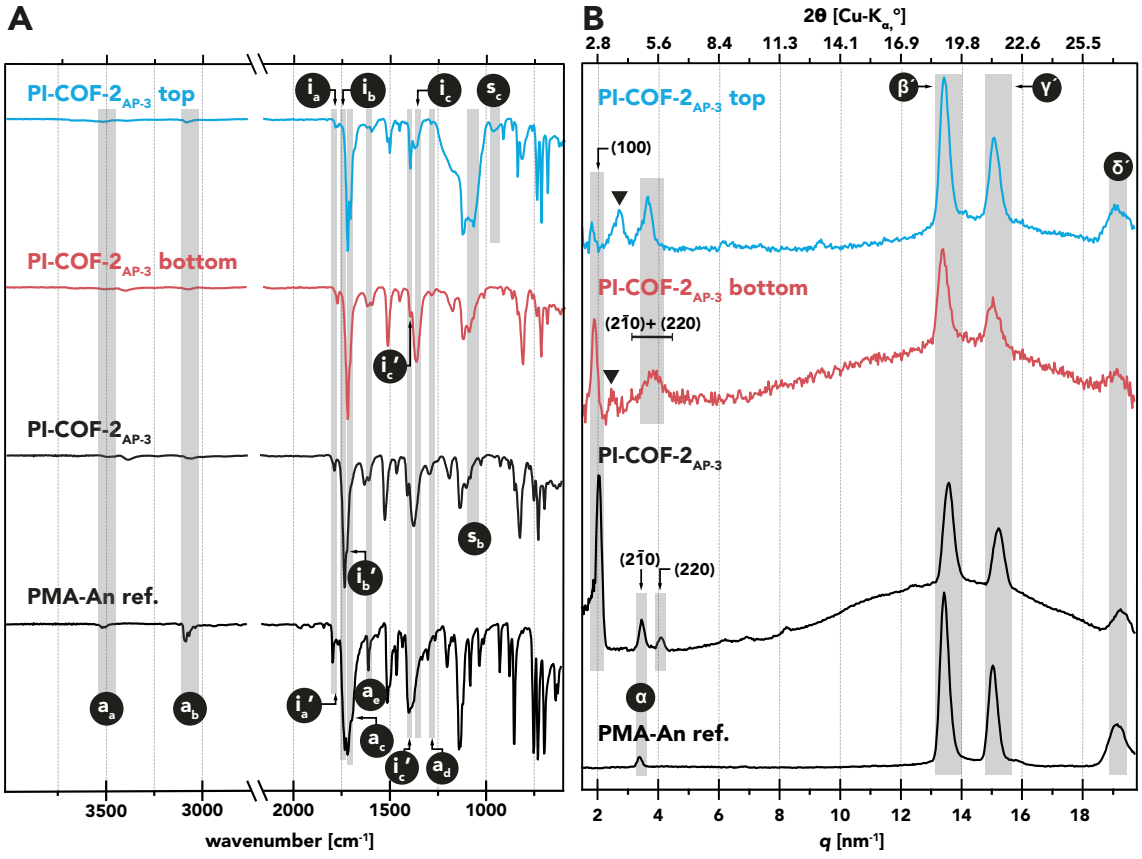

Figure 34: ATR-FT-IR spectroscopy and SAXS analyses of the top and bottom phases of PI-COF-$2_{AP\text{-}3}$. A: ATR-FT-IR analyses of PI-COF-$2_{AP\text{-}3}$ top and bottom phase, the unseparated PI-COF-$2_{AP\text{-}3}$ and the side-product (PMA-An) for reference. B: SAXS of PI-COF-$2_{AP\text{-}3}$ top and bottom phase, the unseparated PI-COF-$2_{AP\text{-}3}$ and the side-product (PMA-An ref.) for reference.

In Figure 34A, the following ATR-FT-IR spectra are depicted: (i) PI-COF-$2_{AP\text{-}3}$ top phase (blue curve), (ii) PI-COF-$2_{AP\text{-}3}$ bottom phase (red curve), as well as (iii) the PI-COF-$2_{AP\text{-}3}$ sample with top and bottom phases mixed during work-up (as already

discussed in Figure 32A), and (iv) PMA-An ref. as references. A closer look on the mixed PI-COF-$2_{AP\text{-}3}$ sample revealed that in addition to the typical imide modes ($\mathbf{i_a}$, $\mathbf{i_b}$ and $\mathbf{i_c}$) a shoulder at $\tilde{\nu} = 1710\,cm^{-1}$ ($\mathbf{i_b}$') was present. This shoulder corresponded to a second species also found in PMA-An. This indicated that PI-COF-$2_{AP\text{-}3}$ was indeed a mixture of PI-COF-2 and the side-product PMA-An. The ATR-FT-IR spectrum (Figure 34A) of the bottom phase (red curve) alone showed the desired imide modes $\mathbf{i_a}$, $\mathbf{i_b}$ and $\mathbf{i_c}$, but still a very weak shoulder $\mathbf{i_c}$' corresponding to PMA-An could be discerned. This pointed at PI-COF-2 being the dominant species in this phase.

The top phase, however, shows a much more distinct mode at the position of the shoulder $\mathbf{i_c}$' at $1395\,cm^{-1}$, and moreover a well pronounced mode $\mathbf{i_b}$'. This strongly suggested that the off-white top phase is composed of predominantly PMA-An, and barely contains any PI-COF-2. Interestingly, two further IR modes were found which were most pronounced in the top phase: (i) $\tilde{\nu} = 1110\text{-}1005\,cm^{-1}$ ($\mathbf{s_b}$), and (ii) $\tilde{\nu} = 995\text{-}930\ cm^{-1}$ ($\mathbf{s_c}$). These modes were assigned to Si-O-Si vibrations and Si-OH stretching modes, respectively. As described in Chapter 4.1, these modes most likely arose as a consequence of HTP carried out in borosilicate glass vessels.[182] Typically, SiO_2 dissolution in HTW and reprecipitation is noticeable only at significantly longer reaction times (around 7 days) than here employed. A possible reason could be, that the strongly basic conditions generated through the presence of several equivalents of aniline accelerated the process in this case.

SAXS measurements on the separated top- and bottom phases of PI-COF-$2_{AP\text{-}3}$ were analyzed as depicted in Figure 34B. In general, the results were in good agreement with ATR-FT-IR spectroscopy in Figure 34A. The unseparated PI-COF-$2_{AP\text{-}3}$ showed a very distinct pattern for a hexagonal unit cell (reflection (100), $(2\bar{1}0)$ and (220)), the reflections observed for PMA-An (α, β', γ', and δ') and finally also a "glassy background". After separation, the top and bottom phases were measured separately, as depicted in the blue and red curves. The top phase (blue) shows a very small reflection (100), and rather intense reflections α, β', γ', and δ'. As this complied with ATR-FT-IR results, it was concluded that the dominant species in this phase is PMA-An, but still small amounts of PI-COF-2

were present. The bottom phase shows the opposite: Large intensity for reflection (100), and comparably less intense reflections α, β', γ', and δ'. Again, this was in good agreement with ATR-FT-IR results, suggesting that this phase is dominated by PI-COF-2 and small residues of PMA-An were present.

Furthermore, ^{13}C-CPMAS solid-state NMR spectroscopy of the separated phases PI-COF-$2_{\text{AP-3}}$ (Figure 35A: top phase in blue and Figure 35B: bottom phase in red) was carried out. Signals **H** ($\sim$164 ppm), **E** ($\sim$137 ppm) and **A** ($\sim$114 ppm) were found at almost identical shifts in both phases. Signal **H** was, in agreement with literature,[57,59,64,85] assigned to the carbonyl carbons of the imide ring (**H**). Its high chemical shift is caused by the deshielding of the C-atom due to the electron withdrawing properties of oxygen. Signal (**E**) (at 136.89 ppm and 137.03 ppm, respectively), was assigned to the quaternary carbon adjacent to the carbonyl carbon of the imide moiety.[223] The most up-field signal **A** could be assigned to the aromatic C-H in between the two imide moieties.[223] All three signals (**H**, **E** and **A**) stemmed from the pyromellitimide moiety present in both phases.

In the bottom phase (red curve in Figure 35B) two signals of quaternary carbons (**G**, 147.24 ppm and **F**, 140.58 ppm) were found, which were not present in the top phase (dashed box Figure 35A). **G** was assigned to the N-substituted phenyl carbon of the triphenylbenzene moiety from the employed TAPB monomer,[57,64] and signal **F** was assigned to the two quaternary carbons building up the biphenyl axis in the triphenylbenzene moiety.[224] Together with ATR-FT-IR, this confirmed the structure of the PI-COF-2 in the bottom phase.

In the top phase, the signal for the biphenyl carbon (**F**) was missing completely (dashed box Figure 35A) and instead, the aromatic quaternary carbon connected to the imide nitrogen (**G**) can now be found at 125.10 ppm (dashed box Figure 35B). This up-field shift could be explained by the absence of the large triphenylbenzene moiety and instead the presence of a single benzene ring.[224] This showed clearly that the triphenylbenzene moiety was absent in the structure and instead PMA reacted with the modulator aniline to the side product PMA-An. This was in good agreement with ATR-FT-IR spectroscopy indicating that the top phase was mainly composed of PMA-An.

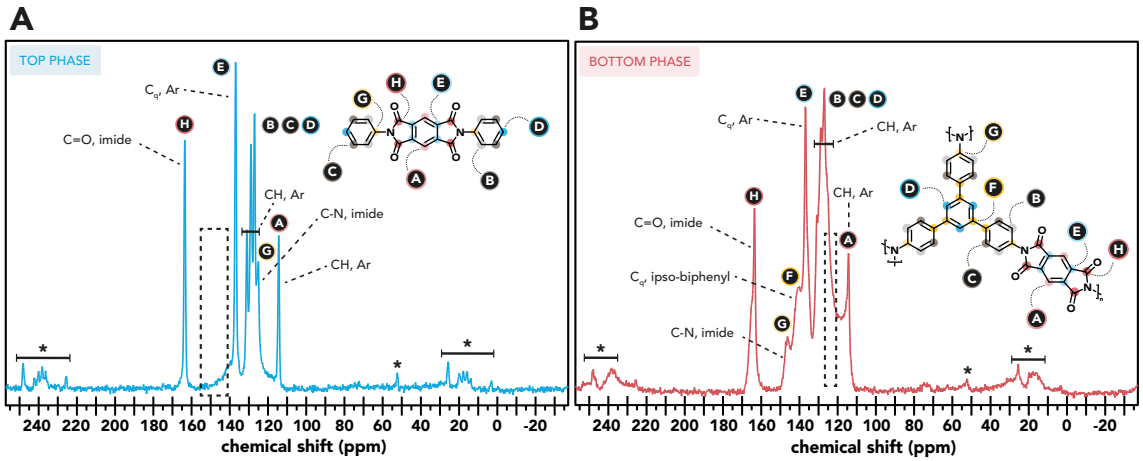

Figure 35: ^{13}C-CPMAS solid-state NMR spectra of PI-COF-2$_{\text{AP-3}}$ (A) top (blue) and (B) bottom phase (red).

Finally, for both phases, the signals from 130.88-126.97 ppm stemmed from H-bearing aromatic carbons (**B**, **C** and **D**), i.e., C-H of the triphenylbenzene and the benzene moiety, respectively.[224] No residual PMA-An could be detected in the bottom phase. This was explained by the limited base line separation of the signals resulting from the polymeric nature of PI-COF-2. No acid (COOH $\sim$ 172-175 ppm) or amide signals (COOH $\sim$ 170-174 ppm) were found, which allowed for concluding that monomers or monomer salt precursors were not present in significant amounts in the products. Spinning side-bands were present and marked with asterisks.[57]

Overall, it became clear that the top phase was indeed mainly composed of PMA-An. The bottom phase contained mainly PI-COF-2, but still significant amounts of PMA-An. Both top and bottom phase contained SiO_2. Consequently, the phases of PI-COF-2$_{\text{AP-3}}$ and PI-COF-2$_{\text{AP-15}}$ indeed behave similarly, however the manual separation (neither in the case of decanting nor when using a Pasteur pipette) did not suffice to afford the desired single species PI-COF-2 as product.

Physical and Chemical Relations of PMA-An within PI-COF-2

So far, it was shown that aaHTP indeed led to high-quality 2D hexagonal PI-COF-2, coexisting with a second crystal phase consisting of smectically arranged side-product PMA-An. Next, the physical and chemical interplay of the side-product phase PMA-An with the PI-COF-2 phase was studied. For example, the small molecule PMA-An could aggregate within the pores or on top of the 2D sheets

of PI-COF-2. As this would alter the diameter of the pores and the thickness of the sheets, form- and structure factor would be affected as well. Consequently, varying ratios of the first three reflections (100), (2$\bar{1}$0) and (220) were expected. A collaboration partner and SAXS specialist provided a mathematical description model which allowed the comparison of the ratios and FWHM of the reflections among the PI-COF-2_{AP} samples (1, 3, 5, and 7 equiv. aniline added; top and bottom phase not separated) depending on the amount of aniline added.

In the used model, the SAXS intensities are described as structure factor $S_{(q)}$ times form factor $F_{(q)}$:

$$I_{(q)} = S_{(q)} \cdot F_{(q)}$$

The chosen form factor $S_{(q)}$ was a large lamella with the thickness H as fit parameter, which was early published by Porod.[225] For the structure factor $F_{(q)}$ the multiple peak model for a hexagonal lattice was used.[226,227] $F_{(q)}$ consists of a sum of peak shape functions for the hexagonal lattice with three main parameters: (i) FWHM, from which the domain size (D) is obtained via the Debye-Scherrer equation $D = \frac{2\pi K}{FWHM}$, (ii) lattice parameter a, and (iii) a parameter ν, which changes the peak shape continuously from a Gaussian profile (in the limit ν towards infinity) to a Lorentzian profile (in the limit ν towards zero). Experimental data were then fitted to this model. In Table 1 the fit parameters FWHM, lattice parameter a, lamellae thickness H and the parameter ν, as well as the derived theoretical diameters (from the lattice parameter) and the domain size are summarized (see Chapter A.1.2 for mathematical details). Due to the overlap of reflections (2$\bar{1}$0) and α (which could belong to both the hexagonal lattice of PI-COF-2 and the S_B lattice of PMA-An), some of the fits are rather poor, especially PI-COF-$2_{AP\text{-}5}$ with a quite low SAXS intensity is affected. Nevertheless, the overall outcome of the fitting was as follows: No matter how much side-product is present in the material, it comprised of rather intact 2D hexagonal unit cells with greater length of coherence (i.e., narrower FWHM) than the benchmark PI-COF-2; i.e., exhibits higher crystallinity with an in-plane dimension of 20-40 nm, which corresponds to approximately 10 times 10 cells. The lattice distances were found to vary statistically (3.31-3.89 nm), consequently it was assumed that PMA-An as second phase did not to impart the crystal

Table 1: The fit parameters FWHM, lattice parameter a, lamellae thickness H and the parameter ν, used for fitting the experimental data to the model, as well as the derived theoretical diameters (from the lattice parameter) and the domain size D.

Sample	a [nm]	theoretical ⌀	FWHM [nm]	D [nm]	H [nm]	ν
PI-COF-2	3.61	3.89	0.282	22.1	1.16	1.6
PI-COF-$2_{\text{AP-1}}$	3.85	4.15	0.162	38.8	0.70	0
PI-COF-$2_{\text{AP-3}}$	3.54	3.81	0.199	31.5	1.11	0
PI-COF-$2_{\text{AP-5}}$	3.77	4.06	0.21	30.0	0.23	0
PI-COF-$2_{\text{AP-7}}$	3.89	4.20	0.152	41.3	0.96	0
PI-COF-$2_{\text{AP-10}}$ top	3.31	3.56	0.380	16.5	1.33	0.72
PI-COF-$2_{\text{AP-15}}$ top	3.63	3.92	0.260	24.2	0.73	0.82

lattice to a great extent, but rather aggregates with itself next to the PI-COF-2 sheets. The thickness H was found to scatter around ~ 1 nm, therefore it was concluded that PI-COF-2 is present as a monolayer. Also, the theoretical diameter of the hexagons was found quite narrowly distributed (3.81-4.20 nm; cf. Fang et al. report on 3.7 nm for PI-COF-2[85])[b] for all samples and did not significantly change with increasing side-product. Therefore, stacking of PMA-An within the pores or otherwise imparting the PI-COF-2 lattice was excluded.

In the case of PI-COF-$2_{\text{AP-10}}$ and PI-COF-$2_{\text{AP-15}}$, SAXS analysis evinced that the top phases comprised mainly of PMA-An, but also PI-COF-2. To find out if this high amount of PMA-An disturbed the hexagonal lattice, the mathematical model was also applied to these samples. Interestingly, the fitting showed that the lattices were still intact (cf. Table 1 lattice parameter a and thickness H are comparable to all other samples). PI-COF-$2_{\text{AP-10}}$ and PI-COF-$2_{\text{AP-15}}$ top however exhibited bigger FWHM and smaller Ds compared to all other PI-COF-2_{AP} samples. This led to the assumption that no matter how much aniline was added, PMA-An did not disturb the COF structure but rather "dilutes" the 2D-monolayers between its smectic layers. I.e., the 2D COF sheets are prevented from stacking on top of each other by intercepting layers of smecitcally arranged PMA-An.

This is in clear contradiction to the bottom phases of both samples as was discussed above: PI-COF-$2_{\text{AP-10}}$ bottom showed distinct signs of degradation and PI-COF-$2_{\text{AP-15}}$ bottom displayed a clearly distorted lattice. This behavior could

[b] theoretical diameters are the mean of inner- and outer diameter of the hexagons, whereas Fang's diameter is given as pore-size, which corresponds to inner diameter and is therefore ~ 0.5 nm smaller than the theoretical diameter.

also be explained by a possible T difference during the heating phase of the HTP process: The ampoules were heated standing up inside a steal autoclave using a heating mantle. As the bottom of the ampoules was in direct contact with the steel walls of the autoclave, the local T might have been higher compared to the T surrounding the rest of the ampoule.

In summary, SAXS analysis allowed for confirming the presence of at least 2D hexagonal PI-COF-2 in high quality. However, it also underlined the presence of the side-product PMA-An as a second crystal phase within the product, which "diluted" the 2D PI-COF-2 sheets but did not impart its crystal structure. Only with really high amounts of aniline (10 and 15 equiv.) degradation and/or distortion of the lattice were observed in the bottom phases of the ampoules.

Microscopy

To study the materials' morphology, SEM, HIM, and TEM of the PI-COF-2_{AP} samples were performed. In Figure 36A SEM images of PI-COF-$2_{AP\text{-}1}$, PI-COF-$2_{AP\text{-}3}$, PI-COF-$2_{AP\text{-}15}$top, and PMA-An ref. are depicted. PI-COF-$2_{AP\text{-}1}$ and PI-COF-$2_{AP\text{-}3}$ show a similar film-type morphology ($\sim$ 10-50 μm lateral extension and $<$ 100 nm thickness), whereas both PI-COF-$2_{AP\text{-}15}$ top phase and PMA-An are better described as platelets ($\sim$ 5-20 μm lateral extension and $<$ 100 nm thickness). The morphological similarity of PI-COF-$2_{AP\text{-}15}$ top phase and PMA-An ref. corroborates the hypothesis on increasing PMA-An content with increasing amount of aniline used. See Figure A12 for SEM images of all other PI-COF-2_{AP} samples. Additionally, to check whether the morphologies found in SEM were not altered by the electron beam during the measurement, HIM, a less sample-altering method, was performed. The images gained from HIM are depicted in Figure 36B and showed morphologies identical to these found in SEM, but at higher resolution. This confirmed the nanoscopic film-like morphology. Furthermore, HIM indicated that parts of the films were even thinner than 200 nm, as indicated by the bright patches on the micrographs.

Additionally, TEM electron diffraction of two different particles of the PI-COF-$2_{AP\text{-}3}$ sample (Figure 36C and D) both showed distinct spots and thus further indicated

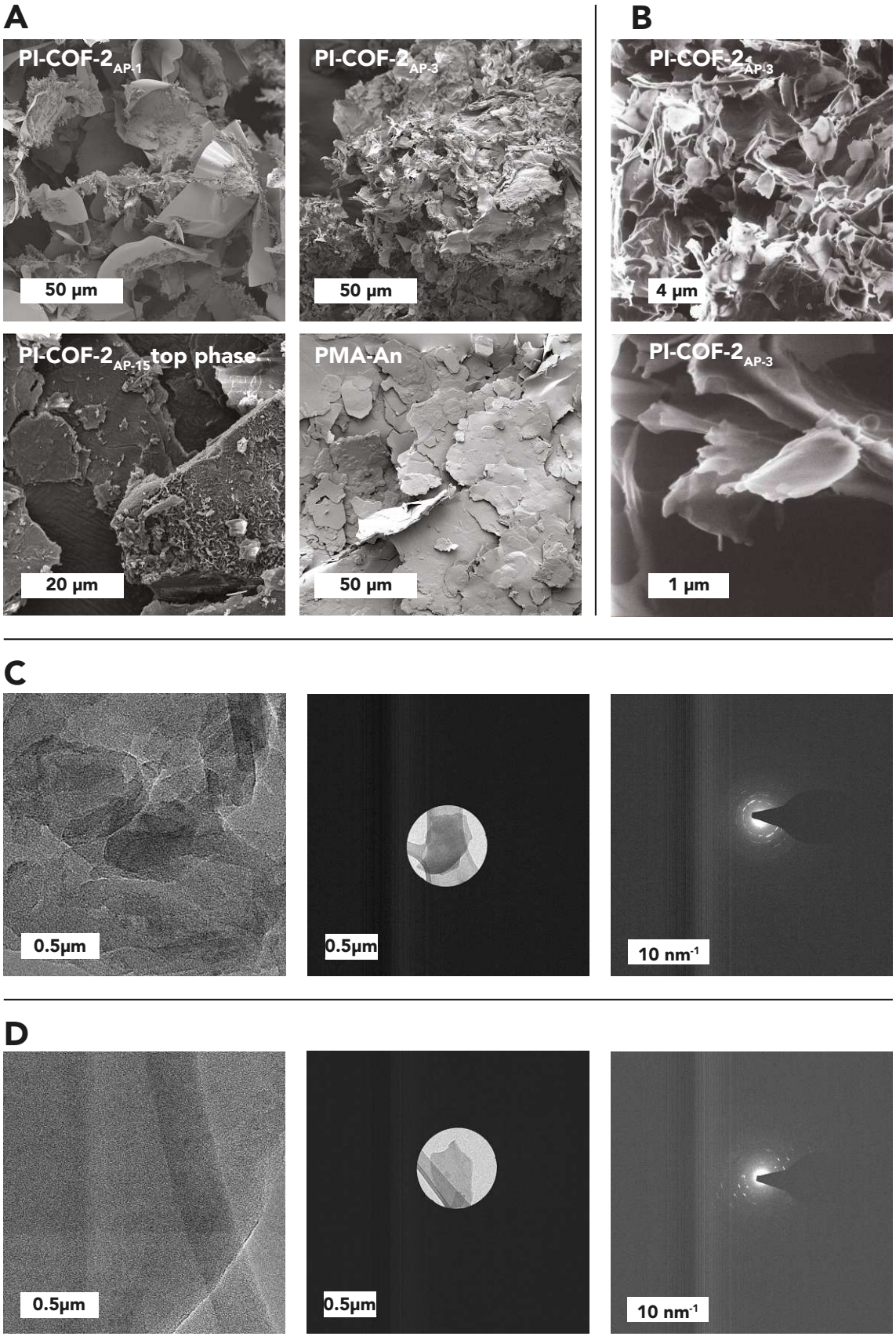

Figure 36: Microscopy of PI-COF-2_{AP} products. A: SEM images of PI-COF-$2_{AP\text{-}1}$, PI-COF-$2_{AP\text{-}3}$, PI-COF-$2_{AP\text{-}15}$ top phase, and PMA-An. B: HIM images of PI-COF-$2_{AP\text{-}3}$. C and D: TEM and TEM-electron diffraction of two different particles of the PI-COF-$2_{AP\text{-}3}$ sample.

a highly crystalline product. However, the diffraction incidents clearly did not display the presence of a 6-fold rotational axis as expected for the hexagonal unit cell of PI-COF-2. In contrast, the diffraction image indicated low symmetry, where at most a C_2 axis could be identified. Therefore, it was assumed that the examined crystallites were PMA-An and not PI-COF-2. Consequently, the diffraction images were not further analyzed or indexed.

Thermogravimetric Analysis

Furthermore, TGA was performed on all PI-COF-2_{AP} samples, as well as PMA-An ref. and the benchmark PI-COF-2 (see Figure 37). All PI-COF-2_{AP} samples showed a degradation step at roughly $T_d \approx 572\,°C$ (i.e., median value where $T_{d,\,min} \approx 560°C$ and $T_{d,\,max} \approx 585°C$; determined via tangents method according to EN ISO 11358 in Figure A8), which is similar to the amorphous PI(TAPB-PMA) discussed in Chapter 4.1 ($T_d \approx 560°C$).

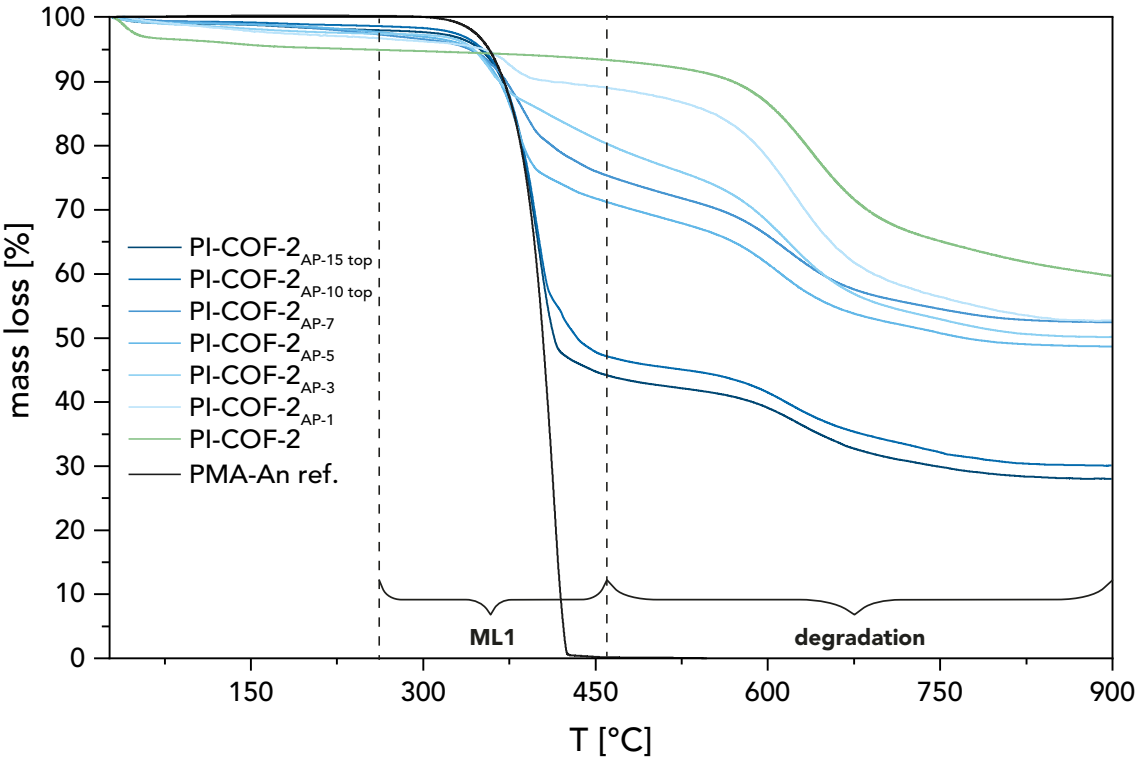

Figure 37: TGA analysis of PI-COF-2_{AP} products: TGA curves of PI-COF-$2_{AP\text{-}1}$ - PI-COF-$2_{AP\text{-}7}$, PI-COF-$2_{AP\text{-}10}$ top phase, PI-COF-$2_{AP\text{-}15}$ top phase, PI-COF-2 benchmark, and PMA-An. The area of the observed mass loss is approximately indicated with dashed lines and marked with ML.

Fang et al. reported on thermal stabilities of up to 535 °C for PI-COF-2, which was significantly lower than for PI-COF-2 prepared by aaHTP and thus further

pointed at higher crystallinity of the here prepared PI-COF-2 component. PMA-An ref. exhibits a much lower T_d at roughly 360 °C. Comparably, all PI-COF-2_{AP} samples showed a first mass loss at $T_{ML} \approx 360$ °C (see Figure 37; ML areas were determined via derivative, see Figure A8). This supported the findings of all other techniques, that a PMA-An phase was present in all samples as a side-product, with the first mass loss corresponding to its degradation. Furthermore, another trend was observed: the more aniline added, the more mass is lost in the first step ($ML_{AP\text{-}1} = 7.5$ wt%, $ML_{AP\text{-}3} = 17.4$ *wt.*%, $ML_{AP\text{-}5} = 26.9$ *wt.*%, and $ML_{AP\text{-}7} = 25.2$ *wt.*%; see Figure A8). The top phases of PI-COF-$2_{AP\text{-}10}$ and PI-COF-$2_{AP\text{-}15}$ also showed mass losses between ~260 and 460 °C with equally high percentages ($ML_{AP\text{-}10}$top = 53.5 *wt.*% and $ML_{AP\text{-}15}$top = 54.5 *wt.*%; see Figure A8). This was in good agreement with SAXS results indicating that both top phases contained PMA-An as well as PI-COF-2.

Low Pressure Gas Sorption Analysis

To study PI-COF-2_{AP}s' microporosity, gas sorption experiments employing N_2 as adsorbate were performed. Nitrogen was chosen because it is most commonly used for COFs and hence provides a comparison with the benchmark PI-COF-2. The samples PI-COF-$2_{AP\text{-}1}$ and PI-COF-$2_{AP\text{-}3}$ bottom were degassed at 120 °C for 16 h before the sorption experiments were performed at 77 K. The obtained adsorption points were used to calculate SA_{BET}. The values found were low: $SA_{BET} = 2.13$ and 17.22 $m^2\,g^{-1}$ for PI-COF-$2_{AP\text{-}1}$ and PI-COF-$2_{AP\text{-}3}$bottom, respectively (see Figure A5 in the appendix for the isotherms) which pointed at the absence of microporosity. In contrast, according to literature the benchmark PI-COF-2 showed a very large SA_{BET} of 1297 $m^2\,g^{-1}$. A possible explanation for the low SA_{BET}s is that in contrast to the benchmark PI-COF-2, PI-COF-2 via aaHTP is not a 3D stacked structure but 2D sheets that are separated by PMA-An layers. Hence no continuous pores are present, which would be necessary for permanent microporosity.

In summary, all solid-state techniques performed allowed for concluding that a PMA-An phase was present in all PI-COF-2_{AP} samples and could not be fully separated by manually separating top and bottom product phases. Nevertheless,

PI-COF-2 was obtained at high crystallinity and large domain size (10x10 cells) by aaHTP, yet pure product free of side-product was not obtained by the here performed approach.

Removal of PMA-An

To obtain pure PI-COF-2, chemically removing the second phase was attempted by (i) breaking up the secondary bonds between the PMA-An molecules by refluxing in concentrated HCl, and (ii) by heat-treating the material in an aluminium crucible with N_2 flow at 400 °C for 10 min. The reasoning to attempt the former approach was prompted by the indication that PMA-An could be dissolved to some extent in $CDCl_3$/TFA-d_1 for NMR, and the reasoning to attempt the latter approach was prompted by PMA-An thermally degrading at ~360 °C. However, both above-described attempts to remove the second phase from PI-COF-2_{AP} samples failed:

(*i*) ATR-FT-IR spectroscopy showed that HCl extraction did not significantly remove PMA-An as $\mathbf{i_b}$' and $\mathbf{i_c}$' were still present (see Figure 38A). Moreover, SAXS data still showed PMA-An reflections β', γ', and δ' next to new reflections in the low angle region (marked with black triangles; see Figure 38B).

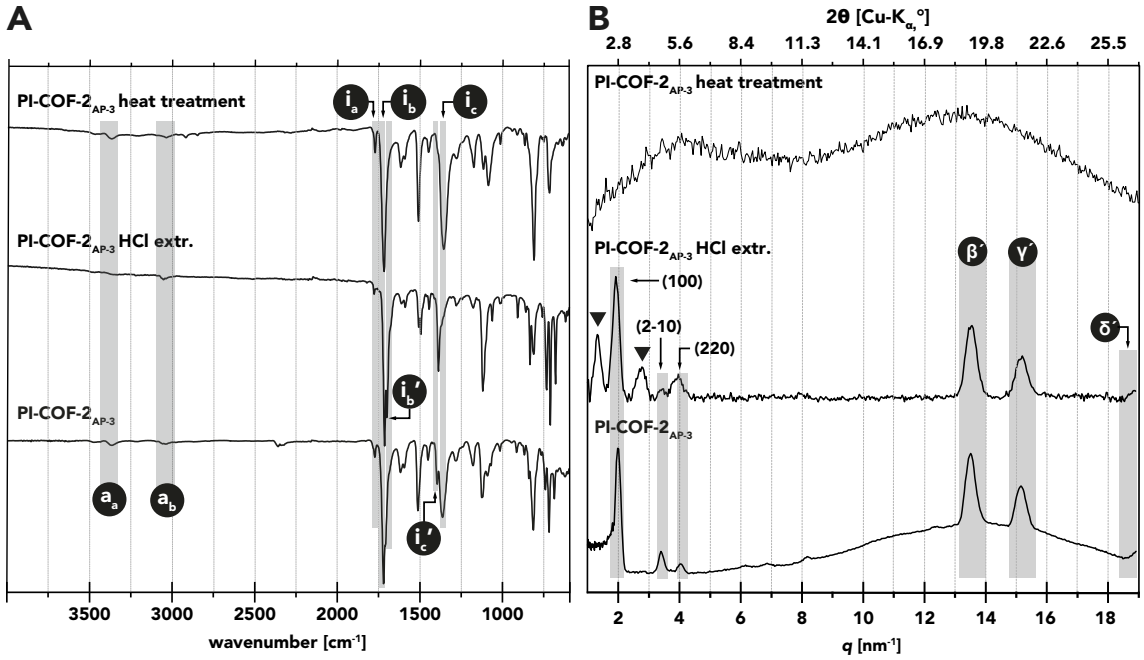

Figure 38: Removal of PMA-An. A: ATR-FT-IR spectra. B: SAXS curves.

(*ii*) ATR-FT-IR measurements of the heat treated sample did not show any modes belonging to PMA-An, pointing at the successful removal. However, SAXS evinced that the heat treatment amorphized the PI-COF-2 component. In fact, such thermally induced amorphization of COFs has been described in 2021 by Evans and co-workers for boronate ester and imine linked COFs.[228]

4.2.4 Aniline-Assisted HTP in Microwave Reactors

As the chemical removal of PMA-An was unsuccessful, the next step was altering the synthetic protocol. Specifically, aaHTP-MW was employed next. In contrast to the flame-sealed ampoules, HTP-MW necessarily includes stirring and hence bears on the one side the risk to homogenize (i.e., downsize the micronscale) the two product phases PI-COF-2 and PMA-An. On the other side, it is also conceivable that stirring and the highly efficient heating using a microwave reactor promote exchange reactions between PMA-An and PI-COF-2 corresponding to the initially targeted dormant species approach.

Several aaHTP-MW experiments were performed, employing two T_Rs (200 and 230 °C), three t_Rs (1, 2, and 4 h) and different amounts of aniline (2, 3, and 4 equiv.) Notably, samples were named using a code: $T_R \,|\, t_R \,|$ equiv. aniline. ATR-FT-IR spectroscopy and SAXS analysis showed the similar results as observed in the ampoule set-up (see Figure 39A and B):

(i) All samples were fully condensed PIs with all three imide modes $\mathbf{i_a} = 1785\,\mathrm{cm^{-1}}$, $\mathbf{i_b} = 1720\,\mathrm{cm^{-1}}$, $\mathbf{i_c} = 1365\,\mathrm{cm^{-1}}$ present and modes stemming from the co-monomers (PMA: $\tilde{\nu}$(O-H) = 3250-2755 $\mathrm{cm^{-1}}$, $\tilde{\nu}$(C=O, acid/ester) = 1695 $\mathrm{cm^{-1}}$ and TAPB: $\tilde{\nu}$(N-H) = 3435 $\mathrm{cm^{-1}}$ and 3355 $\mathrm{cm^{-1}}$) absent in all spectra. All samples were crystalline with reflections corresponding to PI-COF-2 ((100) = 2.1 $\mathrm{nm^{-1}}$, $(2\bar{1}0) = 3.5\,\mathrm{nm^{-1}}$, $(4\bar{1}0) = 7.0\,\mathrm{nm^{-1}}$).

(ii) PMA-An was always found and its amount in the product increased with increasing amount of aniline employed: The sample with the lowest amount of aniline added (230|2|2) only showed a small shoulder at the wavenumber of mode $\mathbf{i_c}$' ($\tilde{\nu} = 1395\,\mathrm{cm^{-1}}$) and a broad amorphous background where the reflections of

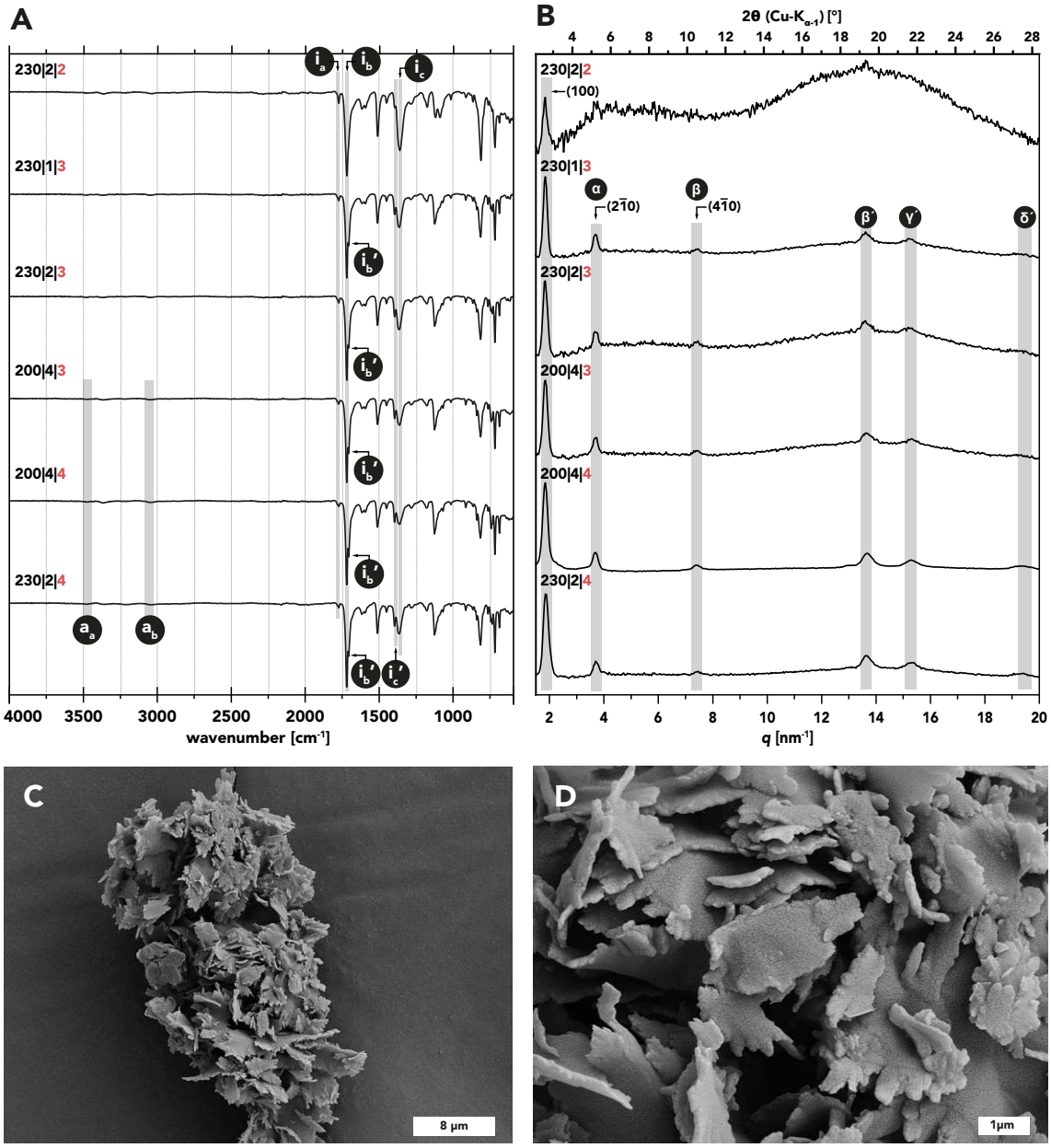

Figure 39: aaHTP-MW of PI-COF-2. A: ATR-FT-IR spectra. B: SAXS curves. C/D: SEM images of 230|1|3.

PMA-An are expected. Samples with higher amounts of aniline added (3 and 4 equiv.) showed pronounced modes stemming from PMA-An's imide moiety ($\mathbf{i_b}$' and $\mathbf{i_c}$') as well as weak amide modes ($\mathbf{a_a} = 3490\,\mathrm{cm^{-1}}$ and $\mathbf{a_b} = 3065\,\mathrm{cm^{-1}}$). Moreover, their SAXS curves exhibited PMA-An's reflections $\alpha = 3.4\ \mathrm{nm^{-1}}$, $\beta = 7.0\,\mathrm{nm^{-1}}$, $\beta' = 13.5\,\mathrm{nm^{-1}}$, $\gamma' = 15.2\,\mathrm{nm^{-1}}$ and $\delta' = 19.3\,\mathrm{nm^{-1}}$. Hence, switching from unstirred aaHTP-AP to a stirred aaHTP-MW was not a remedy for the formation of the side-product PMA-An.

Yet the PI-COF-2 component could be obtained within only $\leq 4\,\mathrm{h}$, which underlined that HTP-MW of PI-COF-2 could be performed- and was drastically accelerated-

in the MW set-up. SEM of the aaHTP-MW products showed similar morphologies as for PI-COF-$2_{AP\text{-}3}$, but with smaller diameters ($\sim$5-10 μm lateral extension, Figure 39C and D), which was to be expected when introducing stirring in the reaction mixture (see Figure A12 for SEM micrographs of all samples). Lastly, N_2 sorption experiment of 230|2|3 evinced that again no microporosity was present in the material (see Figure A5 for isotherms).

Finally, a set of experiments using <1 equiv. of aniline was performed to check if aniline would also be able to modulate PI-COF-2's crystallinity in substoichiometric amounts. If successful, this could be a solution to the issue of having to remove the PMA-An side-product. aaHTP-MW was performed with 0.05, 0.1, and 0.5 equiv. of aniline at $T_R = 200$ and 230 °C, and at $t_R = 2$,3, and 4 h (again, samples were named using a code: $T_R \,|\, t_R \,|$ equiv. aniline). All products were identified as fully condensed PIs according to the presence of characteristic modes ($\mathbf{i_a}$, $\mathbf{i_b}$, $\mathbf{i_c}$) adn the absence of modes stemming from the co-monomers (PMA: $\tilde{\nu}$(O-H) = 3250-2755 cm^{-1}, $\tilde{\nu}$(C=O, acid/ester) = 1695 cm^{-1} and TAPB: $\tilde{\nu}$(N-H) = 3435 cm^{-1} and 3355 cm^{-1}) found via ATR-FT-IR spectroscopy (Figure 40A for 200 °C and Figure A2A for 230 °C samples). Weak amide modes ($\mathbf{a_a}$ and $\mathbf{a_b}$) were present from 0.1 equiv. on. Additionally, 200|3|0.5 featured a second asymmetric C=O mode and a second C-N stretch mode $\mathbf{i_b}$' and $\mathbf{i_c}$'). This suggested that despite the little amount of aniline added, PMA-An was still present in the material.

SAXS measurements showed that all reaction products generated at 230 °C were amorphous (see Figure A2B). In contrast, three of the products synthesized at 200 °C did show Bragg reflections (Figure 40B): First, 200|3|0.5 (the highest amount of aniline within this screening) showed reflections corresponding to PI-COF-2 ((100),(2$\bar{1}$0), and (4$\bar{1}$0)) as well as reflections stemming from PMA-An (α, β, β',and γ'). Consequently, again a product mixture was obtained. Second, when using 0.1 equiv. of aniline, $t_R = 2$ and 3 h produced amorphous PIs. However, increasing t_R to 4 h revealed reflection (100). This indicated that lower amounts of aniline were indeed capable of inducing crystallinity, but require longer t_R.

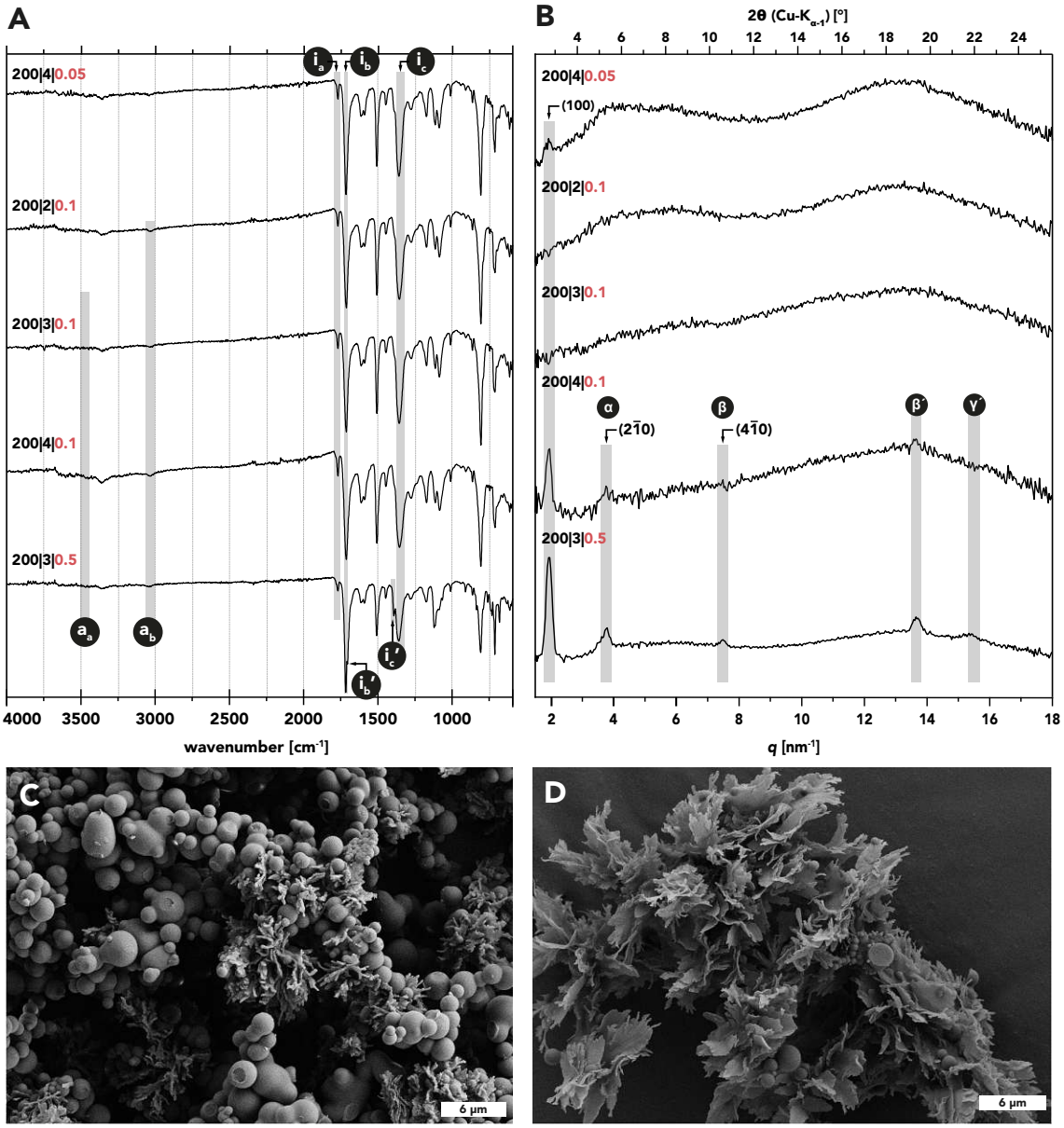

Figure 40: aaHTP-MW of PI-COF-2 using substoichiometric amounts of aniline. A: ATR-FT-IR spectra. B: SAXS curves. C: SEM images of 200|4|0.05 and D: 200|3|0.5.

Using aniline amounts as small as 0.05 equiv., $t_R = 4\,h$ led to a small reflection (100) and no reflections assigned to PMA-An. However, two amorphous halos pointed at the presence of a significant amount of amorphous PI component. Overall, it became clear that reducing the amount of modulator to < 0.5 equiv. required a substantially longer reaction time and that T_R must not exceed 200 °C.

SEM revealed a completely different morphology compared to all the other samples analyzed (see Figure 40C and D and Figure A13). Homogeneously sized spheres were observed to be the majority together with a small amount of film-type

morphologies. In fact, the spherical morphology is similiar to what was described for the amorphous PI-network PI(TAPB-PMA) in the previous Chapter 4.1 as well as the benchmark PI-COF-2 (see Figure A12). The film-type morphology resembles the morphology found for PI-COF-$2_{AP\text{-}3}$, indicating the potential formation of a PI-COF-2 phase.

Summing up, aaHTP-MW was indeed capable of inducing crystallinity in PI(TAPB-PMA) in surprisingly short reaction times. Nevertheless, no pure PI-COF-2 was afforded and again an unseparable product mixture containing the side-product PMA-aniline was obtained. Even employing as little amounts as 0.05 equiv. of aniline led to crystalline PIs with a hexagonal unit cell. Consequently, the postulated dormant species approach did not apply, as it would require a stoichiometric amount (3 equiv.) of aniline for crystallization. Instead, aniline appears to be behaving in a catalytic fashion similar to mineralizers. Unfortunately, reducing the amount of modulator did not circumvent the issue of mixed products.

4.2.5 Summary and Outlook

In this chapter, it was demonstrated that HTP was capable of generating a crystalline version of PI(TAPB-PMA) aka PI-COF-2. To begin with, a proof of concept was established that the corresponding imide moiety was indeed reversible in HT conditions. Therefore, two modelcompounds with different derivatizations were synthesized and characterized. Subsequently, MC1 and MC2 were mixed and exposed to HT conditions. ^{1}H-NMR confirmed that imide metathesis took place.

After proving the imide reversibility in HTW, a strategy was proposed to overcome the issue of consistently amorphous products from the highly reactive monomers TAPB and PMA. The addition of the basic modulator aniline was believed to form a dormant species from the reactive monomer PMA, slowing down the imide condensation reaction. In order to implement this strategy, aaHTP-AP was introduced where various amounts of aniline were added, ranging from 1-15 equivalents. All reaction products were crystalline and exhibited a hexagonal unit cell as expected from the benchmark PI-COF-2. However, the products showed impurities which were identified as the side-product PMA-An via several solid-state techniques. PMA-An ref. was synthesized on purpose and investigated thoroughly. The compound turned out to be highly crystalline, extraordinarily stable and virtually insoluble. SAXS and PXRD analysis showed that its calamitic components arranged in a smectic LC-type fashion which were stabilized via secondary interactions between molecules. A mathematical description model was applied to the experimental SAXS data of PI-COF-2$_{AP}$ samples and showed that the hexagonal unit cell of the PI-COF-2 component was not imparted by PMA-An up to 7 equiv. of added aniline. At 10 and 15 equiv., a distortion of the hexagonal pores and/or decomposition of PI-COF-2 was observed.

To obtain pure PI-COF-2, the chemical removal of PMA-An was attempted. Therefore, acidic extraction and thermal treatment was performed. However, both attempts failed. Therefore, a second HT method was established: aaHTP-MW. Both stoichiometric as well as substoichiometric amounts of aniline were used. Stoichiometric amounts yielded the same product mixtures as aaHTP-AP but within a fraction of the reaction time (72 h vs. 2 h). Substoichiometric amounts still afforded the crystalline PI-COF-2 component, however required at

least 4 h at 200 °C. Furthermore, this finding excluded the proposed hypothesis of a dormant species approach and rather pointed at a somewhat catalytic behavior.

In a nutshell, both aniline-assisted HT-methods, aaHTP-AP and aaHTP-MW, were proven capable of inducing crystallinity in a highly reactive monomer system. Nonetheless, PMA-An impurities remained the bottleneck and could not be eliminated via various strategies. However, as experiments using substoichiometric amounts of aniline showed, future experiments with substantially increased t_R (to >5 d) could potentially lead to pure PI-COF-2.

In the following chapter, it will be discussed if HTP is also able to provide crystalline framework structures without the necessity of the addition of a modulator. Therefore, the use of a different monomer system will be elaborated.

4.3 Hydrogen-Bonded Imide Framework

In the last chapter, it was shown that HTP was able to produce an imide-linked COF. Yet, this was not possible without employing an additive. In this chapter, it will be elaborated that HTP is indeed capable of generating a crystalline framework without the necessity of an additive. Specifically, two new monomer systems and their crystalline products via HTP-AC will be presented. However, it will be argued that the obtained products' macromolecular structures are not COFs but PI-based HOFs (PI-HOFs). The HOFs are believed to consist of linear PI-chains, which are laterally H-bonded via side-groups. Further, it will be proposed that the suggested HOF structures are transformed to linear PI-chains via side-group cleavage when using $T_R = 250\,°C$. Subsequently, this hypothesis will be backed via the products' characterization employing several standard solid-state techniques (ATR-FT-IR spectroscopy, PXRD, ^{13}C-CPMAS solid-state NMR spectroscopy, and SEM) and an extensive thermal analysis via TGA and inert thermal treatment experiments. Moreover, it will be discussed if the products' high crystallinity, of both HOFs and linear PIs, is caused by their reversibility in HTW. Finally, it will be shown that the results of a broad reaction screening further corroborates the hypothesis.

4.3.1 A New Monomer System: Mellitic Acid as Trigonal Tecton

In the previous Chapter 4.2.1, the imide reversibility in HTW per se was established via an imide metathesis reaction. However, this was only possible when precursors were employed which led to small, finite imide molecules. Yet, for inducing crystallinity in the extended structure the addition of aniline was necessary. Further, it was discussed that successful COF synthesis is assumed to be strongly dependent on the monomers' solubility and reactivity. Specifically, it was suggested that the limited solubility of the stiff, aromatic building blocks TAPB and PMA in HTW combined with their fast imidization contribute to the lack of crystallinity.
Therefore, in this work, a different monomer system was explored to check if it would be more suitable for HTP of an imide COF. Consequently, the trigonal planar

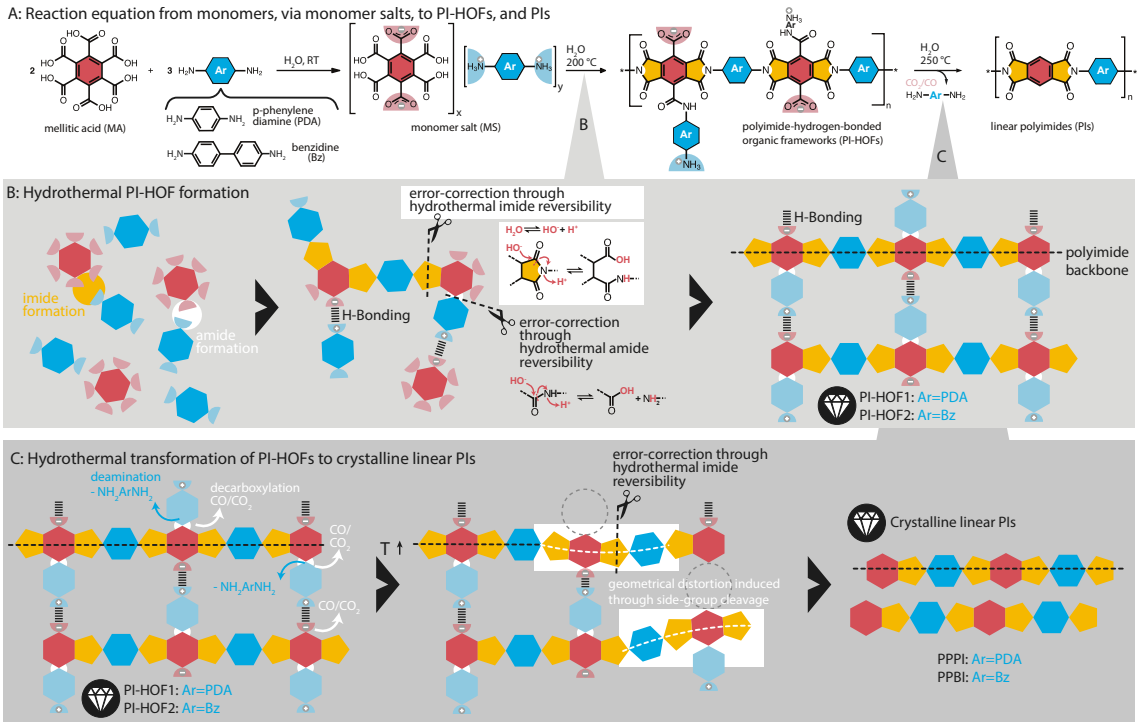

Figure 41: Proposed hypothesis. A: Proposed mechanisms of the hydrothermal transformations to PI-HOFs and subsequently linear crystalline PIs. B: Hydrothermal reaction sequence of the transformations from monomers to MS to PI-HOFs. C: Schematic of the underpinning of crystallinity in the linear PIs, i.e., concurrent side-group cleavage and imide-reversibility. Illustration by Miriam M. Unterlass.

tecton mellitic acid (MA) and two linear tectons, i.e., *p*-phenylene diamine (PDA) and benzidine (Bz) were chosen as precursors (cf. Figure 41A). The comonomer combinations MA-PDA and MA-Bz have to date rarely been exploited synthetically. Three studies reported on MA-PDA *networks* by classical polycondensation,[229–231] and a recent study by Kim et al. in fact reported on the HTP of MA-PDA at 180°C for 12 h.[198] The products were exclusively amorphous spherical microparticles that contained both amide and imide linkages. A simulation study furthermore found that the comonomer combination MA-PDA should lead to an interesting COF.[232]

Notably, MA-PDA and MA-Bz feature opposite functionalities compared to TAPB/PMA (i.e., trigonal (tri-)acid and linear (di-)amine instead of trigonal (tri-)amine and linear (di-)acid). Later on, it turned out that changing the number of functional groups and hence their reactivity and water solubility of tectons was a step in the right direction: Indeed, in 2021 Kim et al. reported on the first HTP of PI-COFs employing the trigonal tecton TPHCA and three linear aromatic amines (*p*-phenylene diamine, benzidine, and diaminoterphenyl) as monomer systems.[103]

Indeed, HTP experiments of both systems (MA-PDA and MA-Bz) at $T_R = 200$ and 250 °C yielded crystalline products. However, diffraction patterns clearly spoke against COFs: Neither reflections below 5 °(2θ, Cu-K_α), nor the corresponding patterns for the proposed hexagonal unit cells for the respective systems were found. Instead, a hypothesis was proposed, which is elaborated before discussing how the different performed solid-state characterizations have allowed for unravelling the products' nature:

It was postulated that HTP generated HOFs composed of linear PI chains that are laterally H-bonded. The hypothesis for formation is illustrated in Figure 41. When subjecting MA with PDA or Bz, respectively, to HT conditions at 200 °C, PI-HOFs (PI-HOF(MA-PDA) and PI-HOF(MA-Bz)) were obtained. These are proposed to comprise linear PI backbones that are decorated with *p*-ammoniumbenzamide (C(O)NH-Ph-NH_3^+) and carboxylate side-groups (CO_2^-), cf. Figure 41A, and form through simultaneous imide formation and error-correction through imide reversibility (Figure 41B). However, when HTP was performed at 250 °C, crystalline linear PIs without side-groups were obtained, namely *p*-phenylene pyromellitimide (PPPI) and *p*-biphenylene pyromellitimide (PBPI). It was proposed that PPPI and PBPI were generated from PI-HOF(MA-PDA) and PI-HOF(MA-Bz) by combined (i) side-group cleavage (decarboxylation and amide hydrolysis with PDA/Bz elimination), and (ii) imide opening and re-closing (error-correction), cf. Figure 41C. Thus, it was further postulated that the chosen monomers create imides that are reversible in HTW. Consequently, this reversibility is supposedly not limited to small molecules but can be exploited to generate crystalline frameworks via HTP. Notably, to the best of my knowledge, HOFs are in all to date reported cases based on small molecule building blocks and no HOF based on a linear backbone was reported so far.[122,142,143,233,234]

In the following, the synthesis and standard solid-state characterizations of the two monomer systems are discussed and it is elaborated how these results led to the postulation of the above described hypothesis.

4.3.2 Synthesis and Characterization

The standard method HTP-AC was chosen for the HTP of MA:PDA or Bz, respectively, (2:3). Therefore, the comonomers were dispersed in distilled water. The dispersion was transferred to a glass liner inside a steel autoclave and was heated to the reaction temperature T_R for the reaction time t_R (see Chapter B.2.2 for details). Initially, two different (T_R/t_R) combinations were employed for both systems: (200 °C; 24 h) and (250 °C; 24 h). The products were successively washed with water, acetone and THF.

Furthermore, as HTP is assumed to always proceed via a MS intermediate (cf. Chapter 4.1.1, page 48), MSs of the two systems were synthesized. Reference spectra were performed to check for the possibility of residual MS in the HTP products. Both MS (MS(MA-PDA) and MS(MA-Bz)) were synthesized in H_2O and THF/H_2O as solvents. MS(MA-PDA) formed via both routes, MS(MA-Bz) did not form fully in pure H_2O, but still contained unreacted Bz when synthesized from aqueous solutions. Therefore, MS(MA-Bz) synthesized by precipitation in H_2O was not used as reference material, but instead the successfully synthesized MS(MA-Bz) from precipitation from THF/H_2O. Organic elemental microanalysis (EA) was used to determine the comonomer ratios of MS(MA-PDA) and MS(MA-Bz) (see appendix for Table A1 and calculations): $MS(MA\text{-}PDA)_{H_2O}$ = 2:3 (MA:PDA) + 7 H_2O; $MS(MA\text{-}PDA)_{THF}$ = 2:3 (MA:PDA) + 0.5 THF + 8 H_2O; $MS(MA\text{-}Bz)_{THF}$ = 2:3 (MA:Bz) + 1 THF.

Moreover, the linear PI reference materials PPPI ref. and PBPI ref. were synthesized from the linear tecton PMA with PDA and Bz as diamines, respectively. The synthesis and characterization of PPPI was already reported in detail by Baumgartner et al., hence the synthesis of PPPI was performed according to their synthetic protocol.[10] PBPI was synthesized similarly, by dispersing in H_2O and sealing in a steel autoclave for 24 h at 200 °C followed by successively washing with water, acetone, and THF, and subsequently drying (see Chapter B.2.2 for details).

Several standard solid-state techniques were used to characterize all products, monomers, MSs, and references, which will be elaborated in the following.

Attenuated Total Reflectance Fourier Transform IR Spectroscopy

ATR-FT-IR spectroscopy was performed of the products, as well as, for comparison, the starting compounds (MA, PDA, Bz), the corresponding linear PIs (PPPI ref. and PBPI ref.), and the corresponding MSs ($MS(MA\text{-}PDA)_{H_2O}$ and $MS(MA\text{-}Bz)_{THF}$) (Figure 42). The following points became clear from ATR-FT-IR spectroscopy for both systems (MA-PDA in Figure 42A and MA-Bz in Figure 42B):

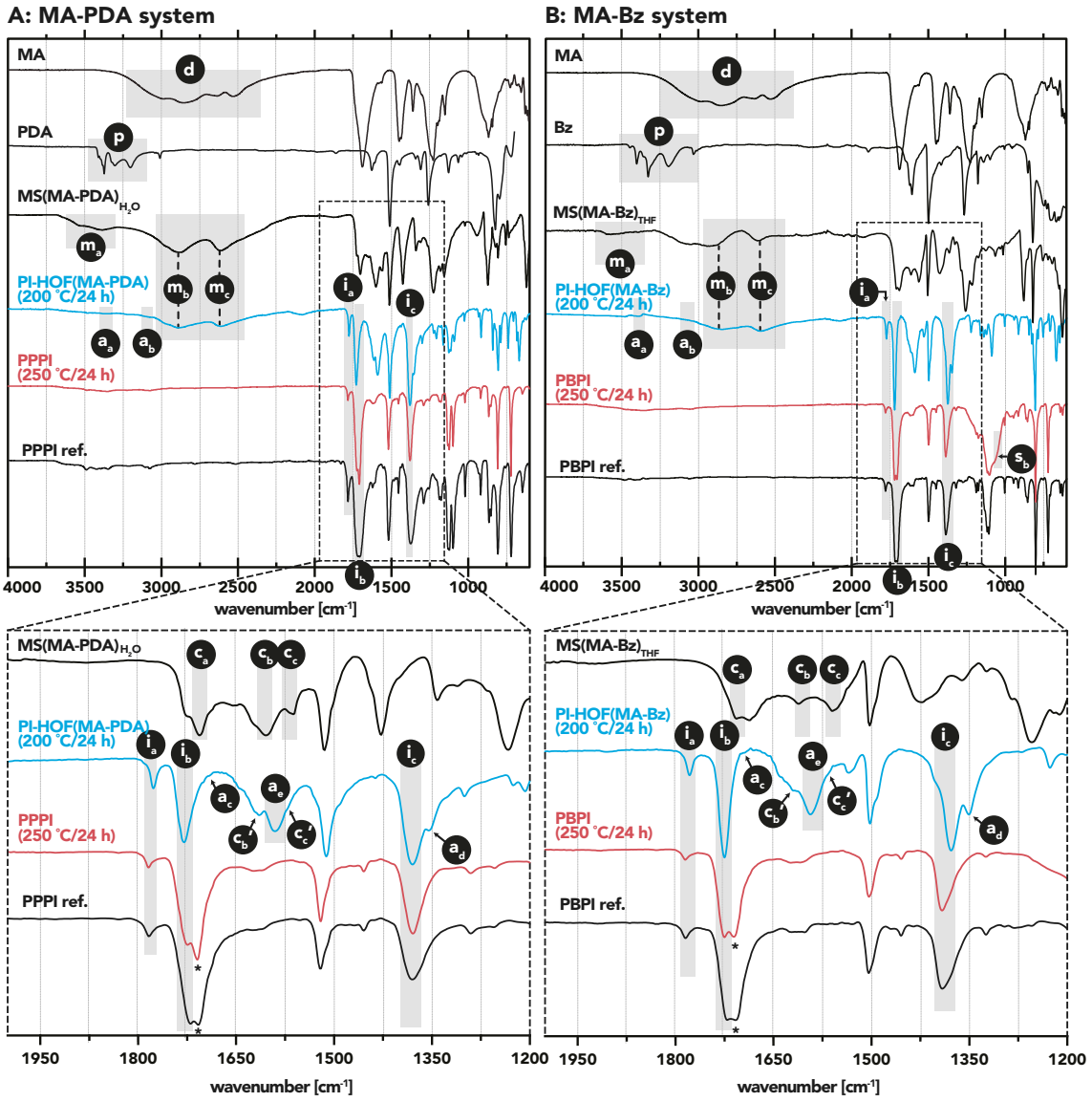

Figure 42: ATR-FT-IR spectra of the products, starting compounds, and reference compounds for both systems. A: ATR-FT-IR spectra of the MA-PDA system. B: ATR-FT-IR spectra of the MA-Bz system. Bottom: Zoom of each spectrum of the area 2000-1200 cm^{-1} including the imide, amide and carboxy modes.

(i) All HTP products (including the reference PIs PPPI ref. and PBPI ref.) show three characteristic imide modes[10] ($\mathbf{i_a}$: $\tilde{\nu}_{as}(C{=}O) \approx 1785\text{-}1780\,cm^{-1}$, $\mathbf{i_b}$: $\tilde{\nu}_{s}(C{=}O) \approx 1725\,cm^{-1}$; $\mathbf{i_c}$: $\tilde{\nu}(C\text{-}N) \approx 1380\,cm^{-1}$) – no matter if synthesized at 200

or 250 °C. This points at successful imide formation and therefore successful HTP of all products. Notably, samples synthesized at 250 °C and linear reference samples (PPPI ref. and PBPI ref.) show a second mode right next to the symmetric C=O stretch $\mathbf{i_b}$ marked with an asterisk $\tilde{\nu}(*) \approx 1710\,\mathrm{cm^{-1}}$. This was also observed for the benchmark system PPPI generated by HTP by Taublaender et al. and is therefore assumed not be related to residual MS or other impurities.[196] The MSs do not feature imide modes, which shows that no polymerization has happened during their synthesis, but solely the anticipated acid-base reaction.

(ii) Samples synthesized at 200 °C (aka PI-HOFs, Figure 42, blue curves) additionally show aryl-ammonium modes[10] ($\mathbf{m_b}$: $\tilde{\nu}$(Ar-NH_3^+, as) $\approx 2895\,\mathrm{cm^{-1}}$; $\mathbf{m_c}$($\tilde{\nu}$(Ar-NH_3^+, s) $\approx 2620\,\mathrm{cm^{-1}}$), and so do MS(MA-PDA) and MS(MA-Bz). Modes $\mathbf{m_b}$ and $\mathbf{m_c}$ are significantly more pronounced in the MSs. This was not a surprise, as $\mathbf{m_b}$ and $\mathbf{m_c}$ were already established as typical for the protonated amine moieties in MSs in Chapter 4.1.1 on page 48. Additionally, a third mode $\mathbf{m_a}$ was identified in the spectrum of the MSs, but not in the samples synthesized at 200 °C ($\mathbf{m_a}$: $\tilde{\nu} \approx 3550$-$3400\,\mathrm{cm^{-1}}$). Again, $\mathbf{m_a}$ was already observed for the MS in Chapter 4.1.1 and was attributed to H-bonding between crystal water, carboxylate and/or carboxylic acids in the solid crystal.[10,188] Therefore, it was assumed that the synthesis of MS(MA-PDA) and MS(MA-Bz) was successful. The presence of $\mathbf{m_b}$ and $\mathbf{m_c}$ in samples synthesized at 200 °C could indicate residual MS in the polymers. However, the exact same modes are also indicative of the proposed ammonium H-bonding motifs between PI-backbones (see Figure 41A).

(iii) Samples obtained at $T_R = 200$ °C (Figure 42, blue curves) furthermore showed five characteristic amide modes[205] ($\mathbf{a_a}$: $\tilde{\nu}$(amide A/B) $\approx$ 33485-3365 $\mathrm{cm^{-1}}$); $\mathbf{a_b}$: $\tilde{\nu}$(N-H)) ≈ 3075-$3065\,\mathrm{cm^{-1}}$; and in the zooms: $\mathbf{a_c}$: $\tilde{\nu}$(C=O, Amide I) $\approx 1690\,\mathrm{cm^{-1}}$ $\mathbf{a_e}$: $\tilde{\nu}$(C-N/N-H, Amide II) ≈ 1595-$1590\,\mathrm{cm^{-1}}$); $\mathbf{a_d}$: $\tilde{\nu}$(C-N/N-H, Amide III) ≈ 1355-$1350\,\mathrm{cm^{-1}}$. All of them were very weak, except $\mathbf{a_e}$ ($1615\,\mathrm{cm^{-1}}$). The amide modes nicely corroborate the hypothesis of a linear PI-backbone decorated with aryl-ammonium side-chains via amide linkers as described in Figure 41A.

(iv) Carboxylic acid C=O mode ($\mathbf{c_a}$ $\tilde{\nu}$(O=C-OH^-, as.) ≈ 1705-$1685\,\mathrm{cm^{-1}}$) and carboxylate C=O modes ($\mathbf{c_b}$ $\tilde{\nu}$(O=C-O^-, as.) $\approx 1610\,\mathrm{cm^{-1}}$ and $\mathbf{c_c}$ $\tilde{\nu}$(O=C-O^-, s.) ≈ 1565-$1560\,\mathrm{cm^{-1}}$) are well pronounced in the MSs' spectra (cf. zooms in Figure 42A and

B).[10] These modes stem from the carboxylate moieties of the deprotonated mellitic acid. Similar but slightly shifted modes ($\mathbf{c_b}$' $\tilde{\nu}$(O=C-O$^-$, as.) ≈ 1620-1615 cm^{-1} and $\mathbf{c_c}$' $\tilde{\nu}$(O=C-O$^-$, s.) ≈ 1570-1565 cm^{-1}) appear as shoulders in the spectra of the PI-HOFs, while $\mathbf{c_a}$ is completely missing. According to the above stated HOF hypothesis, the $\mathbf{c_b}$ and $\mathbf{c_c}$ shoulders found in the PI-HOFs' spectra were attributed to the carboxylate side-groups on the PI-backbone. However, as $\mathbf{c_b}$/$\mathbf{c_c}$ and $\mathbf{c_b}$'/$\mathbf{c_c}$' partly coincide, the attributions cannot be made with certainty.

(v) The samples synthesized at 250 °C (red curves; Figure 42) and the two linear reference PIs (PPPI ref. and PBPI ref., top curves in Figure 42) do not show Ar-NH_3^+ modes, nor carboxylate modes, nor amide modes. In fact, the spectra of the samples obtained at 250 °C and their corresponding references are almost identical. This led to the assumption that the samples synthesized at 250 °C are chemically identical to the linear PIs synthesized as references and are therefore referred to as PPPI and PBPI, respectively, from now on.

(vi) Modes corresponding to the monomers (MA, PDA, Bz) were not found in any of the products (modes stemming from carboxylic acid dimers **d**: $\tilde{\nu}$ = 3250-2755 cm^{-1} and primary amine (-NH_2) modes **p**: $\tilde{\nu}$(N-H) = 3500-3300 cm^{-1}). Therefore, the presence of unreacted monomers was excluded for all samples.

(vii) The MA-Bz sample (aka PBPI) synthesized at T_R = 250 °C additionally featured $\tilde{\nu}$(Si-O-Si) ≈ 1120 and 1095 cm^{-1} (Figure 42B mode $\mathbf{s_b}$), arising from partial dissolution of the glass liner of the autoclave and subsequent SiO_2 precipitation at high T_R and long t_R.[182]

In summary, the ATR-FT-IR spectroscopy results corroborated the hypothesis of hydrothermal PI formation between MA and PDA and Bz, respectively, and the additional presence of amide, ammonium, and carboxylate functions, when the products were generated at 200 °C. The presence of amide modes clearly speaks for the above proposed hypothesis that linear PI-chains are decorated with side-chains via amide bonds. The ammonium and carboxylate functions can either be attributed to residual MS or to the H-bonding motifs between a linear PI-backbone as suggested in Figure 41A. When using 250 °C, spectra identical to the linear references PPPI ref. and PBPI ref. were found. In order to find out if the aryl-ammonium modes are in fact involved in H-bonding between the proposed

PI-backbones, further analyses were performed.

Powder X-Ray Diffraction Analysis

PXRD measurements of all samples and reference compounds (Figure 43) clearly evinced that all products were crystalline, and that depending on T_R, different diffraction patterns were obtained for both systems.

In Figure 43A, PXRD results for the system MA-PDA are depicted. At $T_R = 200\,°C$ (PI-HOF(MA-PDA), blue curve in Figure 43A), PXRD measurements showed a distinct pattern, which neither fit any of the monomers, nor the MS. Therefore, it could be excluded that the aryl-ammonium- and carboxylate modes found via ATR-FT-IR spectroscopy stem from residual monomer salt or the monomers themselves. The reflections were numbered using Greek letters from α to ι: $\alpha = 8.56\,°(2\theta,\ \text{Cu-K}_\alpha)$, $\beta = 15.4\,°(2\theta,\ \text{Cu-K}_\alpha)$, $\gamma = 19.2\,°(2\theta,\ \text{Cu-K}_\alpha)$, $\delta = 19.7\,°(2\theta,\ \text{Cu-K}_\alpha)$, $\epsilon = 23.2\,°(2\theta,\ \text{Cu-K}_\alpha)$, $\zeta = 26.9\,°(2\theta,\ \text{Cu-K}_\alpha)$, $\eta = 27.6\ °(2\theta,\ \text{Cu-K}_\alpha)$, and $\iota = 29.6\,°(2\theta,\ \text{Cu-K}_\alpha)$. The reflections did not fit the corresponding (and initially aimed at) COF, which would show a pattern typical of hexagonal structures and with major reflections at lower angles and the ratios of the first three d-spacings would correspond to $1{:}\sqrt{3}{:}2$.[85,232]

The pattern found at $T_R = 250\,°C$ (Figure 43A, red curve) was completely different compared to the one at $T_R = 200\,°C$. Strikingly, it exhibited exactly the same reflections as reported by Baumgartner et al. in their study on the HTP of the linear PPPI (cf. gray highlights in 43A).[10] Using this work as reference (PPPI ref.), indexing was performed and MA-PDA at $T_R = 250\,°C$ (supported by the findings via ATR-FT-IR spectroscopy) could be identified as linear PPPI exhibiting the following (hkl) reflections: $(001) = 7.3\,°(2\theta,\ \text{Cu-K}_\alpha)$, $(002) := 14.4\,°(2\theta,\ \text{Cu-K}_\alpha)$, $(110) := 19.7\,°(2\theta,\ \text{Cu-K}_\alpha)$, $(003) = 21.5\,°(2\theta,\ \text{Cu-K}_\alpha)$, $(120) = 27.1\,°(2\theta,\ \text{Cu-K}_\alpha)$, $(121) = 28.1\,°(2\theta)$, $(004) = 29.1\,°(2\theta,\ \text{Cu-K}_\alpha)$, $(122) = 30.8\,°(2\theta,\ \text{Cu-K}_\alpha)$, and $(202) = 36.5\,°(2\theta,\ \text{Cu-K}_\alpha)$.

In Figure 43B, PXRD results for the MA-Bz system are depicted. This system behaved analogously to MA-PDA: At $T_R = 200\,°C$ (PI-HOF(MA-Bz), blue curve in Figure 43B), MA-Bz exhibited a completely different PXRD pattern was observed than for MS(MA-Bz) and the corresponding monomers. The observed reflections were again numbered with Greek letters from α_1 to ι_1 in 43B: $\alpha_1 = 6.0\,°(2\theta,\ \text{Cu-K}_\alpha)$,

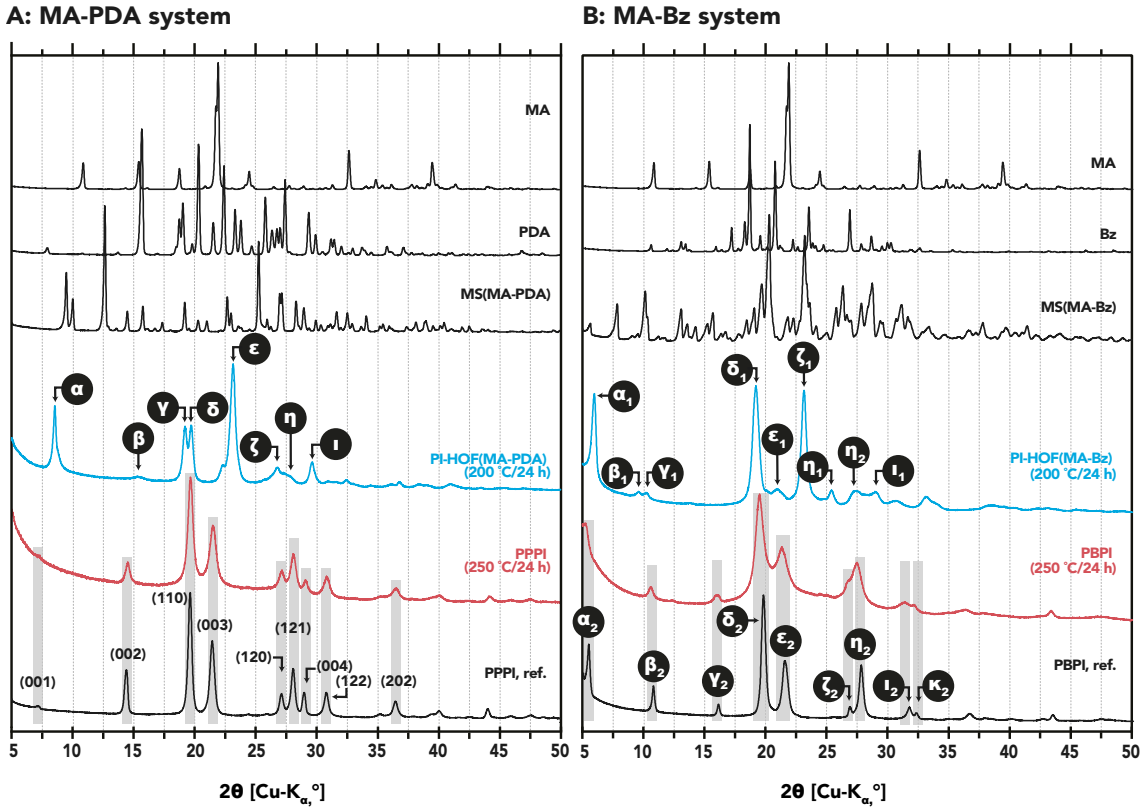

Figure 43: PXRD patterns of PI-HOF(MA-PDA) and PI-HOF(MA-Bz) (200 °C/24 h), their linear counterparts PPPI and PBPI (250 °C/24 h), the reference linear PIs, and the corresponding MS, as well as the used monomers (MA, PDA, Bz).

$\beta_1 = 9.7\,^\circ\,(2\theta,\ \text{Cu-K}_\alpha)$, $\gamma_1 = 10.3\,^\circ\,(2\theta,\ \text{Cu-K}_\alpha)$, $\delta_1 = 19.2\,^\circ\,(2\theta,\ \text{Cu-K}_\alpha)$, $\epsilon_1 = 20.9\,^\circ\,(2\theta,\ \text{Cu-K}_\alpha)$, $\zeta_1 = 23.2\,^\circ\,(2\theta,\ \text{Cu-K}_\alpha)$, $\eta_1 = 25.5\,^\circ\,(2\theta,\ \text{Cu-K}_\alpha)$, $\eta_2 = 27.4\,^\circ\,(2\theta,\ \text{Cu-K}_\alpha)$, and $\iota_1 = 29.0\,^\circ\,(2\theta,\ \text{Cu-K}_\alpha)$. Consequently, as was concluded for MA-PDA, the MA-Bz system at $T_\text{R} = 200\,^\circ\text{C}$ did not include any residual MS or monomers, nor matched its reflections a typical hexagonal COF pattern.

At $T_\text{R} = 250\,^\circ\text{C}$, again a pattern completely different than that observed at 200 °C but exactly the same as for the linear PBPI ref. was observed. However, no indexing was performed due to missing literature. Therefore, the reflections were numbered with Greek letters (from α_2 to κ_2) and are highlighted in gray in Figure 43B: $\alpha_2 = 5.2\,^\circ\,(2\theta,\ \text{Cu-K}_\alpha)$, $\beta_2 = 10.6\,^\circ\,(2\theta,\ \text{Cu-K}_\alpha)$, $\gamma_2 = 16.0\,^\circ\,(2\theta,\ \text{Cu-K}_\alpha)$, $\delta_2 = 19.5\,^\circ\,(2\theta,\ \text{Cu-K}_\alpha)$, $\epsilon_2 = 21.4\,^\circ\,(2\theta,\ \text{Cu-K}_\alpha)$, $\zeta_2 = 26.8\,^\circ\,(2\theta,\ \text{Cu-K}_\alpha)$, $\eta_2 = 27.4\,^\circ\,(2\theta,\ \text{Cu-K}_\alpha)$, $\iota_2 = 31.4\,^\circ\,(2\theta)$, and $\kappa_2 = 32.2\,^\circ\,(2\theta,\ \text{Cu-K}_\alpha)$. These matching incidents combined with identical ATR-FT-IR spectra led to the identification of MA-Bz at $T_\text{R} = 250\,^\circ\text{C}$ as the linear PBPI. However, in contrast to PBPI ref., PBPI's reflections are not as nicely baseline separated which could be interpreted as amorphous background. Furthermore, as ATR-FT-IR spectroscopy showed modes

corresponding to SiO_2 (cf. Figure 42B; $\mathbf{s_b}$: $\tilde{\nu}$(Si-O-Si) $\approx$ 1120 and 1095 cm^{-1}), it is conceivable that the amorphous background in the PXRD pattern stems from dissolved silica during HTP.

In short, PXRD measurements evinced that both systems, MA-PDA and MA-Bz, exhibit the PXRD patterns of their linear references PPPI and PBPI, respectively, when reacted at $T_R = 250\,°C$. However, when reacted at $T_R = 200\,°C$, PXRD measurements showed that crystalline structures were obtained, which were neither MS, monomers, nor COFs. The found patterns could be, in accordance with ATR-FT-IR spectroscopy, the reflections of PI-HOF structures. Therefore, MA-PDA and MA-Bz samples at $T_R = 200\,°C$ were termed PI-HOF(MA-PDA) and PI-HOF(MA-Bz), respectively. To gain further information from a different perspective, ^{13}C-CPMAS solid-state NMR spectroscopy was performed and the results are discussed next.

^{13}C Cross Polarization Magic Angle Spinning NMR Spectroscopy

^{13}C-CPMAS solid-state NMR analysis is shown in Figure 44, signal assignment was performed in accordance with literature.[224,235,236] The PI-HOFs featured signals at $\sim$170 ppm, which were assigned to amide and carboxylate carbons of the pendant side groups (PI-HOF(MA-PDA), Figure 44A: 171.3 ppm, 169.6 ppm, 167.8 ppm; PI-HOF(MA-Bz), Figure 44B: 169.4 ppm). While PI-HOF(MA-PDA) featured three signals in this region, PI-HOF(MA-Bz) only exhibited one signal. This was interpreted as a strong indication that the PI-HOFs were already decarboxylated to some degree, with PI-HOF(MA-Bz) having more of these defects of already cleaved side-groups. These amide/carboxylate signals were absent in PPPI and very small for PBPI which both had well-pronounced C_{Ar}-H^1 signals (signal A; Figure 44A and B) instead (PPPI: 115.6 ppm; PBPI: 115.5 ppm).

The fact that PBPI still featured a small peak at 169.4 ppm points at the structure not being completely decarboxylated/deaminated but still bearing residual side-chains. That these side-chains were neither detected via ATR-FT-IR spectroscopy and PXRD measurements leads to the conclusion that their abundance is rather low and therefore under the detection limit of the used characterization techniques. Imide carbonyl carbon atom signals were present in all samples at $\sim$164 ppm

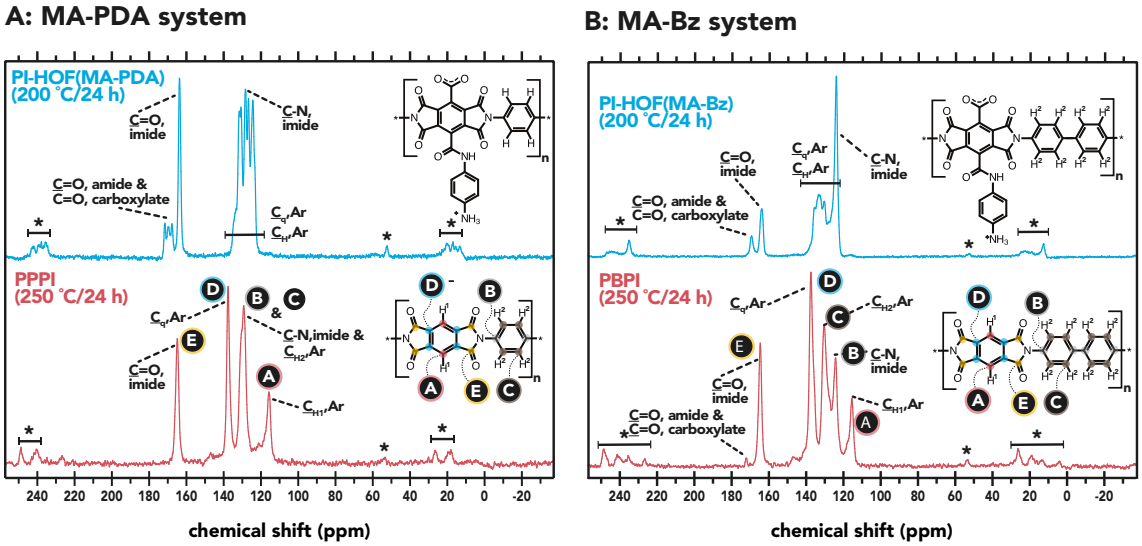

Figure 44: ^{13}C CPMAS NMR spectra of the products in blue (200/24 h) and in red (250 °C/24 h). A: MA-PDA system, and B: MA-Bz system.

(PI-HOF(MA-PDA): 163.6 ppm; PI-HOF(MA-Bz): 163.8 ppm; PPPI: 164.8 ppm; PBPI: 164.7 ppm). The remaining peaks were overall attributed to all remaining carbon atoms (cf. Figure 44). Notably, the PI-HOFs' aromatic carbon signals were found in the typical region (∼120-135 ppm) and overlapped to complex multiplets (PI-HOF(MA-PDA): 120.3-137.2 ppm; PI-HOF(MA-Bz): 120.9-141.7 ppm).

Organic Elemental Microanalysis

EA was performed on vacuum dried samples of PI-HOF(MA-PDA)/PI-HOF(MA-Bz), PPPI/PBPI and their references. The compositions determined via EA could not be matched with the postulated repeating units of the HOFs nor the linear PIs considering the uncertainty of the EA method of ±0.3 *wt.*% (see Table 2 for exact values and Figure 45 for a bar chart representation).

In Figure 45A and B, the theoretical *wt.*% values (light blue bars) and the EA results (blue bars) of PI-HOF(MA-PDA) and PI-HOF(MA-Bz) (at 200 °C/24 h), are illustrated using bar charts. Although the overall composition of the PI-HOFs roughly fit the theoretical composition, deviations up to 3 *wt.* % for carbon and ∼2.5 *wt.* % for oxygen were observed. A possible explanation would be a berthollide-type (non-stoichiometric) character of the materials, where side-chains are not present in stoichiometric amounts. It is conceivable that such defects in the crystal lattice are caused by decarboxylation/deamination during the HTP process, yet are not detected via ATR-FT-IR spectroscopy or PXRD measurements. However, ^{13}C-

CPMAS solid-state NMR spectroscopy of PI-HOF(MA-Bz) did show missing peaks in the region of C=O amide/carboxylate, corroborating the hypothesis of possible defects in the structure.

Furthermore, the C:O ratios (see Table 2) were found to be smaller for both PI-HOFs compared to their calculated values. Polar polymer networks such as PI-HOF(MA-PDA) and PI-HOF(MA-Bz) provide highly active and structured pores. Small molecules like water can be attached by hydrogen bonds or dipole interaction and are not completely removed by vacuum drying, which would explain the elevated oxygen content.

Table 2: Elemental analysis results of PI-HOF(MA-PDA), PI-HOF(MA-Bz), PPPI, PBPI, and their references compared to the calculated weight percentages of their postulated structures.

	wt. % C	*wt.* % H	*wt.* % N	*wt.* % O	C:N	C:O
PI-HOF(MA-PDA)$_{calc.}$	61.54	2.58	11.96	23.91	6.00	3.43
PI-HOF(MA-PDA)	58.30	2.92	10.99	26.66	6.19	2.91
PPPI$_{calc.}$	66.21	2.08	9.65	22.05	8.00	4.00
PPPI	59.36	2.56	9.62	20.53	7.20	3.85
PPPI ref.	63.61	2.55	9.72	23.12	7.64	3.67
PI-HOF(MA-Bz)$_{calc.}$	69.68	3.25	9.03	18.05	9.00	5.14
PI-HOF(MA-Bz)	66.89	3.32	8.40	20.24	8.94	4.40
PBPI$_{calc.}$	72.13	2.75	7.65	17.48	11.00	5.50
PBPI	52.68	2.71	6.07	23.18	10.13	3.03
PBPI ref.	70.74	3.23	8.03	17.74	10.14	5.29

In Figure 45C and D, the theoretical *wt.*% values (light red bars) and the EA results of PPPI ref./PBPI ref. (gray bars) and PPPI/PBPI (red bars) (at 200 °C/24 h) are depicted. Black error bars at calculated bars indicate the tolerance interval of ± 0.3 *wt.*%.

For PPPI a similar behavior as for PI-HOF(MA-PDA) was observed: overall the compositions of PPPI is close to the theoretical values, however the carbon content deviates quite drastically (∼ 6 *wt.* %). Furthermore, C:N values are lower than expected pointing at residual amide side-chains.

PBPI largely deviates from the theoretical values ($\Delta_C = 19.45$ *wt.* %, $\Delta_N = 1.58$ *wt.* %, and $\Delta_O = 5.71$ *wt.* %). Furthermore, PBPI's C:O ratio differs the most compared to theoretical values among all samples (3.03 experimental vs. 5.50 calculated; see Table 2). This supports what was found in ^{13}C-CPMAS solid-state NMR spectroscopy:

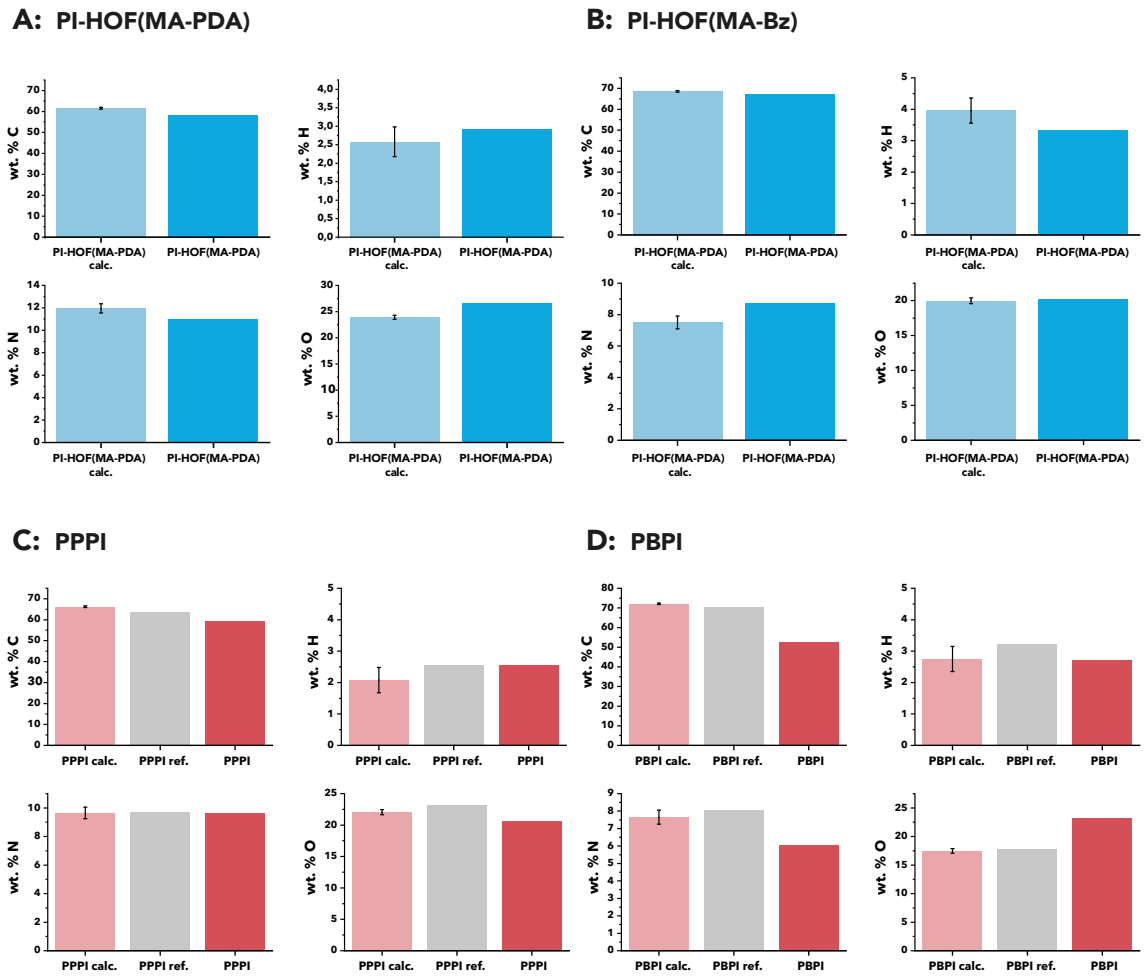

Figure 45: Bar charts of EA results itemized in *wt.*% C, *wt.*% H, *wt.*% N, and *wt.*% O. A: PI-HOF(MA-PDA) calc. (light blue) compared with MA-PDA at 200 °C/24 h (blue). B: PI-HOF(MA-Bz)$_{calc.}$ (light blue) compared to MA-Bz 24 h/200 °C (blue). C: PPPI calc. (light red) compared to PPPI ref. (gray) and MA-PDA at 250 °C/24 h (red). D: PBPI$_{calc.}$ (light red) compared to PBPI ref. (gray) and MA-Bz at 250 °C/ 24 h (red). Black error bars at calculated bars indicate the tolerance interval of ± 0.3 *wt.*%.

The decarboxylation/deamination during the HTP process was not complete, leaving residual side chains attached to the linear PBPI backbone.

Notably, also the for reference synthesized linear PPPI ref. and PBPI ref. deviated from their calculated compositions. Again, this could be caused by physisorbed water within the polymer. Another reason would be that the linear PIs also bear defects in the bulk. For example, the amorphous share of PPPI ref. and PBPI ref. (which naturally was not detected via PXRD) could be largely non stoichiometric leading to ill-fitting EA results.

Scanning Electron Microscopy

In Figure 46, SEM images of the MSs (MS(MA-PDA)$_{H_2O}$, MS(MA-PDA)$_{THF}$ and

$MS(MA\text{-}Bz)_{THF}$), PI-HOF(MA-PDA)/PI-HOF(MA-Bz) (200 °C/24 h), PPPI/PBPI (250 °C/24 h) and their reference compounds (PPPI ref./PBPI ref.) are shown.

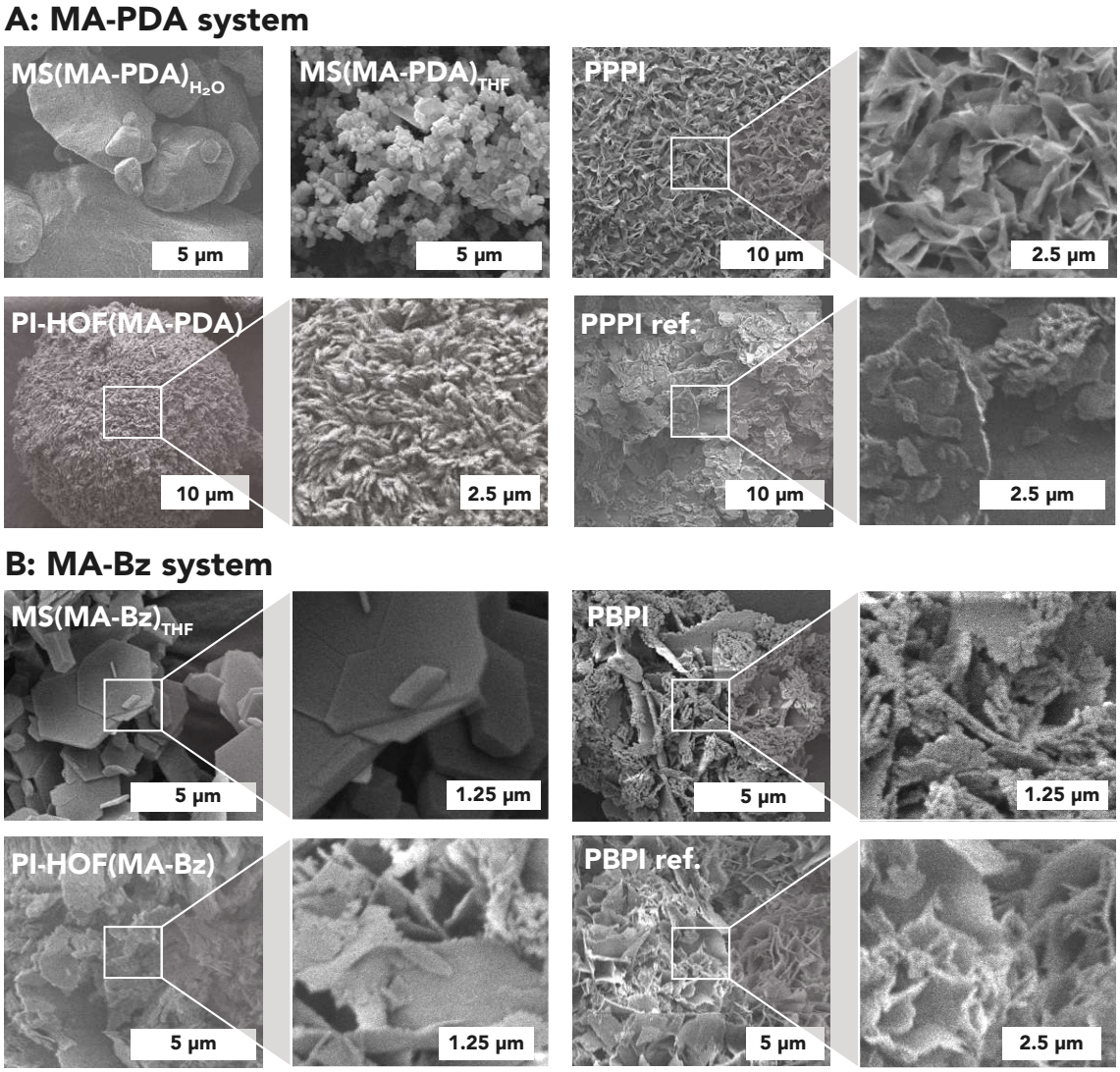

Figure 46: SEM imaging. A: MA-PDA system: $MS(MA\text{-}PDA)_{H_2O}$ and $MS(MA\text{-}PDA)_{THF}$, PI-HOF(MA-PDA) (200 °C/24 h), PPPI (250 °C/24 h), and PPPI ref.. B: MA-Bz system: $MS(MA\text{-}Bz)_{THF}$, PI-HOF(MA-Bz) (200 °C/24 h), PBPI (250 °C/24 h), and PBPI ref..

In Figure 46A, the MA-PDA system is depicted. MS(MA-PDA) synthesized in H_2O exhibited large, angular particles ($\sim$2-10 μm) with a smooth surface and rounded edges. In contrast, $MS(MA\text{-}PDA)_{THF}$ showed much smaller, cuboid particles, with lateral extension $< 1\,\mu$m. The morphologies found for PI-HOF(MA-PDA) and PPPI turned out to be quite different to both $MS(MA\text{-}PDA)_{H_2O}$ and $MS(MA\text{-}PDA)_{THF}$: PI-HOF(MA-PDA) formed stunning spherical particles of approximately 20 μm in diameter, which seemed to be hierarchically structured and composed of nanoscopic,

angular particles. PPPI and PPPI ref. were rather composed of sheet-like particles decorated with flower-like morphologies.

In Figure 46B, the MA-Bz system is depicted. $MS(MA\text{-}Bz)_{THF}$ formed sharp, angular platelets which partly exhibited hexagonal shapes with diameters ranging from 1-3 μm. Contrarily, PI-HOF(MA-Bz), as well as PBPI obtained at 250°C and the reference PI showed angular and flower-like morphologies.

Low Pressure Gas Sorption Analysis

To investigate the porosity of the PI-HOFs, CO_2 sorption experiments were performed (see Figure A6). Both PI-HOF(MA-PDA) and PI-HOF(MA-Bz) showed no porosity ($SA_{BET} < 40\,m^2g^{-1}$). This could be due to multiply interpenetrated frameworks or even the collapse of pores upon solvent removal. In general, it is considered quite challenging to induce permanent porosity in HOF materials (see Chapter 2.2.2.2).

Solid-State Heat Treatment

The above described solid-state characterization techniques pointed at the transformation of crystalline PI-HOF structures to linear and crystalline PPPI and PBPI. However, it was not clear how the transformation took place in HTW and if the products' high crystallinity, of both PI-HOFs and linear PIs, is indeed caused by their reversibility in HTW. A possible alternative reaction pathway to imide reopening and reforming (cf. error checking via reversibility) in solution is a transformation in the solid-state during HT conditions, i.e., when solubility is too low. That such a pathway is conceivable was discussed by Unterlass et al. in 2011. In this mechanistic study of HTP of aromatic PI, two possible reaction pathways are described: (i) in solution polymerization and (ii) a topochemical transformation[c] in the solid-state.[193]

Furthermore, recent studies showed that monomer salt crystals were successfully polymerized in the solid-state yielding PIs.[194,216] Consequently, a transformation of PI-HOF to PPPI/PBPI in the solid-state was also conceivable.

[c] "A transition in which the crystal lattice of the product phase shows one or more crystallographically equivalent, orientational relationships to the crystal lattice of the parent phase."[237] The exact mechanism is still subject of research and debate in the community.

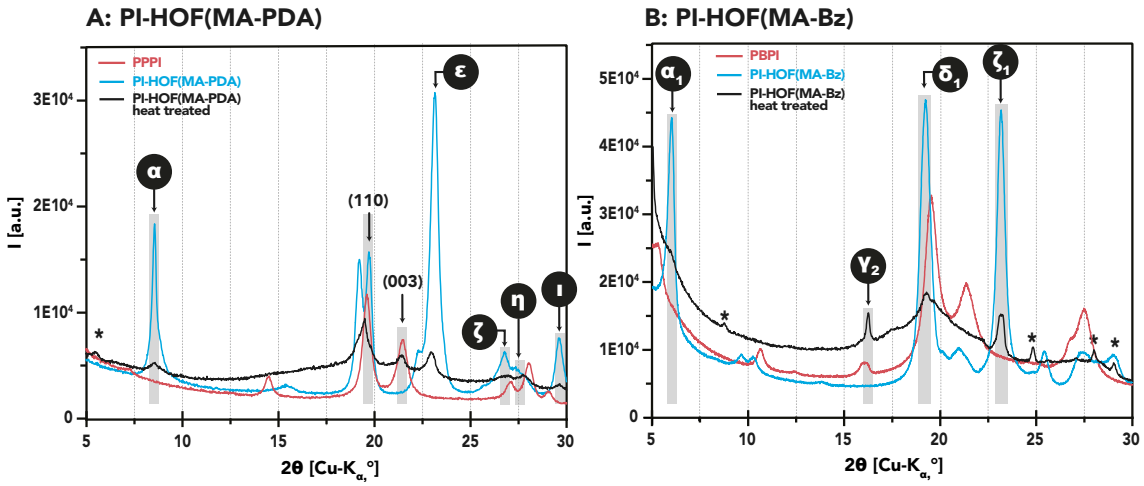

Figure 47: PXRD patterns of heat treated PI-HOFs. A: Diffractograms of PI-HOF(MA-PDA) after heat treatment at 350 °C (black), PI-HOF(MA-PDA) pristine (blue), and PPPI (red). The heat treated sample exhibits a broad amorphous halo with reflections of both PI-HOF(MA-PDA) (α, ϵ, ζ, η, and ι) and PPPI ((110) and (003)). B: Diffractograms of PI-HOF(MA-Bz) after heat treatment at 350 °C (black), PI-HOF(MA-Bz) pristine (blue), and PBPI (red). The heat treated sample exhibits a broad amorphous halo with reflections of both PI-HOF(MA-Bz) (α_2, δ_2, and ζ_2) and PBPI (γ_1). Reflections marked with asterisks do not match any reflections found for PI-HOFs, nor their linear counterparts.

To test this hypothesis, PI-HOF(MA-PDA) and PI-HOF(MA-Bz) were subjected to a heating experiment in the solid state. After keeping both at 350°C under N_2 for 15 min, largely amorphous solids were obtained (cf. 47). In Figure 47A, the diffraction pattern of PI-HOF(MA-PDA) after heat treatment is depicted in addition to the diffractograms of PI-HOF(MA-PDA) and PPPI. The heat treated sample features a broad amorphous halo on top of which a few broad reflections are situated. These reflections partly overlap with PI-HOF(MA-PDA) reflections (8.6° (2θ, Cu-K$_\alpha$) ≙ α, 22.9° (2θ, Cu-K$_\alpha$) ≙ ϵ, 26.9° (2θ, Cu-K$_\alpha$) ≙ ζ, 27.8° (2θ, Cu-K$_\alpha$) ≙ η, and 29.6° (2θ, Cu-K$_\alpha$) ≙ ι) and in part with PPPI reflections (19.5° (2θ, Cu-K$_\alpha$) ≙ (110) and 21.4° ≙ (003) (2θ, Cu-K$_\alpha$)).

In Figure 47B, PI-HOF(MA-Bz)'s diffractogram after heat treatment is displayed together with PI-HOF(MA-Bz) and PPPI for comparison. As for the MA-PDA system, the pattern is mainly characterized through a broad amorphous halo, which features several broad reflections on top. These correspond mostly to either reflections of PI-HOF(MA-Bz) (notably 5.9° (2θ, Cu-K$_\alpha$) ≙ α_1, 19.3° (2θ, Cu-K$_\alpha$) ≙ δ_1, 23.2° (2θ, Cu-K$_\alpha$) ≙ ζ_1 (2θ, Cu-K$_\alpha$)) or PBPI (16.2° (2θ, Cu-K$_\alpha$) ≙ γ_2). There are several low-intensity reflections at 8.7° and above ∼24°(2θ, Cu-K$_\alpha$), which neither matched PI-HOF(MA-Bz) nor PBPI (marked with asterisks).

As mainly amorphous products were obtained, it was concluded that the side-group cleavage from PI-HOFs to crystalline PPPI/PBPI was not a solid-state transformation, but indeed required HT conditions for the formation of crystalline linear PIs from the PI-HOFs. Since HTW must allow for error-correcting the side-group free PIs, it was inferred that error-correction also enabled the PI-HOF crystallization in the first place.

To gain further insights in the T_R dependent results of the HTP of MA with PDA/Bz, a thorough thermal analysis was performed. Therefore, standard TGA was carried out first, followed by a set-up termed inert thermal treatment coupled to mass spectrometry (ITT-MS) which is discussed in the next section.

4.3.3 Thermal Analysis

First, TGA was performed to determine at which temperatures the systems showed mass losses (T_{ML}) in the solid state. All samples (except PI-HOF(MA-Bz)) depicted an inital mass loss until 100 °C, which was attributed to physisorbed water leaving the material upon heating (gray areas in Figure 48A and B, similar to what was found for PI(TAPB-PMA) in Chapter 4.1). As visible in Figure 48, for both products synthesized at 200 °C, i.e., PI-HOF(MA-PDA) and PI-HOF(MA-Bz), a two-step signature was found (PI-HOF(MA-PDA):$T_{ML1} \approx 342$ °C, $T_{ML2} \approx 589$ °C; PI-HOF(MA-Bz): $T_{ML1} \approx 325$ °C, $T_{ML2} \approx 590$°C, as via tangents' method corresponding to EN ISO 11358). The areas for the mass losses T_{ML1} for PI-HOF(MA-PDA) and PI-HOF(MA-Bz) were determined via calculating the derivatives of the TGA curves (see Figure A7). From this, the lost weight percentages were determined to be 27.0 % and 26.8 % for PI-HOF(MA-PDA) and PI-HOF(MA-Bz), respectively. The theoretical mass losses, in respect to losing side-chains, were calculated to be 36.6 % for PI-HOF(MA-PDA) and for PI-HOF(MA-Bz) 41.0 % using the equation below. Molecular weights (MW) were taken from the respective repeating units of the polymers: $M_{HOF(MA-PDA)} = 486.76\ g\,mol^{-1}$, $M_{HOF(MA-PDA)} = 620.58\ g\,mol^{-1}$, $M_{PPPI} = 290.23\ g\,mol^{-1}$ and $M_{PBPI} = 366.33\ g\,mol^{-1}$.

$$ML1_{calc.} = \frac{M_{HOF(MA-PDA)/(MA-Bz)} - M_{PPPI/PBPI}}{M_{HOF(MA-PDA)/(MA-Bz)}} \cdot 100$$

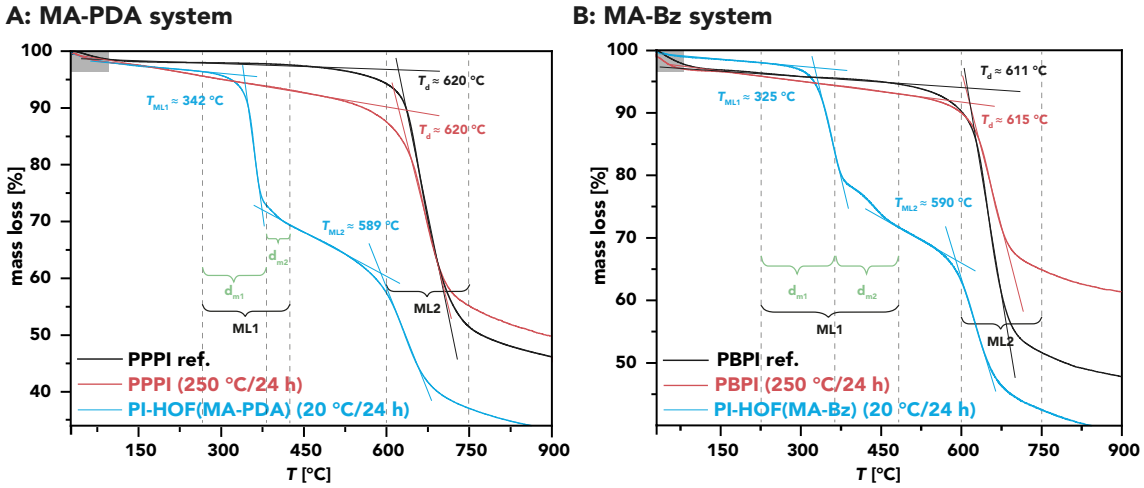

Figure 48: TGA analyses of the products and reference compounds for both systems. Gray area shows initial mass loss attributed to physisorbed water leaving the material. Tangents in corresponding colors depict T were mass losses/decomposition was observed. A: MA-PDA system; B: MA-Bz system.

Furthermore, when calculating the derivatives of the TGA curves of PI-HOF(MA-PDA) and PI-HOF(MA-Bz) it became clear that T_{ML1} in fact consisted of two separate steps (d_{m1} and d_{m2}). These mass losses (see Figure 48, in green) were compared to the percentages of the suggested side-groups leaving the structure upon heating (d_{m1} calc. = PDA or Bz, and d_{m2} calc. = $CO_2 + CO$).

The results are summarized in Table 3 and showed that both, but especially PI-HOF(MA-Bz)'s ML1 meas. deviated from their theoretical values ML1 calc. ($\Delta_{\mathrm{tot.}} = 11.0\%$ and 14.2%). When taking a closer look at the two separate steps of ML1, it turns out that PI-HOF(MA-PDA)'s d_{m1} meas. is almost identical to PI-HOF(MA-Bz)'s d_{m1} calc., but d_{m2} meas. is only about a fourth of the calculated value. PI-HOF(MA-Bz)'s d_{m1} meas. was found to be two thirds of the calculated value, whereas its d_{m2} meas. was only half of d_{m2} calc.

The overall lower *wt.* % detected than calculated point at both PI-HOF(MA-PDA) and PI-HOF(MA-Bz) (with a greater effect on PI-HOF(MA-Bz) than PI-HOF(MA-PDA)) were already partly cleaved of their side-groups during HTP. This is in line with what was discussed for ^{13}C-CPMAS solid-state NMR spectroscopy measurements and EA results.

When subjecting the products synthesized at 250 °C/24 h (PPPI and PBPI) to TGA, only a single mass loss was observed, corresponding to thermal degradation (T_{d}(MA-PDA, 250 °C) ≈ 620 °C, T_{d}(MA-Bz, 250 °C) ≈ 615 °C; Figure 48). The same T_{d}'s were obtained for both reference PIs: T_{d} (PPPI ref.) ≈ 620 °C and T_{d}

(PBPI ref.) ≈ 611 °C (Figure 48).

Table 3: Summary of the measured and calculated percentages of the respective mass loss steps during TGA analysis of PI-HOF(MA-PDA) and PI-HOF(MA-Bz).

	PI-HOF(MA-PDA)	PI-HOF(MA-Bz)
ML1 calc.	38.0%	41.0%
ML1 meas.	27.0%	26.8%
$\Delta_{tot.}$	11.0%	14.2%
d_{m1} calc.	23.1%	30.0%
d_{m1} neas.	23.8%	19.6%
Δ_{m1}	0.7%	10.4%
d_{m2} calc.	15.4%	11.6%
d_{m2} meas.	3.5%	6.4%
Δ_{m2}	11.9%	5.2%

In order to determine what happened during the mass losses of PI-HOF(MA-PDA) and PI-HOF(MA-Bz), ITT-MS measurements were performed. There, the dry powders were heated from 30-900 °C in a quartz-glass reactor under inert gas flow, and any gaseous products were conducted to a mass spectrometer (Figure 49). For PI-HOF(MA-PDA) m/z of CO_2, CO, and a small amount of H_2O were found at ∼352 °C, corresponding to T_{ML1}(PI-HOF(MA-PDA)) ≈ 340 °C from TGA. In the case of PI-HOF(MA-Bz), a similar behavior was observed, where m/z of CO_2 and CO were detected at ∼421°C (cf. T_{ML1}(PI-HOF(MA-Bz)) ≈ 326 °C from TGA), but no water was released. The diamines' (PDA and Bz, respectively) m/z were not detected in either case. Yet, after the analysis, the respective diamine (identified by ^{1}H-NMR; see Figure A11) was found in the cooling trap between the heating mantle and mass spectrometer. This is in agreement with the generally known tendency of aromatic amines to sublimate.[238] Above 600 °C, several distinct mass peaks were found to be released, which corresponded to the material's full thermal deterioration to a carbonaceous char (cf. T_{ML2}). When performing ITT-MS of PPPI and PBPI (synthesized from MA and PDA/Bz at 250 °C), the majority of gaseous products were detected at 600 °C and 728 °C with similar m/z as obtained from the second degradation step (T_{ML2}) for PI-HOF(MA-PDA)/PI-HOF(MA-Bz), which was also correlated with carbonization. PPPI additionally showed a very

small peak at ~352 °, which indicated that the material still contained residual side-groups which were not cleaved completely at $T_R = 250$ °C.

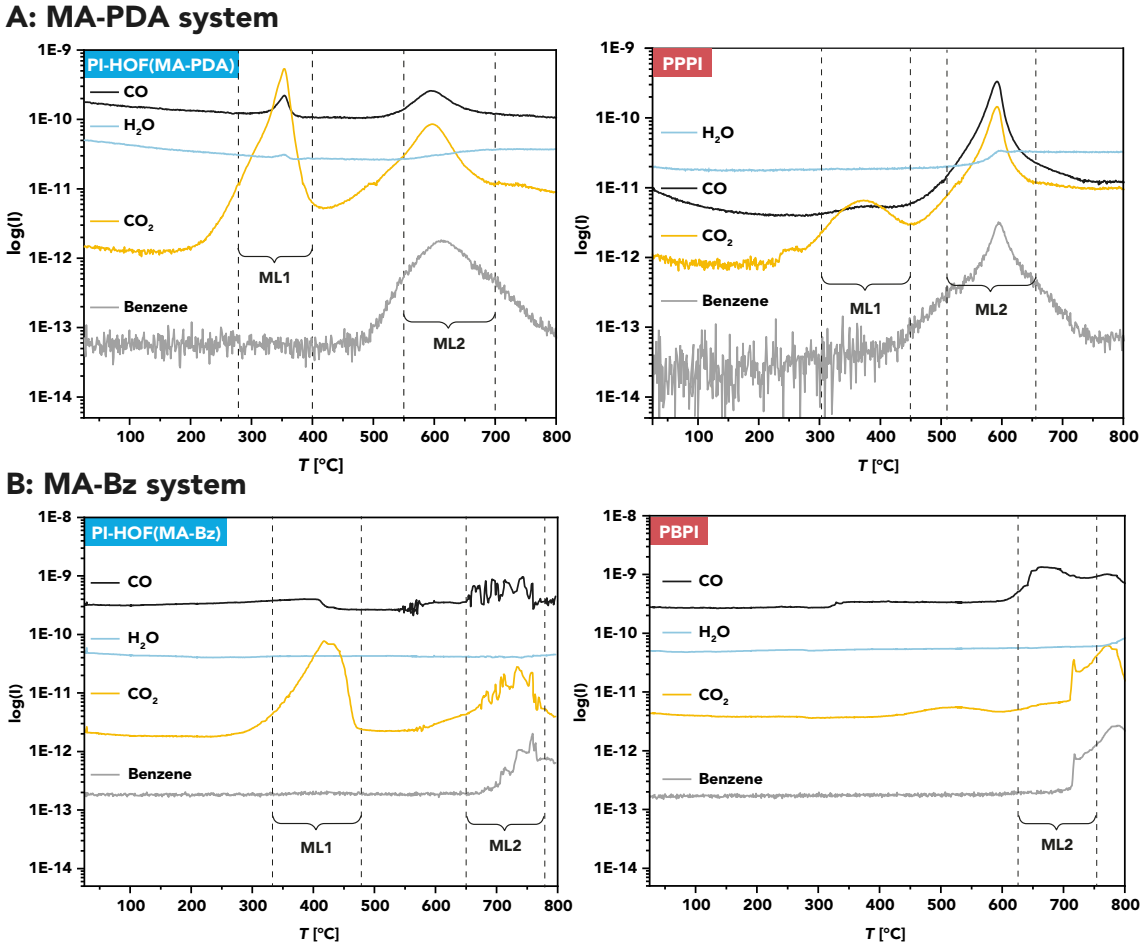

Figure 49: Inert thermal treatment coupled to mass spectrometry analyses of the products for both systems. A: MA-PDA system; B: MA-Bz system.

From these results, two conclusions are derived: (i) In a first mass loss, PI-HOF(MA-PDA) and PI-HOF(MA-Bz) were stripped off its *p*-ammoniumbenzamide and CO_2^- side-groups via decarboxylation leading to the release of CO_2, and amide cleavage leading to the release of CO and release of PDA/Bz[239] (which sublimated before reaching the MS). (ii) At the second mass loss, the materials degraded to a carbon char.

To summarize, a hypothesis is postulated that HTP generated HOFs instead of COFs for the comonomers MA with PDA or Bz, respectively. The HOFs are thought to be built up by linear PI chains, in contrast to conventional HOFs, which

are built-up by small molecules.[122,142,143,233,234] When the PI-HOFs were subjected to increased temperatures in the solid-state, their side-groups were cleaved off through decarboxylation and deamination, leading to linear, yet largely amorphous PIs. In contrast, when subjected to higher temperatures (250 °C) in HTW, the side-group cleavage occurred simultaneously with error-correction, which generated fully crystalline linear PI products.

4.3.4 Reaction Screening

To verify the thus far presented hypothesis, a more intensive t_R-screening using HTP-AC was performed. The following conditions were chosen: $t_R = 2$, 4, 6, 8, 24, 48, 72 and 168 h at $T_R = 200$ °C and $t_R = 2$, 4, 6, 8, 24, and 48 h at $T_R = 250$ °C. The products were characterized via ATR-FT-IR spectroscopy and PXRD analysis.

Attenuated Total Reflectance Fourier Transform IR Spectroscopy

ATR-FT-IR spectroscopy of these products showed a clear trend: with increasing t_R the modes in ATR-FT-IR spectra that correlate with PI-HOF(MA-PDA) and PI-HOF(Ma-Bz) gradually disappeared (see Figure 50 for $T_R = 200$ °C and 51 for $T_R = 250$ °C:

(i) 200 °C (Figure 50)

At 200 °C, all samples of both systems ($t_R = 2$, 4, 6, 8, 24, 48, 72, and 168 h; cf. Figure 50A and B) showed the before established imide modes ($\mathbf{i_a}$: $\tilde{\nu}_{as}$(C=O) ≈ 1770 cm^{-1}, $\mathbf{i_b}$: $\tilde{\nu}_s$(C=O) ≈ 1725 cm^{-1}; $\mathbf{i_c}$: $\tilde{\nu}$(C-N) ≈ 1375 cm^{-1}). Moreover, MA-PDA at 7 d featured the mode $\mathbf{s_b}$:$\tilde{\nu}$(Si-O-Si) ≈ 1120 and 1095 cm^{-1} again pointing at partial dissolution of the glass liner during HTP, which is already known to be the case for long t_R [182].

In Figure 50C and D, zooms of selected samples (MA-PDA and MA-Bz at 200 °C/2, 6 or 8, 72 h and 7 d) are depicted. The aryl-ammonium modes ($\mathbf{m_b}$: $\tilde{\nu}$(Ar-NH$_3^+$, as) ≈ 2850 cm^{-1}; $\mathbf{m_c}$($\tilde{\nu}$(Ar-NH$_3^+$, s) ≈ 2580 cm^{-1}), attributed to the PI-HOF species, were present in all cases except for MA-PDA at 168 h (= 7 d). The modes assigned to the amide moiety within the PI-HOF species (green highlights, $\mathbf{a_e}$: $\tilde{\nu}$(C(O)-NH, Amide I) ≈ 1615 cm^{-1}); $\mathbf{a_d}$: $\tilde{\nu}$(C-N/N-H, Amide III) ≈ 1355 cm^{-1}) decreased with in-

creasing t_R until at 7 d they were barely visible for MA-Bz and completely disappeared for MA-PDA. Overall, the two systems behaved in a similar fashion in terms of decreasing modes attributed to the PI-HOF species.

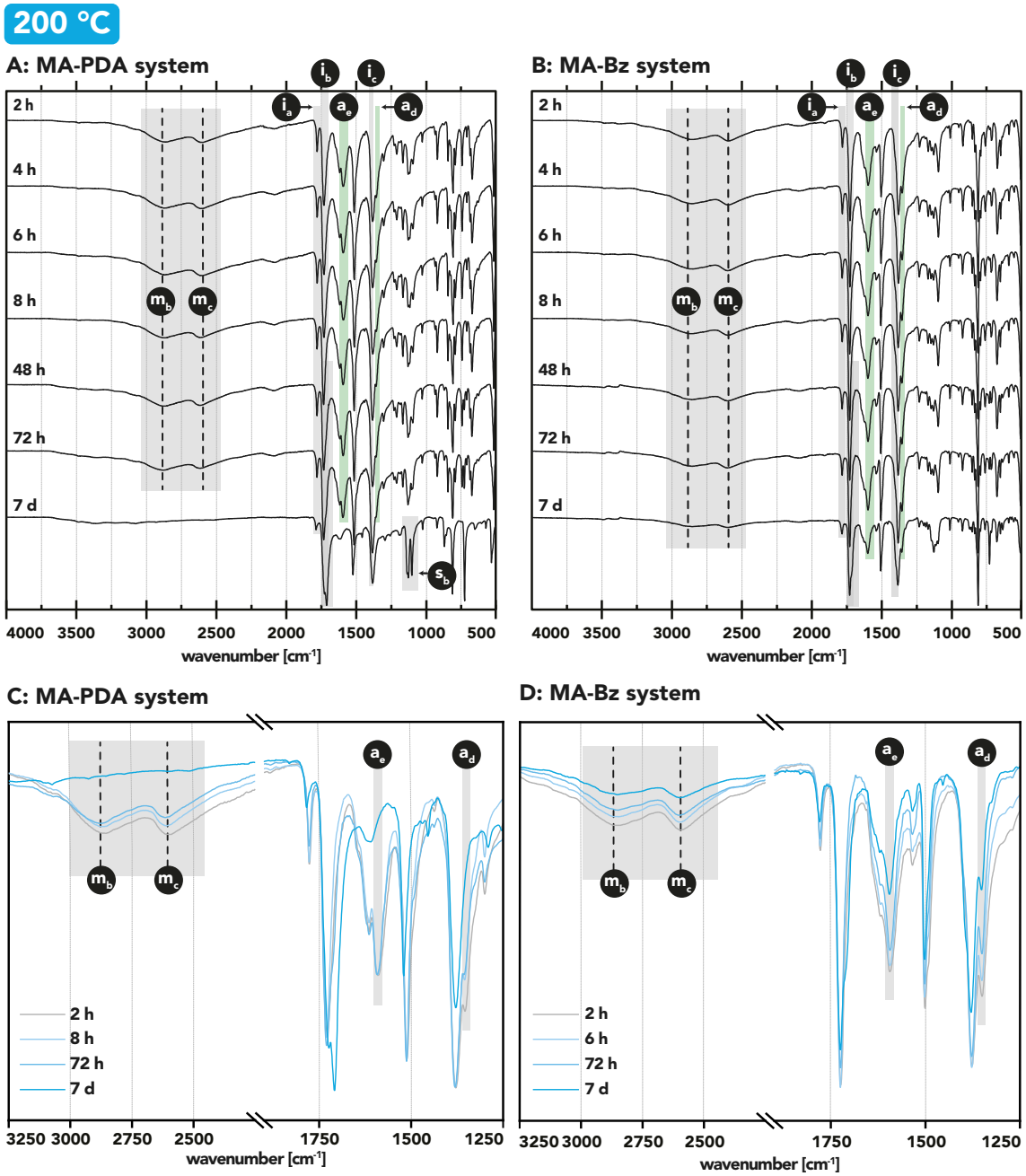

Figure 50: ATR-FT-IR spectra of the screening products at 200 °C. (A): MA-PDA system 2-168 h; (B): MA-Bz system 2-168 h; (C) zoom of MA-PDA system 2, 8, 72 h and 7 d; (D) zoom of MA-Bz system 2, 6, 72 h and 7 d.

(ii) 250 °C (Figure 51)

At 250 °C, again all of the samples displayed imide modes, however mode $\mathbf{s_b}$: $\tilde{\nu}$(Si-O-Si) already appeared at $t_R \geq 2$ h and increased steadily to a point where the imide

modes were reduced to weak shoulders (cf. Fig51A and B, especially MA-Bz/48 h). Therefore, the screening was aborted at $t_R = 48$ h for both systems.

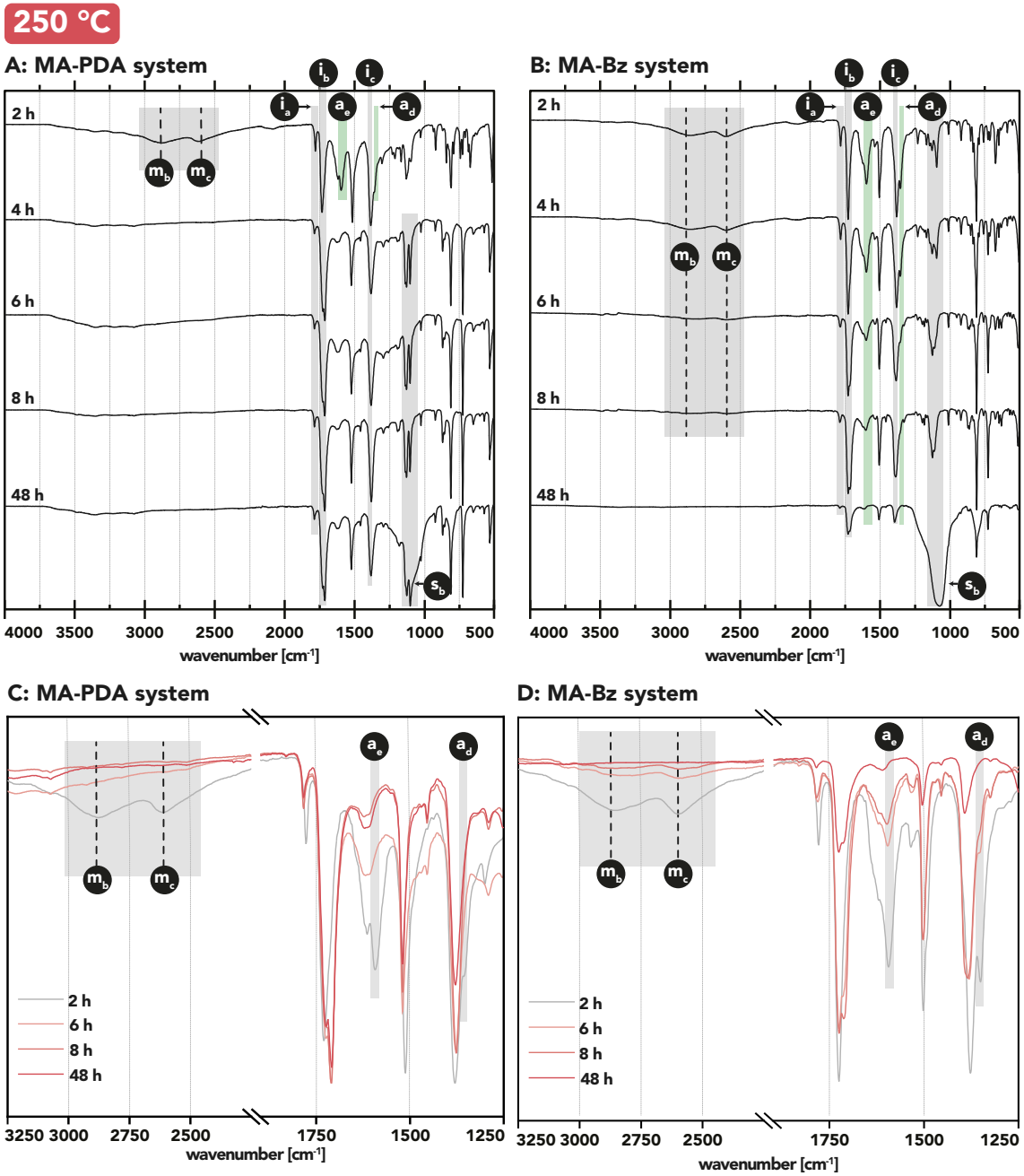

Figure 51: ATR-FT-IR spectra of the screening products at 250 °C. (A): MA-PDA system 2-48 h; (B): MA-Bz system 2-48 h; (C) zoom of MA-PDA system 2, 6, 8 and 48 h; (D) zoom of MA-Bz system 2, 6, 8 and 48 h.

In Figure 51C and D, zooms of selected samples (MA-PDA and MA-Bz at 250 °C/2, 6, 8, and 48 h) are depicted. In the case of MA-PDA, aryl-ammonium modes ($\mathbf{m_b}$ and $\mathbf{m_c}$) were only visible at $t_R = 2$ h (cf. Figure 51A and C). MA-Bz samples showed $\mathbf{m_b}$ and $\mathbf{m_c}$ modes for longer, yet gradually decreasing until barely discernible at $t_R = 8$ h (cf. Figure 51D). The same trend was true for the amide modes ($\mathbf{a_d}$ and $\mathbf{a_e}$,

green highlights): MA-PDA only showed $\mathbf{a_d}$ and $\mathbf{a_e}$ at $t_R = 2\,h$ and MA-Bz displayed a downwards trend in terms of intensity.

Summing up, both systems behaved similarly, where with increasing t_R modes corresponding to PI-HOF species decreased, however MA-Bz seemed to have a significantly slower process.

Powder X-Ray Diffraction Analysis

To check if the crystallinity of the screening products correlated with the trend observed via ATR-FT-IR spectroscopy, PXRD was carried out (see Figure 52 and Figure 54). Indeed a similar trend became apparent: Some reflections that correlated with PI-HOF(MA-PDA)/(MA-Bz) (blue highlights in Figure 52 and Figure 54) decreased, while other reflections that were characteristic for PPPI/PBPI (gray highlights in Figure 52 and Figure 54A) increased in intensity with increasing t_R:

(i) 200 °C (Figure 52)

At 200 °C, all MA-PDA samples showed the pattern assigned to PI-HOF(MA-PDA), except at 168 h (= 7 d), which displayed the exact pattern of PPPI (52A). This was in line with ATR-FT-IR results, where modes assigned to PI-HOF(MA-PDA) ($\mathbf{m_b}$, $\mathbf{m_c}$, $\mathbf{a_d}$, and $\mathbf{a_d}$) were solely absent in the spectrum of MA-PDA at 7 d. Additionally, from $t_R \geq 48\,h$ on, the PPPI reflections (002) = 14.4 °(2θ, Cu-K$_\alpha$), (003) = 21.5 °(2θ, Cu-K$_\alpha$), and (121) = 28.0 °(2θ, Cu-K$_\alpha$) (cf. Figure 52A, gray highlights) increased gradually.

In the case of MA-Bz, all samples synthesized at 200 °C featured the reflections found for PI-HOF(MA-Bz) (cf. Figure 52B). However, from $t_R \geq 48\,h$, three reflections which were assigned to PBPI increased gradually: $\alpha_2 = 5.2\,°(2\theta$, Cu-K$_\alpha)$, $\epsilon_2 = 21.4\,°(2\theta$, Cu-K$_\alpha)$, and $\eta_2 = 27.4\,°(2\theta$, Cu-K$_\alpha)$ (gray highlights, Figure 52B). Overall, the two systems behaved in a similar fashion in terms of increasing intensities of reflections attributed to PPPI/PBPI.

In order to determine if the degree of crystallinity of the samples with patterns assigned to PI-HOF(MA-PDA)/(MA-Bz) (t_R = 2-72 h) varies, the FWHM of a selected reflection ($\epsilon = 23.1\,°$ (2θ, Cu-K$_\alpha$) and $\zeta_1 = 23.2\,°$ (2θ, Cu-K$_\alpha$)) was determined. The results are summarized in Table 4 and depicted in Figure 53. The MA-PDA system (Figure 53A) shows two groups of FWHM values: t_R = 2-6 h scatter around

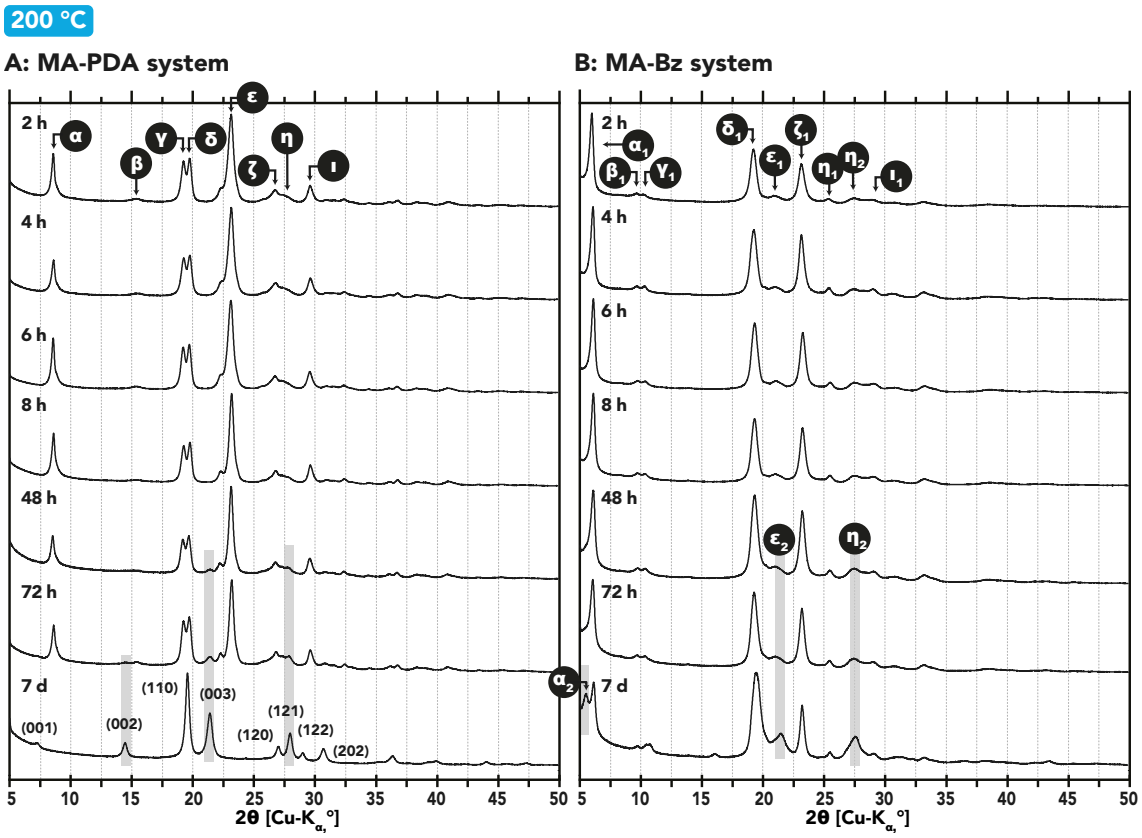

Figure 52: PXRD patterns of the screening products at 200 °C.(A): MA-PDA system, 2-168 h, (B): MA-PDA, 2-48 h.

a median of 0.56 and $t_R = 8$-72 h scatter around a median of 0.45 (see Chapter A.1.4 for calculations). In between those two groups there is a sharp downwards step in FWHM from $t_R = 6$ to $t_R = 8$ h which corresponds to an increase in sharpness of the corresponding reflection and hence a higher degree of crystallinity. After $t_R = 8$ h, no significant change in FWHM was observed.

Table 4: FWHM of the XRD patterns of PI-HOF(MA-PDA) and PI-HOF(MA-Bz) of the reflections at 23.1 °and 23.2 °(2θ, Cu-K_α), respectively.

t_R [h]	PI-HOF(MA-PDA)	PI-HOF(MA-Bz)
2	0.56	0.67
4	0.55	0.56
6	0.57	0.57
8	0.45	0.57
24	0.52	0.54
48	0.44	0.57
72	0.45	0.54

In the case of MA-Bz (Figure 53B), all FWHM values are within one group except $t_R = 2$ h, which is outside the confidence interval (with the highest FWHM value

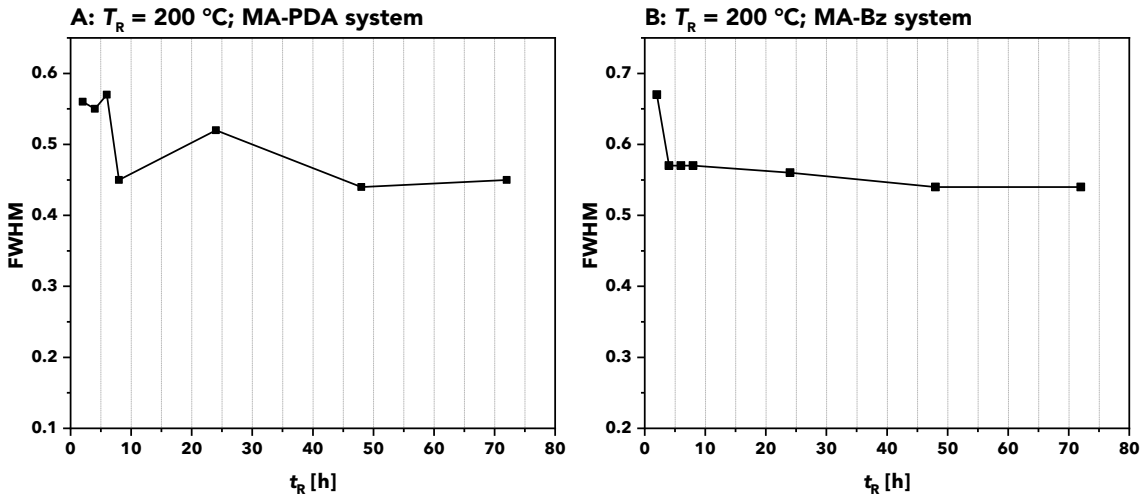

Figure 53: FWHM of a selected reflection (ϵ for MA-PDA and ζ_1 for MA-Bz) of the screening products (200 °C, 2-72 h). FWHM vs. t_R for A: MA-PDA system and B: MA-Bz system.

0.67 exceeding the upper limit 2^{*s}MAD = 0.60; see Chapter A.1.4 for calculations). Again a distinct decrease in FWHM, i.e., an increase in sharpness from $t_R = 2$ h to $t_R = 4$ h was observed. Afterwards, no significant change in FWHM was the case, which led to the assumption that the degree of crystallinity did not change after $t_R = 4$ h.

In summary, both MA-PDA and MA-Bz showed a tendency of longer reaction times leading to higher degrees of crystallinity.

(ii) 250 °C (Figure 54)

At 250 °C, PXRD results of the MA-PDA system were in line with ATR-FT-IR spectroscopy: only the lowest $t_R = 2$ h resulted in the pattern correlated with PI-HOF(MA-PDA). Moreover, small peaks of PPPI reflection (003) was already visible, pointing at the presence of a mixture of the two structures. All other samples' (t_R = 4-48 h) patterns were almost identical with PPPI.

PXRD measurements of the MA-Bz system at 250 °C also confirmed what was found via ATR-FT-IR spectroscopy. A slow transition from the PI-HOF(MA-Bz) pattern towards the PBPI pattern was observed. Specifically, reflections $\alpha_1 = 6.0$ °(2θ, Cu-K$_\alpha$), $\zeta_1 = 23.2$ °(2θ, Cu-K$_\alpha$) and $\eta_1 = 25.5$(2θ, Cu-K$_\alpha$) (blue highlights, cf. Figure 54B) corresponding to PI-HOF(MA-Bz) decreased gradually until they disappeared completely at $t_R = 48$ h.

Moreover, reflections α_2, β_2, γ_2, ϵ_2, and η_2 (corresponding to PBPI; gray highlights in Figure 54B) increased with increasing t_R. At $t_R = 48$ h, an amorphous halo

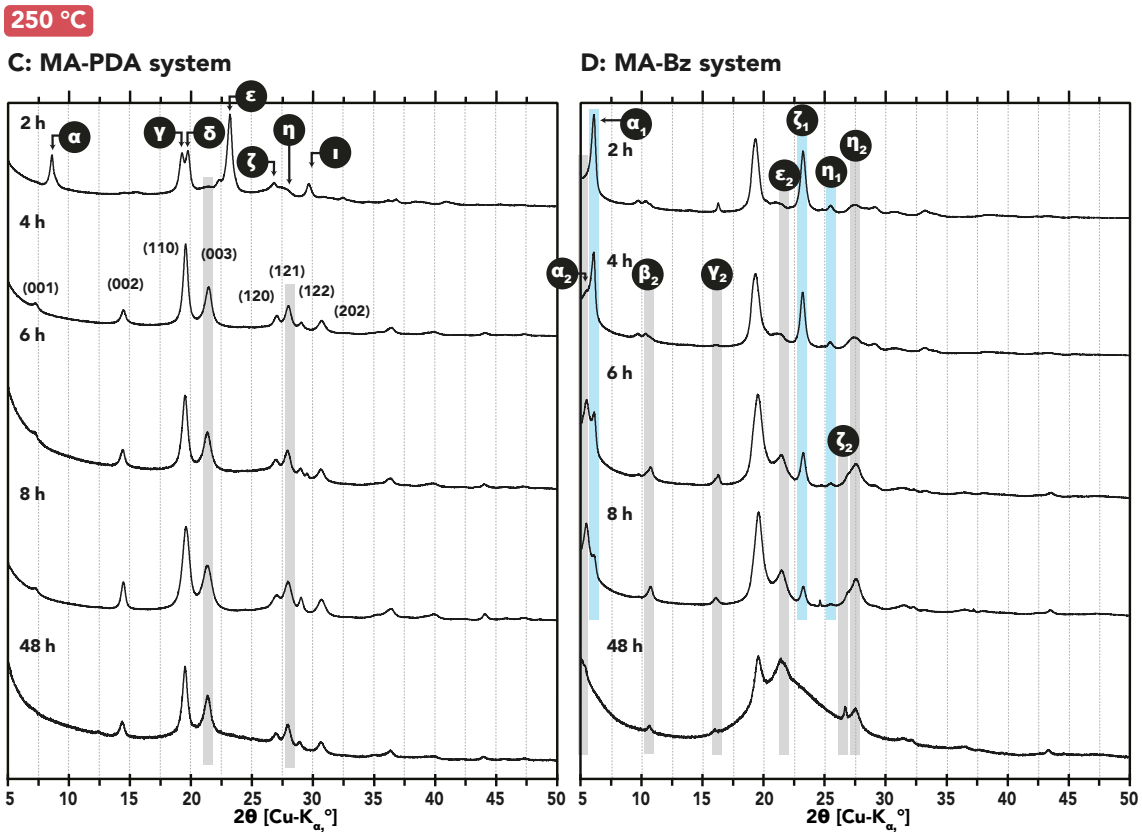

Figure 54: PXRD patterns of the screening products at 250 °C. A: MA-Bz system, 2-168 h, and B: MA-Bz system,2-48 h.

between 15 and 30 °(2θ, Cu-K_α) could be discerned, pointing at the presence of a SiO_2 species as implied by ATR-FT-IR spectroscopy.

In summary, ATR-FT-IR spectroscopy and PXRD results corroborated the previously stated hypothesis that the side-groups disappeared with increasing t_R and T_R. Consequently, PI-HOFs were gradually transformed to their linear counter parts PPPI and PBPI. As suggested by the slow decrease of modes in ATR-FT-IR spectra and reflections in PXRD, the point of conversion could not be delimited to a certain set of reaction conditions but was rather a gradual process. Therefore, it was assumed that the postulated structures (PI-HOF(MA-PDA)/(MA-Bz) and PPPI/PBPI) contained defects and could not be obtained purely, which further underpins the assumption of berthollide type materials as inferred from ^{13}C-CPMAS solid-state NMR spectroscopy, EA and ITT-MS analyses.

4.3.5 Summary and Outlook

In this chapter, it was shown that HTP is indeed capable of generating highly crystalline framework structures without the need of the addition of a modulator. However, not the expected PI-COFs were afforded from the two systems MA-PDA and MA-Bz, but two other frameworks. A hypothesis was postulated that instead HTP led to HOFs based on linear polyimide (PI) building blocks, based on preliminary results from HTP-AC at $T_R = 200$ and 250 °C at $t_R = 24$ h. The PI chains were thought to be laterally H-bonded through carboxylate and *p*-ammoniumbenzamide side-groups and that PI-HOFs crystallized through simultaneous imide formation and re-opening (error-correction) at 200°C. They featured some degree of side-group cleavage already appearing during the synthesis, i.e., the structures bearing defects that made them comparable to non-stoichiometric inorganic compounds of the berthollide type. HTP at higher T_R (i.e., 250°C) supposedly engendered cleavage of the PI-HOFs' side-groups and simultaneous error-correction of the PI backbones, leading to crystalline linear PIs (PPPI and PBPI). This hypothesis was supported by the results from various solid-state techniques: ATR-FT-IR spectroscopy and PXRD measurements clearly showed modes and reflections matching the postulated PI-HOF structures for the 200 °C samples. On the other hand, the 250 °C samples were lacking the modes of the proposed side-chains in ATR-FT-IR spectra and showed PXRD patterns matching the ones of their linear PI analogues.

Subsequently, TGA evinced that the PI-HOF samples featured two mass losses upon heating whereas PPPI and PBPI only showed one (i.e., degradation). ITT-MS identified the first mass losses to be caused by the release of CO and CO_2 gases and the sublimation of the respective aromatic amine, which together make up the *p*-ammoniumbenzamide side-groups.

Moreover, the hypothesis was supported by the results from an extensive reaction screening, where HTP-AC was carried out using 200 and 250 °C and eight t_Rs.

Finally, heating the PI-HOFs in the solid-state also cleaved the side-groups, yet generated largely amorphous PI products. This showed that the strong imide function is hydrothermally reversible, and that HTW was able to generate crystalline extended organic molecules linked by strong functions through error-correction.

Nevertheless, the HOF structures and the transformation process to the respective linear PIs were not unequivocally confirmed regardless of the many solid-state techniques carried out. To shine a brighter light on the real structures, the generation of computer simulations of the proposed structures remain subject of future investigations.

5 Conclusions and Perspectives

In the past, HTP has been proven a potent method to obtain linear, PI materials. In this work, it was shown that the power of HTW can also be employed for 3D network PIs. Pristine- as well as additive-assisted HTP methods were developed and optimized to gain access to the realm of imide-based OPNs, both amorphous and crystalline.

First, the general feasibility of generating a 3D PI network via HTP was shown. Using a pristine HTP-AC set-up employing nothing but water and the monomers (a trigonal aromatic amine TAPB and a linear carboxylic acid PMA) yielded an amorphous, highly T stable ($> 550\,^{\circ}\mathrm{C}$) and ultramicro- and macroporous PI network. In depth understanding of the network's formation was gained via isolating its MS intermediate as well as investigating its micromorphological evolution dependent on t_{R}, T_{R}, and the addition of HOAc. Furthermore, up-scaling was achieved using HTP-MW and subsequent warmpressing afforded an ultramicroporous and mechanically well performing PI-pellet. Therefore, it was shown that a fully green route from synthesis to processed PI is possible, making HTP a promising and environmentally friendly method for high performance PI materials. To make such PI networks via HTP amenable to e.g., gas sorption applications in the future, it is proposed to improve activation strategies (i.e., CO_2 activation) for achieving useful micropores in addition the ultramicro- and macropores.

Second, HTW's capability of generating crystalline PI frameworks was demonstrated. It was shown that HTW indeed possesses reversibility fostering properties for imide moieties. Therefore, a small molecule model system was investigated and its imide metathesis in HT conditions demonstrated. However, extending this to an extended structure with high molecular weight from the monomers TAPB and PMA required the addition of the basic modulator aniline. Henceforth, the aaHTP

of crystalline PI-COF exhibiting a hexagonal unit cell was possible. However, this method was limited due to the formation of an inseparable side-product mixture (PMA-An) caused by the reaction of aniline with PMA. Applying a mathematical description model on the obtained SAXS data gave valuable insights in the solid-state behavior of PMA-An itself and within the PI-COF. The results of the fitting allowed for postulating that the obtained PI-COF comprises of 2D sheets, which are dispersed between smectically arranged PMA-An layers. Consequently, no permanent porosity was obtained. A remedy for the formation of the side-products was sought after, yet neither switching to HTP-MW, nor reducing the amount of aniline, nor post-synthetical removal was successful. Using substoichiometric amounts (≤ 0.05 equiv.) of aniline in aaHTP-MW showed the most promising results. Therefore, it was suggested that increasing the t_R significantly (to $\gg 4$ h) could yield the desired PI-COF single phase. Another approach to obtain PI-COFs via HTP could be the use of a less nucleophilic modulator in order to prevent side-product formation. Furthermore, as argued by LOTSCH and co-workers, enhancing the availability of the monomers as well as oligomers to error-correction during the COF formation could be achieved via the addition of n-alkyl alcohols or the use of monomers with higher solubility.[202]

Finally, switching the system to monomers with higher water solubility allowed for the formation of crystalline PI framework without the necessity of an additive. The combination of the trigonal carboxylic acid MA with two linear amines afforded crystalline PIs using HTP-AC at $T_R = 200$ °C. However, instead of PI-COFs, it was assumed that PI-HOFs were obtained made up of linear PI backbones which are laterally H-bonded via side-groups. Their formation is proposed to proceed via reversibility and error-correction under HT conditions. When $T_R = 250$ °C was used, the side-groups are believed to be cleaved off the backbone and after further error-correction in HTW, crystalline linear PIs were obtained. As solid-state heat treatment of the PI-HOFs yielded largely amorphous products, HTW was deemed responsible for providing the prerequisites for reversibility, and hence crystallinity, in the second step. Despite the comprehensive solid-state analysis, further investigations are necessary to back the proposed hypothesis, such as structure energy optimizations and simulations of the proposed structure.

All of these findings showed that HTP is a powerful method and its potential has just been started to be unlocked. By extending HTP's scope to the first PI network, the environmentally benign method was lifted to a new level of highly functional and green materials. This leaves one optimistic that HT methods might contribute to a more sustainable but also technologically advanced future.

6 References

[1] Sustainable Development Goals. 2022; https://sdgs.un.org/goals.

[2] European Comission. 2022; https://ec.europa.eu/info/strategy/priorities-2019-2024/european-green-deal{_}en.

[3] Goodman, L. Liquid Crystal Displays. *Journal of Vacuum Science and Technology* **1973**, *10*, 804–823.

[4] Tarascon, J. M.; Armand, M. Issues and challenges facing rechargeable lithium batteries. *Nature* **2001**, *414*, 359–367.

[5] Marvel, C. S. *Macromolecular Chemistry-4*; Springer: Boston, MA, 1968; pp 351–368.

[6] Hergenrother, P. M. The use, design, synthesis, and properties of high performance/high temperature polymers: An overview. *High Performance Polymers* **2003**, *15*, 3–45.

[7] Ramgobin, A.; Fontaine, G.; Bourbigot, S. Thermal Degradation and Fire Behavior of High Performance Polymers. *Polymer Reviews* **2019**, *59*, 55–123.

[8] Dawson, R.; Cooper, A. I.; Adams, D. J. Nanoporous organic polymer networks. *Progress in Polymer Science (Oxford)* **2012**, *37*, 530–563.

[9] Gu, Y.; Zhao, J.; Johnson, J. A. Polymer Networks: From Plastics and Gels to Porous Frameworks. *Angewandte Chemie - International Edition* **2020**, *59*, 5022–5049.

[10] Baumgartner, B.; Bojdys, M. J.; Unterlass, M. M. Geomimetics for green polymer synthesis: Highly ordered polyimides via hydrothermal techniques. *Polymer Chemistry* **2014**, *5*, 3771–3776.

[11] Taublaender, M. J.; Mezzavilla, S.; Thiele, S.; Glöcklhofer, F.; Unterlass, M. M. Hydrothermal Generation of Conjugated Polymers Using the Example of Pyrrone Polymers and Polybenzimidazoles. *Angewandte Chemie - International Edition* **2020**, *59*, 15050–15060.

[12] Li, G.; Yu, K.; Noordijk, J.; Meeusen-Wierts, M. H.; Gebben, B.; Oude Lohuis, P. A.; Schotman, A. H.; Bernaerts, K. V. Hydrothermal polymerization towards fully biobased polyazomethines. *Chemical Communications* **2020**, *56*, 9194–9197.

[13] Li, J.; Celiz, A. D.; Yang, J.; Yang, Q.; Wamala, I.; Whyte, W.; Seo, B. R.; Vasilyev, N. V.; Vlassak, J. J.; Suo, Z.; Mooney, D. J. Tough adhesives for diverse wet surfaces. *Science* **2017**, *357*, 378–381.

[14] Ramarad, S.; Khalid, M.; Ratnam, C. T.; Chuah, A. L.; Rashmi, W. Waste tire rubber in polymer blends: A review on the evolution, properties and future. *Progress in Materials Science* **2015**, *72*, 100–140.

[15] Long, L.; Wang, S.; Xiao, M.; Meng, Y. Polymer electrolytes for lithium polymer batteries. *Journal of Materials Chemistry A* **2016**, *4*, 10038–10039.

[16] Rogers, J. A.; Someya, T.; Huang, Y. Materials and mechanics for stretchable electronics. *Science* **2010**, *327*, 1603–1607.

[17] Mc Keown, N. B.; Budd, P. M. Polymers of intrinsic microporosity (PIMs): Organic materials for membrane separations, heterogeneous catalysis and hydrogen storage. *Chemical Society Reviews* **2006**, *35*, 675–683.

[18] Flory, P. J. Molecular size distribution in three dimensional polymers. II. Trifunctional branching units. *Journal of the American Chemical Society* **1941**, *63*, 3091–3096.

[19] Dušek, K.; Dušková-Smrčková, M. Polymer Networks. *Macromolecular Engineering: Precise Synthesis, Materials Properties, Applications* **2011**, *3*, 1687–1730.

[20] Gu, Y.; Zhao, J.; Johnson, J. A. A (Macro)Molecular-Level Understanding of Polymer Network Topology. *Trends in Chemistry* **2019**, *1*, 318–334.

[21] Geyer, R.; Jambeck, J. R.; Law, K. L. Production, use, and fate of all plastics ever made. *Science Advances* **2017**, *3*, e1700782.

[22] Hawker, C. J. Molecular Weight Control by a "Living" Free-Radical Polymerization Process. *Journal of the American Chemical Society* **1994**, *116*, 11185–11186.

[23] Kato, M.; Kamigaito, M.; Sawamoto, M.; Higashimura, T. Polymerization of Methyl Methacrylate with the Carbon Tetrachloride/Dichlorotris-(triphenylphosphine)ruthenium(II)/ Methylaluminum Bis(2,6-di-tert-butylphenoxide) Initiating System: Possibility of Living Radical Polymerization. *Macromolecules* **1995**, *28*, 1721–1723.

[24] Matyjaszewski, K. Atom Transfer Radical Polymerization (ATRP): Current status and future perspectives. *Macromolecules* **2012**, *45*, 4015–4039.

[25] Chiefari, J.; Chong, Y. K.; Ercole, F.; Krstina, J.; Jeffery, J.; Le, T. P.; Mayadunne, R. T.; Meijs, G. F.; Moad, C. L.; Moad, G.; Rizzardo, E.; Thang, S. H. Living free-radical polymerization by reversible addition - Fragmentation chain transfer: The RAFT process. *Macromolecules* **1998**, *31*, 5559–5562.

[26] Perrier, S. 50th Anniversary Perspective: RAFT Polymerization - A User Guide. *Macromolecules* **2017**, *50*, 7433–7447.

[27] Carothers, W. H. Studies on polymerization and ring formation. I. An introduction to the general theory of condensation polymers. *Journal of the American Chemical Society* **1929**, *51*, 2548–2559.

[28] Klotzenburg, S.; Maskos, M.; Nuyken, O. *Polymer chemistry*; Springer: Berlin Heidelberg, 2017; pp 1–583.

[29] Flory, P. J. Molecular Size Distribution in Three Dimensional Polymers. VI. Branched Polymers Containing A-R-Bf-1 Type Units. *Journal of the American Chemical Society* **1952**, *74*, 2718–2723.

[30] Ren, S.; Dawson, R.; Laybourn, A.; Jiang, J. X.; Khimyak, Y.; Adams, D. J.; Cooper, A. I. Functional conjugated microporous polymers: From 1,3,5-benzene to 1,3,5-triazine. *Polymer Chemistry* **2012**, *3*, 928–934.

[31] Cao, S.; Li, B.; Zhu, R.; Pang, H. Design and Synthesis of Covalent Organic Frameworks towards Energy and Environment Fields. *Chemical Engineering Journal* **2018**, *355*, 602–623.

[32] Gracia, R.; Mecerreyes, D. Polymers with redox properties: materials for batteries, biosensors and more. *Polym. Chem.* **2013**, *4*, 2206–2214.

[33] Bhanja, P.; Das, S. K.; Bhunia, K.; Pradhan, D.; Hayashi, T.; Hijikata, Y.; Irle, S.; Bhaumik, A. A New Porous Polymer for Highly Efficient Capacitive Energy Storage. *ACS Sustainable Chemistry and Engineering* **2018**, *6*, 202–209.

[34] Xu, Y.; Jin, S.; Xu, H.; Nagai, A.; Jiang, D. Conjugated microporous polymers: Design, synthesis and application. *Chemical Society Reviews* **2013**, *42*, 8012–8031.

[35] Bastide, J.; Leibler, L. Large-Scale Heterogeneities in Randomly Cross-Linked Networks Large-scale. *Macromolecules* **1988**, *21*, 2647–2649.

[36] Yue, K.; Liu, G.; Feng, X.; Li, L.; Lotz, B.; Cheng, S. Z. A few rediscovered and challenging topics in polymer crystals and crystallization. *Polymer Crystallization* **2018**, *1*, e10053.

[37] Côté, A. P.; Benin, A. I.; Nathan W, O.; Michael, O.; Adam J, M.; Omar M, Y. Porous , Crystalline , Covalent Organic Frameworks. *Science* **2005**, *310*, 1166–1171.

[38] Thommes, M.; Kaneko, K.; Neimark, A. V.; Olivier, J. P.; Rodriguez-Reinoso, F.; Rouquerol, J.; Sing, K. S. Physisorption of gases, with special reference to the evaluation of surface area and pore size distribution (IUPAC Technical Report). *Pure and Applied Chemistry* **2015**, *87*, 1051–1069.

[39] Cheng, H.; Hu, E.; Hu, Y. Impact of mineral micropores on transport and fate of organic contaminants: A review. *Journal of Contaminant Hydrology* **2012**, *129-130*, 80–90.

[40] Möller, K.; Bein, T. Mesoporosity – a new dimension for zeolites. *Chemical Society Reviews* **2013**, *42*, 3689–3707.

[41] Kärger, J. Transport phenomena in nanoporous materials. *ChemPhysChem* **2015**, *16*, 24–51.

[42] Weitkamp, J.; Puppe, L. *Catalysis and Zeolites*, 1st ed.; Springer Berlin Heidelberg: Berlin, Heidelberg, 1999; pp 1–566.

[43] Yuan, Z. Y.; Su, B. L. Insights into hierarchically meso-macroporous structured materials. *Journal of Materials Chemistry* **2006**, *16*, 663–677.

[44] Chen, L.; Zhang, R.; Min, T.; Kang, Q.; Tao, W. Pore-scale study of effects of macroscopic pores and their distributions on reactive transport in hierarchical porous media. *Chemical Engineering Journal* **2018**, *349*, 428–437.

[45] Budd, P. M.; Ghanem, B. S.; Makhseed, S.; McKeown, N. B.; Msayib, K. J.; Tattershall, C. E. Polymers of intrinsic microporosity (PIMs): robust, solution-processable, organic nanoporous materials. *Chemical Communications* **2004**, *4*, 230–231.

[46] Addicoat, M. A.; Tsotsalas, M. Covalently linked organic networks. *Frontiers in Materials* **2015**, *2*, 1–5.

[47] Kaur, P.; Hupp, J. T.; Nguyen, S. T. Porous organic polymers in catalysis: Opportunities and challenges. *ACS Catalysis* **2011**, *1*, 819–835.

[48] Davankov, V. A.; Tsyurupa, M. P. Structure and properties of hypercrosslinked polystyrene-the first representative of a new class of polymer networks. *Reactive Polymers* **1990**, *13*, 27–42.

[49] Silverstein, M. S.; Cameron, N. R.; Hillmyer, M. A. In *Porous Polymers*; Silverstein, M. S., Cameron, N. R., Hillmyer, M. A., Eds.; John Wiley & Sons, Inc.: Hoboken, New Jersey, 2011; pp 3–31.

[50] Huang, J.; Turner, S. R. Hypercrosslinked Polymers: A Review. *Polymer Reviews* **2018**, *58*, 1–41.

[51] Wood, C. D.; Bien, T.; Trewin, A.; Hongjun, N.; Bradshaw, D.; Rosseinsky, M. J.; Khimyak, Y. Z.; Campbell, N. L.; Kirk, R.; Stöckel, E.; Cooper, A. I. Hydrogen storage in microporous hypercrosslinked organic polymer networks. *Chemistry of Materials* **2007**, *19*, 2034–2048.

[52] Germain, J.; Fréchet, J. M.; Svec, F. Hypercrosslinked polyanilines with nanoporous structure and high surface area: Potential adsorbents for hydrogen storage. *Journal of Materials Chemistry* **2007**, *17*, 4989–4997.

[53] Germain, J.; Svec, F.; Fréenet, J. M. Preparation of size-selective nanoporous polymer networks of aromatic rings: Potential adsorbents for hydrogen storage. *Chemistry of Materials* **2008**, *20*, 7069–7076.

[54] Ghanem, B. S.; McKeown, N. B.; Budd, P. M.; Al-Harbi, N. M.; Fritsch, D.; Heinrich, K.; Starannikova, L.; Tokarev, A.; Yampolskii, Y. Synthesis, characterization, and gas permeation properties of a novel group of polymers with intrinsic microporosity: PIM-polyimides. *Macromolecules* **2009**, *42*, 7881–7888.

[55] Ghanem, B. S.; Hashem, M.; Harris, K. D.; Msayib, K. J.; Xu, M.; Budd, P. M.; Chaukura, N.; Book, D.; Tedds, S.; Walton, A.; McKeown, N. B. Triptycene-based polymers of intrinsic microporosity: Organic materials that can be tailored for gas adsorption. *Macromolecules* **2010**, *43*, 5287–5294.

[56] Budd, P. M.; Ghanem, B.; Msayib, K.; McKeown, N. B.; Tattèrshall, C. A nanoporous network polymer derived from hexaazatrinaphthylene with potential as an adsorbent and catalyst support. *Journal of Materials Chemistry* **2003**, *13*, 2721–2726.

[57] Li, G.; Wang, Z. Microporous polyimides with uniform pores for adsorption and separation of CO2 gas and organic vapors. *Macromolecules* **2013**, *46*, 3058–3066.

[58] Li, G.; Zhang, B.; Yan, J.; Wang, Z. Microporous polyimides with functional groups for the adsorption of carbon dioxide and organic vapors. *Journal of Materials Chemistry A* **2016**, *4*, 11453–11461.

[59] Tian, D.; Zhang, H. Z.; Zhang, D. S.; Chang, Z.; Han, J.; Gao, X. P.; Bu, X. H. Li-ion storage and gas adsorption properties of porous polyimides (PIs). *RSC Advances* **2014**, *4*, 7506–7510.

[60] Tian, B.; Zheng, J.; Zhao, C.; Liu, C.; Su, C.; Tang, W.; Li, X.; Ning, G. H. Carbonyl-based polyimide and polyquinoneimide for potassium-ion batteries. *Journal of Materials Chemistry A* **2019**, *7*, 9997–10003.

[61] Weber, J.; Su, Q.; Antonietti, M.; Thomas, A. Exploring polymers of intrinsic microporosity - Microporous, soluble polyamide and polyimide. *Macromolecular Rapid Communications* **2007**, *28*, 1871–1876.

[62] Alghunaimi, F.; Ghanem, B.; Alaslai, N.; Swaidan, R.; Litwiller, E.; Pinnau, I. Gas permeation and physical aging properties of iptycene diamine-based microporous polyimides. *Journal of Membrane Science* **2015**, *490*, 321–327.

[63] Wang, Z.; Zhang, B.; Yu, H.; Sun, L.; Jiao, C.; Liu, W. Microporous polyimide networks with large surface areas and their hydrogen storage properties. *Chemical Communications* **2010**, *46*, 7730–7732.

[64] Wang, Z.; Zhang, B.; Yu, H.; Li, G.; Bao, Y. Synthetic control of network topology and pore structure in microporous polyimides based on triangular triphenylbenzene and triphenylamine units. *Soft Matter* **2011**, *7*, 5723–5730.

[65] Rao, K. V.; Haldar, R.; Kulkarni, C.; Maji, T. K.; George, S. J. Perylene based porous polyimides: Tunable, high surface area with tetrahedral and pyramidal monomers. *Chemistry of Materials* **2012**, *24*, 969–971.

[66] Wang, Z.; Wang, D.; Jin, J. Microporous polyimides with rationally designed chain structure achieving high performance for gas separation. *Macromolecules* **2014**, *47*, 7477–7483.

[67] Taylor, D.; Dalgarno, S. J.; Xu, Z.; Vilela, F. Conjugated porous polymers: Incredibly versatile materials with far-reaching applications. *Chemical Society Reviews* **2020**, *49*, 3981–4042.

[68] Chen, L.; Honsho, Y.; Seki, S.; Jiang, D. Light-harvesting conjugated microporous polymers: Rapid and highly efficient flow of light energy with a porous polyphenylene framework as antenna. *Journal of the American Chemical Society* **2010**, *132*, 6742–6748.

[69] Vilela, F.; Zhang, K.; Antonietti, M. Conjugated porous polymers for energy applications. *Energy and Environmental Science* **2012**, *5*, 7819–7832.

[70] Cooper, A. I. Conjugated microporous polymers. *Advanced Materials* **2009**, *21*, 1291–1295.

[71] Novotney, J. L.; Dichtel, W. R. Conjugated porous polymers for TNT vapor detection. *ACS Macro Letters* **2013**, *2*, 423–426.

[72] Liu, X.; Xu, Y.; Jiang, D. Conjugated microporous polymers as molecular sensing devices: Microporous architecture enables rapid response and enhances sensitivity in fluorescence-on and fluorescence-off sensing. *Journal of the American Chemical Society* **2012**, *134*, 8738–8741.

[73] Jiang, J. X.; Su, F.; Trewin, A.; Wood, C. D.; Campbell, N. L.; Niu, H.; Dickinson, C.; Ganin, A. Y.; Rosseinsky, M. J.; Khimyak, Y. Z.; Cooper, A. I. Conjugated microporous poly(aryleneethynylene) networks. *Angewandte Chemie - International Edition* **2007**, *46*, 8574–8578.

[74] Ma, B. C.; Ghasimi, S.; Landfester, K.; Vilela, F.; Zhang, K. A. Conjugated microporous polymer nanoparticles with enhanced dispersibility and water compatibility for photocatalytic applications. *Journal of Materials Chemistry A* **2015**, *3*, 16064–16071.

[75] Xie, Z.; Wei, Y.; Zhao, X.; Li, Y.; Ding, S.; Chen, L. Facile construction of butadiynylene based conjugated porous polymers by cost-effective Glaser coupling. *Materials Chemistry Frontiers* **2017**, *1*, 867–872.

[76] Kuhn, P.; Antonietti, M.; Thomas, A. Porous, covalent triazine-based frameworks prepared by ionothermal synthesis. *Angewandte Chemie - International Edition* **2008**, *47*, 3450–3453.

[77] Ding, X.; Han, B.-H. Metallophthalocyanine-Based Conjugated Microporous Polymers as Highly Efficient Photosensitizers for Singlet Oxygen Generation. *Angewandte Chemie* **2015**, *127*, 6636–6639.

[78] Wei, Y.; Chen, W.; Zhao, X.; Ding, S.; Han, S.; Chen, L. Solid-state emissive cyanostilbene based conjugated microporous polymers: Via cost-effective Knoevenagel polycondensation. *Polymer Chemistry* **2016**, *7*, 3983–3988.

[79] Li, B.; Guan, Z.; Yang, X.; Wang, W. D.; Hussain, I.; Song, K.; Tan, B.; Li, T. Multifunctional microporous organic polymers. *Journal of Materials Chemistry A* **2014**, *2*, 11930–11939.

[80] Dawson, R.; Laybourn, A.; Clowes, R.; Khimyak, Y. Z.; Adams, D. J.; Cooper, A. I. Functionalized conjugated microporous polymers. *Macromolecules* **2009**, *42*, 8809–8816.

[81] Dawson, R.; Laybourn, A.; Khimyak, Y. Z.; Adams, D. J.; Cooper, A. I. High surface area conjugated microporous polymers: The importance of reaction solvent choice. *Macromolecules* **2010**, *43*, 8524–8530.

[82] Schmidt, J.; Werner, M.; Thomas, A. Conjugated microporous polymer networks via yamamoto polymerization. *Macromolecules* **2009**, *42*, 4426–4429.

[83] Jiang, J. X.; Su, F.; Trewin, A.; Wood, C. D.; Niu, H.; Jones, J. T.; Khimyak, Y. Z.; Cooper, A. I. Synthetic control of the pore dimension and surface area in conjugated microporous polymer and copolymer networks. *Journal of the American Chemical Society* **2008**, *130*, 7710–7720.

[84] Diercks, C. S.; Yaghi, O. M. The atom, the molecule, and the covalent organic framework. *Science* **2017**, *355*.

[85] Fang, Q.; Zhuang, Z.; Gu, S.; Kaspar, R. B.; Zheng, J.; Wang, J.; Qiu, S.; Yan, Y. Designed synthesis of large-pore crystalline polyimide covalent organic frameworks. *Nature Communications* **2014**, *5*, 1–8.

[86] Yaghi, O. M.; Kalmutzki, M. J.; Diercks, C. S. *Introduction to Reticular Chemistry*; 2019.

[87] Desiraju, G. R. Chemistry beyond the molecule. *Nature* **2001**, *412*, 397–400.

[88] Lehn, J.-M. Supramolecular Chemistry: Receptors, Catalysts, and Carriers. *Science* **1985**, *227*, 4689.

[89] Rowan, S. J.; Cantrill, S. J.; Cousins, G. R.; Sanders, J. K.; Stoddart, J. F. Dynamic covalent chemistry. *Angewandte Chemie - International Edition* **2002**, *41*, 898–952.

[90] Feng, X.; Ding, X.; Jiang, D. Covalent organic frameworks. *Chemical Society Reviews* **2012**, *41*, 6010–6022.

[91] Lanni, L. M.; Tilford, R. W.; Bharathy, M.; Lavigne, J. J. Enhanced hydrolytic stability of self-assembling alkylated two-dimensional covalent organic frameworks. *Journal of the American Chemical Society* **2011**, *133*, 13975–13983.

[92] Uribe-Romo, F. J.; Hunt, J. R.; Furukawa, H.; Klöck, C.; O'Keeffe, M.; Yaghi, O. M. A crystalline imine-linked 3-D porous covalent organic framework. *Journal of the American Chemical Society* **2009**, *131*, 4570–4571.

[93] Uribe-Romo, F. J.; Doonan, C. J.; Furukawa, H.; Oisaki, K.; Yaghi, O. M. Crystalline covalent organic frameworks with hydrazone linkages. *Journal of the American Chemical Society* **2011**, *133*, 11478–11481.

[94] Smith, B. J.; Overholts, A. C.; Hwang, N.; Dichtel, W. R. Insight into the crystallization of amorphous imine-linked polymer networks to 2D covalent organic frameworks. *Chemical Communications* **2016**, *52*, 3690–3693.

[95] Kandambeth, S.; Dey, K.; Banerjee, R. Covalent Organic Frameworks: Chemistry beyond the Structure. *Journal of the American Chemical Society* **2019**, *141*, 1807–1822.

[96] Fang, Q.; Wang, J.; Gu, S.; Kaspar, R. B.; Zhuang, Z.; Zheng, J.; Guo, H.; Qiu, S.; Yan, Y. 3D Porous Crystalline Polyimide Covalent Organic Frameworks for Drug Delivery. *Journal of the American Chemical Society* **2015**, *137*, 8352–8355.

[97] Haase, F.; Lotsch, B. V. Solving the COF trilemma: Towards crystalline, stable and functional covalent organic frameworks. *Chemical Society Reviews* **2020**, *49*, 8469–8500.

[98] Wang, T.; Xue, R.; Chen, H.; Shi, P.; Lei, X.; Wei, Y.; Guo, H.; Yang, W. Preparation of two new polyimide bond linked porous covalent organic frameworks and their fluorescence sensing application for sensitive and selective determination of Fe3+. *New Journal of Chemistry* **2017**, *41*, 14272–14278.

[99] Lv, J.; Tan, Y. X.; Xie, J.; Yang, R.; Yu, M.; Sun, S.; Li, M. D.; Yuan, D.; Wang, Y. Direct Solar-to-Electrochemical Energy Storage in a Functionalized Covalent Organic Framework. *Angewandte Chemie - International Edition* **2018**, *57*, 12716–12720.

[100] Zhu, X.; An, S.; Liu, Y.; Hu, J.; Liu, H.; Tian, C.; Dai, S.; Yang, X.; Wang, H.; Abney, C. W. Efficient removal of organic dye pollutants using covalent organic frameworks. *American Institute of Chemical Engineers* **2017**, *63*, 3470–3478.

[101] Jiang, L.; Tian, Y.; Sun, T.; Zhu, Y.; Ren, H.; Zou, X.; Ma, Y.; Meihaus, K. R.; Long, J. R.; Zhu, G. A Crystalline Polyimide Porous Organic Framework for Selective Adsorption of Acetylene over Ethylene. *Journal of the American Chemical Society* **2018**, *140*, 15724–15730.

[102] Kim, T. W.; Jun, S.; Ha, Y.; Yadav, R. K.; Kumar, A.; Yoo, C. Y.; Oh, I.; Lim, H. K.; Shin, J. W.; Ryoo, R.; Kim, H.; Kim, J.; Baeg, J. O.; Ihee, H. Ultrafast charge transfer coupled with lattice phonons in two-dimensional covalent organic frameworks. *Nature Communications* **2019**, *10*, 1–10.

[103] Kim, T.; Joo, S. H.; Gong, J.; Choi, S.; Min, J. H.; Kim, Y.; Lee, G.; Lee, E.; Park, S.; Kwak, S. K.; Lee, H.-S.; Kim, B.-S. Geomimetic Hydrothermal Synthesis of Polyimide-Based Covalent Organic Frameworks. *Angewandte Chemie* **2021**,

[104] Zhao, N.; Liu, J. M.; Yang, F. E.; Lv, S. W.; Wang, J.; Wang, S. Easy Green Construction of a Universal Sensing Platform Based on Crystalline Polyimide Covalent Organic Frameworks with Sensitive Fluorescence Response to Metal Ions and Antibiotics. *ACS Applied Bio Materials* **2021**, *4*, 995–1002.

[105] Haldar, S.; Rase, D.; Shekhar, P.; Jain, C.; Vinod, C. P.; Zhang, E.; Shupletsov, L.; Kaskel, S.; Vaidhyanathan, R. Incorporating Conducting Polypyrrole into a Polyimide COF for Carbon-Free Ultra-High Energy Supercapacitor. *Advanced Energy Materials* **2022**, *12*.

[106] Yang, X.; Gong, L.; Liu, X.; Zhang, P.; Li, B.; Qi, D.; Wang, K.; He, F.; Jiang, J. Mesoporous Polyimide-Linked Covalent Organic Framework with

Multiple Redox-Active Sites for High-Performance Cathodic Li Storage. *Angewandte Chemie - International Edition* **2022**, *61*, e202207043.

[107] Shuai, G.; Rui, H.; Jingjing, C.; Xi, C.; Kun, L.; Iftikhar, H.; Guiyu, L.; Zhiqiang, W.; Qingmeng, G.; Hao, G.; Muqing, L.; Kaili, Z.; Zhouguang, L. A star-shaped polyimide covalent organic framework for high-voltage lithium-ion batteries. *Materials Chemistry Frontiers* **2022**, *6*, 2545–2550.

[108] Kazarian, S. G.; Vincent, M. F.; Bright, F. V.; Liotta, C. L.; Eckert, C. A. Specific intermolecular interaction of carbon dioxide with polymers. *Journal of the American Chemical Society* **1996**, *118*, 1729–1736.

[109] Rabbani, M. G.; Sekizkardes, A. K.; Kahveci, Z.; Reich, T. E.; Ding, R.; El-Kaderi, H. M. A 2D mesoporous imine-linked covalent organic framework for high pressure gas storage applications. *Chemistry - A European Journal* **2013**, *19*, 3324–3328.

[110] Zhai, L.; Huang, N.; Xu, H.; Chen, Q.; Jiang, D. A backbone design principle for covalent organic frameworks: the impact of weakly interacting units on CO2 adsorption. *Chemical Communications* **2017**, *53*, 4242–4245.

[111] Wan, S.; Gándara, F.; Asano, A.; Furukawa, H.; Saeki, A.; Dey, S. K.; Liao, L.; Ambrogio, M. W.; Botros, Y. Y.; Duan, X.; Seki, S.; Stoddart, J. F.; Yaghi, O. M. Covalent organic frameworks with high charge carrier mobility. *Chemistry of Materials* **2011**, *23*, 4094–4097.

[112] Ding, S. Y.; Gao, J.; Wang, Q.; Zhang, Y.; Song, W. G.; Su, C. Y.; Wang, W. Construction of covalent organic framework for catalysis: Pd/COF-LZU1 in Suzuki-Miyaura coupling reaction. *Journal of the American Chemical Society* **2011**, *133*, 19816–19822.

[113] Stegbauer, L.; Schwinghammer, K.; Lotsch, B. V. A hydrazone-based covalent organic framework for photocatalytic hydrogen production. *Chemical Science* **2014**, *5*, 2789–2793.

[114] Wan, S.; Guo, J.; Kim, J.; Ihee, H.; Jiang, D. A photoconductive covalent organic framework: Self-condensed arene cubes composed of eclipsed 2D polypyrene sheets for photocurrent generation. *Angewandte Chemie - International Edition* **2009**, *48*, 5439–5442.

[115] Tilford, R. W.; Mugavero, S. J.; Pellechia, P. J.; Lavigne, J. J. Tailoring microporosity in covalent organic frameworks. *Advanced Materials* **2008**, *20*, 2741–2746.

[116] Zhao, S.; Dong, B.; Ge, R.; Wang, C.; Song, X.; Ma, W.; Wang, Y.; Hao, C.; Guo, X.; Gao, Y. Channel-wall functionalization in covalent organic frameworks for the enhancement of CO2 uptake and CO2/N2 selectivity. *RSC Advances* **2016**, *6*, 38774–38781.

[117] Wang, L.; Xie, H.; Lin, Y.; Wang, M.; Sha, L.; Yu, X.; Yang, J.; Zhao, J.; Li, G. Covalent organic frameworks (COFs)-based biosensors for the assay of disease biomarkers with clinical applications. *Biosensors and Bioelectronics* **2022**, 114668.

[118] Wang, S.; Pang, Y.; Hu, S.; Lv, J.; Lin, Y.; Li, M. Copper sulfide engineered covalent organic frameworks for pH-responsive chemo/photothermal/chemodynamic synergistic therapy against cancer. *Chemical Engineering Journal* **2023**, *451*, 138864.

[119] Huang, N.; Zhai, L.; Xu, H.; Jiang, D. Stable Covalent Organic Frameworks for Exceptional Mercury Removal from Aqueous Solutions. *Journal of the American Chemical Society* **2017**, *139*, 2428–2434.

[120] Bourda, L.; Krishnaraj, C.; Van Der Voort, P.; Van Hecke, K. Conquering the crystallinity conundrum: Efforts to increase quality of covalent organic frameworks. *Materials Advances* **2021**, *2*, 2811–2845.

[121] He, Y.; Xiang, S.; Chen, B. A microporous hydrogen-bonded organic framework for highly selective C 2H2/C2H4 separation at ambient temperature. *Journal of the American Chemical Society* **2011**, *133*, 14570–14573.

[122] Lin, R. B.; He, Y.; Li, P.; Wang, H.; Zhou, W.; Chen, B. Multifunctional porous hydrogen-bonded organic framework materials. *Chemical Society Reviews* **2019**, *48*, 1362–1389.

[123] Jiang, J.; Zhao, Y.; Yaghi, O. M. Covalent Chemistry beyond Molecules. *Journal of the American Chemical Society* **2016**, *138*, 3255–3265.

[124] Brunet, P.; Simard, M.; Wuest, J. D. Molecular tectonics. Porous hydrogen-bonded networks with unprecedented structural integrity. *Journal of the American Chemical Society* **1997**, *119*, 2737–2738.

[125] Li, P.; He, Y.; Arman, H. D.; Krishna, R.; Wang, H.; Weng, L.; Chen, B. A microporous six-fold interpenetrated hydrogen-bonded organic framework for highly selective separation of C2H4/C2H6. *Chemical Communications* **2014**, *50*, 13081–13084.

[126] Li, P.; He, Y.; Zhao, Y.; Weng, L.; Wang, H.; Krishna, R.; Wu, H.; Zhou, W.; O'Keeffe, M.; Han, Y.; Chen, B. A rod-packing microporous hydrogen-bonded organic framework for highly selective separation of C2H2/CO2at room temperature. *Angewandte Chemie - International Edition* **2015**, *54*, 574–577.

[127] Wang, H.; Bao, Z.; Wu, H.; Lin, R. B.; Zhou, W.; Hu, T. L.; Li, B.; Zhao, J. C. G.; Chen, B. Two solvent-induced porous hydrogen-bonded organic frameworks: Solvent effects on structures and functionalities. *Chemical Communications* **2017**, *53*, 11150–11153.

[128] Zerkowski, J. A.; MacDonald, J. C.; Whitesides, G. M. Investigations into the Robustness of Secondary and Tertiary Architecture of Hydrogen-Bonded Crystalline Tapes. *Chemistry of Materials* **1994**, *6*, 1250–1257.

[129] Zentner, C. A.; Lai, H. W.; Greenfield, J. T.; Wiscons, R. A.; Zeller, M.; Campana, C. F.; Talu, O.; Fitzgerald, S. A.; Rowsell, J. L. High surface area and Z' in a thermally stable 8-fold polycatenated hydrogen-bonded framework. *Chemical Communications* **2015**, *51*, 11642–11645.

[130] Li, Y. L.; Alexandrov, E. V.; Yin, Q.; Li, L.; Fang, Z. B.; Yuan, W.; Proserpio, D. M.; Liu, T. F. Record Complexity in the Polycatenation of Three Porous Hydrogen-Bonded Organic Frameworks with Stepwise Adsorption Behaviors. *Journal of the American Chemical Society* **2020**, *142*, 7218–7224.

[131] Pulido, A. et al. Functional materials discovery using energy-structure-function maps. *Nature* **2017**, *543*, 657–664.

[132] Chen, T. H.; Popov, I.; Kaveevivitchai, W.; Chuang, Y. C.; Chen, Y. S.; Daugulis, O.; Jacobson, A. J.; Miljanic, O. Thermally robust and porous noncovalent organic framework with high affinity for fluorocarbons and CFCs. *Nature Communications* **2014**, *5*, 1–8.

[133] Luo, X. Z.; Jia, X. J.; Deng, J. H.; Zhong, J. L.; Liu, H. J.; Wang, K. J.; Zhong, D. C. A microporous hydrogen-bonded organic framework: Exceptional stability and highly selective adsorption of gas and liquid. *Journal of the American Chemical Society* **2013**, *135*, 11684–11687.

[134] Yan, W.; Yu, X.; Yan, T.; Wu, D.; Ning, E.; Qi, Y.; Han, Y. F.; Li, Q. A triptycene-based porous hydrogen-bonded organic framework for guest incorporation with tailored fitting. *Chemical Communications* **2017**, *53*, 3677–3680.

[135] Lü, J.; Perez-Krap, C.; Suyetin, M.; Alsmail, N. H.; Yan, Y.; Yang, S.; Lewis, W.; Bichoutskaia, E.; Tang, C. C.; Blake, A. J.; Cao, R.; Schröder, M. A Robust Binary Supramolecular Organic Framework (SOF) with high CO2adsorption and selectivity. *Journal of the American Chemical Society* **2014**, *136*, 12828–12831.

[136] Lü, J.; Perez-Krap, C.; Trousselet, F.; Yan, Y.; Alsmail, N. H.; Karadeniz, B.; Jacques, N. M.; Lewis, W.; Blake, A. J.; Coudert, F. X.; Cao, R.; Schröder, M. Polycatenated 2D Hydrogen-Bonded Binary Supramolecular Organic Frameworks (SOFs) with Enhanced Gas Adsorption and Selectivity. *Crystal Growth and Design* **2018**, *18*, 2555–2562.

[137] Yamamoto, A.; Uehara, S.; Hamada, T.; Miyata, M.; Hisaki, I.; Tohnai, N. Diamondoid porous organic salts toward applicable strategy for construction of versatile porous structures. *Crystal Growth and Design* **2012**, *12*, 4600–4606.

[138] Morshedi, M.; Thomas, M.; Tarzia, A.; Doonan, C. J.; White, N. G. Supramolecular anion recognition in water: synthesis of hydrogen-bonded supramolecular frameworks. *Chemical Science* **2017**, *8*, 3019–3025.

[139] Zhou, D. D.; Xu, Y. T.; Lin, R. B.; Mo, Z. W.; Zhang, W. X.; Zhang, J. P. High-symmetry hydrogen-bonded organic frameworks: Air separation and crystal-to-crystal structural transformation. *Chemical Communications* **2016**, *52*, 4991–4994.

[140] Feriante, C.; Evans, A. M.; Jhulki, S.; Castano, I.; Strauss, M. J.; Barlow, S.; Dichtel, W. R.; Marder, S. R. New mechanistic insights into the formation of imine-linked two-dimensional covalent organic frameworks. *Journal of the American Chemical Society* **2020**, *142*, 18637–18644.

[141] Liu, T.; Wang, B.; He, R.; Arman, H.; Schanze, K. S.; Xiang, S.; Li, D.; Chen, B. A novel hydrogen-bonded organic framework for the sensing of two representative organic arsenics. *Canadian Journal of Chemistry* **2020**, *98*, 352–357.

[142] Wang, B.; Lin, R. B.; Zhang, Z.; Xiang, S.; Chen, B. Hydrogen-Bonded Organic Frameworks as a Tunable Platform for Functional Materials. *Journal of the American Chemical Society* **2020**, *142*, 14399–14416.

[143] Hisaki, I.; Xin, C.; Takahashi, K.; Nakamura, T. Designing Hydrogen-Bonded Organic Frameworks (HOFs) with Permanent Porosity. *Angewandte Chemie - International Edition* **2019**, *58*, 11160–11170.

[144] Yang, W.; Greenaway, A.; Lin, X.; Matsuda, R.; Blake, A. J.; Wilson, C.; Lewis, W.; Hubberstey, P.; Kitagawa, S.; Champness, N. R.; Schröder, M. Exceptional thermal stability in a supramolecular organic framework: Porosity and gas storage. *Journal of the American Chemical Society* **2010**, *132*, 14457–14469.

[145] Wang, H.; Li, B.; Wu, H.; Hu, T. L.; Yao, Z.; Zhou, W.; Xiang, S.; Chen, B. A Flexible Microporous Hydrogen-Bonded Organic Framework for Gas Sorption and Separation. *Journal of the American Chemical Society* **2015**, *137*, 9963–9970.

[146] Chandra, S.; Kundu, T.; Kandambeth, S.; Babarao, R.; Marathe, Y.; Kunjir, S. M.; Banerjee, R. Phosphoric acid loaded azo (-N=N-) based covalent organic framework for proton conduction. *Journal of the American Chemical Society* **2014**, *136*, 6570–6573.

[147] Xu, H.; Tao, S.; Jiang, D. Proton conduction in crystalline and porous covalent organic frameworks. *Nature Materials* **2016**, *15*, 722–726.

[148] Karmakar, A.; Illathvalappil, R.; Anothumakkool, B.; Sen, A.; Samanta, P.; Desai, A. V.; Kurungot, S.; Ghosh, S. K. Hydrogen-Bonded Organic Frameworks (HOFs): A New Class of Porous Crystalline Proton-Conducting Materials. *Angewandte Chemie* **2016**, *128*, 10825–10829.

[149] Unterlass, M. M. Creating geomimetic polymers. *Materials Today* **2015**, *18*, 242–243.

[150] Byrappa, K.; Yoshimura, M. *Handbook of Hydrothermal Technology*; William Andrew, 2013; pp 1–845.

[151] Schafhäutl, A. Die neuesten geologischen Hypothesen und ihr Verhältnis zur Naturwissenschaft überhaupt. *Gelehrte Anzeigen München* **1845**, *20*, 577.

[152] Morey, G. W. Hydrothermal Synthesis. *American Ceramic Society* **1953**, *36*, 279–285.

[153] Nacken, R. Artificial Quartz Crystals, etc. *US Office of Technical Services Report* **1946**, PB–18–748 and 28–897.

[154] Barrer, R. Syntheses and Reactions of Modernite. *J. Chem. Soc.* **1948**, 2158.

[155] Thomas, L. A.; Wooster, N.; Wooster, W. A. The hydrothermal synthesis of quartz. *Discussions of the Faraday Society* **1949**, *5*, 341–345.

[156] Cundy, C. S.; Cox, P. A. The Hydrothermal Synthesis of Zeolites: History and Development from the Earliest Days to the Present Time. *Chemical Reviews* **2003**, *103*, 663–702.

[157] Laudise, R. A.; Ballman, A. A. Hydrothermal Synthesis of Sapphire. *Journal of the American Chemical Society* **1958**, *80*, 2655–2657.

[158] Zhao, X.-Z.; Roy, R.; Cherian, K. A.; Badzian, A. Hydrothermal growth of diamond in metal–C–H 2 O systems. *Nature* **1997**, *385*, 513–515.

[159] Chang, C.-C.; Wu, H.-L.; Kuo, C.-H.; Huang, M. H. Hydrothermal Synthesis of Monodispersed Octahedral Gold Nanocrystals with Five Different Size Ranges and Their Self-Assembled Structures. *Chem. Mater* **2008**, *20*, 7570–7574.

[160] Byrappa, K.; Keerthiraj, N.; Byrappa, S. M. *Handbook of Crystal Growth: Bulk Crystal Growth: Second Edition*, second edi ed.; Elsevier B.V., 2015; Vol. 2; pp 535–575.

[161] Yoshimura, M.; Byrappa, K. Hydrothermal processing of materials: Past, present, and future. *Journal of Materials Science* **2008**, *43*, 45–72.

[162] Walker, A. C. Hydrothermal Synthesis of Quartz Crystals. *Journal of the American Ceramic Society* **1953**, *36*, 250–256.

[163] Akiya, N.; Savage, P. E. Roles of Water for Chemical Reactions in High-Temperature Water. *Chemical Reviews* **2002**, *102*, 2725–2750.

[164] Mizan, T. I.; Savage, P. E.; Ziff, R. M. Temperature Dependence of Hydrogen Bonding in Supercritical Water. *Journal of Physical Chemistry* **1996**, *100*, 403–408.

[165] Sengers, J. V.; Watson, J. T. R. Improved International Formulations for the Viscosity and Thermal Conductivity of Water Substance. *Journal of Physical and Chemical Reference Data* **1986**, *15*, 1291.

[166] Uematsu, M.; Frank, E. U. Static Dielectric Constant of Water and Steam. *Journal of Physical and Chemical Reference Data* **2009**, *9*, 1291.

[167] Siskin, M.; Katritzky, A. R. Reactivity of Organic Compounds in Superheated Water: General Background. *Chemical Reviews* **2001**, *101*, 825–835.

[168] Chen, J.; Vacchio, M. J.; Wang, S.; Chernova, N.; Zavalij, P. Y.; Whittingham, M. S. The hydrothermal synthesis and characterization of olivines and related compounds for electrochemical applications. *Solid State Ionics* **2008**, *178*, 1676–1693.

[169] Byrappa, K.; Nirmala, B.; Lokanatha Rai, K.; Yoshimura, M. *Crystal Growth Technology*; 2003; pp 335–364.

[170] Gersten, B. L. *Crystal Growth Technology*; William Andrew Publishing, 2003; pp 299–333.

[171] Hodgkin, J.; Jackson, M.; Loder, J. Epoxy resins based on diaminobisimide compounds. 1991; `https://patents.google.com/patent/EP0552197A1/en`.

[172] Hawthorne, D. G.; Hodgkin, J. H.; Jackson, M. B.; Loder, J. W.; Morton, T. C. Preparation and characterization of some new diaminobisimides. *High Performance Polymers* **1994**, 287–301.

[173] Chiefari, J.; Dao, B.; Groth, A. M.; Hodgkin, J. H. Water as Solvent in Polyimide Synthesis: Thermoset and Thermoplastic Examples. *High Performance Polymers* **2003**, *15*, 269–279.

[174] Chiefari, J.; Dao, B.; Groth, A. M.; Hodgkin, J. H. Water as solvent in polyimide synthesis II: Processable aromatic polyimides. *High Performance Polymers* **2006**, *18*, 31–44.

[175] Chiefari, J.; Dao, B.; Groth, A. M.; Hodgkin, J. H. Water as solvent in polyimide synthesis III: Towards the synthesis of polyamideimides. *High Performance Polymers* **2006**, *18*, 437–451.

[176] Baumgartner, B.; Puchberger, M.; Unterlass, M. M. Towards a general understanding of hydrothermal polymerization of polyimides. *Polymer Chemistry* **2015**, *6*, 5773–5781.

[177] Baumgartner, B.; Bojdys, M. J.; Skrinjar, P.; Unterlass, M. M. Design strategies in hydrothermal polymerization of polyimides. *Macromolecular Chemistry and Physics* **2016**, *217*, 485–500.

[178] Stewart, D.; Antypov, D.; Dyer, M. S.; Pitcher, M. J.; Katsoulidis, A. P.; Chater, P. A.; Blanc, F.; Rosseinsky, M. J. Stable and ordered amide frameworks synthesised under reversible conditions which facilitate error checking. *Nature Communications* **2017**, *8*, 1–10.

[179] Thote, J.; Barike Aiyappa, H.; Rahul Kumar, R.; Kandambeth, S.; Biswal, B. P.; Balaji Shinde, D.; Chaki Roy, N.; Banerjee, R. Constructing covalent organic frameworks in water via dynamic covalent bonding. *IUCrJ* **2016**, *3*, 402–407.

[180] Lu, J.; Lin, F.; Wen, Q.; Qi, Q. Y.; Xu, J. Q.; Zhao, X. Large-scale synthesis of azine-linked covalent organic frameworks in water and promoted by water. *New Journal of Chemistry* **2019**, *43*, 6116–6120.

[181] Martín-Illán, J.; Rodríguez-San-Miguel, D.; Rodríguez-San-Miguel, D.; Franco, C.; Imaz, I.; Maspoch, D.; Maspoch, D.; Puigmartí-Luis, J.; Zamora, F.; Zamora, F.; Zamora, F.; Zamora, F. Green synthesis of imine-based covalent organic frameworks in water. *Chemical Communications* **2020**, *56*, 6704–6707.

[182] Lahnsteiner, M.; Caldera, M.; Moura, H. M.; Cerrón-Infantes, D. A.; Roeser, J.; Konegger, T.; Thomas, A.; Menche, J.; Unterlass, M. M. Hydrothermal polymerization of porous aromatic polyimide networks and machine learning-assisted computational morphology evolution interpretation. *Journal of Materials Chemistry A* **2021**, *9*, 19754–19769.

[183] Baumgartner, B.; Svirkova, A.; Bintinger, J.; Hametner, C.; Marchetti-Deschmann, M.; Unterlass, M. M. Green and highly efficient synthesis of perylene and naphthalene bisimides in nothing but water. *Chemical Communications* **2017**, *53*, 1229–1232.

[184] Dudd, L. M.; Venardou, E.; Garcia-Verdugo, E.; Licence, P.; Blake, A. J.; Wilson, C.; Poliakoff, M. Synthesis of benzimidazoles in high-temperature water. *Green Chemistry* **2003**, *5*, 187–192.

[185] Amaya-García, F. A.; Caldera, M.; Koren, A.; Kubicek, S.; Menche, J.; Unterlass, M. M. Green hydrothermal synthesis of fluorescent 2,3-diarylquinoxalines and large-scale computational comparison to existing alternatives. *ChemSusChem* **2021**, *14*, 1853–1863.

[186] Taublaender, M. J.; Glöcklhofer, F.; Marchetti-Deschmann, M.; Unterlass, M. M. Green and Rapid Hydrothermal Crystallization and Synthesis of Fully Conjugated Aromatic Compounds. *Angewandte Chemie - International Edition* **2018**, *57*, 12270–12274.

[187] Dallinger, D.; Kappe, C. O. Microwave-Assisted Synthesis in Water as Solvent. *Chemical Reviews* **2007**, *107*, 2563–2591.

[188] Leimhofer, L.; Baumgartner, B.; Puchberger, M.; Prochaska, T.; Konegger, T.; Unterlass, M. M. Green one-pot synthesis and processing of polyimide-silica hybrid materials. *Journal of Materials Chemistry A* **2017**, *5*, 16326–16335.

[189] Wilson, D.Stezenberger, H.; Hergenrother, P. *Polyimides*; Springer Science+Business Media, LLC: New York, 1990; p 297.

[190] Tashiro, K. Molecular theory of mechanical properties of crystalline polymers. *Progress in Polymer Science* **1993**, *18*, 377–435.

[191] Shen, C.; Bao, Y.; Wang, Z. Tetraphenyladamantane-based microporous polyimide for adsorption of carbon dioxide, hydrogen, organic and water vapors. *Chemical Communications* **2013**, *49*, 3321–3323.

[192] Dao, B.; Hodgkin, J.; Morton, T. C. Important factors controlling synthesis of imides in water. *High Performance Polymers* **1999**, *11*, 205–218.

[193] Unterlass, M. M.; Kopetzki, D.; Antonietti, M.; Weber, J. Mechanistic study of hydrothermal synthesis of aromatic polyimides. *Polymer Chemistry* **2011**, *2*, 1744–1753.

[194] Unterlass, M. M.; Emmerling, F.; Antonietti, M.; Weber, J. From dense monomer salt crystals to CO2 selective microporous polyimides via solid-state polymerization. *Chemical Communications* **2014**, *50*, 430–432.

[195] Taublaender, M. J.; Reiter, M.; Unterlass, M. M. Exerting Additive-Assisted Morphological Control during Hydrothermal Polymerization. *Macromolecular Chemistry and Physics* **2018**, *219*, 1700397.

[196] Taublaender, M. J.; Reiter, M.; Unterlass, M. M. Highly Crystalline, Nanostructured Polyimide Microparticles via Green and Tunable Solvothermal Polymerization. *Macromolecules* **2019**, *52*, 6318–6329.

[197] Rangel-Rangel, E.; Weber, J.; de la Campa, J. G.; Iglesias, M.; Maya, E. M. Pluronic-assisted hydrothermal synthesis of microporous polyimides. Application as supports for heterogenized transition metal catalysts. *Microporous and Mesoporous Materials* **2017**, *239*, 287–295.

[198] Kim, T.; Park, B.; Lee, K. M.; Joo, S. H.; Kang, M. S.; Yoo, W. C.; Kwak, S. K.; Kim, B. S. Hydrothermal Synthesis of Composition- and Morphology-Tunable Polyimide-Based Microparticles. *ACS Macro Letters* **2018**, *7*, 1480–1485.

[199] Dao, B.; Groth, A. M.; Hodgkin, J. Differential reactivity of aromatic diamines during polyimide formation in water. *European Polymer Journal* **2009**, *45*, 1607–1616.

[200] Ritter, N.; Senkovska, I.; Kaskel, S.; Weber, J. Intrinsically microporous poly(imide)s: Structure-porosity relationship studied by gas sorption and X-ray scattering. *Macromolecules* **2011**, *44*, 2025–2033.

[201] Abell, A. B.; Willis, K. L.; Lange, D. A. Mercury intrusion porosimetry and image analysis of cement-based materials. *Journal of Colloid and Interface Science* **1999**, *211*, 39–44.

[202] Maschita, J.; Banerjee, T.; Lotsch, B. V. Direct and Linker-Exchange Alcohol-Assisted Hydrothermal Synthesis of Imide-Linked Covalent Organic Frameworks. *Chemistry of Materials* **2022**, *34*, 2249–2258.

[203] Musgo, J.; Echeverría, J. C.; Estella, J.; Laguna, M.; Garrido, J. J. Ammonia-catalyzed silica xerogels: Simultaneous effects of pH, synthesis temperature, and ethanol:TEOS and water:TEOS molar ratios on textural and structural properties. *Microporous and Mesoporous Materials* **2009**, *118*, 280–287.

[204] Bett, W.; Cradock, S. Preparation of some silyl esters and study of their vibration spectra in gas and condensed phases. *Monatshefte für Chemie* **1980**, *111*, 193–198.

[205] Litovchenko, G. D.; Volokhina, A. V.; Papkov, S. P.; Sokolova, T. S.; Kudryavtsev, I. IRSspectra and Structure of Poly-p-Phenyleneterephthalamide. **1974**, *20*, 345–348.

[206] Tobin, M. C.; Carrano, M. J. Infrared spectra of polymers. I. Effect of crystallinity on the infrared spectrum of polyethylene and on the infrared spectra of nylon 6 and nylon 11. *The Journal of Chemical Physics* **1956**, *25*, 1044–1052.

[207] Lahnsteiner, M.; Moura, H. M.; Unterlass, M. M. Scanning electron microscopy images of polyimide networks from hydrothermal polymerization. 2021; `https://zenodo.org/record/4544904`.

[208] Morey, G. W.; Fournier, R. O.; Rowe, J. J. The solubility of quartz in water in the temperature interval from 25° to 300° C. *Geochimica et Cosmochimica Acta* **1962**, *26*, 1029–1043.

[209] Crundwell, F. K. On the Mechanism of the Dissolution of Quartz and Silica in Aqueous Solutions. *ACS Omega* **2017**, *2*, 1116–1127.

[210] Bennett, P. C.; Melcer, M. E.; Siegel, D. I.; Hassett, J. P. The dissolution of quartz in dilute aqueous solutions of organic acids at 25°C. *Geochimica et Cosmochimica Acta* **1988**, *52*, 1521–1530.

[211] Mitsyuk, B. M. Mechanism of silica dissolution and state of silicic acid in hydrothermal solutions. *Theoretical and Experimental Chemistry* **1984**, *19*, 554–559.

[212] Oehler, J. H. Hydrothermal crystallization of silica gel. *Bulletin of the Geological Society of America* **1976**, *87*, 1143–1152.

[213] Shtukenberg, A. G.; Punin, Y. O.; Gunn, E.; Kahr, B. Spherulites. *Chemical Reviews* **2012**, *3*, 1805–1838.

[214] Frondel, C. Characters of quartz fibers. *American Mineralogist* **1978**, *63*, 17–27.

[215] Yu, S. H.; Cölfen, H. Bio-inspired crystal morphogenesis by hydrophilic polymers. *Journal of Materials Chemistry* **2004**, *14*, 2124–2147.

[216] Kriechbaum, K.; Cerrón-Infantes, D. A.; Stöger, B.; Unterlass, M. M. Shape-Anisotropic Polyimide Particles by Solid-State Polycondensation of Monomer Salt Single Crystals. *Macromolecules* **2015**, *48*, 8773–8780.

[217] Konegger, T.; Liersch, A.; Gierl, C.; Scheffler, M. Bulk Ceramic Composites Derived from a Preceramic Polysilazane with Alumina and Zirconia Fillers. *Advanced Engineering Materials* **2013**, *15*, 394–406.

[218] E. Belowich, M.; Fraser Stoddart, J.; Belowich, M. E.; Stoddart, J. F. Dynamic imine chemistry. *Chemical Society Reviews* **2012**, *41*, 2003–2024.

[219] Vitaku, E.; Dichtel, W. R. Synthesis of 2D Imine-Linked Covalent Organic Frameworks through Formal Transimination Reactions. *Journal of the American Chemical Society* **2017**, *139*, 12911–12914.

[220] Ma, T.; Kapustin, E. A.; Yin, S. X.; Liang, L.; Zhou, Z.; Niu, J.; Li, L. H.; Wang, Y.; Su, J.; Li, J.; Wang, X.; Wang, W. D.; Wang, W.; Sun, J.; Yaghi, O. M. Single-crystal x-ray diffraction structures of covalent organic frameworks. *Science* **2018**, *361*, 48–52.

[221] Kuehl, V. A.; Wenzel, M. J.; Parkinson, B. A.; de Sousa Oliveira, L.; Hoberg, J. O. Pitfalls in the synthesis of polyimide-linked two-dimensional covalent organic frameworks. *Journal of Materials Chemistry A* **2021**, *9*, 15301–15309.

[222] Seddon, J. M. *Handbook of Liquid Crystals*; 2008; pp 635–679.

[223] Martinez-Richa, A.; Vera-Graziano, R. A solid-state NMR study of aromatic polyimides based on 4,4'-diaminotriphenylmethane. *Journal of Applied Polymer Science* **1998**, *70*, 1053–1064.

[224] Varner, S. J.; Vold, R. L.; Hoatson, G. L. Characterization of polyimides by 13C and 1H solid state nuclear magnetic resonance. *Solid State Nuclear Magnetic Resonance* **1998**, *12*, 71–85.

[225] Porod, G. Die Röntgenkleinwinkelstreuung von dichtgepackten kolloiden Systemen - I. Teil. *Kolloid-Zeitschrift* **1951**, *124*, 83–114.

[226] Freiberger, N.; Glatter, O. Small-angle scattering from hexagonal liquid crystals. *Journal of Physical Chemistry B* **2006**, *110*, 14719–14727.

[227] Förster, S.; Timmann, A.; Konrad, M.; Schellbach, C.; Meyer, A.; Funari, S. S.; Mulvaney, P.; Knott, R. Scattering curves of ordered mesoscopic materials. *Journal of Physical Chemistry B* **2005**, *109*, 1347–1360.

[228] Evans, A. M.; Ryder, M. R.; Ji, W.; Strauss, M. J.; Corcos, A. R.; Vitaku, E.; Flanders, N. C.; Bisbey, R. P.; Dichtel, W. R. Trends in the thermal stability of two-dimensional covalent organic frameworks. *Faraday Discussions* **2021**, *225*, 226–240.

[229] Shim, Jae Hu; Yu, Il Yeung; Kim, T. Y. Thermostable synthetic resin polymellitimides. *Hwahak Konghak* **1973**, *11*, 251–61.

[230] Shim, J.-H. Novel thermostable radial polymellitimides. *Materials Science Monographs* **1984**, *21*, 61–68.

[231] Shim, Jae-Hu; Lee, H.-M. Studies on preparation and thermostability of polyimides. *Polymer (Korea)* **1980**, *4*, 321–30.

[232] Trewin, A.; Cooper, A. I. Predicting microporous crystalline polyimides. *CrystEngComm* **2009**, *11*, 1819–1822.

[233] Huang, Q.; Li, W.; Mao, Z.; Qu, L.; Li, Y.; Zhang, H.; Yu, T.; Yang, Z.; Zhao, J.; Zhang, Y.; Aldred, M. P.; Chi, Z. An exceptionally flexible hydrogen-bonded organic framework with large-scale void regulation and adaptive guest accommodation abilities. *Nature Communications* **2019**, *10*.

[234] Yu, B.; Li, L.; Liu, S.; Wang, H.; Liu, H.; Lin, C.; Liu, C.; Wu, H.; Zhou, W.; Li, X.; Wang, T.; Chen, B.; Jiang, J. Robust Biological Hydrogen-Bonded Organic Framework with Post-Functionalized Rhenium(I) Sites for Efficient Heterogeneous Visible-Light-Driven CO2 Reduction. *Angewandte Chemie - International Edition* **2021**, *60*, 8983–8989.

[235] Hong, J.; Harbison, G. S. Determination of the structure of oriented samples using two-dimensional solid state NMR techniques. *Colloids and Surfaces* **1990**, *45*, 313–321.

[236] Rauche, M.; Ehrling, S.; Krause, S.; Senkovska, I.; Kaskel, S.; Brunner, E. New insights into solvent-induced structural changes of 13C labelled metal-organic frameworks by solid state NMR. *Chemical Communications* **2019**, *55*, 9140–9143.

[237] Clark, J. B.; Hastie, J. W.; Kihlborg, L. H. E.; Metselaar, R.; Thackeray, M. M. Definitions of Terms Relating to Phase Transitions of the Solid State. *Pure and Applied Chemistry* **1994**, *66*, 577–594.

[238] Yagofarov, M. I.; Nagrimanov, R. N.; Solomonov, B. N. Thermochemistry of phase transitions of aromatic amines: Estimation of the sublimation enthalpy at 298.15 K through the fusion enthalpy. *Journal of Chemical Thermodynamics* **2017**, *113*, 301–307.

[239] Achhammer, B. G.; Reinhart, F. W.; Kline, G. M. *Mechanism of the Degradation of Polyamides*; 1951; Vol. 46.

7 Statement of Contribution

Here, all contributions to this thesis are listed according to chapters and authors/collaborators are assigned to the corresponding tasks via initials. If a task was performed by more than one person, initials are ordered alphabetically.

Task abbreviations:

DAT	continuous data evaluation and discussion
TGA	thermogravimetric analysis measurements
INC	initiation and coordination of the project
IRS	infrared spectroscopy measurements
ITT-MS	inert thermal treatment coupled to mass spectrometry experiments
NMR	solution nuclear magnetic resonance measurements
ssNMR	solid state nuclear magnetic resonance measurements
SEM	scanning electron microscopy measurements
TEM	transmission electron microscopy
HIM	Helium ion microscopy
SYN	synthesis
PXRD	powder X-ray diffraction measurements
SAXS	small angle X-ray scattering measurements
BET	low pressure gas sorption measurements
MIP	mercury intrusion porosimetry
EA	organic elemental microanalysis measurements
US	upscaling
DSC	differential calorimetry measurements
WP	warm pressing
MECH	mechanical analysis
MI	model calculations and indexing of SAXS data

Initials:

ML	Marianne Lahnsteiner
MMU	Miriam M. Unterlass
HM	Hipassia Moura
DA	D. Alonso Cerrón-Infantes
HP	Herwig Peterlik
JR	Jérôme Roeser
TK	Thomas Konegger
RK	Ranjit Kulkarni
JT	Johannes Theiner
HK	Hanspeter Kählig
GP	Gernot Pacholik
JB	Johannes Bernardi
FA	Frances Allen

Chapter 4.1

DAT (MMU, ML), INC (MMU), SYN (ML), IRS (ML), XRD (ML), NMR (ML), SEM (HM, ML), TGA (ML), BET (JR, RK), MIP (TK), US (DA), DSC (DA), MECH (TK), WP (TK)

Chapter 4.2

DAT (MMU, ML), INC (MMU), SYN (HM, ML), IRS (HM, ML), XRD (HM, ML), NMR (ML), ssNMR (HK), SEM (HM, ML), TGA (ML), BET (HM), SAXS (HP), MI (HP), TEM (JB), HIM (FA)

Chapter 4.3

DAT (MMU, ML), INC (MMU), SYN (EH, ML), IRS (EH, ML), XRD (ML), NMR (ML), ssNMR (HK), SEM (ML), TGA (ML), BET (JR), ITT-MS (GP, ML), EA (JT)

A Appendix

A.1 Calculations

A.1.1 Indexing of PMA-An Bragg Reflections

An orthorhombic model was sufficient to identify nearly all observed peaks of PMA-An (ML281) using the image plate at a distance of 5.5 cm. For the evaluation of the lattice constants, the peaks shown with indices in Fig.30 were used. The sum of the squared difference between the calculated and the observed peak positions in q-space was minimized for a number of N identified peaks with respect to the lattice parameters (a, b, c):

$$\sum_{i=1}^{N}(q_{max,calc} - q_{max,exp})^2 = min.$$

The final results for the lattice constants were $a = 0.471$ nm, $b = 0.436$ nm, and $c = 1.801$ nm.

```
In[•]:= ml281 = {3.483, 6.965, 10.45, 13.74, 15.36, 16.13, 17.58, 19.3, 21.06, 22.52, 23.9,
          24.55, 25.55, 26.56, 27.58, 28.7, 29.7, 30.9, 31.55, 32.38, 32.86, 35.84, 37.97}

Out[•]= {3.483, 6.965, 10.45, 13.74, 15.36, 16.13, 17.58, 19.3, 21.06, 22.52, 23.9,
         24.55, 25.55, 26.56, 27.58, 28.7, 29.7, 30.9, 31.55, 32.38, 32.86, 35.84, 37.97}

In[•]:= ml281c = {13.62, 14.4, 15.2, 15.95, 17.6, 19.2, 19.9, 20.9, 21.4, 21.82, 22.49, 23.7,
          24.5, 25.38, 26.39, 27.46, 27.8, 28.6, 29.6, 30.8, 31.3, 32.5, 33.7, 35.6, 35.7}

Out[•]= {13.62, 14.4, 15.2, 15.95, 17.6, 19.2, 19.9, 20.9, 21.4, 21.82, 22.49, 23.7,
         24.5, 25.38, 26.39, 27.46, 27.8, 28.6, 29.6, 30.8, 31.3, 32.5, 33.7, 35.6, 35.7}

In[•]:= FindMinimum[ (qtriclinic[aaa, bbb, ccc, Pi / 2, Pi / 2, Pi / 2, 0, 0, 1] - ml281[[1]]) ^2 +
          (qtriclinic[aaa, bbb, ccc, Pi / 2, Pi / 2, Pi / 2, 0, 0, 2] - ml281[[2]]) ^2 +
          (qtriclinic[aaa, bbb, ccc, Pi / 2, Pi / 2, Pi / 2, 0, 0, 3] - ml281[[3]]) ^2 +
          ( (qtriclinic[aaa, bbb, ccc, Pi / 2, Pi / 2, Pi / 2, 1, 0, 0] +
                 qtriclinic[aaa, bbb, ccc, Pi / 2, Pi / 2, Pi / 2, 0, 0, 4]) / 2 - ml281c[[1]]) ^2
           (qtriclinic[aaa, bbb, ccc, Pi / 2, Pi / 2, Pi / 2, 0, 1, 0] - ml281c[[2]]) ^2 +
          (qtriclinic[aaa, bbb, ccc, Pi / 2, Pi / 2, Pi / 2, 1, 0, 2] - ml281c[[3]]) ^2 +
          (qtriclinic[aaa, bbb, ccc, Pi / 2, Pi / 2, Pi / 2, 0, 1, 2] - ml281c[[4]]) ^2 +
          (qtriclinic[aaa, bbb, ccc, Pi / 2, Pi / 2, Pi / 2, 0, 0, 5] - ml281c[[5]]) ^2 +
          (qtriclinic[aaa, bbb, ccc, Pi / 2, Pi / 2, Pi / 2, 1, 0, 4] - ml281c[[6]]) ^2 +
          ((qtriclinic[aaa, bbb, ccc, Pi / 2, Pi / 2, Pi / 2, 0, 1, 4] +
                qtriclinic[aaa, bbb, ccc, Pi / 2, Pi / 2, Pi / 2, 1, 1, 0] +
                qtriclinic[aaa, bbb, ccc, Pi / 2, Pi / 2, Pi / 2, 1, 1, 1]) / 3 - ml281c[[7]]) ^2 +
          ((qtriclinic[aaa, bbb, ccc, Pi / 2, Pi / 2, Pi / 2, 0, 0, 6] +
                qtriclinic[aaa, bbb, ccc, Pi / 2, Pi / 2, Pi / 2, 1, 1, 2]) / 2 - ml281c[[8]]) ^2 +
          (qtriclinic[aaa, bbb, ccc, Pi / 2, Pi / 2, Pi / 2, 1, 0, 5] - ml281c[[10]]) ^2 +
          ((qtriclinic[aaa, bbb, ccc, Pi / 2, Pi / 2, Pi / 2, 0, 1, 5] +
                qtriclinic[aaa, bbb, ccc, Pi / 2, Pi / 2, Pi / 2, 1, 1, 3]) / 2 - ml281c[[11]]) ^2 +
          (qtriclinic[aaa, bbb, ccc, Pi / 2, Pi / 2, Pi / 2, 0, 1, 6] - ml281c[[14]]) ^2,
         {aaa, 0.4, 0.5}, {bbb, 0.4, 0.5},
         {ccc, 1.75, 1.85}]

Out[•]= {0.0844095, {aaa → 0.470914, bbb → 0.436363, ccc → 1.80089}}
```

```
In[•]:= aa := 0.470914;
        bb := 0.436363;
        cc := 1.80089;
        angle := 90 Degree;
        qtriclinic[aa, bb, cc, Pi / 2, Pi / 2, angle, 0, 0, 1]
        qtriclinic[aa, bb, cc, Pi / 2, Pi / 2, angle, 0, 0, 2]
        qtriclinic[aa, bb, cc, Pi / 2, Pi / 2, angle, 0, 0, 3]
        qtriclinic[aa, bb, cc, Pi / 2, Pi / 2, angle, 0, 0, 4]
        qtriclinic[aa, bb, cc, Pi / 2, Pi / 2, angle, 1, 0, 0]
        Print[]
        qtriclinic[aa, bb, cc, Pi / 2, Pi / 2, angle, 0, 1, 0]
        qtriclinic[aa, bb, cc, Pi / 2, Pi / 2, angle, 1, 0, 2]
        qtriclinic[aa, bb, cc, Pi / 2, Pi / 2, angle, 0, 1, 2]
        qtriclinic[aa, bb, cc, Pi / 2, Pi / 2, angle, 0, 0, 5]
        qtriclinic[aa, bb, cc, Pi / 2, Pi / 2, angle, 1, 0, 4]
        Print[]
        qtriclinic[aa, bb, cc, Pi / 2, Pi / 2, angle, 1, 1, 0]
        qtriclinic[aa, bb, cc, Pi / 2, Pi / 2, angle, 0, 1, 4]
        qtriclinic[aa, bb, cc, Pi / 2, Pi / 2, angle, 1, 1, 1]
        qtriclinic[aa, bb, cc, Pi / 2, Pi / 2, angle, 0, 0, 6]
        qtriclinic[aa, bb, cc, Pi / 2, Pi / 2, angle, 1, 1, 2]
        qtriclinic[aa, bb, cc, Pi / 2, Pi / 2, angle, 1, 0, 5]
        qtriclinic[aa, bb, cc, Pi / 2, Pi / 2, angle, 1, 1, 3]
        qtriclinic[aa, bb, cc, Pi / 2, Pi / 2, angle, 0, 1, 5]
        qtriclinic[aa, bb, cc, Pi / 2, Pi / 2, angle, 0, 0, 7]
        qtriclinic[aa, bb, cc, Pi / 2, Pi / 2, angle, 1, 0, 6]
        qtriclinic[aa, bb, cc, Pi / 2, Pi / 2, angle, 0, 1, 6]

Out[•]= 3.48893

Out[•]= 6.97787

Out[•]= 10.4668

Out[•]= 13.9557

Out[•]= 13.3425


Out[•]= 14.399

Out[•]= 15.057

Out[•]= 16.0007

Out[•]= 17.4447

Out[•]= 19.3077


Out[•]= 19.6304

Out[•]= 20.0523

Out[•]= 19.9381
```

Out[•]= 20.9336

Out[•]= 20.8337

Out[•]= 21.9622

Out[•]= 22.2465

Out[•]= 22.6196

Out[•]= 24.4225

Out[•]= 24.8242

Out[•]= 25.4076

A.1.2 Small Angle X-Ray Scattering Model

In the used model, the SAXS intensities are described as structure factor $S_{(q)}$ times form factor $F_{(q)}$.

$$I_{(q)} = S_{(q)} \cdot F_{(q)}$$

For the structure factor, the multiple peak model was used[226,227], which consists of a sum of peak shape functions for the hexagonal lattice with mainly three parameters, the lattice distance for the center of the peak positions in reciprocal space, the FWHM of the peaks, from which the domain size is obtained by the Debye-Scherrer equation ($D = \frac{2\pi K}{FWHM}$), and a parameter ν, which changes the peak shape continuously from a Gaussian profile (in the limit nu towards infinity) to a Lorentzian profile (in the limit ν towards zero).

For the form factor, a large lamella with a thickness (height) H was used, which was early published by Porod[225]:

$$F_L(q) = \frac{2\pi}{q^2} H \left(\frac{sin(\frac{qH}{2})}{\frac{qH}{2}}\right)^2$$

The thickness of the lamella was numerically "smeared out" to describe a small size distribution of the thickness with a Gaussian profile of $\sigma = 0.2\,\mathrm{nm}$ half-width and a maximum of the peak position in real space at x_0:

$$F_L(q) = \int dx\, F_L(q(x)) \frac{1}{\sigma\sqrt{2\pi}} exp\left(-\frac{1}{2}\left(\frac{x - x_0}{\sigma}\right)^2\right)$$

```
In[•]:= (* Freiberger and Glatter J. Phys. Chem. B 2006, 110, 14719 *)
        kleingamma[nu_] := Sqrt[Pi] Gamma[(nu + 1) / 2] / Gamma[nu / 2]
        m[h_, k_] := If[h == k, 6, If[k == 0, 6, If[h == 0, 6, 12]]]
        qhk[h_, k_, g_] := (4 Pi / (g Sqrt[3])) Sqrt[h^2 + h k + k^2]
        lhk[q_, h_, k_, g_, nu_, delta_] := 2 / (Pi delta)
          Abs[(Gamma[nu / 2 + I kleingamma[nu] 2 (q - qhk[h, k, g]) / (Pi delta)]) / Gamma[nu / 2]]^2
        streu[q_, g_, nu_, delta_, c_] := c 2 / (Sqrt[3] g^2)
          Sum[m[h, k] × lhk[q, h, k, g, nu, delta], {h, 0, 4}, {k, 0, 4}]

        (* gleichmässige Dicke d, unendliche Fläche. G. Porod. Die
         Röntgenkleinwinkelstreuung von dichtgepackten kolloiden Systemen I,
        II. Kolloid-Z., 124,83-114 (1951) und 125,51-57, 109-122 (1952). *)
        lamelle[q_, xx_] := 2 Pi / q^2 xx (Sin[q xx / 2] / (q xx / 2))^2
        lamellenfun[q_, Dicke_?NumberQ, sigma_?NumberQ] := NIntegrate[
          lamelle[q, x] × gaussdistr[x, Dicke, sigma], {x, Dicke - 5 sigma, Dicke + 5 sigma}]
```

```
In[•]:= zielfun4[ampl2_, ra2_, g2_, fwhm2_, nu2_, dicke_, ddeltadicke_] :=
         Sum[(ampl2 lamellenfun[ML164[[i]][[1]], dicke, ddeltadicke] ×
               streu[ML164[[i]][[1]], g2, nu2, fwhm2, 1] - ML164[[i]][[2]])^2, {i, 1, 190}]
```

```
In[•]:= pp1 =
         FindMinimum[zielfun4[ampl23, 1, g23, fwhm23, nu23, dicke23, 0.2], {ampl23, 300, 900},
          {g23, 3.5, 3.7}, {fwhm23, 0.2, 0.3}, {nu23, 0.5, 3}, {dicke23, 0.5, 2}]
Out[•]= {154.036,
         {ampl23 → 37.6071, g23 → 3.61172, fwhm23 → 0.28243, nu23 → 1.58692, dicke23 → 1.15627}}
```

```
In[•]:= 3.61172 × 2 / Sqrt[3]
        3.61172 × 1.0774
        2 Pi / 0.2843
Out[•]= 4.17046

Out[•]= 3.89127

Out[•]= 22.1005
```

In[•]:=
```
ampl := pp1[[2]][[1]][[2]];

g := pp1[[2]][[2]][[2]];
fwhm := pp1[[2]][[3]][[2]];
nu := pp1[[2]][[4]][[2]];
dicke1 := pp1[[2]][[5]][[2]];
ddeltadicke1 := 0.2;

t2 = Plot[ampl lamellenfun[q, dicke1, ddeltadicke1] × streu[q, g, nu, hwhm, 1],
   {q, 1, 10}, PlotRange → {{1, 8}, {0, 110}}, PlotStyle → {Red}];
Show[ML164img, t2, PlotRange → {{1, 8}, {0, 110}}]
Show[ML164img, t2, PlotRange → {{1, 8}, {0, 10}}]
```

Out[•]=

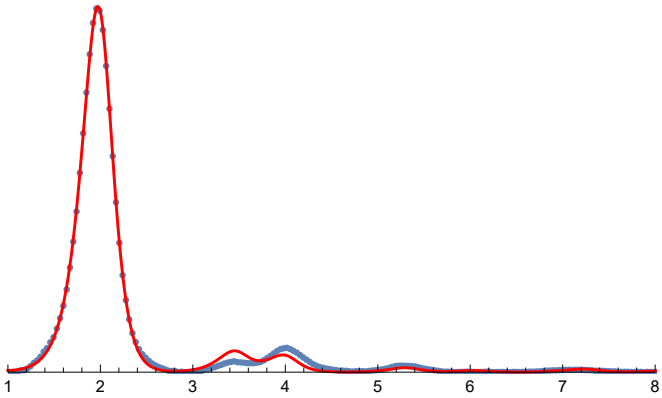

Out[•]=

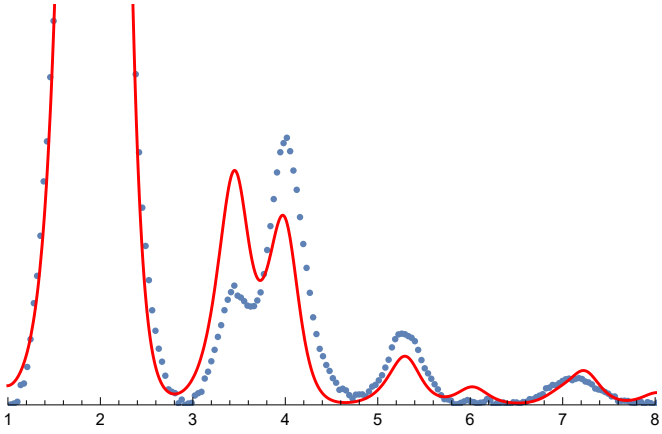

In[•]:=
```
out = Table[
   {N[q, 2], ampl lamellenfun[q, dicke1, ddeltadicke1, 1, 0] × streu[q, g, nu, hwhm, 1]},
   {q, 0.5, 8, 0.05}];
Export["mathfit_ML164lamelle.dat", out, "Table"]
```

Out[•]= mathfit_ML164lamelle.dat

```
In[•]:= zielfun4[ampl2_, ra2_, g2_, fwhm2_, nu2_, dicke_, ddeltadicke_] :=
         Sum[(ampl2 lamellenfun[ML189[[i]][[1]], dicke, ddeltadicke] ×
               streu[ML189[[i]][[1]], g2, nu2, fwhm2, 1] - ML189[[i]][[2]])^2, {i, 20, 96}] +
          Sum[(ampl2 lamellenfun[ML189[[i]][[1]], dicke, ddeltadicke] ×
               streu[ML189[[i]][[1]], g2, nu2, fwhm2, 1] - ML189[[i]][[2]])^2, {i, 118, 190}]

In[•]:= pp1 = FindMinimum[zielfun4[ampl23, 1, g23, fwhm23, nu23, dicke23, 0.2], {ampl23, 30, 50},
          {g23, 3.5, 3.7}, {fwhm23, 0.2, 0.3}, {nu23, 0.5, 3}, {dicke23, 0.5, 2}]

Out[•]= {7184.88, {ampl23 → 24.7575, g23 → 3.85225,
          fwhm23 → 0.161754, nu23 → -1.9489 × 10^-9, dicke23 → 0.694594}}

In[•]:= 3.85225 × 2 / Sqrt[3]
        3.85225 × 1.0774
        2 Pi / 0.161754

Out[•]= 4.4482

Out[•]= 4.15041

Out[•]= 38.8441
```

```
In[•]:= ampl := pp1[[2]][[1]][[2]];

        g := pp1[[2]][[2]][[2]];
        fwhm := pp1[[2]][[3]][[2]];
        nu := pp1[[2]][[4]][[2]];
        dicke1 := pp1[[2]][[5]][[2]];
        ddeltadicke1 := 0.2;

        t2 = Plot[ampl lamellenfun[q, dicke1, ddeltadicke1] × streu[q, g, nu, hwhm, 1],
            {q, 1, 10}, PlotRange → {{1, 8}, {0, 110}}, PlotStyle → {Red}];
        Show[ML189img, t2, PlotRange → {{1, 8}, {0, 110}}]
        Show[ML189img, t2, PlotRange → {{1, 8}, {0, 10}}]
```

Out[•]=

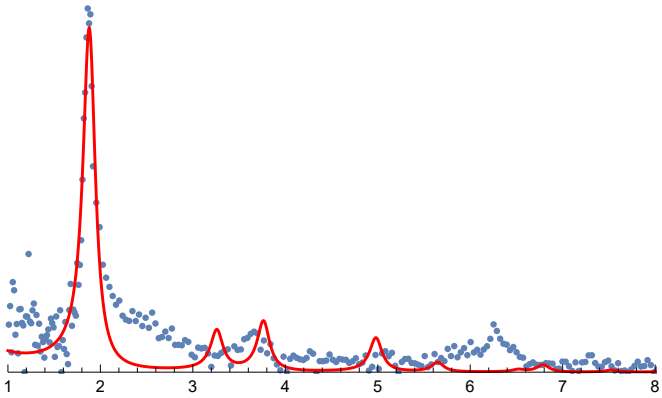

Out[•]=

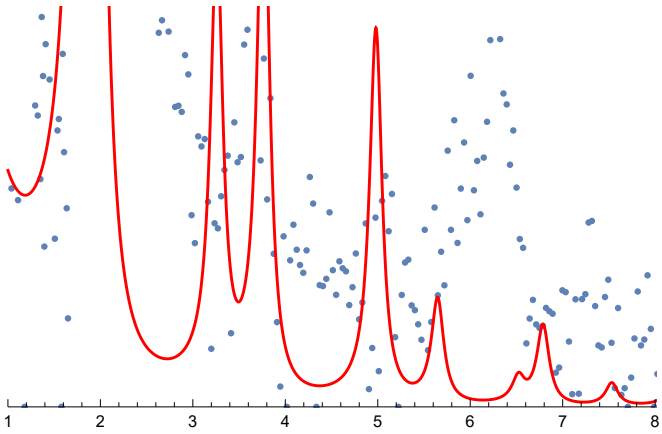


```
In[•]:= out = Table[
            {N[q, 2], ampl lamellenfun[q, dicke1, ddeltadicke1, 1, 0] × streu[q, g, nu, hwhm, 1]},
            {q, 0.5, 8, 0.05}];
        Export["mathfit_ML189lamelle.dat", out, "Table"]
```

Out[•]= mathfit_ML189lamelle.dat

```
In[•]:= zielfun4[ampl2_, ra2_, g2_, fwhm2_, nu2_, dicke_, ddeltadicke_] :=
         Sum[(ampl2 lamellenfun[ML196[[i]][[1]], dicke, ddeltadicke] ×
               streu[ML196[[i]][[1]], g2, nu2, fwhm2, 1] - ML196[[i]][[2]])^2, {i, 20, 96}] +
          Sum[(ampl2 lamellenfun[ML196[[i]][[1]], dicke, ddeltadicke] ×
               streu[ML196[[i]][[1]], g2, nu2, fwhm2, 1] - ML196[[i]][[2]])^2, {i, 118, 190}]

In[•]:= pp1 = FindMinimum[zielfun4[ampl23, 1, g23, fwhm23, nu23, dicke23, 0.2], {ampl23, 30, 50},
          {g23, 3.5, 3.7}, {fwhm23, 0.2, 0.3}, {nu23, 0.5, 3}, {dicke23, 0.5, 2}]

Out[•]= {1210.37, {ampl23 → 29.1934, g23 → 3.53478,
          fwhm23 → 0.199313, nu23 → -0.0307204, dicke23 → 1.10583}}

In[•]:= 3.53478 × 2 / Sqrt[3]
        3.53478 × 1.0774
        2 Pi / 0.199313

Out[•]= 4.08161

Out[•]= 3.80837

Out[•]= 31.5242
```

In[•]:=
```
ampl := pp1[[2]][[1]][[2]];

g := pp1[[2]][[2]][[2]];
fwhm := pp1[[2]][[3]][[2]];
nu := pp1[[2]][[4]][[2]];
dicke1 := pp1[[2]][[5]][[2]];
ddeltadicke1 := 0.2;

t2 = Plot[ampl lamellenfun[q, dicke1, ddeltadicke1] × streu[q, g, nu, hwhm, 1],
   {q, 1, 10}, PlotRange → {{1, 8}, {0, 110}}, PlotStyle → {Red}];
Show[ML196img, t2, PlotRange → {{1, 8}, {0, 110}}]
Show[ML196img, t2, PlotRange → {{1, 8}, {0, 10}}]
```

Out[•]=

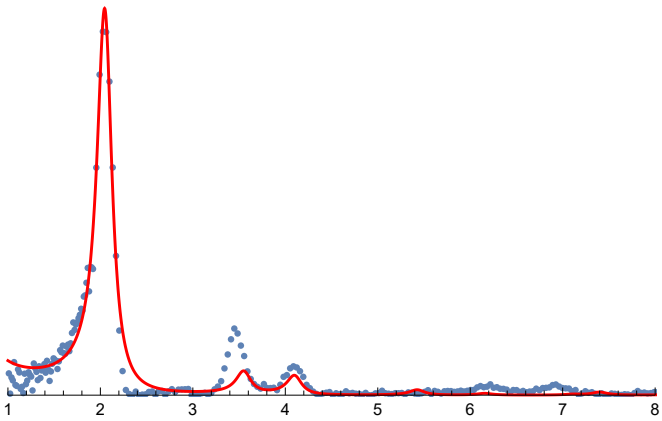

Out[•]=

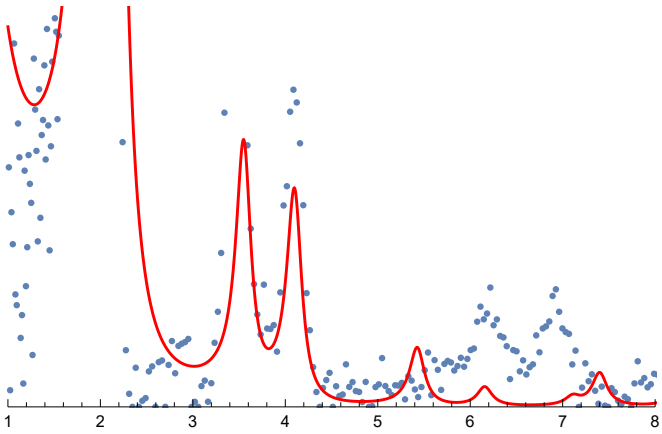

In[•]:=
```
out = Table[
   {N[q, 2], ampl lamellenfun[q, dicke1, ddeltadicke1, 1, 0] × streu[q, g, nu, hwhm, 1]},
   {q, 0.5, 8, 0.05}];
Export["mathfit_ML196lamelle.dat", out, "Table"]
```

Out[•]= mathfit_ML196lamelle.dat

```
In[•]:= zielfun4[ampl2_, ra2_, g2_, fwhm2_, nu2_, dicke_, ddeltadicke_] :=
         Sum[(ampl2 lamellenfun[ML269[[i]][[1]], dicke, ddeltadicke] ×
               streu[ML269[[i]][[1]], g2, nu2, fwhm2, 1] - ML269[[i]][[2]])^2, {i, 1, 64}] +
          Sum[(ampl2 lamellenfun[ML269[[i]][[1]], dicke, ddeltadicke] ×
               streu[ML269[[i]][[1]], g2, nu2, fwhm2, 1] - ML269[[i]][[2]])^2, {i, 83, 150}]

In[•]:= pp1 = FindMinimum[zielfun4[ampl23, 1, g23, fwhm23, nu23, dicke23, 0.2], {ampl23, 30, 50},
          {g23, 3.5, 3.7}, {fwhm23, 0.2, 0.3}, {nu23, 0.5, 3}, {dicke23, 0.5, 2}]

Out[•]= {185.889,
         {ampl23 → 23.4226, g23 → 3.91191, fwhm23 → 0.178817, nu23 → 110 145., dicke23 → 1.60484}}

In[•]:= 3.91191 × 2 / Sqrt[3]
        3.91191 × 1.0774
        2 Pi / 0.178817

Out[•]= 4.51708

Out[•]= 4.21469

Out[•]= 35.1375
```

```
ampl := pp1[[2]][[1]][[2]];

g := pp1[[2]][[2]][[2]];
fwhm := pp1[[2]][[3]][[2]];
nu := pp1[[2]][[4]][[2]];
dicke1 := pp1[[2]][[5]][[2]];
ddeltadicke1 := 0.2;

t2 = Plot[ampl lamellenfun[q, dicke1, ddeltadicke1] × streu[q, g, nu, hwhm, 1],
   {q, 1, 10}, PlotRange → {{1, 8}, {0, 110}}, PlotStyle → {Red}];
Show[ML269img, t2, PlotRange → {{1, 8}, {0, 110}}]
Show[ML269img, t2, PlotRange → {{1, 8}, {0, 10}}]
```

Out[•]=

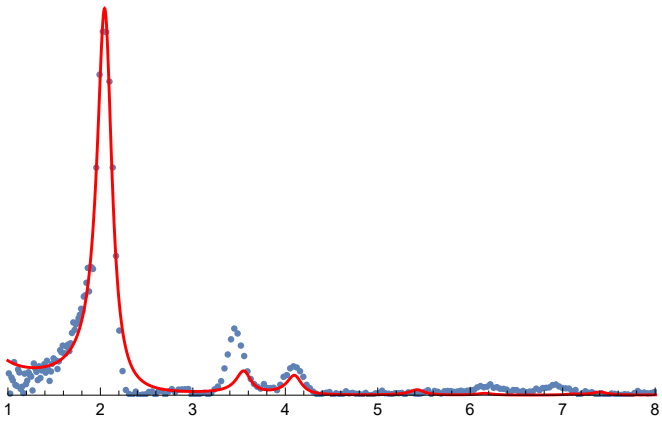

Out[•]=

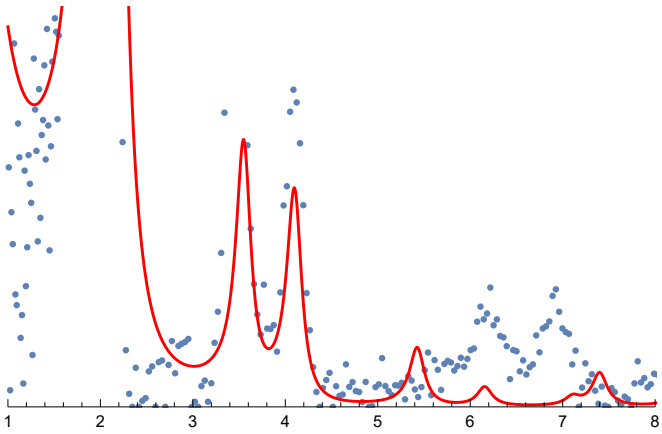

In[•]:=
```
out = Table[
   {N[q, 2], ampl lamellenfun[q, dicke1, ddeltadicke1, 1, 0] × streu[q, g, nu, hwhm, 1]},
   {q, 0.5, 8, 0.05}];
Export["mathfit_ML269lamelle.dat", out, "Table"]
```

Out[•]= mathfit_ML269lamelle.dat

```
In[•]:= zielfun4[ampl2_, ra2_, g2_, fwhm2_, nu2_, dicke_, ddeltadicke_] :=
         Sum[(ampl2 lamellenfun[ML188[[i]][[1]], dicke, ddeltadicke] ×
               streu[ML188[[i]][[1]], g2, nu2, fwhm2, 1] - ML188[[i]][[2]])^2, {i, 25, 75}] +
          Sum[(ampl2 lamellenfun[ML188[[i]][[1]], dicke, ddeltadicke] ×
               streu[ML188[[i]][[1]], g2, nu2, fwhm2, 1] - ML188[[i]][[2]])^2, {i, 76, 96}] +
          Sum[(ampl2 lamellenfun[ML188[[i]][[1]], dicke, ddeltadicke] ×
               streu[ML188[[i]][[1]], g2, nu2, fwhm2, 1] - ML188[[i]][[2]])^2, {i, 118, 190}]

In[•]:= pp1 = FindMinimum[zielfun4[ampl23, 1, g23, fwhm23, nu23, dicke23, 0.2], {ampl23, 30, 50},
           {g23, 3.5, 3.7}, {fwhm23, 0.2, 0.3}, {nu23, 0.5, 3}, {dicke23, 0.5, 2}]

Out[•]= {10 704.6, {ampl23 → 67.5466, g23 → 3.76422,
           fwhm23 → 0.209322, nu23 → 0.0000846866, dicke23 → 0.224577}}

In[•]:= pp1[[2]][[2]][[2]] 2 / Sqrt[3]
        pp1[[2]][[2]][[2]] 1.07754
        2 Pi / pp1[[2]][[3]][[2]]

Out[•]= 4.34655

Out[•]= 4.0561

Out[•]= 30.0168
```

In[•]:=
```
ampl := pp1[[2]][[1]][[2]];

g := pp1[[2]][[2]][[2]];
fwhm := pp1[[2]][[3]][[2]];
nu := pp1[[2]][[4]][[2]];
dicke1 := pp1[[2]][[5]][[2]];
ddeltadicke1 := 0.2;

t2 = Plot[ampl lamellenfun[q, dicke1, ddeltadicke1] × streu[q, g, nu, hwhm, 1],
   {q, 1, 10}, PlotRange → {{1, 8}, {0, 110}}, PlotStyle → {Red}];
Show[ML188img, t2, PlotRange → {{1, 8}, {0, 110}}]
Show[ML188img, t2, PlotRange → {{1, 8}, {0, 10}}]
```

Out[•]=

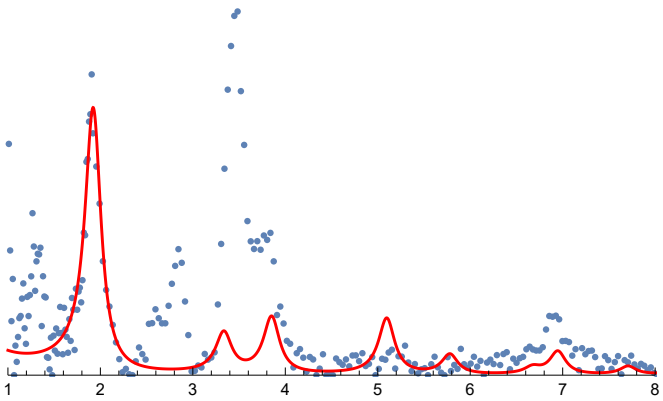

Out[•]=

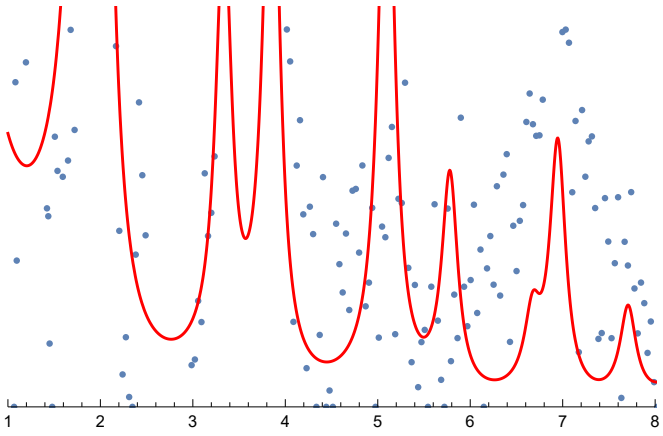

In[•]:=
```
out = Table[
   {N[q, 2], ampl lamellenfun[q, dicke1, ddeltadicke1, 1, 0] × streu[q, g, nu, hwhm, 1]},
   {q, 0.5, 8, 0.05}];
Export["mathfit_ML188lamelle.dat", out, "Table"]
```

Out[•]= mathfit_ML188lamelle.dat

```
In[•]:= zielfun4[ampl2_, ra2_, g2_, fwhm2_, nu2_, dicke_, ddeltadicke_] :=
         Sum[(ampl2 lamellenfun[ML195[[i]][[1]], dicke, ddeltadicke] ×
               streu[ML195[[i]][[1]], g2, nu2, fwhm2, 1] - ML195[[i]][[2]])^2, {i, 20, 96}] +
          Sum[(ampl2 lamellenfun[ML195[[i]][[1]], dicke, ddeltadicke] ×
               streu[ML195[[i]][[1]], g2, nu2, fwhm2, 1] - ML195[[i]][[2]])^2, {i, 118, 190}]

In[•]:= pp1 = FindMinimum[zielfun4[ampl23, 1, g23, fwhm23, nu23, dicke23, 0.2], {ampl23, 30, 50},
          {g23, 3.5, 3.7}, {fwhm23, 0.2, 0.3}, {nu23, 0.5, 3}, {dicke23, 0.5, 2}]

Out[•]= {3809.25, {ampl23 → 19.3794, g23 → 3.89316,
          fwhm23 → 0.152196, nu23 → -1.60306 × 10^-6, dicke23 → 0.963523}}

In[•]:= pp1[[2]][[2]][[2]] 2 / Sqrt[3]
        pp1[[2]][[2]][[2]] 1.07754
        2 Pi / pp1[[2]][[3]][[2]]

Out[•]= 4.49544

Out[•]= 4.19504

Out[•]= 41.2834
```

In[•]:=
```
ampl := pp1[[2]][[1]][[2]];

g := pp1[[2]][[2]][[2]];
fwhm := pp1[[2]][[3]][[2]];
nu := pp1[[2]][[4]][[2]];
dicke1 := pp1[[2]][[5]][[2]];
ddeltadicke1 := 0.2;

t2 = Plot[ampl lamellenfun[q, dicke1, ddeltadicke1] × streu[q, g, nu, hwhm, 1],
   {q, 1, 10}, PlotRange → {{1, 8}, {0, 110}}, PlotStyle → {Red}];
Show[ML195img, t2, PlotRange → {{1, 8}, {0, 110}}]
Show[ML195img, t2, PlotRange → {{1, 8}, {0, 10}}]
```

Out[•]=

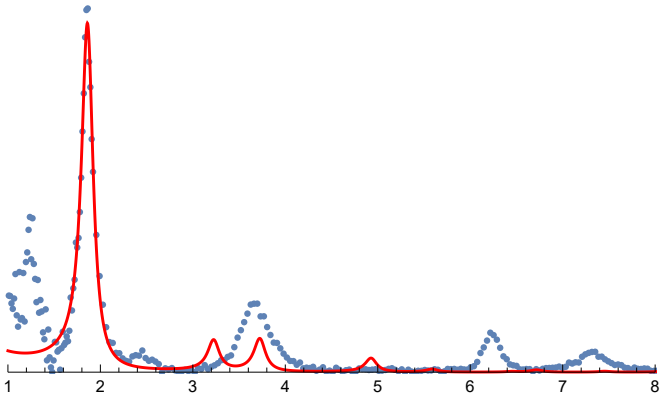

Out[•]=

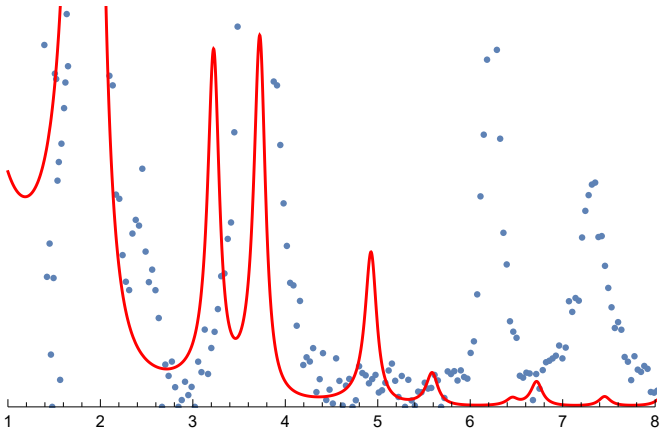

In[•]:=
```
out = Table[
   {N[q, 2], ampl lamellenfun[q, dicke1, ddeltadicke1, 1, 0] × streu[q, g, nu, hwhm, 1]},
   {q, 0.5, 8, 0.05}];
Export["mathfit_ML195lamelle.dat", out, "Table"]
```

Out[•]= mathfit_ML195lamelle.dat

```
In[•]:= zielfun4[ampl2_, ra2_, g2_, fwhm2_, nu2_, dicke_, ddeltadicke_] :=
         Sum[(ampl2 lamellenfun[ML173[[i]][[1]], dicke, ddeltadicke] ×
               streu[ML173[[i]][[1]], g2, nu2, fwhm2, 1] - ML173[[i]][[2]])^2, {i, 5, 57}] +
          Sum[(ampl2 lamellenfun[ML173[[i]][[1]], dicke, ddeltadicke] ×
               streu[ML173[[i]][[1]], g2, nu2, fwhm2, 1] - ML173[[i]][[2]])^2, {i, 79, 150}]

In[•]:= pp1 = FindMinimum[zielfun4[ampl23, 1, g23, fwhm23, nu23, dicke23, 0.2], {ampl23, 30, 50},
           {g23, 3.3, 3.6}, {fwhm23, 0.3, 0.4}, {nu23, 0.5, 1}, {dicke23, 0.5, 2}]

Out[•]= {914.165,
         {ampl23 → 57.8919, g23 → 3.30903, fwhm23 → 0.379726, nu23 → 0.718535, dicke23 → 1.33221}}

In[•]:= pp1[[2]][[2]][[2]] 2 / Sqrt[3]
        pp1[[2]][[2]][[2]] 1.07754
        2 Pi / pp1[[2]][[3]][[2]]

Out[•]= 3.82094

Out[•]= 3.56561

Out[•]= 16.5466
```

```
In[•]:= ampl := pp1[[2]][[1]][[2]];

        g := pp1[[2]][[2]][[2]];
        fwhm := pp1[[2]][[3]][[2]];
        nu := pp1[[2]][[4]][[2]];
        dicke1 := pp1[[2]][[5]][[2]];
        ddeltadicke1 := 0.2;

        t2 = Plot[ampl lamellenfun[q, dicke1, ddeltadicke1] × streu[q, g, nu, hwhm, 1],
            {q, 1, 10}, PlotRange → {{1, 8}, {0, 110}}, PlotStyle → {Red}];
        Show[ML173img, t2, PlotRange → {{1, 8}, {0, 110}}]
        Show[ML173img, t2, PlotRange → {{1, 8}, {0, 10}}]
```

Out[•]=

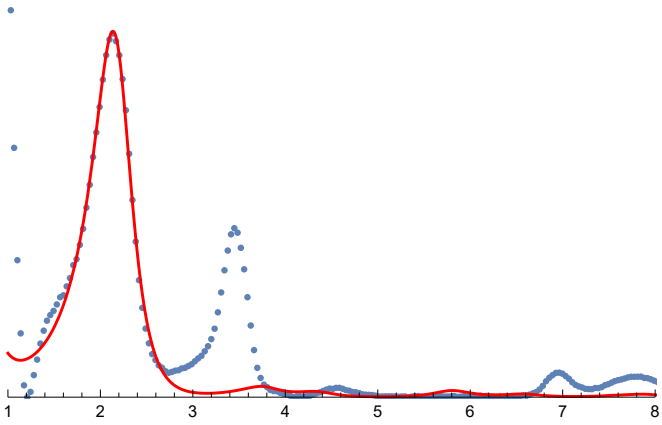

Out[•]=

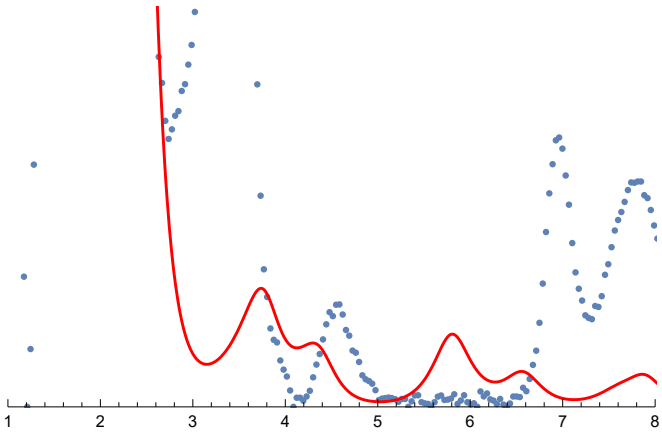


```
In[•]:= out = Table[
            {N[q, 2], ampl lamellenfun[q, dicke1, ddeltadicke1, 1, 0] × streu[q, g, nu, hwhm, 1]},
            {q, 0.5, 8, 0.05}];
        Export["mathfit_ML173lamelle.dat", out, "Table"]
```

Out[•]= mathfit_ML173lamelle.dat

In[•]:=

```
In[•]:= zielfun4[ampl2_, ra2_, g2_, fwhm2_, nu2_, dicke_, ddeltadicke_] :=
         Sum[(ampl2 lamellenfun[ML172[[i]][[1]], dicke, ddeltadicke] ×
               streu[ML172[[i]][[1]], g2, nu2, fwhm2, 1] - ML172[[i]][[2]])^2, {i, 5, 57}] +
          Sum[(ampl2 lamellenfun[ML172[[i]][[1]], dicke, ddeltadicke] ×
               streu[ML172[[i]][[1]], g2, nu2, fwhm2, 1] - ML172[[i]][[2]])^2, {i, 79, 150}]

In[•]:= pp1 = FindMinimum[zielfun4[ampl23, 1, g23, fwhm23, nu23, dicke23, 0.2], {ampl23, 30, 50},
          {g23, 3.3, 3.6}, {fwhm23, 0.3, 0.4}, {nu23, 0.5, 1}, {dicke23, 0.5, 2}]

Out[•]= {2496.12, {ampl23 → 26.1996, g23 → 3.63412,
          fwhm23 → 0.259583, nu23 → 0.824331, dicke23 → 0.732361}}

In[•]:= pp1[[2]][[2]][[2]] 2 / Sqrt[3]
        pp1[[2]][[2]][[2]] 1.07754
        2 Pi / pp1[[2]][[3]][[2]]

Out[•]= 4.19632

Out[•]= 3.91591

Out[•]= 24.2049
```

In[•]:=
```
ampl := pp1[[2]][[1]][[2]];

g := pp1[[2]][[2]][[2]];
fwhm := pp1[[2]][[3]][[2]];
nu := pp1[[2]][[4]][[2]];
dicke1 := pp1[[2]][[5]][[2]];
ddeltadicke1 := 0.2;

t2 = Plot[ampl lamellenfun[q, dicke1, ddeltadicke1] × streu[q, g, nu, hwhm, 1],
   {q, 1, 10}, PlotRange → {{1, 8}, {0, 110}}, PlotStyle → {Red}];
Show[ML172img, t2, PlotRange → {{1, 8}, {0, 110}}]
Show[ML172img, t2, PlotRange → {{1, 8}, {0, 10}}]
```

Out[•]=

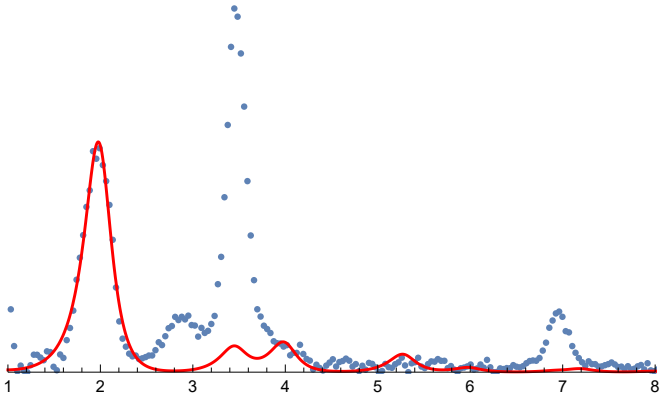

Out[•]=

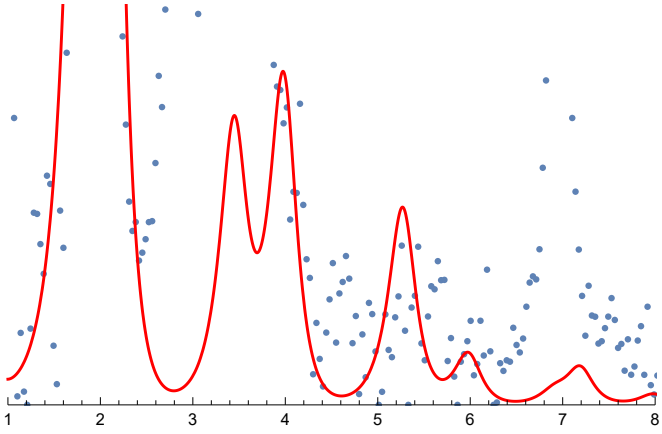

In[•]:=
```
out = Table[
   {N[q, 2], ampl lamellenfun[q, dicke1, ddeltadicke1, 1, 0] × streu[q, g, nu, hwhm, 1]},
   {q, 0.5, 8, 0.05}];
Export["mathfit_ML172lamelle.dat", out, "Table"]
```

Out[•]= mathfit_ML172lamelle.dat

A.1.3 Organic Elemental Microanalysis

Mass percentages for the corresponding elements of MS(MA-PDA)$_{H_2O}$, MS(MA-PDA)$_{THF}$, and MS(MA-Bz)$_{THF}$ including the amount of residual solvent (either H_2O or THF) n_S were calculated using the equation below. The amount of the cation (either PDA or Bz) was held constant at $n_C = 1$ and n_A and n_S were varied in order to fit the elemental analysis results (see Table A1).

$$wt.\% = \frac{n_A \chi_A M_A + \chi_C M_C + n_S \chi_S M_S}{n_A M_A + 1 M_C + n_S M_S}$$

n_A = number of the anion mellitic acid
n_S = number of the solvent molecules (H_2O or THF)
χ_A = mole fraction of the anion mellitic acid
χ_C = mole fraction of the cation (PDA or Bz)
χ_S = mole fraction of the solvent molecules (H_2O or THF)
M_A = molecular mass of mellitic acid
M_C = molecular mass of the cation (PDA, Bz)
M_S = molecular mass of the solvent molecules (H_2O or THF)

Table A1: EA results and calculated values for MS(MA-PDA)$_{H_2O}$, MS(MA-PDA)$_{THF}$, and MS(MA-Bz)$_{THF}$.

	wt. % C	*wt.* % H	*wt.* % N	*wt.* % O	C:N	C:O
MS(MA-PDA)$_{H_2O}$	43.92	4.52	7.34	43.17	6.98	1.36
MS(MA-PDA)$_{H_2O}$ calc.	44.49	4.48	7.52	43.51	6.90	1.36
MS(MA-PDA)$_{THF}$	43.74	4.33	7.17	42.55	7.12	1.37
MS(MA-PDA)$_{THF}$ calc.	44.45	4.77	7.11	43.67	7.28	1.36
MS(MA-Bz)$_{THF}$	58.58	4.74	6.71	31.10	10.18	2.51
MS(MA-Bz)$_{THF}$ calc.	58.72	4.31	6.42	30.55	10.68	2.56

A.1.4 Statistical Evaluation of PXRD FWHM

FWHM of selected reflections from PXRD patterns of the screening samples (Chapter 4.3.4) were statistically evaluated. To identify trends and possible outliers, a robust method employing the *median* and the scale estimator "Median Absolute Deviation" (MAD) instead of mean and standard deviation was used.

$$MAD = \underset{1 \leq i \leq n}{median} \, | \, x_i - x_M \, |$$

The estimator is only consisted after correction with a factor giving ^{s}MAD:

$$^{s}MAD = \frac{MAD}{0.675} = 1.834 \cdot \, MAD$$

As confidence interval, twice the ^{s}MAD was used:

$$median \pm 2 \cdot \, ^{s}MAD$$

A.2 Data, Plots, and Microscopy Images

A.2.1 ATR-FT-IR Spectra and X-Ray Patterns

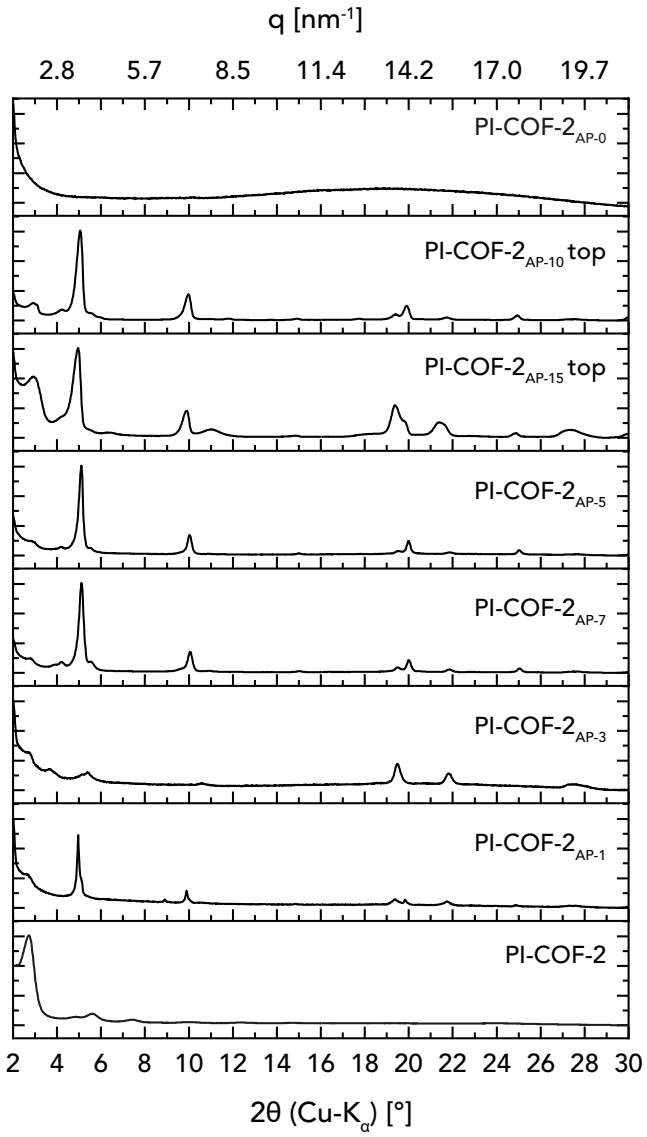

Figure A1: PXRD patterns of PI-COF-2_{AP-0} - PI-COF-2_{AP-15} and PI-COF-2 benchmark.

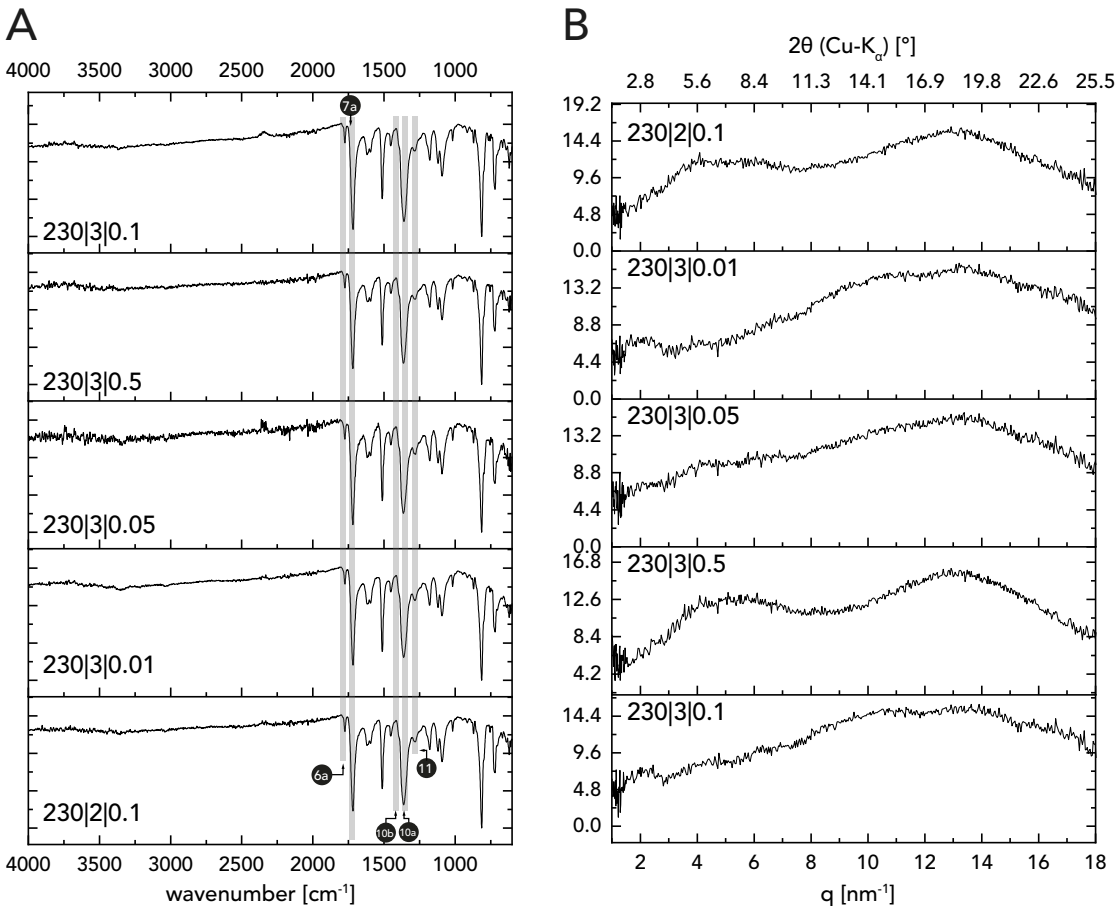

Figure A2: ATR-FT-IR spectra and PXRD patterns of PI-COF-2 samples via aaHTP-MW at 230 °C. A: All ATR-FT-IR spectra show the typical imide modes **6a** $\tilde{\nu}$ (C=O)as = 1785 cm^{-1}, **7a** $\tilde{\nu}$ (C=O)s = 1720 cm^{-1}, and **10a** $\tilde{\nu}$ (C-N) = 1365 cm^{-1}. None of them show a second set of imide modes. Furthermore, only two amide vibration were found, which is a small shoulder at **10b** $\tilde{\nu}$ = 1395 cm^{-1} and **11** $\tilde{\nu}$ = 1285 cm^{-1}. B: All SAXS patterns featured amorphous halos and no Bragg reflections.

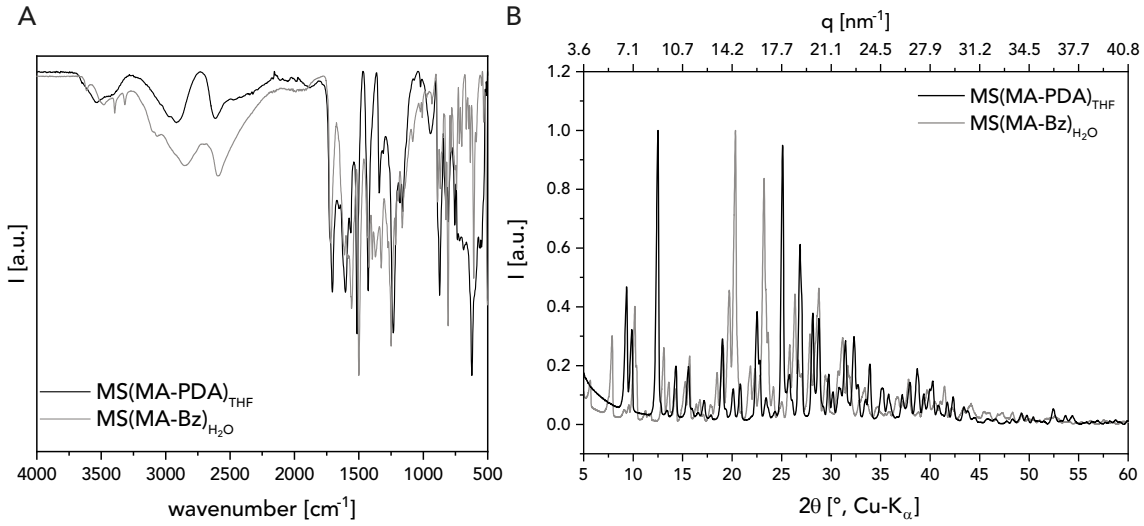

Figure A3: A: ATR-FT-IR and B: PXRD of MS(MA-PDA)$_{THF}$ and MS(MA-Bz)$_{H_2O}$.

A.2.2 Gas Sorption and Mecury Intrusion Porosimetry

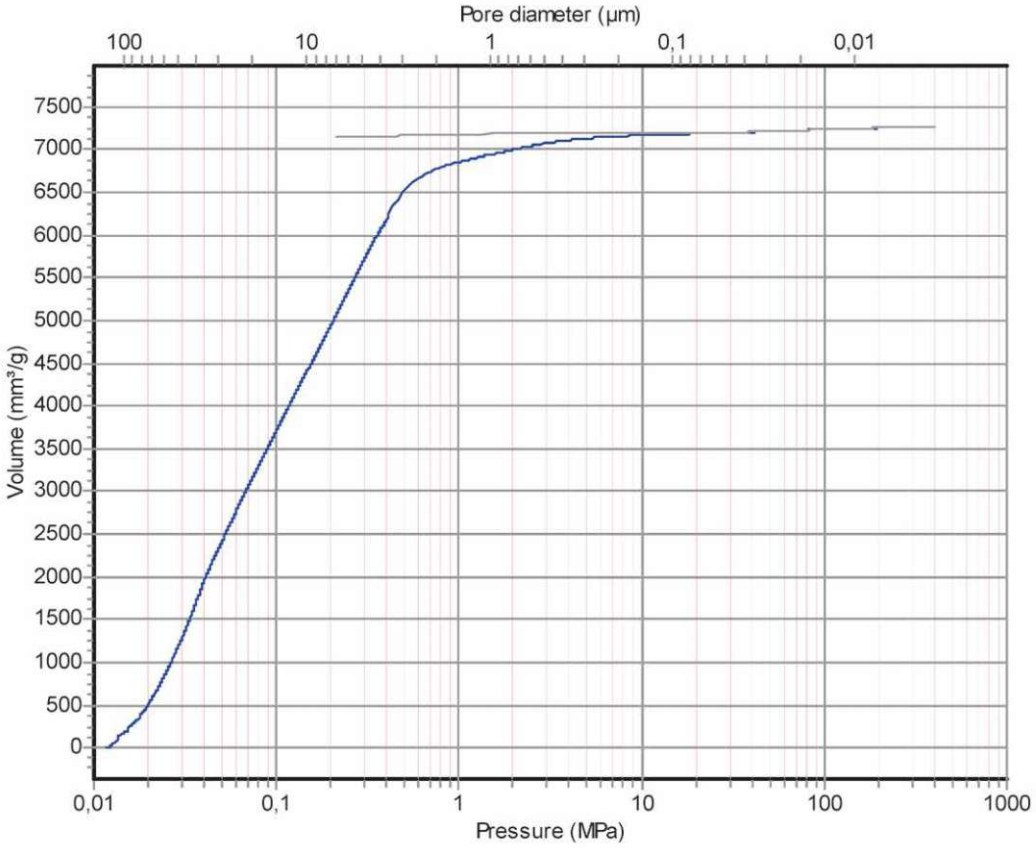

Figure A4: Intrusion and extrusion curve of MIP measurements of the PI(TAPB-PMA) monolith.

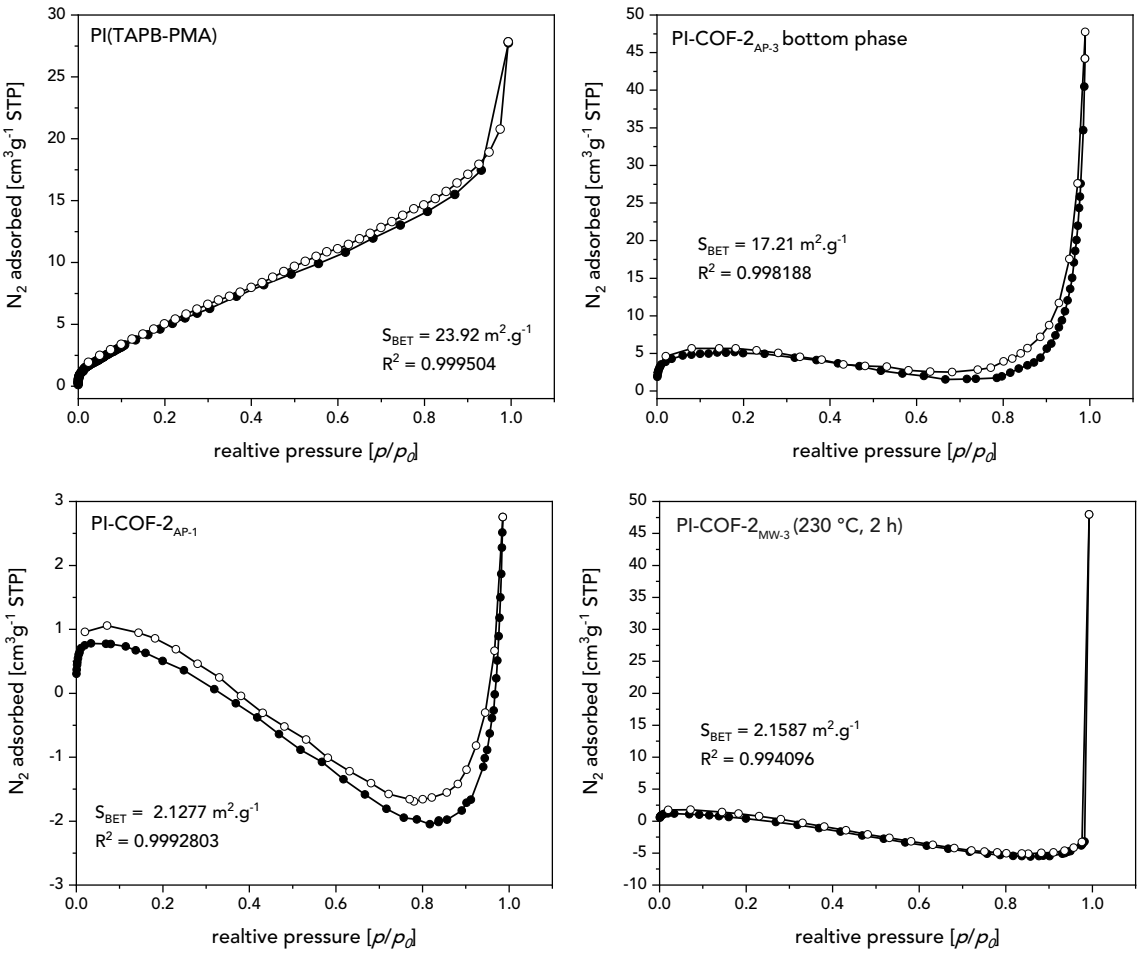

Figure A5: Low pressure N_2 gas sorption isotherms of PI(TAPB-PMA), PI-COF-2_{AP-1}, PI-COF-2_{AP-3} and PI-COF-2 via aaHTP-MW synthesized at 230 °C and 2 h.

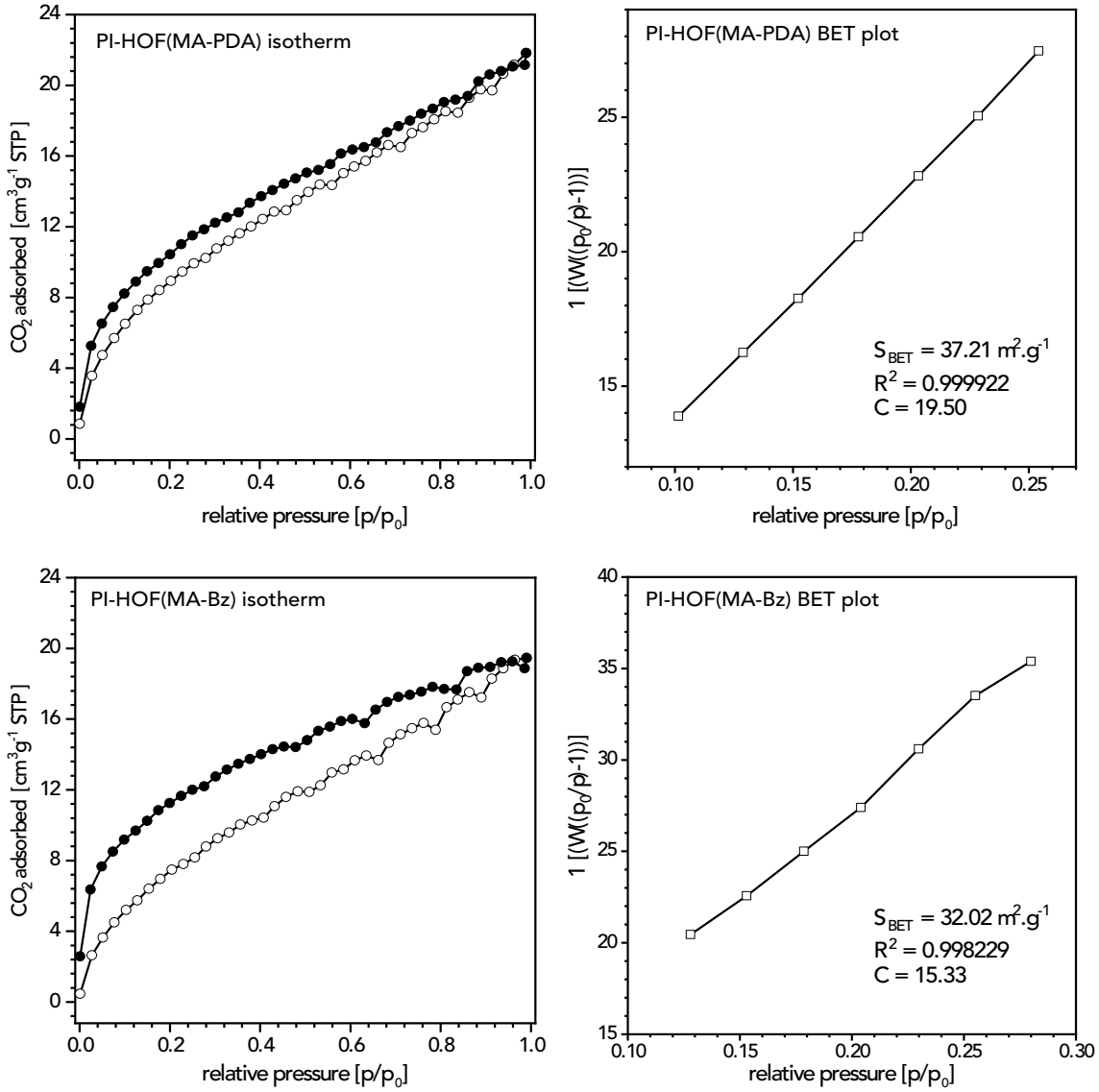

Figure A6: Low pressure CO_2 gas sorption isotherms and BET plots of PI-HOF(MA-PDA) and PI-HOF(MA-Bz).

A.2.3 Thermogravimetric Analysis Plots

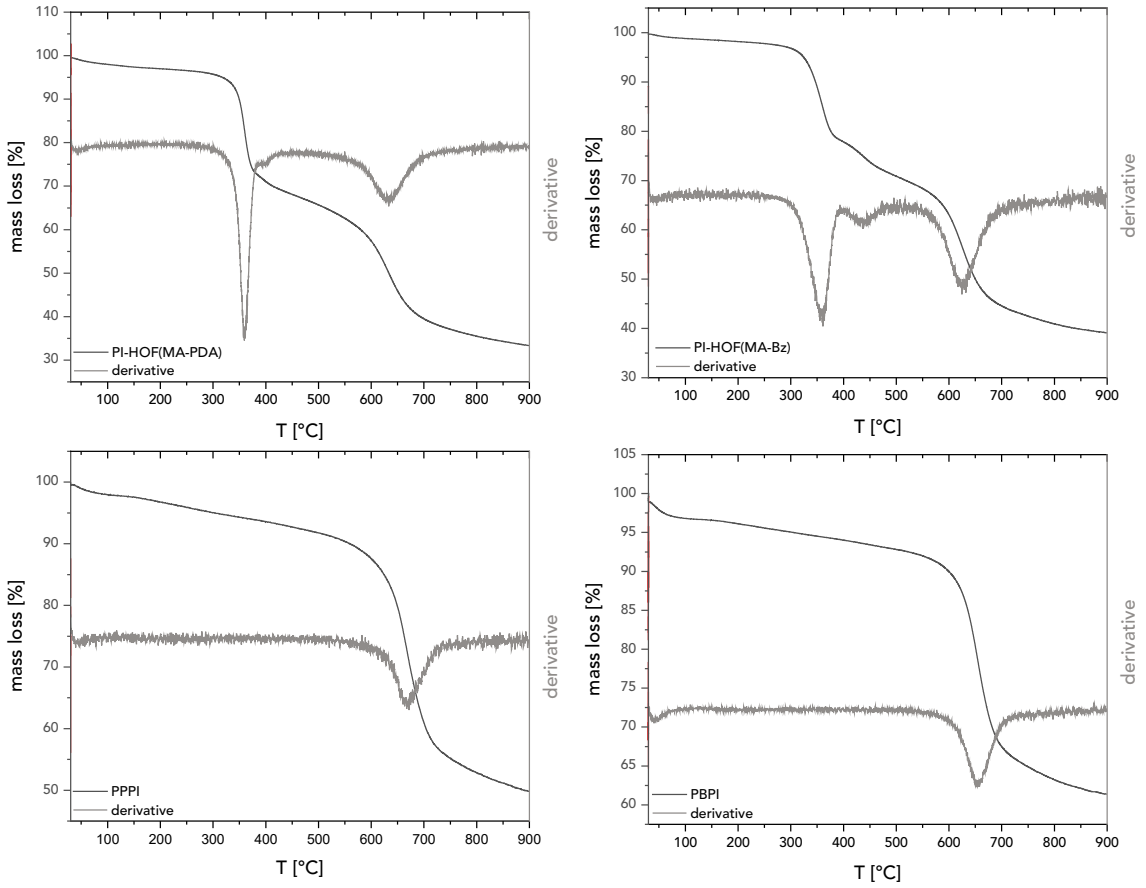

Figure A7: TGA curves of PI-HOF samples, PPPI, and PBPI and their derivatives (gray).

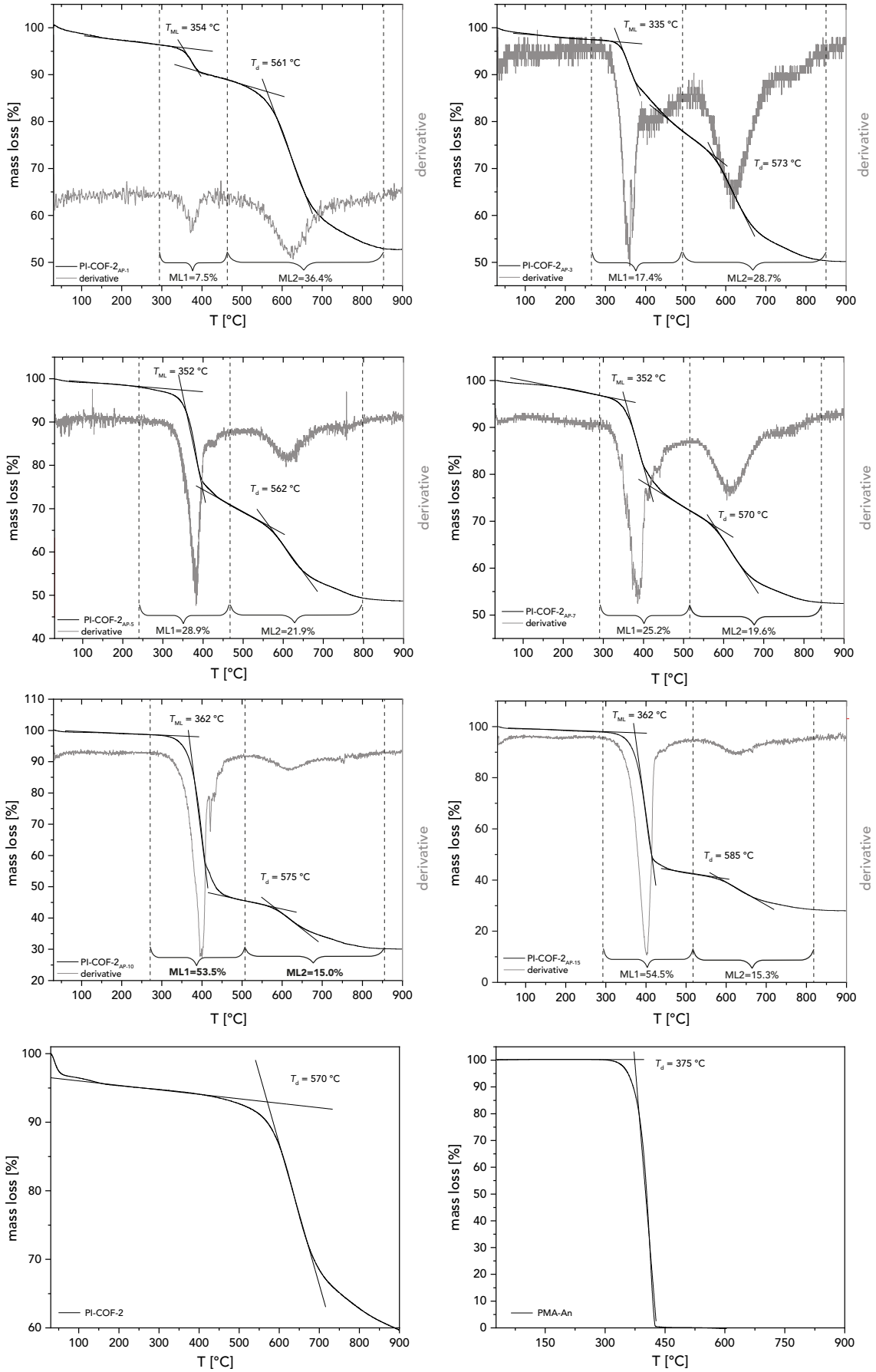

Figure A8: TGA curves of PI-COF-2 samples via HTP-AP with tangents (black) and derivatives (gray).

A.2.4 Solution ^{1}H-NMR Spectra

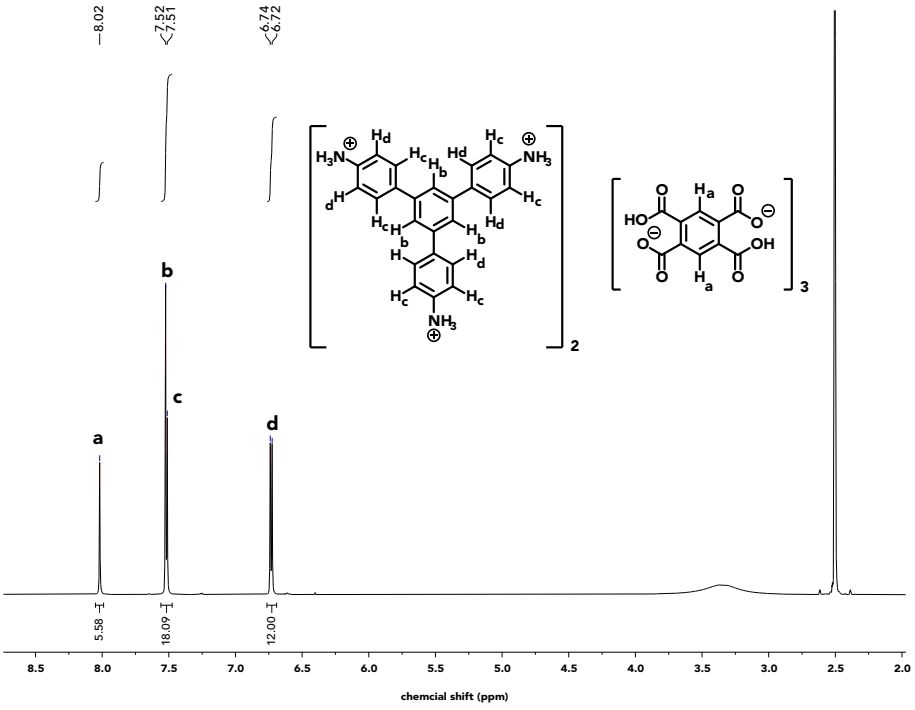

Figure A9: ^{1}H-NMR spectrum of Ms(TAPB-PMA) $[H_3TAPB^{3+}]_2[PMA^{2-}]_3$.

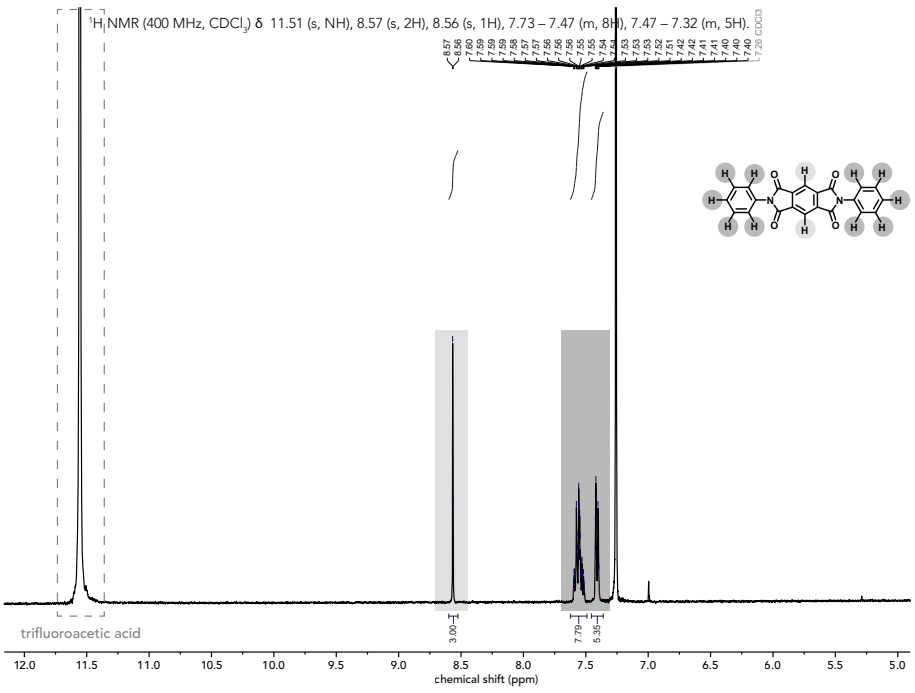

Figure A10: ^{1}H-NMR spectrum of PMA-An.

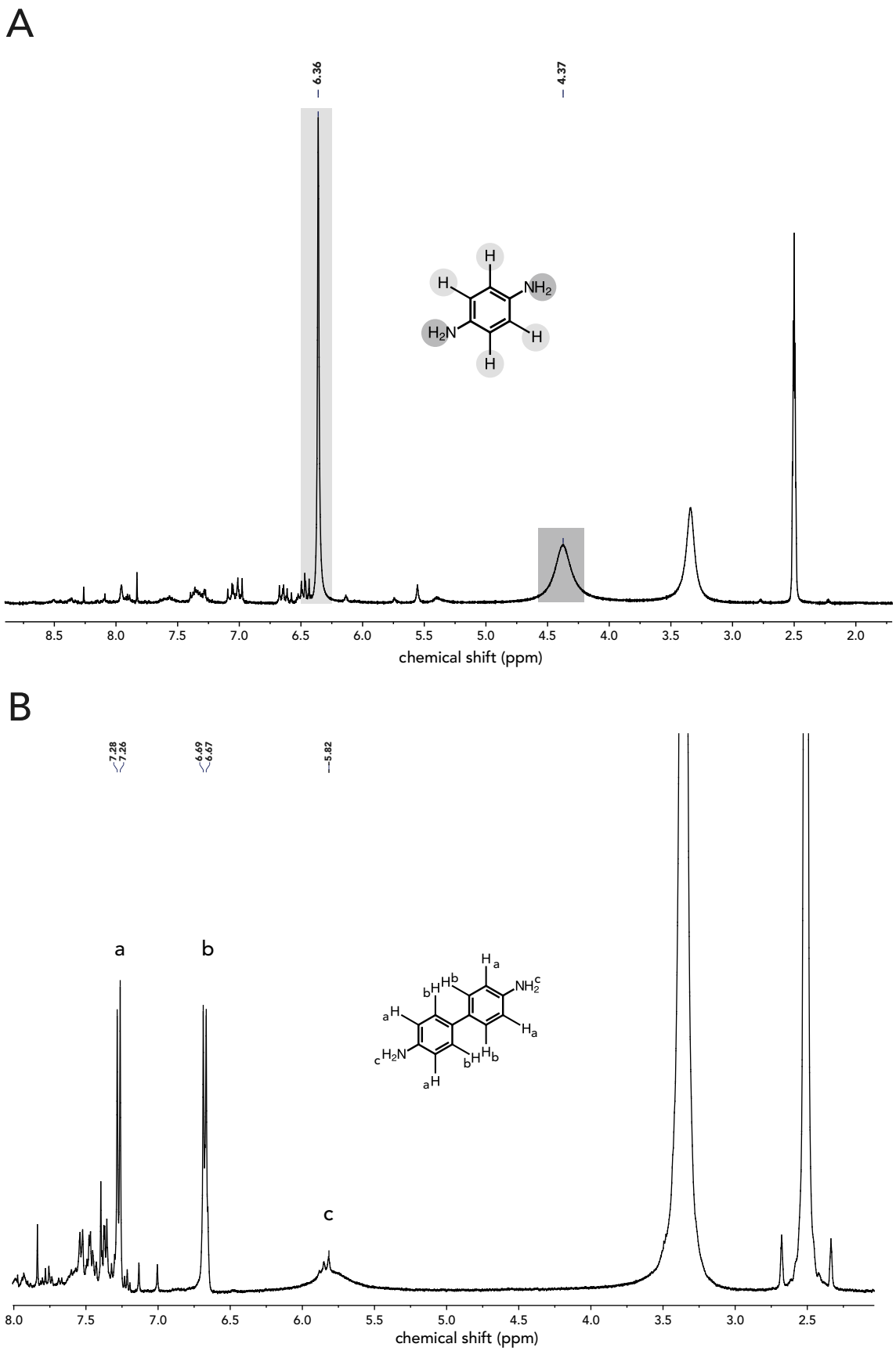

Figure A11: ^{1}H-NMR spectrum of the sublimated phases after ITT-MS of A: PI-HOF(MA-PDA) and B: PI-HOF(MA-Bz).

A.2.5 Scanning Electron Microscopy Images

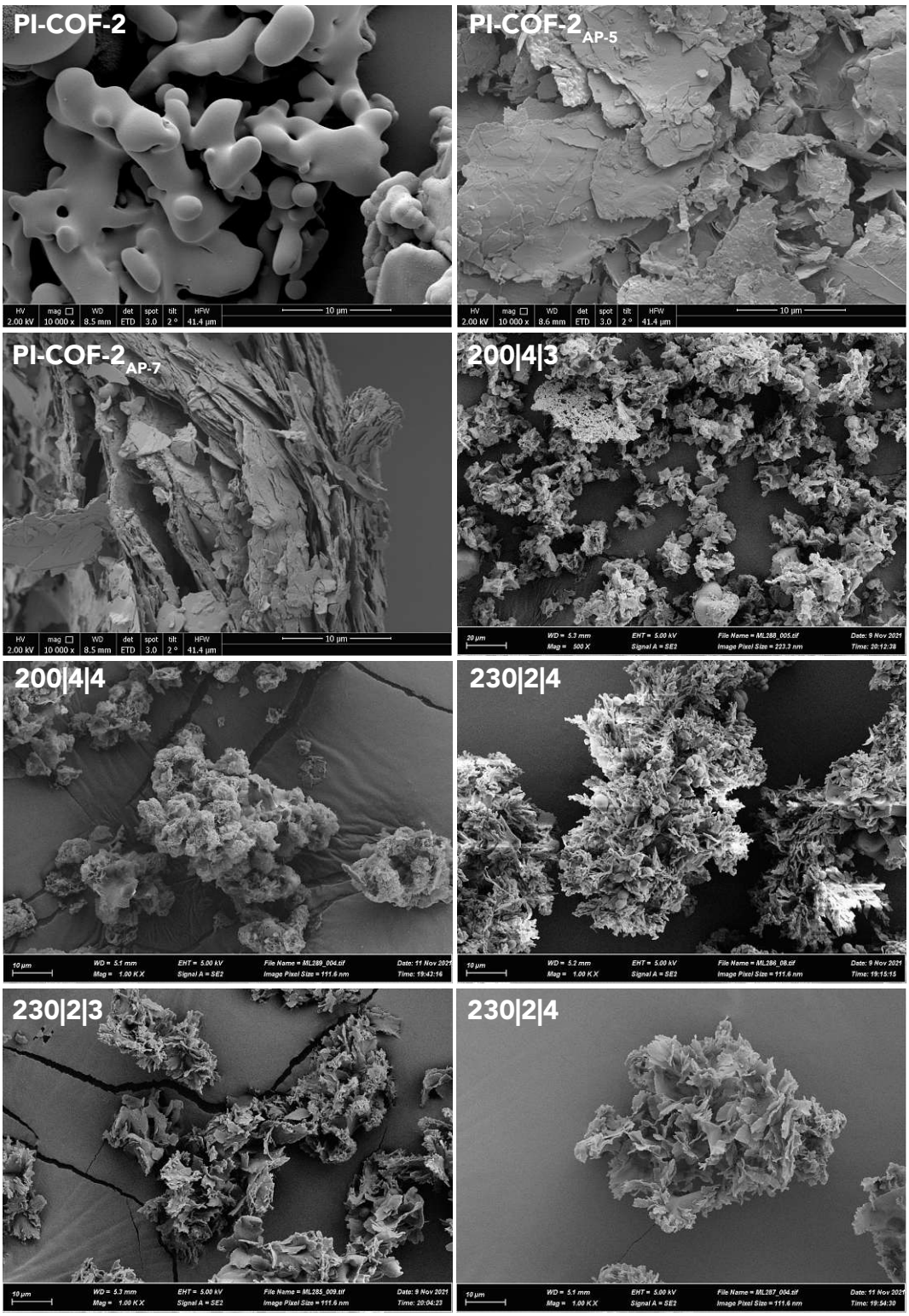

Figure A12: SEM images of PI-COF-2 benchmark, PI-COF-$2_{\text{AP-5}}$, PI-COF-$2_{\text{AP-7}}$ and microwave samples with stoichiometric amounts of aniline added (sample code: $T_{\text{R}}|t_{\text{R}}|$equiv. aniline).

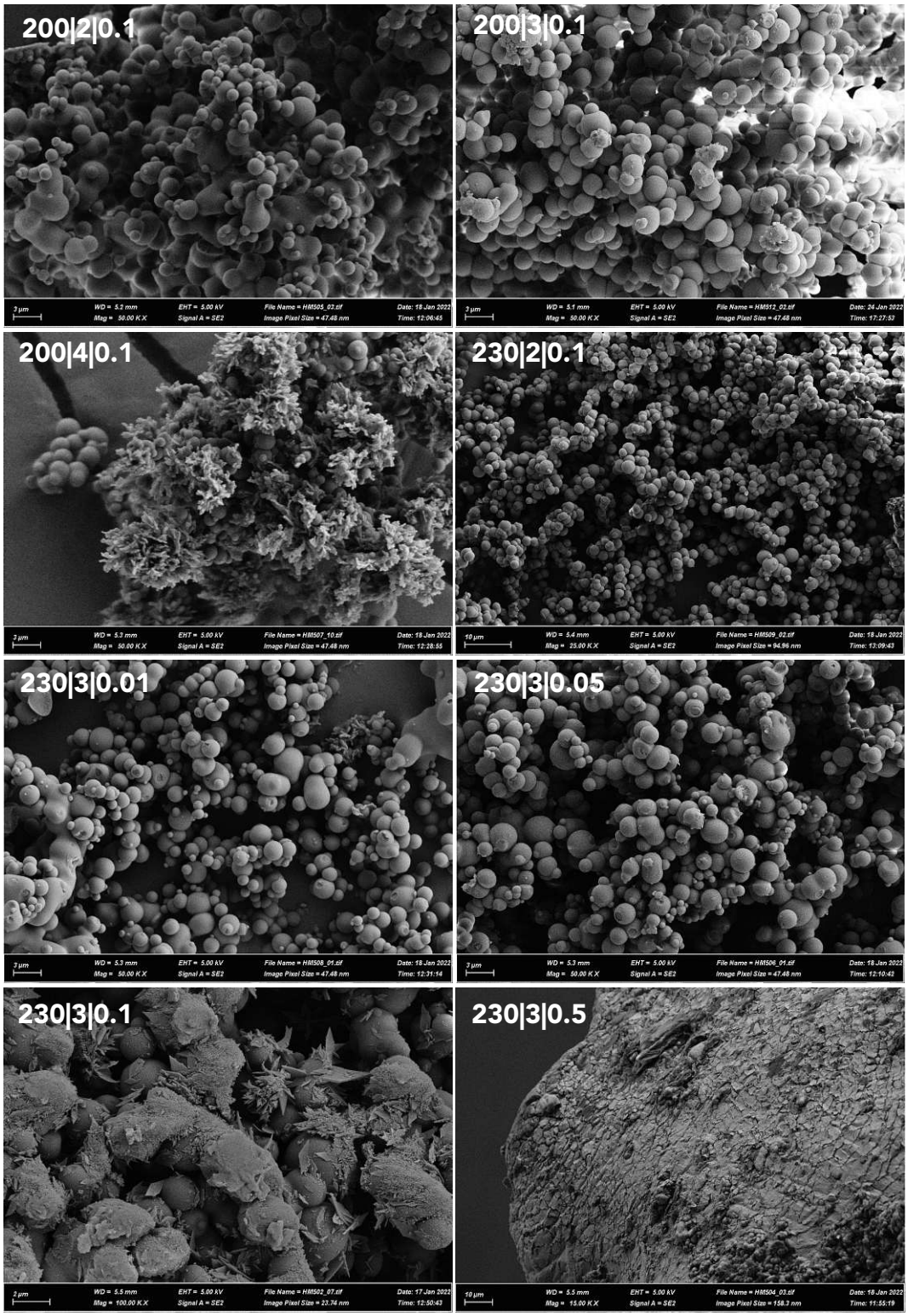

Figure A13: SEM images of PI-COF-2 samples via aaHTP-MW with stoichiometric amounts of aniline added (sample code: $T_R|t_R|$equiv. aniline).

A.2.6 Energy Optimized 3D Structures

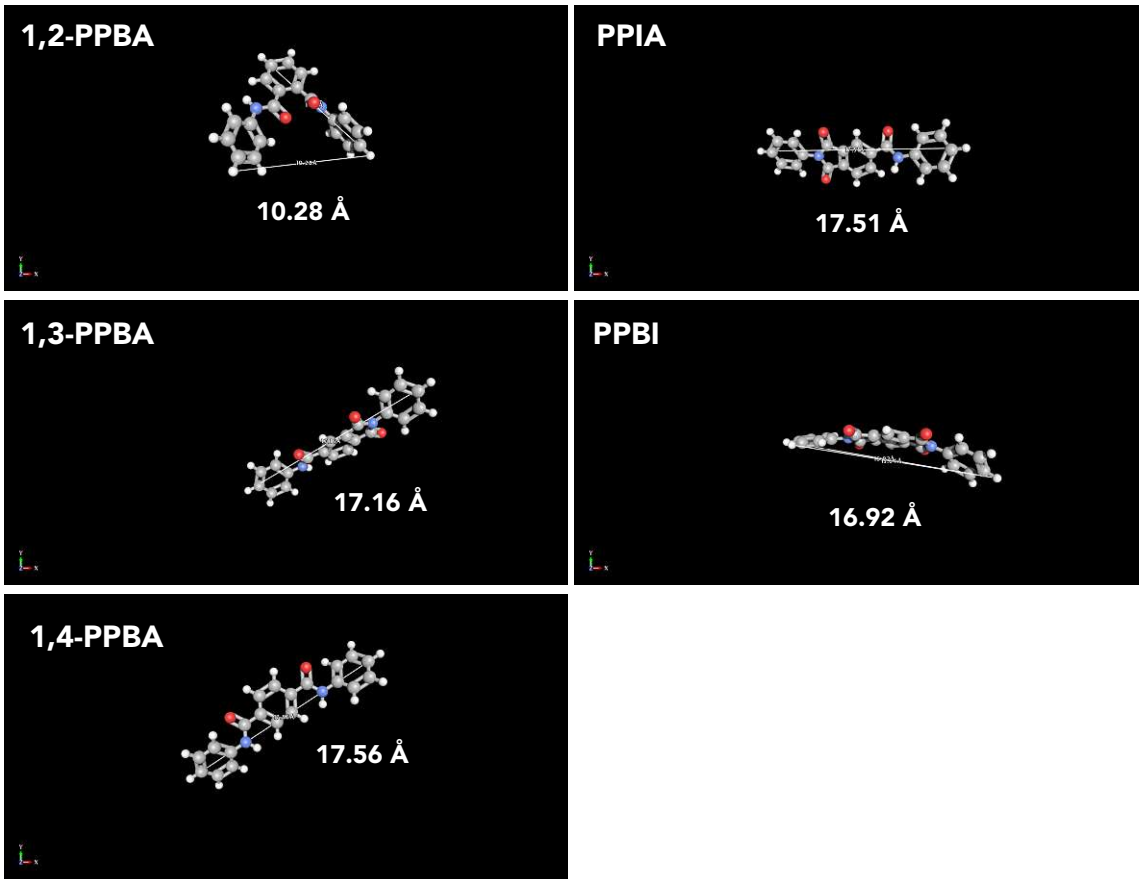

Figure A14: Energy optimized 3D structures of PMA-An: 1,2-PPBA, 1,3-PPBA, 1,4-PPBA, PPIA, and PPBI obtained via GAFF minimization in ChemDoodle 3D.

B Experimental

B.1 Instruments and Methods

B.1.1 Attenuated Total Reflectance Fourier Transform Infrared Spectroscopy

Attenuated total reflectance Fourier transform infrared (ATR-FTIR) spectra were recorded on a Bruker Tensor 27 working in ATR MicroFocusing MVP-QL with a diamond crystal. Resolution was set to $4\,cm^{-1}$ and spectra were recorded from $4000\,cm^{-1}$ to $500\,cm^{-1}$.

B.1.2 Powder X-Ray Diffractometry

Reflection Measurements
A PANalyticalX'Pert Pro multi-purpose diffractometer (MPD) in Bragg Brentano geometry operating with a Cu anode at 45 kV, 40 mA and an X-Celerator multichannel detector was used. Samples were in most cases ground and mounted as loose powders on silicon single crystal sample holders. For some samples with extremely low density, Vaseline was used for mounting. The method used for recording diffraction patterns between 1 and 30 °(2θ) employed 74.970 s/step, and the method used for patterns between 5 and 60 °(2θ) employed 160.0 s/step. Both methods comprised of a step size of 0.0201° and sample holders were rotated with 4 s/turn during the measurement.

Transmission Measurements
A PANalytical Empyrean Series 2 diffractometer in transmission mode operating with a Cu anode at 45 kV, 40 mA and a GaliPIX3D detector was used. Samples were fixed in between two Kapton tapes. The method used for recording diffraction patterns between 1 and 30 °(2θ) employed 87.68 s/step and a step size of 0.0143°.

B.1.3 Small Angle X-Ray Scattering

SAXS experiments were performed in a Nanostar (Bruker AXS) with X-rays from a microfocus source (Incoatec, High Brilliance, Cu-Kα radiation ($\lambda = 0.1542\,\mathrm{nm}$)) and a 2D position sensitive detector (Vantec 2000, Bruker AXS). SAXS data were collected at two to three different sample-to-detector distances (108 cm, 28 cm, 13 cm) to cover a wide q-range. The ground powders were placed between two tapes and measured for 600 or 1200 under vacuum, depending on the scattering intensities of the samples and the sample-to-detector distances. SAXS patterns of the samples and the background (the tapes) were radially integrated to determine the SAXS intensities in dependence of the scattering vector $q = (\frac{4\pi}{\lambda}) \cdot \sin\theta$, with 2θ being the scattering angle and $\lambda = 0.1542\,\mathrm{nm}$ the X-ray wavelength. The background was subtracted with a factor taking the transmission of sample and background into account. The factor was obtained from intensities of the primary beam measured with a partly transparent beamstop. All patterns were azimuthally integrated.

Additional wide angle X-ray scattering (WAXS) experiments were performed to determine the crystalline structure, in the same equipment as for SAXS, but data were collected with an image plate system (FUJI FLA 7000). The image plate has a small hole for simultaneous SAXS/WAXS measurements. By this, additionally the sample position can be controlled. The measurement time was increased to 1800 seconds. The whole system operates in vacuum, which reduces the background. Background correction was performed analogous to the SAXS evaluation by integrating the WAXS patterns for the samples and the background (tape without sample) and subtracting the latter with the correct transmission factor.

B.1.4 Differential Scanning Calorimetry

DSC measurements were performed on a DSC832 Mettler Toledo machine with a heating rate of $5\,\mathrm{K\,min^{-1}}$ and a nitrogen gas flow of $10\,\mu\mathrm{l\,min^{-1}}$. The temperature ranged measured was 30-400 °C.

B.1.5 Thermogravimetric Analysis

Thermogravimetric analysis was carried out using a Netzsch TG 209 analyzer at a heating rate of $10\,\mathrm{K\,min^{-1}}$ under nitrogen atmosphere, equipped with NETZSCH Proteus (Version 4.3) software.

B.1.6 Inert Thermal Treatment Coupled to Mass Spectrometry

A quartz glass reactor was equipped with a temperature-controlled heating mantle. The gases formed during the heating process were led through a connection to a mass spectrometer using 30 mL min^{-1} of either He or Argon. The investigated T-range was 25-900 °C.

B.1.7 Organic Elemental Microanalysis

The composition of the samples was characterised by organic elemental microanalysis. C, H, N and S were measured simultaneously using an Eurovector EA 3000 CHNS-O instrument (2007). The oxygen-content was measured using high temperature pyrolysis in a HT 1500 system (Hekatech, 2012) in combination with the EA 3000.

C/H/N/S-Analysis

0.75 to 2.5 of sample was weighed in using a tin foil vial which was wrapped to prevent material loss. The instruments uses "flash combustion" at 1.000 °C to digest the material at elevated oxygen pressure using high purity helium as carrier gas. The analyte species CO_2, H_2O are formed with WO_3 (tungstic oxide) on Al_2O_3 oxidation catalyst. Under these conditions, NO_x and SO_x are the products formed from nitrogen and sulphur. These substances are reduced at elemental copper and totally converted to elemental nitrogen (N_2) and SO_2. The copper also serves as trap for excess oxygen. The resulting gas mixture is transferred on line to a gas chromatography (GC)-column with Thermal Conductivity Detection (TCD).

O-Analysis

0.75 to 2.0 mg of sample were prepared in silver foil vials which has a very low O-blank. The material is reduced on granulated carbon at 1.480 °C in high purity helium. Carbon monoxide (CO) is the only oxygen compound resulting under these conditions. The product gas passes a freezing trap in liquid nitrogen and is analysed using a molecular sieve GC-column and a TCD. Nitrogen and hydrogen are clearly separated from the analyte peak.

Data Evaluation

The chromatograms from both analytical methods are transformed to ASCII-tables and evaluated using laboratory developed software and scripts (SCADA 5.99, 1995). Peak areas are used for quantification. Calibration is based on a minimum of two different reference substances using NIST certified standard reference material. Groups of four to six standard measurements are used after 12 to 15 analytical runs. Blank

values are taken from empty sample vials. Box car averages of the calibration factors are used to compensate for the changing flow rate due to residual ashes in the reactor tube. The LOQ is 0.05 *wt.*% C, H, N and O and 0.02 for sulphur. The EA-methods' uncertainty depends on the concentration range but never exceeds an absolute value of ± 0.3 *wt.*%.

B.1.8 Nuclear Magnetic Resonance Spectroscopy

Solution ^{1}H-NMR Spectroscopy

1H-NMR spectra were recorded on a Bruker AC400 or AC600 spectrometer (400 and 600 MHz). Chemical shifts are reported in ppm (δ) relative to tetramethylsilane and calibrated using solvent residual peaks. Data are shown as follows: Chemical shift, multiplicity (s = singlet, d = doublet, t = triplet, q = quartet, *quin* = quintet, m = multiplet, b= broad signal), coupling constant (J, Hz) and integration.

^{13}C-CPMAS solid-state NMR Spectroscopy

The spectra were acquired on a Bruker Avance NEO 500 wide bore system (Bruker BioSpin, Rheinstetten, Germany) using a 4 mm triple resonance magic angle spinning (MAS) probe in a dual set-up. The resonance frequency for ^{13}C NMR was 125.78 MHz, and 500.22 MHz for ^{1}H, respectively. The MAS rotor spinning speed was set to 14 kHz. Cross polarization (CP) was achieved by a ramped contact pulse with a contact time of 3 ms. During acquisition ^{1}H was high power decoupled using SPINAL with 64 phase permutations. The chemical shifts are reported in ppm and are referenced external for ^{13}C to adamantane by setting the low field signal to 38.48 ppm.

B.1.9 Microscopy Methods

Light Microscopy

Light microscopy was carried out using a Leica microsystems microscope with input voltages 100-240 V ($\sim$15 W) and 50/60 Hz.

Scanning Electron Microscopy

SEM was carried out with a Quanta 200F FEI microscope. Typically, the samples were measured at 5 kV, with a working distance of 9 mm and spot size 2.0. Prior to imaging, samples were loaded onto carbon-tape on steel sample holders and coated by sputtering with a 17 nm thick layer of Au/Pd 60/40 alloy with a Quarum Q105T S sample preparation system.
Images for part of the samples from Chapter 4.2.4 were acquired in a field emission scanning electron microscope (SEM) Analytic SEM Zeiss Gemini 500 microscope, using 5 kV acceleration. Prior to the analysis, the powders were sprinkled over a carbon tape, and the samples were coated with a 17 nm layer of Au/Pd 60/40 alloy

in a Safematic CCU-010 LV Low Vacuum sputtering device.

Transmission Electron Microscopy
TEM measurements were carried out using a TECNAI F20 microscope equipped with X-FEG using 200 kV acceleration voltage. The sample was mounted on a carbon coated Cu-grid prior to measurement.

Helium Ion Microscopy
A "Zeiss Orion NanoFab" was used for measuring HIM. The powder was placed on a standard carbon tape. The measurement was done at UC Berkeley by Dr. Frances Allen.

B.1.10 Low Pressure Gas Sorption Measurements

N_2 as Analyzing Gas
Nitrogen adsorption/desorption using a Quantachrome Instruments Autosorb 1C, surface area analyser at 77 K. Samples were degassed at 140 °C for 24 h under vacuum before analysis. Brunauer-Emmett- Teller (BET) surface area was calculated in relative pressure range (p/p_0) from 0.05 to 0.35.

CO_2 as Analyzing Gas
Low pressure CO2 physisorption isotherms were measured volumetrically at 195 K and 273 K up to 1 bar using an Autosorb-IQ-MP from Quantachrome equipped with a Quantachrome CryoCooler for temperature regulation. Isotherm points chosen to calculate the BET surface area were subject to the consistency criteria detailed by Rouquerol.[38] The pore size distribution was derived from the adsorption isotherms at 273 K using the Monte Carlo model for carbon adsorbents.

B.1.11 Mercury Intrusion Porosimetry

Mercury intrusion porosimetry was carried out using PASCAL 140/440, Thermo Fisher Scientifc. The pore size distribution of the benchmark PI(TAPB-PMA) (t_R = 24 h and T_R = 200 °C) and the warm pressed pellet, assuming a contact angle of 140 °. The benchmark PI(TAPB-PMA) exhibited a maximum intrusion pressure was 400 MPa, corresponding to a minimum accessible pore opening diameter of 4 nm. In case of the PI(TAPB-PMA) pellet, an apparent compression of the sample at intrusion pressures above 100 MPa was observed. Therefore, a compressibility correction was applied to the intrusion curve.

B.1.12 Warm Pressing

The powders were introduced into a steel cavity with an inner diameter of 40 mm and were uniaxially compacted at 80 MPa. As release agent between the steel punches and the powder, Kapton foil was used. The temperature of the die was increased to 350 °C (heating rate 6 K min^{-1}), and the maximum temperature was held for 2 h. The pressure was adjusted accordingly when required. After cooling to room temperature, the pressure was reduced and the compacted part was removed from the mold.[217]

B.1.13 Flexural Strength Measurements

A three-point flexural test set-up, following EN ISO 178 was used. Test specimens with dimensions of 5 x 1.6 x 30 mm were obtained using a diamond cutting disc. A total of three specimens were tested until fracture using a crosshead speed of 1 mm min^{-1} (Universal testing machine Model 1474, Zwick, Germany).

B.2 Syntheses

B.2.1 Chemicals

Pyromellitic acid (PMA, >98 %, Merck), *p*-phenylene diamine (PDA, 98 %, TCI), benzidine (Bz, 98 %, Sigma Aldrich), phthalic anhydride (PA, 99 %, Sigma Aldrich), 4-methylphthalic anhydride (MPA, 95 %, Sigma Aldrich), 1,3,5-tris(4-aminophenyl)benzene (TAPB, 97 %, TCI) were purchased and used as received. Aniline (Sigma Aldrich) was distilled prior to usage. For HTP, deionized and degassed (using argon) water was used.

B.2.2 General Procedures

Monomer Salt Synthesis

(*i*) MS(TAPB-PMA) Synthesis in Water

TAPB (1 equiv., 1 mmol) and PMA (1.5 equiv., 1.5 mmol) were weighed in to a round bottom flask and suspended in 10 mL of deionized water. The white suspension was stirred at room temperature overnight. In the course of the reaction, the suspension turned green. The solid was filtered, washed with water and very little acetone and subsequently dried in vacuo. Yield: 785,3 mg (54 %). ^{1}H NMR (600 MHz, DMSO-d_6) δ 8.02 (s, 6H), 7.52 (s, 6H), 7.51 (d, 12H), 6.73 (d, J = 8.4 Hz, 12H) ppm.

(*ii*) MS(MA-Bz)/(MA-PDA) Synthesis in Water
Amine (PDA or Bz, 1.5 equiv.) and MA (1 equiv.) were weighed into a round bottom flask and suspended in 10 mL of deionized and degassed water under N_2 atmosphere. The white suspension was stirred at RT overnight. The pale violet solid was filtered, washed with cold water and subsequently dried in vacuo at 80 °C overnight. Note that MS(MA-Bz) still contained residual unreacted Bz, which could not be removed by washing.

(*iii*) MS(MA-Bz)/(MA-PDA) Synthesis in THF/H_2O
Amine (PDA or Bz, 1.5 equiv.) was dissolved in 3 mL THF and MA (1 equiv.) was dissolved in THF/H_2O (3:2 mL). The amine solutions were added respectively to the solution of MA, and in both cases a precipitate formed immediately. The precipitate was pale violet for MS(MA-Bz) and off-white for MS(MA-PDA). The suspension was stirred at RT for one hour. The solids were filtered, washed thoroughly with THF and acetone, and then dried *in vacuo* at 80 °C overnight.

Hydrothermal Polymerization
HT experiments at $T_R = 200$ °C were performed in Teflon-lined Parr Instruments general purpose acid digestion vessels with $V = 45$ mL, experiments at $T_R = 250$ °C were performed in Berghof DAB-2 Pressure Digestion System vessels with with textitV = 50 mL a Teflon inlet with $V = 25$ mL. All autoclave systems were used with boroxine- and quartz glass liners with $V = 20$ mL. Microwave assisted HTP was carried out in a Anton Paar Monowave 400 using G30 vessels and Anton Paar Multiwave Pro using N8QX vessels. HTP in ampoules was carried out using borosilicate glass tubes with a length of approximately 10 cm and a diameter of 2 cm, wall thickness ∼2 mm and a total volume of roughly 20 mL.

HTP-AC of PI(TAPB-PMA)
TAPB (1 equiv., 0.2 mmol) and PMA (1.5 equiv., 0.3 mmol) were weighed into a glass liner and suspended in 10 mL H_2O. After ultrasonication for 10 min, the glass liner was sealed in a steel autoclave and heated to 200 °C or 250 °C for 2-168 h under autogenous pressure (∼18 and 40 bar, respectively). The brownish precipitate was filtered via a Büchner funnel (13-15 μm particle retention) and washed with water, acetone (techn.) and THF. Afterwards ∼75 mg of the product (ranging from brown powder to spongy monolith depending on the conditions) was dried at 80 °C in a vacuum oven overnight.

HTP-AC of MA-PDA and MA-Bz
MA (1 equiv., 0.2 mmol) and the corresponding amine (PDA or Benzidine, 1.5 equiv., 0.3 mmol) were weighed into a glass liner and suspended in 10 mL H_2O. After ultrasonication for 10 min, the glass liner was sealed in a steel autoclave and heated to 200 °C or 250 °C for 2-168 h under autogenous pressure (∼18 and

40 bar). The precipitate was filtered via a Büchner funnel (13-15 μm particle retention) and washed subsequently with water, acetone (techn.) and THF. Yields: Y(PI-HOF(MA-PDA), 200 °C, 24 h) = 75 mg; Y(PI-HOF(MA-Bz), 200 °C, 24 h) = 170 mg. The products (dark brown and beige powders) were dried at 80 °C in vacuo oven overnight, prior to further analysis.

HTP-AC of PBPI ref.

PMA (1 equiv., 0.2 mmol) and Benzidine (1 equiv., 0.2 mmol) were weighed into a glass liner and suspended in 10 mL H_2O. After ultrasonication for 10 min, the glass liner was sealed in a steel autoclave and heated to 200 °C for 24 h under autogenous pressure ($\sim$ 18 and 40 bar). The precipitate was filtered via a Büchner funnel (13-15 μm particle retention) and washed subsequently with water, acetone (techn.) and THF. Yield = 51 mg. The product (beige powder) was dried at 80 °C in a vacuum oven overnight, prior to further analysis.

HTP-AP of PI-COF-2$_{AP}$

TAPB (1 equiv., 0.2 mmol) and PMA (1.5 equiv., 0.3 mmol) were weighed into a borosilicate glass ampoule and suspended in 10 mL degassed H_2O. Aniline (0-15 equiv.) was added and then the reaction mixture was sonicated for 5 min. After 3-4 freeze-pump-thaw cycles, the ampoule was flame-sealed under vacuum. The ampoules were placed in a 1 L steel batch autoclave filled with 300 mL deionized water. The batch autoclave was heated to 200 °C and held at that temperature for 72 h. Afterwards, the reactor was cooled down to RT and the ampoules cracked open. The product was collected (in some cases two phases could be manually separated) via filtration using a Büchner funnel. The product was washed with water, acetone (techn.), and ethanol. Subsequently, the product was Soxhlet extracted in THF overnight. Finally, the product (brown powder) was dried overnight, in vacuo, at 80 °C.

HTP-MW of PI(TAPB-PMA)

(i) HTP-MW using Monowave 400

TAPB (1 eq., 0.2 mmol) and PMA (1.5 equiv., 0.3 mmol) were weighed into a microwave reactor (Anton Paar, G30) and suspended in 10 mL H2O. After adding a stirring bar, the reactor was closed with a cap including a PTFE septum and placed in the microwave. The vessel was heated as fast as possible to 200 °C, stirred with 600 rpm, and held at that temperature for 4 h. Upon heating the reaction mixture turned first green, then blue and finally, when the temperature was reached, a brown precipitate was formed. Afterwards, the reactor was cooled down to 70 °C and the brown precipitate was collected via filtration over a Büchner funnel. The product was washed with water, acetone, ethanol and THF. Finally, the product (brown powder, $\sim$ 73 mg) was dried overnight, in vacuo, at 80 °C.

(*ii*) HTP-MW using Multiwave Pro

TAPB (1 eq., 0.8 mmol) and PMA (1.5 equiv., 1.2 mmol) were weighed into a microwave reactor (Anton Paar, N8QX), suspended in 40 mL H_2O and a stirring bar was added. In total four of these reactors were put in to the Anton Paar Multiwave Pro and heated within 20 min to 250 °C and held there for 4 h while stirring on the highest level. Afterwards, the reactors were cooled down to 70 °C using compressed air. The reactors were opened, the brown powders of all four reactors were collected via filtration over a Büchner funnel, washed with water, EtOH and acetone (techn.). The procedure was repeated four times and the 16 batches were combined. The product was then dried in vacuo. Total yield: 7.364 g.

aaHTP-MW of PI-COF-2

TAPB (1 equiv., 0.2 mmol) and PMA (1.5 equiv., 0.3 mmol) were weighed into a microwave reactor (Anton Paar, G30) and suspended in 10 mL degassed H_2O. Aniline (0.01-4 equiv.) was added and then the reaction mixture was sonicated for 5 min. After adding a stirring bar, the reactor was closed with a cap including a PTFE septum and placed in the Anton Paar Monowave 400. The vessel was heated as fast as possible to 200 or 230 °C, stirred with 600 rpm, and held at that temperature for 1-4 h. Afterwards, the reactor was cooled down to 70 °C and the brown precipitate was collected via filtration. The product was washed with water, acetone, and ethanol. Finally, the product (brown powder) was dried overnight, in vacuo, at 80 °C. Yield: ∼95 mg.

PMA-An Synthesis

PMA (1 equiv., 0.8 mmol) was weighed into a microwave reactor (Anton Paar, G30) and suspended in 10 mL degassed H_2O. Aniline (2 equiv., 1.6 mmol) was added and then the reaction mixture was sonicated for 5 min. After adding a stirring bar, the reactor was closed with a cap including a PTFE septum and placed in the Anton Paar Monowave 400. The vessel was heated as fast as possible to 230 °C, stirred with 600 rpm, and held at that temperature for 1 h. Afterwards, the reactor was cooled down to 70 °C and the off-white precipitate was collected via filtration over a Büchner funnel. The product was washed with water, acetone (techn.), and ethanol. Finally, the product (off-white powder) was dried overnight, in vacuo, at 80 °C. Yield: 211 mg (72.5 %, if no mixture was obtained). ^{1}H NMR (400 MHz, $CDCl_3$) δ 11.51 (s, NH), 8.57 (s, 2H), 8.56 (s, 1H), 7.73 – 7.47 (m, 8H), 7.47 – 7.32 (m, 5H) ppm.

Model Compound Synthesis (MC1 and MC2)

TAPB (1 equiv., 0.2 mmol) and phthalic anhydride (MC1) or methyl-phthalic anhydride (MC2) (4 equiv., 0.8 mmol) were weighed into a microwave reactor (Anton Paar, G30) and suspended in 10 mL degassed H_2O. After adding a stirring bar, the reactor was closed with a cap including a PTFE septum and placed in the Anton Paar Monowave 400. The vessel was heated as fast as possible to 230 °C,

stirred with 600 rpm, and held at that temperature for 2 h. Afterwards, the reactor was cooled down to 70 °C and the brown precipitate was collected via filtration. The product was washed with hot water (80 °C), ethanol, and acetone (techn.). Finally, the product was dried overnight, in vacuo, at 80 °C. Yield: MC1 = 70 mg (47 %); ^{1}H NMR (400 MHz, $CDCl_3$) δ 8.10 – 8.00 (m, 3H), 7.97 – 7.79 (m, 12H), 7.52 (dd, = 8.7, 1.8 Hz, 12H) ppm. MC2 = 73 mg (47 %); ^{1}H NMR (400 MHz, $CDCl_3$) δ 8.00 – 7.79 (m, 19H), 7.70 (d, J = 7.6 Hz, 4H), 7.57 – 7.44 (m, 7H), 2.61 (s, CH_3) ppm.

Imide Exchange Reaction in HTP Conditions

MC1 (1 equiv., 0.05 mmol) and MC2 (1 equiv., 0.05 mmol) were suspended in 10 mL degassed H_2O in a glass vial. After sonicating for 5 min, it was sealed in a steel bomb autoclave (Parr) and kept in an oven at 200°C overnight. After the reactor cooled down to RT, the brown powder was filtered and washed with hot water, ethanol, and acetone (techn.). Finally, the product was dried overnight, in vacuo, at 80 °C. Yield: 63 mg. ^{1}H NMR (400 MHz, $CDCl_3$) δ 8.10 – 8.00 (m, 7H), 7.98 – 7.80 (m, 30H), 7.76 – 7.63 (m, 4H), 7.56 –7.43 (m, 15H), 2.61 (s, 9H), 2.59 (s, CH_3) ppm.

C | List of Publications

Publications

(3) N. Goujon, M. Lahnsteiner, D. A. Cerrón-Infantes, H. M. Moura, D. Mantione, M. M. Unterlass*, and David Mecerreyes*: "Dual redox-active porous polyimides as high performance and versatile electrode material for next-generation batteries", *Mater. Horiz.*, **2023**, doi: 10.1039/D2MH01335E

(2) M. Lahnsteiner, M. Caldera, H. M. Moura, D. A. Cerrón-Infantes, J. Roeser, T. Konegger, A. Thomas, J. Menche, and M. M. Unterlass*: "Hydrothermal Polymerization of Porous Aromatic Polyimide Networks and Machine Learning-Assisted Computational Morphology Evolution Interpretation", *J. Mater. Chem. A*, **2021**, 9, 19754-19769. doi: 10.1039/d1ta01253c

(1) M. Lahnsteiner, A. Kastner, J. Mayr, A. Roller, B. K. Keppler, and C. R. Kowol*: "Improving the Stability of Maleimide-Thiol Conjugation for Drug Targeting", *Chem. Eur. J.* **2020**, 26, 15867-15870. doi: 10.1002/chem.202003951

Conference Contributions

(4) "Monodisperse porous polyimide network particles: No need for crystallinity?", M. Lahnsteiner, H. M. Moura and M. M. Unterlass, **Symposium on Porous Organic Polymers 2019** (POPs 2019), 9^{th}-12^{th} September, 2019, Heidelberg, Germany.

(3) "Chemical Synthesis in Hot Water- A Method for Sunstainable Chemical Production?" Marianne Lahnsteiner, D. Alonso Cerrón-Infantes, Hipassia M. Moura, Patrick W. Fritz, Musthafa M. Iqbal, Olivier Gazil, Elias K. Bumbaris, Miriam M. Unterlass. **20. Österreichischer CCCA Klimatag**, 24^{th}-26^{th} April 2019, TU Wien, Vienna Austria.

(2) "Chemical Synthesis in Hot Water- A Method for Sunstainable Chemical Production?" Marianne Lahnsteiner, D. Alonso Cerrón-Infantes, Hipassia M. Moura, Patrick W. Fritz, Musthafa M. Iqbal, Olivier Gazil, Elias K. Bumbaris, Miriam M. Unterlass. **International Symposium: Global Sustainable Development Goals in a Mediatized World**, April 4^{th} – 5^{th} 2019, Austrian Academy of Sciences, Vienna, Austria

(1) "The Hydrothermal Route to Polyimide Networks" Marianne Lahnsteiner, Hipassia M. Moura, Miriam M. Unterlass. **31. Deutsche Zeolith-Tagung Dresden**, March 6^{th}-8^{th} 2019, TU Dresden, Germany

AWARD

(1) Poster Prize at the 31. Deutsche Zeolith-Tagung 2019, TU Dresden, Germany